AFGL-TR-87-0066

Calculation of Source and Structural
Parameters at Regional and Teleseismic
Distances

Charl A. Langston

AD-A183 008

Pennsylvania State University
114 Kern Building
University Park, PA 16802

28 February 1987

Final Report
2 January 1985-2 January 1987

APPROVED FOR PUBLIC RELEASE; DISTRIBUTION UNLIMITED

AIR FORCE GEOPHYSICS LABORATORY
AIR FORCE SYSTEMS COMMAND
UNITED STATES AIR FORCE
HANSCOM AIR FORCE BASE, MASSACHUSETTS 01731

87 8 4 027

REPORT DOCUMENTATION PAGE

1a. REPORT SECURITY CLASSIFICATION	1b. RESTRICTIVE MARKINGS
Unclassified	A183008

2a. SECURITY CLASSIFICATION AUTHORITY	3. DISTRIBUTION/AVAILABILITY OF REPORT
	Approved for public release;
2b. OECLASSIFICATION/DOWNGRAOING SCHEDULE	distribution unlimited

4. PERFORMING ORGANIZATION REPORT NUMBER(S)	5. MONITORING ORGANIZATION REPORT NUMBER(S)
	AFGL-TR-87-0066

6a. NAME OF PERFORMING ORGANIZATION	6b. OFFICE SYMBOL (If applicable)	7a. NAME OF MONITORING ORGANIZATION
Pennsylvania State University		Air Force Geophysics Laboratory

6c. AOORESS (City, State and ZIP Code)	7b. AOORESS (City, State and ZIP Code)
114 Kern Building University Park, PA 16802	Hanscom AFB Massachusetts 01731

8a. NAME OF FUNOING/SPONSORING ORGANIZATION	8b. OFFICE SYMBOL (If applicable)	9. PROCUREMENT INSTRUMENT IOENTIFICATION NUMBER
AFGL		F19628-85-K-0010

8c. AOORESS (City, State and ZIP Code)	10. SOURCE OF FUNDING NOS.
Hanscom AFB, MA 01731	

PROGRAM ELEMENT NO.	PROJECT NO.	TASK NO.	WORK UNIT NO.
61101E	5A10	DA	AE

11. TITLE (Include Security Classification) Calculation of Source and Structural Parameters at Regional and Teleseismic Distances

12. PERSONAL AUTHOR(S) Langston, Charles A.

13a. TYPE OF REPORT	13b. TIME COVERED	14. OATE OF REPORT (Yr., Mo., Day)	15. PAGE COUNT
Final	FROM 1/2/85 TO 1/2/87	1987, February 28	322

16. SUPPLEMENTARY NOTATION

17. COSATI CODES			18. SUBJECT TERMS (Continue on reverse if necessary and identify by block number)
FIELD	GROUP	SUB. GR.	Synthetic Seismograms, Wave Number Integration, Source Parameters, Regional Wave Propagation, Waveguide Scattering, T-Matrix, Upper Mantle Structure, Australia, India

19. ABSTRACT (Continue on reverse if necessary and identify by block number)

Wave number integration and generalized ray theory methods for computation of synthetic seismograms have been used to model short-period local and near-regional seismograms from small (Ml 2.5 - 4.0) earthquakes located in Australia and India. When the effect of crustal structure is adequately known, source depth can be determined with an accuracy of 1 km or less from sP and Rg wave arrivals within the observed wave forms. The determination of source depth directly from the wave form data offers a method of discrimination of explosives from earthquakes using sparse station distribution since it is unlikely that explosions will be emplaced below depths of a few kilometers.

A method for computing the wavefield for SH and P-SV line sources in an elastic layer-over-halfspace model with corrugated boundaries has been developed to study the effect of imperfections in a crustal waveguide. The formulation allows the computation of the wave field at any point within the model. The formulation is appropriate for the study of scattered high frequency crustal phases such as Pg and Lg and mantle phases such as Pn and

20. DISTRIBUTION/AVAILABILITY OF ABSTRACT	21. ABSTRACT SECURITY CLASSIFICATION
UNCLASSIFIED/UNLIMITED ☐ SAME AS RPT. ☒ OTIC USERS ☐	Unclassified

22a. NAME OF RESPONSIBLE INDIVIDUAL	22b. TELEPHONE NUMBER (Include Area Code)	22c. OFFICE SYMBOL
James Lewkowicz	(617) 377-3028	AFGL/LWH

DD FORM 1473, 83 APR   EDITION OF 1 JAN 73 IS OBSOLETE.

Block 19. Abstract (continued)

Sn.

Source parameters of selected earthquakes have been obtained from inversion of teleseismic body wave data for use in regional wave propagation studies. These included the 14 October 1968 Meckering, Australia, event and a suite of five moderate earthquakes occurring in Africa.

Upper mantle structure in the Eastern U.S. and Western Atlantic was examined using P waves from an intermediate depth earthquake under Hispaniola. The relative amplitude and timing of triplicated phases from the 670 km discontinuity observed in the data was used to refine existing velocity models for the area. The results of this study suggest that the locations of this upper mantle discontinuity is 670 km rather than 650 km as published in a previous study.

Table of Contents

List of Scientists Contributing to this Report

```
Charles A. Langston  - Principal Investigator
Vijay K. Varadan    - Faculty Associate
Vasundra V. Varadan - Faculty Associate
Akhlesh Lakhtakia   - Research Associate
David J. Alves      - Research Assistant
Nancy L. Niemann    - Research Assistant
Kristin S. Vogfjord - Research Assistant
Gregory S. Wagner   - Research Assistant
```

Introduction

The analysis and understanding of short-period regional
phases from explosions and earthquakes is a major theme in CTBT
issues. If a total ban on underground testing is to be ade-
quately monitored, then the means must be available to discrimi-
nate between explosions and earthquakes down to very small seis-
mic magnitudes and at relatively short distances. Small seismic
magnitudes ensures that short-period data must be examined and
that high frequency wave propagation within various crustal
structures must be understood to unravel the source effect from
wave propagation effects.

A major effort in this research has been in the computation
of short-period synthetic seismograms to explain data from local
and regional earthquakes. In particular, Section 1 describes a
study of very shallow foreshocks and aftershocks associated with
the 1968 Meckering, Australia, earthquake. Vertical component
short-period seismograms were modeled in order to investigate the
excitation of depth phases within the P arrival and the excita-
tion of short-period Rg.

The purpose of this study was to find accurate depth discri-
minants in the local seismograms themselves rather than relying
on standard earthquake locations. This will be important in ana-
lyzing data from a sparse national network to determine source
type and depth. Depth is an important parameter in source dis-
crimination since the likelihood that an event is a presumed
explosion is small if the event can be accurately located below
several kilometers. In the Meckering study, both the existence

of sP in the P wave form as well as large Rg/S ratios served to produce very accurate depth estimates from single station data at ranges of 60 to 95 km from the source. The results of this study yielded several interesting conclusions concerning the nature of wave propagation in shield areas and in the tectonic implications of extremely shallow faulting during the Meckering event. Ancillary work was performed on the teleseismic and static uplift data associated with the Meckering main shock and is presented in Section 5.

Section 2 describes another study of near-regional wave forms from small foreshocks and aftershocks associated with the 1967 Koyna, India, earthquake. In this case, a different distance range as well as crustal structure was considered with the same goals in mind. Synthetic seismograms were computed to gain an understanding of the wave propagation at distances of 100 to 150 km in order to investigate possible depth-dependent phases in the observed data. This study was less successful because crustal triplications generally obscured the interference between direct and surface reflections in the body waves. General inferences on depth were possible if short-period Rg was observed in the data.

The general conclusion of these studies on short-period wave propagation was that short-period wave forms can be interpreted to infer source depth accurately if an appropriate distance range is available for the data and if wave propagation effects due to the crustal model are understood. This research will be extended in future work to consider data collected in other areas and at other distance ranges. It is conceivable that isolated phases, such as Pn, may be usefully modeled at short-periods to yield

accurate depth estimates.

Sections 3 and 4 are concerned with the theoretical development of a method to compute synthetic seismograms in layered media with corrugated boundaries. A layer-over-halfspace model was considered with the free surface of the layer allowed to be corrugated. SH and P-SV line sources were considered in Sections 3 and 4, respectively. This kind of problem is important in considering the effect of waveguide imperfections on the propagation of regional seismic phases of all types. The results show that even simple periodic corrugations cause very complex spectra for elastic waves. Displacements were considered on the free surface as well as in the lower halfspace.

A reconnaissance study was made of earthquake sources in the African continent and is presented in Section 6. The purpose of this study was to determine accurate earthquake source mechanisms and depths to use in analysis of regional wave forms from the same events. Although CTBT issues are mainly concerned with regional wave propagation in the Soviet Union, it is important to gain experience in effects of wave propagation in different crustal and mantle environments. Shield areas, for example, have certain similarities in Q and velocity structures. These similarities are stressed when it is important to infer the character of wave propagation in areas of the Soviet Union for which there is little data from the character of wave propagation in other, known areas. The African continent is an area which has not been studied in detail but has a nuclear test site as well as a network of stations and regional earthquakes. The results of Section 6 are being used in an on-going study of the depth effect in

regional seismograms.

Section 7 contains a study of upper mantle structure as determined by P wave forms. This work was supported by a previous AFOSR contract and carried over into the present AFGL contract. A basic premise in studies of body wave propagation in the upper mantle is the effect of the seismic source is sufficiently well known to infer the smaller effects of triplications due to mantle discontinuities. In this study, an intermediate depth earthquake which occurred beneath Hispaniola was used to examine the effect of mantle triplications for Eastern U.S. and Western Atlantic structure. It was thought that the effective source function of the intermediate depth event would be simpler than those used in previous studies since near-source reflections and reverberations could be avoided. In this way the mantle triplication effect would be more clearly seen. The results show that mantle effects are still difficult to model in the long-period P wave data even for this event. However, intermediate-period data recorded at DWWSSN stations clearly showed the triplication from the 670 km discontinuity. Such mantle studies would benefit from data recorded between standard long-period and short-period frequency bands.

SECTION 1

Depth of Faulting During the 1968 Meckering, Australia,
Earthquake Sequence Determined from Wave Form Analysis
of Local Seismograms

by

Charles A. Langston

December 3, 1986

Submitted to the Journal of Geophysical Research

Department of Geosciences
The Pennsylvania State University
University Park, Pennsylvania 16802

Abstract

Wave forms for eleven foreshocks and 48 aftershocks of the Ms 6.8 Meckering earthquake recorded at the WWSSN station MUN are analyzed to determine the depth distribution of faulting during this unusual intraplate earthquake sequence. Clear depth phases including sP and Rg are seen in the local seismograms at distances of 60 to 95 km and are studied using synthetic seismograms computed using generalized ray theory and wavenumber integration techniques. Large Rg/S ratios seen on the vertical component short-period data for many events imply source depths less than 2 km. The short-period P wave form contains the best depth estimator in the form of sP so that depth can be estimated to within an uncertainty of about 1 km for most events. The foreshocks cluster at less than 2 km depth and most aftershocks occur within 1 km of the surface. A few aftershocks occur as deep as 7 km. These results are consistent with a previous teleseismic wave form study in which faulting was inferred to start near the surface at 1.5 km depth with rupture proceeding downward and not exceeding 6 km depth. These results coupled with previous stress studies in the Australian shield and models of crustal strength show that faulting in a cold shield area is a near-surface phenomenon and implies that most of the crust is too strong to be fractured.

Introduction

The occurrence of intraplate seismicity represents an oppor-
tunity to examine the state of stress within the major plate
regimes of the earth as well as inferring mechanisms of failure
in the crust (Richardson et al, 1979; Bergman and Solomon, 1980).
However, intraplate seismicity is little understood in comparison
to seismicity associated with interplate areas. Models of epi-
sodic faulting on well defined faults along plate boundaries seem
to have little meaning when applied to earthquakes in apparently
nondescript areas of the plate interior. It is not entirely
clear what the role of prexisting faults is within many plate
interiors and what the source of stress is which ultimately
causes these events (e.g., Zoback and Zoback, 1980).

A stress model based on plate boundary forces and geometry
has had some success in explaining the directions of principal
stress inferred from stress measurements and fault plane solu-
tions of intraplate events in many of earth's plates (Richardson
et al, 1979; Cloetingh and Wortel, 1985). However, the questions
of failure mechanisms for continental intraplate earthquakes and
earthquake recurrence intervals have yet to be satisfactorily
addressed.

In this paper, the depth extent of faulting during the 1968
Meckering, Australia, earthquake sequence is examined to infer
patterns of crustal strength in an intraplate shield area under
substantial deviatoric stress. The Meckering main shock (Ms 6.8)
is one of the largest intraplate events to have been recorded and
also produced spectacular fault scarps within the southwest Aus-

tralian shield (Everingham and Doyle, 1969; Gordon, 1971; Gordon and Lewis, 1980). The main event was the subject of a teleseismic body wave study by Vogfjord and Langston (1987). Also incorporating a static dislocation model of published releveling measurements across the fault scarp, they determined that faulting during the main event did not exceed a depth of about six km. Interpretation short-period P waves also suggested that faulting initiated near the surface at about 1.5 km depth and propagated downward to a similar depth.

The unusual nature of extremely shallow rupture initiation, surface faulting, and limited depth extent of faulting was explained by a strength model of the crust after Meisner and Strehlau (1982) and Strehlau (1986). Measured heat flow in the area is about 40 mW/m^2 (Cull and Denham, 1979) suggesting that the crust is relatively cold and should fail in a brittle fashion following a frictional sliding strength relationship down to Moho depths. The brittle-ductile transition is substantially depressed compared to a crustal column with higher heat flow, which effectively makes the crustal strength almost everywhere much higher than plausible ambient stresses. Near surface stress measurements in the area (Denham et al, 1980) show relatively high deviatoric stress of about 20 MPa near the surface with an assumed depth gradient less than the strength curve implied by frictional sliding. The only area within the crust that can fail, according to this model, is within a few km of the surface where deviatoric stress exceeds the crustal strength. This model is significantly different from models proposed for interplate faulting where aseismic slip on a fault in the brittle-ductile

transition of the lower crust eventually forces the brittle upper crust to fail in an earthquake (e.g., Strehlau, 1986).

Several questions naturally follow from Vogfjord and Langston's(1987) study as well as implications of the proposed strength model. First, it is important to determine whether the rupture initiation point of the main event was near the top of the fault plane or elsewhere. The short-period modeling study was somewhat ambiguous due to the occurrence of a substantial foreshock a few seconds before the onset of large fault motions. Second, it is also useful to check the inferred depth of faulting of the main event. Third, the crustal strength model implies that most events within the Southwest Australian seismic zone have source depths no greater than a few km. The only exception should be large events like the Meckering earthquake which can dynamically rupture into relatively high strength areas of the crust. Thus, it is important to determine source depths for other events to test the model.

Short-period wave form data from Meckering foreshocks and aftershocks recorded at the WWSSN station at Mundaring, Australia, will be examined to determine source depth and to address the first two issues above. These source depth results coupled with studies of other moderate earthquakes in the area will also be used to partially address the implications of the strength model on source depths for the seismic zone. A major assumption of this study is that the foreshocks and aftershocks follow closely the faulting behavior of the main event. It will be assumed that if the foreshocks cluster at a certain depth, then this is the depth that rupture initiated during the main event.

The depth extent of aftershocks will be assumed to follow the
depth extent of faulting for the main event. It will be seen
that the foreshock and aftershock depths agree closely with
results from the teleseismic study.

The aftershock wave forms will be modeled utilizing pre-
viously determined velocity structure for the area and a wavenum-
ber integration technique to compute complete seismograms. The
excitation of short-period Rg and the body wave phase sP will be
used to precisely constrain source depths to within one km for
many of the events. The simplicity of the velocity structure and
its effect on wave propagation at ranges of 60 to 95 km makes the
study of these phases possible.

It will be demonstrated that even these short-period data
recorded at single station can be used to precisely constrain
some source parameters of small earthquakes. These methods may
find some use in the analysis of events recorded by sparse local
networks and in the discrimination of explosions from earth-
quakes. In the later case, discrimination can occur if an
event's depth is determined to be greater than a few km excluding
plausible scenarios for the emplacement of an underground nuclear
test (e.g. Dahlman and Israelson, 1977).

Foreshock and Aftershock Data

Figure 1 is a map of a portion of the Southwest Australian
seismic zone showing the location of Mundaring station (MUN) and
the fault and aftershock zone of the Meckering earthquake. Mun-
daring station is at a distance of 60 to 95 km from events asso-

ciated with the Meckering event and wave paths are entirely
within the Archean Yilgarn block of Australia. Immediately to
the west of Mundaring is the Perth basin bounded by the Darling
fault which underwent several kilometers of normal offset from
Permian time throughout the Mesozoic. See Gordon and Lewis(1980)
for an overview of geologic structure and history of the area.

The structure of this part of the Yilgarn block has been stu-
died by seismic reflection and refraction techniques and by gra-
vity interpretation (Mathur, 1974; Drummond and Mohamed,1986).
Table 1 displays crustal velocity structures determined from
these studies which will be incorporated in synthetic seismogram
calculations later in the paper. The crust between the Meckering
area and Mundaring appears to be relatively homogeneous with no
significant sedimentary section near the surface. Both struc-
tures show relatively high P-velocities of about 6.1 km/sec near
the surface indicative of the crystalline granitic terrain seen
in the surface geology. There is a substantial intermediate
velocity layer at 10 km depth in the Mathur(1974) model which
grades into a high velocity lower crust at only 17 km depth. The
more recent Drummond and Mohamed(1986) model is smoother showing
very small positive velocity gradients with depth and with an
area of higher gradient near 13 km. Topography between Mundaring
and Meckering shows very little relief.

A list of foreshocks and aftershocks above Richter magnitude
3.0 for the Meckering event was published in Gordon and Lewis
(1980) and was used to initially examine the WWSSN archives for
data recorded at MUN. An effort was made to obtain all principal
foreshocks and major aftershocks which occurred within three days

after the main event. Other events were obtained as available. In addition to events listed in Gordon and Lewis(1980), a significant number of somewhat smaller events were discovered and used in the analysis.

Events used in this study are listed in Table 2 by P arrival time at MUN. The S-P time and maximum trace amplitude on the vertical component were read where possible to estimate distance and local magnitude, respectively. Distance was computed using phase identifications from the synthetic seismogram computations. Local magnitude was computed using the Richter(1958) formula for California events and corrected for the WWSSN short-period instrument magnification at MUN. Magnitudes computed this way generally agreed with those listed in Gordon and Lewis(1980) to within 0.1 magnitude units, although Doyle et al(1968) state that local magnitude at MUN is computed using the maximum horizontal motions. The size of events examined in this study range from about Ml 2.5 to 4.2.

Locations for those events shown in Figure 1 were determined from data from a sparse regional network. Location error is probably better than 25 km (Doyle et al, 1968). Distance determinations used in this study relied on the S-P time and comparison with synthetics rather than the published locations. All observed events at MUN could then be treated in a consistent manner. S-P times could be read to at least 0.5 sec in all cases which implies a distance error of ± 4.5 km for either crustal model assuming a Vs/Vp ratio appropriate for a Poisson solid.

Figure 2 shows three-component wave forms for two aftershocks which occurred on 14 October. These data were hand digitized

from copies of the analog seismograms from MUN and accurately show the main features of the original seismograms. The two events shown are characteristic of the foreshock and aftershock data. A large number of events show close similarity to the 7:38 aftershock in which the vertical wave form contains a relatively small P arrival and a major secondary phase at about 12 seconds after P. A careful comparison of the horizontal components with the vertical shows that the S arrival is always about 9 seconds after P since most events are at similar distances. The large secondary arrival on the vertical component characteristically shows normal dispersion and arrives at the expected Rayleigh wave time for the crustal structure. It is very difficult to examine the relative phase of peaks and troughs of this Rayleigh wave between the vertical and horizontal components since the data are band limited by the WWSSN short-period instrument response. The data are also difficult to digitize because of typically high Rayleigh amplitudes for most events above local magnitude 3.0. However, a careful comparison of the vertical and EW components for this presumed Rayleigh phase seen in relatively small events shows retrograde elliptical motion. This Rayleigh phase is designated Rg in Figure 2 after Ewing et al (1957). They use the name Rg for the fundamental Rayleigh wave with periods of 8 to 12 seconds propagating within continents at regional distances. The Rg phase as used here is understood to be the fundamental Rayleigh wave at one second period seen at relatively short distance.

In comparison to the very simple wave form of the 7:38 event is the 8:38 event (Figure 2) which shows larger body wave phases relative to the expected Rg phase and greater overall complexity.

The P arrival appears to have at least two distinct arrivals within it compared to the 7:38 P wave and it is difficult or impossible to see the dispersion of Rg in the S wave coda. Events of this type are more rare than those displaying the large Rg phase.

Figure 3 displays six aftershocks showing the typical variability seen in the vertical wave form. Usually the Rg phase is well developed but may range in size from being comparable to the S wave amplitude to an order of magnitude larger than the S wave. Presumably, these relative amplitude variations are caused by different source mechanisms between events and source depth. The radiation pattern of each phase will depend on mechanism and the excitation of the Rg wave should be expected to decrease exponentially with source depth. The initial working hypothesis that is suggested by this cursory analysis of the data is that it may be possible to estimate bounds on the source depth from Rg relative amplitudes alone. The mitigating factors will be wave propagation effects for the body wave phases in the crust and the unknown source mechanism.

Only the vertical wave forms were used in the analysis that follows. Since these events are not accurately located and because of the practical difficulties of digitizing short-period data from analog records, the use of horizontal components of motion was confined to determining S arrival times. Any vector rotation of these horizontal data to obtain radial and tangential motions for study would probably be of very poor quality because of unknowns in back azimuth to the source due to epicenter error and because of the digitization. In fact, many of the Rg phases

shown in the figures were obtained by digitizing the peaks and troughs, which could be seen on the records, and then linearly interpolating for plotting purposes. The Rg analysis of all events was further simplified by simply measuring the peak-to-peak amplitudes directly from the seismogram. Likewise, P and S amplitudes were also read although the P wave form is used for another purpose below.

Synthetic Seismogram Calculation

Synthetic seismograms were computed to investigate the excitation of the Rg phase relative to the body wave phases as a function of source depth. Because the total wave field is needed for this problem, a wavenumber integration method was employed to compute the Green's functions required for constructing moment tensor point sources. Details of the technique may be found in Barker(1984) and Apsel(1979). An integral over real wavenumber is performed using an adaptive Filon method. The kernel of the integral contains a product of the vertical wave function and a Bessel function of integer order depending on the type of seismic source. The vertical wave function is computed using a propagator matrix formalism for plane elastic layers which are homogeneous and isotropic. Anelastic attenuation is included using complex-valued wave velocities. The moment tensor formalism given by Langston(1981, 1983) is used to combine the four Green's functions needed for computation of vertical displacement from a general moment tensor source.

Vertical displacement seismograms for ranges of 60 to 90 km

were calculated for the Mathur(1974) model of Table 1. The
short-period WWSSN instrument response and a Brune (1970) time
function with a corner frequency of 1 hz were convolved with
these displacement Green's functions to produce the final syn-
thetic seismograms. The wavenumber integration was carried out
over the interval between 0.01 and 0.4 sec/km (in ray parameter)
which was sufficient to include all body and surface wave phases
for the structure model. A Nyquist frequency of 5 hz was assumed
and 256 frequency samples computed to yield a time series after
inverse Fourier transforming of 512 points at 0.1 sec sampling.

Figure 4 displays vertical displacement synthetic seismograms
for a range of 80 km, the average distance of the foreshocks and
aftershocks from MUN. Wave forms for five different source
depths show that the excitation of the Rg wave decreases with
depth as expected, relative to the body wave phases, and is only
well developed for sources above 4 km depth. The character of
the wave forms for the 0.25 km source depth is similar to some of
the data wave forms of Figure 3.

At this point it should be mentioned that the original Mathur
(1974) crustal model did not have the thin low velocity layer at
the top of the section as shown in Table 1. Initial synthetic
seismogram calculations without the layer produced a single
undispersed Rayleigh pulse. The published refraction data did
not resolve the upper 0.5 km of the crust. However, the disper-
sion of the short-period Rg data clearly suggests that a posi-
tive velocity gradient exists near the surface. Theoretical dis-
persion curves given by Ewing et al(1957) were used to approxi-
mately match the observed dispersion and to obtain an equivalent

layer thickness for a layer with a modest velocity contrast
appropriate for near surface granitic rocks (Press, 1966). It
was important to produce a dispersed Rg wave form more in accord
with the data to investigate the amplitude dependence of the Rg
wave with near surface structure. Dispersion will tend to lower
maximum amplitudes since energy is spread out over time. How-
ever, the net effect of the lower velocities near the surface was
to increase amplitude in nearly the same amount that dispersion
decreased amplitude, in comparison to the body waves. The behav-
ior of the body waves remained the same between models.

Figure 5 shows the typical variation of relative amplitude
expected as a function of range. There are some changes in
relative amplitudes mainly due to structure effects on the body
waves. In fact, maximum amplitudes of the wave form appear
roughly constant over this distance range because of wide angle
reflections from the shallow intermediate crustal layer. This
overcomes the differences in geometric spreading expected by a
simple direct body wave $(1/r)$ and a simple surface wave $(1/r^{0.5})$.

It can be expected that variations in Q and scattering along
the path of transmission will affect Rg amplitudes. The Q struc-
ture assumed in the seismogram calculation is reasonable for a
continental area but may be somewhat high. However, a 1 hz sur-
face wave propagating over 80 km is only attenuated to about 80%
of its nominal value with this structure. Using a Q of 250
instead of 500 for shear waves reduces a 1 hz surface wave to 70%
of its unattenuated value. Scattering is probably minimal along
the path since topographic changes are minimal. Most effects of
scattering, if they occur, will tend to reduce surface wave

amplitudes while lengthening the surface wave coda with scattered energy. Thus, the seismograms presented here will maximize the expected Rg phase amplitudes. Any effects of Q and scattering will reduce the observed Rg amplitudes tending to make an event appear deeper than it really may be. Therefore, source depths interpreted from these synthetic Rg amplitudes will tend to be overestimated, all other factors being equal.

A straightforward interpretation of Figure 4 would suggest that Rg relative amplitudes of one or more are only possible for sources less than 4 km in depth. However, it is possible that source orientation may affect the amplitudes of all phases such that Rg may be near a radiation pattern minimum when the body waves are large, even for a very shallow source. To investigate this, a grid search process was set up to sample all possible fault orientations for Rg/S and Rg/P ratios. A 10 degree increment was assumed for changes in dislocation dip, rake, and strike. The maximum Rg, S, and P amplitudes were found for specified time windows of the synthetic seismogram which included these phases, ratios taken, and the ratios were then placed in bins with an integer interval. It was found that the Rg/S ratio was the most robust measure of source depth since it appeared possible to get nearly any Rg/P ratio for any source depth. This is logical since the Rayleigh wave from a dislocation source is closely tied to the shear wave potential and it is not difficult to produce nodal P waves for specified azimuths and incidence angles.

For a source depth of 0.25 km the range of Rg/S varied from 4 to 20. The range of values for Rg/S assuming other source depths

varied generally from 0 to a well defined maximum. Figure 6 shows the maximum Rg/S ratio as a function of source depth and range for these trials. This graph is to be interpreted as providing a maximum estimate for source depth based on a measured Rg/S ratio. High Rg/S ratios of 10 or greater imply sources with depths less than 2 km for observations within the assume distance ranges. A low Rg/S ratio may still be possible for a 2 km depth source but there is no way from the ratio itself to determine this. The low ratio will be interpreted as being due to a larger source depth with the understanding that this will be maximum estimate of depth.

In addition to the Rg wave depth effect, note the character of the body wave phases in Figure 4. As the source becomes deeper, the simple P pulse for near-surface sources splits into a distinctive double arrival. The isotropic source does not show this effect suggesting that the second arrival in the other synthetics is an S to P conversion. Indeed, an analysis of the P wave forms using ray and generalized ray theory shows that the secondary phase after direct P is the surface reflection sP.

Body wave phases may be expected to be sensitive to details of structure. In the Mathur(1974) model, the initial P arrivals are dominated by wide angle reflections from both top and bottom interfaces of the 6.7 km/sec layer (Table 1). Alternatively, the Drummond and Mohamed(1986) model consists of smooth gradient zones throughout the crust and would produce true turning rays. Figure 7 displays a synthetic P wave record section for a CLVD source at 4 km depth incorporating the velocity structure of both crustal models. These synthetics were computed used generalized

ray theory (Helmberger and Harkrider, 1978). The gradient model
was constructed by using a number of thin layers and responses
computed by summing all primary reflections from each interface
in the model.

Since the Mathur model consists of only a few discrete
layers, the wave forms show several small arrivals between P and
sP due to wide angle pP reflections from the two interfaces of
the 6.7 km/sec layer (column A, Figure 7). The gradient model
results (column B) display simpler wave forms overall but contain
the emergence of a phase at distances greater than 90 km. The
high velocity gradient near the Moho produces a triplication in
the wave form for these distances. Even with this complication,
sP is still an easily seen phase in the wave form. Overall, both
crustal models allow for the development of an unambiguous sP
phase. However, it is clear that relative amplitudes will depend
on model details. The phase pP is not well developed at this
range primarily because of the inefficiency of the free surface
reflection at the appropriate ray parameters. The S-to-P conver-
sion is near a maximum while P reflection is near a minimum.

These modeling results suggest that secondary phases in the P
wave form, if seen, will be sP. Source depth can be determined
from such arrivals by simply reading the sP-P time and using the
ray theory approximation

$$t_{sP-P} = H (\eta_\alpha + \eta_\beta)$$

to solve for depth. Here η_α and η_β are the vertical slow-

nesses for P and S waves, respectively. The appropriate ray parameter, p, is 1/6.2 sec/km. This equation was tested by using the wavenumber synthetic seismograms (e.g. Figure 4). The sP-P times were read from the synthetic wave forms, depth calculated from equation (1) and these values compared to the actual depths used in the synthetic calculations. The depth determined by ray theory agreed to within 0.5 km.

If sP phases can be seen, then it is possible to infer absolute source depth very accurately. Timing between peaks on observed wave forms can easily be read to 0.3 sec which gives a possible depth error of only 1 km. This will be taken to be the error of the determination if the separation between phases is clear. However, there still exists the possibility that other crustal structure arrivals, like the arrivals from the Moho of the Drummond and Mohamed model shown in Figure 7, may make this ambiguous. In this case, we rely on the data to make an argument in self-consistency. It was seen that events with the same S-P times can have a single P arrival, implying a very shallow source depth, or two clear P arrivals implying P and sP and a larger depth. Also, it was seen that events with a single P arrival occurred at ranges from 68 to 89 km implying that the Drummond and Mohamed model may need some modification in structure near the Moho to push the triplication out to greater ranges.

Analysis of Foreshock and Aftershock Data

The experience gained by examining the synthetic seismograms
suggests two ways of treating the data to determine source depth.
The first consists of estimating the maximum allowable source
depth from the Rg/S ratio. To do this, it is only necessary to
read the maximum amplitudes of the Rg and S phases from seismo-
gram copies, take the ratio, and read off the maximum depth from
the curves of Figure 6. The other method consists of examining
the P arrivals to determine the timing of inferred sP phases and
compute the source depth from equation (1). These are very
simple techniques for interpreting the data but are probably the
only techniques warranted by the data at this time. The use of
wave form inversion techniques to determine mechanism or other
parameters depends on the veracity of the crustal model used and
the quality of the digital wave form data. Since the data are
from a single station, are not conducive to accurate digitiza-
tion, and because crustal models for the area are still only
approximate it seems unwise to pursue such inversions.

Vertical component seismograms for the events listed in Table
2 were examined to obtain the Rg/S ratio. This ratio was taken
for those events where the Rg phase was on scale and is listed in
the table. P waves of events with clear P phases were digitized
for display purposes to show the picks of sP. The sP-P time was
read from the digitized wave form and interpreted to obtain
source depth. All depth results are shown in Table 2.

Figure 8 shows vertical wave forms of foreshocks which were
clear enough on the record to be digitized. Note that the wave

forms are nearly identical for all these events implying close hypocentral locations and source mechanisms. The Rg/S ratio is 5 for all events suggesting a maximum source depth of 3 km.

P wave forms from all foreshocks are shown in Figure 9. All except the foreshock immediately preceding the main event (00:04 event of Figure 9) and the 5:24 event show a distinctive double P arrival. Figure 10 shows synthetic P waves calculated using generalized ray theory and the Drummond and Mohamed model of Table 1. The source mechanism assumed is a pure thrust fault (or CLVD). Note the detail of splitting of the P wave pulse into P and sP as a function of source depth. The time interval between peaks indicated by the arrows in Figure 10 is a good measure of sP-P time. The data wave forms of Figure 9 show this characteristic interference in the double P arrival. Measuring this time separation in the data yields an estimate of the source depth. The arrows in Figure 9 show the inferred arrival of sP which is interfering with direct P. The source depth implied by this timing is 2 km for the first four events and 1.7 km or less for the remaining foreshocks.

Note that the S-P times are all within the reading error implying that distance is nearly the same for all foreshocks. Also note that the P waves can be simple or showing the interference of sP and P at the same distance strongly suggesting that the interference effect is not due to triplications from crustal structure. It is also highly unlikely that most events would show the same wave form complexity due to multiple ruptures. Furthermore, foreshock depths determined from the Rg/S ratio is consistent with the sP depths.

Figure 11 shows P wave forms for 13 aftershocks of 14 October. They have been arranged in order of apparent depth based on the observation of sP in the wave form. The 8:47 event is included to show a nodal P arrival. These data show that the P wave forms can have significant differences in apparent sP-P time intervals for events at nearly the same range. For example the 8:18 and 8:38 events have the same S-P time, yet both the Rg/S ratios and sP observations demonstrate that the 8:18 event is significantly shallower than the 8:38 event. A check of the synthetic seismograms demonstrated that source depth does not significantly change the S-P times for a constant distance.

Potentially, there is one ambiguity in these interpretations which arises from the case where the Rg/S ratio implies significant depth but the P wave form shows no sP phase. It is conceivable that sP could be nodal compared to P because of source mechanism. This should be a rare occurrence but cannot be discounted. Alternatively, a small Rg/S ratio does not really imply a large source depth as seen in the grid testing result. However, the true source depth in these cases will be ambiguous so that bounds are all that can be determined.

Figures 12 and 13 show sP picks for the other aftershock data. Some picks are equivocal particularly for those P waves where it appears that sP closely follows P. In these cases, the event still must be shallow. Most events have very simple pulse-like wave forms implying near surface rupture.

Discussion and Conclusions

A compilation of maximum source depths (Figure 14) inferred from Rg/S ratios shows about 17 events with default depths at 5 to 6 km but with most events occurring above 3 km. Only the 8:04 event of Figure 11 showed no obvious Rg wave which could be interpreted. This aftershock was inferred to be at 7.6 km depth from it's sP-P time and is the deepest event found. The frequency of events with source depth found using sP times is shown in Figure 15. Again, most of the events occurred above 3 km but it appears that seismicity is concentrated near the surface and falls off exponentially with depth.

Figure 14 is biased towards 'deep' hypocenters because of the nature of the Rg analysis. Figure 15 may be slightly biased towards very shallow events for those interpretations which may be affected by nodal sP. There may also be some bias in the choice of data in this magnitude range but it is not known in what direction the bias could push the distribution. A study of the records showed many smaller events which could be seen only by their Rg waves. If these events were included they would certainly increase the number of events at depths shallower than 3 km. However, events of the same moment that occurred deeper would be undetectable since they would not generate high amplitude Rg phases. In the largest events Rg went off scale and was unavailable; these are the events in Table 2 for which Ml is not given. However, these larger events concentrate at about 2 km depth as determined by sP. Thus, it appears that very shallow source depths are characteristic of this earthquake sequence.

It is interesting to note that the excitation of Rg by very shallow events will allow small moment earthquakes to be classified as relatively large events if Ml is calculated. This should be addressed in any future study of earthquake magnitude - moment relationships for the area. The synthetic Rg amplitudes suggest that magnitudes may be biased upwards by a full unit for very shallow events.

Felt reports and descriptions of local damage (Gordon and Lewis, 1980) are consistent with this characteristic of near-surface rupture. Gordon and Lewis(1980) report the formation of tensional ground cracking and structural damage during one of the magnitude 3.0 aftershocks. There are other felt reports in which shaking was only felt locally which would be consistent with near-surface rupture. Although the main shock produced much of the surface deformation, complex cracking and faulting occurred away from the main scarps during the aftershock sequence.

The dislocation source mechanism was assumed here for the analysis of all foreshocks and aftershocks. The complex surface ruptures and ground cracking observed during the aftershock sequence implies that a number of fault mechanisms are possible in the data and that the very shallowest events could have a general moment tensor source description. A tensional crack, for example, will be explosion-like containing a large isotropic component to the radiation pattern (Langston, 1983). Vertical wave forms will be similar to the isotropic wave form seen in Figure 4. Indeed, a few of the events, like the 7:38 event of Figure 2, showed very similar wave forms with very large Rg/S ratios. Assumption of a tension crack type of mechanism will not affect

the depth results significantly since it is likely that tension cracking is only possible near the surface. Also, Rg excitation decays more quickly with depth for the isotropic source Green's function than for the dislocation Green's functions. Thus, large Rg phases will still imply shallow source depths.

The foreshocks show a remarkable clustering in depth as revealed both by the Rg/S analysis and from sP observations. It appears that the sequence initiated at 2 km depth with later events occurring somewhat higher at about 1.7 km. The depth noticeably decreased by direct comparison of the wave form inter- ference of sP and P between foreshocks. The foreshock just before the main event appears to be surface focus for all practi- cal purposes. Vogfjord and Langston(1987) suggested that rup- ture during the main event started at about 1.5 km. These fore- shock interpretations support this extremely shallow initiation point if the assumption of foreshock clustering at the mainshock hypocenter is true.

Vogfjord and Langston(1987) also show from the static uplift data and teleseismic wave form models that the fault surface of the main event cannot be significantly deeper than 6 km. There are very few aftershocks which have depths greater than 6 km with the deepest event being at 7.6 km. Thus, the overall shallow distribution of events in combination with the deepest after- shocks is also consistent with the maximum depth of faulting.

The picture that emerges here is that faulting in this intra- plate shield area is a near-surface phenomenon. Focal mechanisms and source depths determined for other moderate events in the Southwest seismic zone show similar behavior. Fredrich et al

(1986) studied the 1979 Cadoux event (M 6.1), which broke the surface, and found thrusting at hypocentral depths of only 2 km. The 1970 Calingiri earthquake (M 5.9) also produced a prominent fault scarp within the shield (Gordon and Lewis, 1980). Considering the size of the Meckering earthquake and the 37 km long fault scarps that it produced, it is evident that this area is currently unique among the seismogenic regions of the earth.

Some models of faulting, particularly applied to interplate areas such as the San Andreas fault zone, have a large fault affected by ductile rheology below the brittle, seismogenic region. Slip in the ductile region before an earthquake stresses the crack tip near the brittle-ductile transition causing an instability for the occurrance of future event on the fault (Thatcher, 1983; Strehlau, 1986). An alternative model has slip occurring during an earthquake in the upper brittle layer causing large stresses to build up at the brittle-ductile transition causing the same kind of instability. Seismogenic rupture occurs almost exclusively in the upper brittle layer with only minor rupture into the ductile region (Strehlau, 1986). Rupture initiates in this high strength transition zone between the brittle and ductile layers of the lithosphere. A variation of such a model has been proposed by Gordon and Wellman(1971) and Gordon and Lewis(1980) for the occurrence of the Meckering event. They suggest that aseismic slip on a deep shear zone within the crust stressed the upper portion of the crust to eventually cause failure during the Meckering earthquake.

In contrast with this model is the inferred rupture behavior of the Meckering event which initiated near the surface on the

upper third of the fault plane and propagated downward to termi-
nate at only 6 km depth. This behavior is consistent with a model
suggested by Furlong (personal communication) and Vogfjord and
Langston(1987) which was described above. In this model the
strength of the Australian shield exceeds the ambient deviatoric
stresses everywhere except near the surface. The fault is driven
simply by high deviatoric stresses. The high strength of the
crust requires that faulting stops before penetrating too deeply
into the crust. Rupture proceeds down-dip in a manner suggested
by Strehlau(1986) until dynamic frictional resistance exceeds
the stresses induced by faulting at the crack tip.

The southwest seismic zone of Australia may be an area that
has interesting possibilities for physical experiments. Because
the hypocentral region is only at 2 km depth or so it would be
very feasible to drill into it with existing technology. Gauges
could be emplaced over the length of the borehole to measure
physical properties such as temperature, strain, stress, and the
state of pore fluids. Such an area would be an accessible earth-
quake laboratory in which physical and seismic monitoring would
yield information on the formation of continental intraplate
events. Because of the homogeneity of crustal structure and
topography in the area, complications of structure normally found
in most tectonic areas of the world would be avoided or mini-
mized. It may also be possible to perform limited physical
experiments in the generation of man-made earthquakes depending
on physical conditions found in the upper crust (e.g., Rayleigh
et al, 1972). In any case, scientific study of such an area
would be complimentary to those sites along active interplate

fault zones which are currently heavily instrumented.

This faulting model also has some implications for earth-quakes in other shield areas of the earth. For example, a stress model suggested by Cloetingh and Wortel(1985) for the Indian-Australian plate implies that much of peninsular India is under high deviatoric compressive stress. Inasmuch that this shield region of India is an area of moderate seismicity, it is possible to determine accurate source depths using teleseismic wave form methods. Source depths from a few events have been determined (e.g. see Langston and Franco-Spera, 1986) and do suggest similar shallow faulting at depths less than 5 km.

The use of wave forms to infer source parameters is not a new idea, but it is interesting to see how much information may be obtained from an analysis of vertical component short-period data from a single station. It was possible to determine source depth from these data principally because the seismic structure between source and receiver was simple and because the data were recorded at a range where structure effects were minimal. It might be expected that a significant low-velocity sedimentary section at the surface would have complicated the seismograms to such an extent that depth phases would have been obscured. A receiver at a greater range would record triplicated body wave phases, again obscuring surface reflections if such triplications could not be accurately modeled. The gentle topography of Southwestern Aus-tralia serves to make Rg wave propagation efficient; it would be expected that large changes in topography would scatter this phase. Nevertheless there are large continental areas of the earth where similar conditions exist and similar methods may be

usefully employed. Indeed, it is possible, in principle, to employ wave form analysis in those areas which are more compli- cated but have been extensively studied so that wave propagation effects are well understood. These kinds of methods would sup- plement network analysis of local seismicity in determining source parameters even for those networks which are instrumented with only short-period vertical seismometers.

Acknowledgements

References

Apsel, R., Dynamic Green's functions for layered media and applications to boundary value problems, Ph.D. Thesis, University of California, San Diego, La Jolla, California, 349 pages, 1979.

Barker, J.S., A seismological analysis of the May 1980 Mammoth Lakes, California, earthquakes, Ph.D. Thesis, Pennsylvania State University, University Park, Pennsylvania 16802, 279 pages, 1984.

Bergman, E.A. and S.C. Solomon, Oceanic intraplate earthquakes: implications for local and regional intraplate stress, J. Geophys. Res., 85, 5389-5410, 1980.

Brune, J., Tectonic stress and the spectra of seismic shear waves from earthquakes, J. Geophys. Res., 75, 4997-5009, 1970.

Cloetingh, S. and R. Wortel, Regional stress field of the Indian plate, Geophys. Res. Let., 12, 77-80, 1985.

Cull, J.P. and D. Denham, Regional variations in Australian heat flow, B.M.R. J. Aust. Geol. Geophys., 4, 1-13, 1979.

Dahlman, O. and H. Israelson, Monitoring underground nuclear Explosions, Elsevier, Amsterdam-Oxford-New York, 440 pages, 1977.

Denham,D., L.G. Alexander, and G. Worotnicki, The stress field near the sites of the Meckering(1968) and Calingiri (1970) earthquakes, Western Australia, _Tectonophysics_, _67_, 283-317, 1980.

Doyle, H.A., I.B. Everingham and D.J. Sutton, Seismicity of the Australian continent, _J. Geol. Soc. Australia_, _15_, 295-312, 1968.

Drummond, B.J. and R.E. Mohamed, Crustal structure in the southwest seismic zone, western Australia (Abstract), _Eighth Australian Geological Convention, Geol. Soc. Aust._, Flinders University, Adelaide, 59, 1986.

Everingham, I.B. and H.A. Doyle, Thrust fault scarp in the western Australian shield, _Nature_, _223_, 701-703, 1969.

Ewing, W.M., W.S. Jardetzky, F. Press, _Elastic Waves in Layered Media_, McGraw-Hill Book Co., New York, 380 pages, 1957.

Fredrich, J.T., R. McCaffrey, and D. Denham, Source parameters of large Australian earthquakes (Abstract), _EOS_, _67_, 305, 1986.

Gordon, F.R., Faulting during the earthquake at Meckering, western Australia: 14 October 1968, _R. Soc. New Zealand Bull._, _9_, 85-93, 1971.

Gordon, F.R. and H.W. Wellman(1971). A mechanism for the Meckering earthquake, R. Soc. New Zealand Bull., 9, 95-96.

Gordon, F.R. and J.D. Lewis, The Meckering and Calingiri earthquakes October 1968 and March 1970, Geol. Surv. Western Australia, Bull. 126, 229 pages, 1980.

Helmberger, D.V. and D.G. Harkrider, Modeling earthquakes with generalized ray theory, in Proc. of IUTAM Symposium: Modern problems in elastic wave propagation, J. Miklowitz and J. Achenback, eds., John Wiley and Sons, New York, 1978.

Langston, C.A., Source inversion of seismic waveforms: the Koyna, India, earthquakes of 13 September 1967, Bull. Seism. Soc. Am., 71, 1-24, 1981.

Langston, C.A., Kinematic analysis of strong motion P and SV waves from the Sterling event, J. Geophys. Res., 88, 3486-3497, 1983.

Langston, C.A. and M. Franco-Spera, Modeling of the Koyna, India, aftershock of 12 December 1967, Bull. Seism. Soc. Am., 75, 651-660, 1985.

Mathur, S.P., Crustal structure in southwestern Australia from seismic and gravity data, Tectonophysics, 24, 151-182, 1974.

Meissner, R. and J. Strehlau, Limits of stresses in continental crusts and their relation to the depth-frequency distribution of shallow earthquakes, Tectonics, 1, 73-89, 1982.

Press, F., Seismic Velocities, from Handbook of Physical Constants, G.S.A. Memoir 97, 1966.

Rayleigh, C.B., J.H. Healy, and J.D. Bredehoeft, Faulting and crustal stress at Rangely, Colorado, in Flow and Fracture of Rocks, Geophys. Monogr. Ser., 16, ed. by H.C. Heard, et al., 275-284, 1972.

Richardson, R.M., S.C. Solomon, and N.H. Sleep, Tectonic stress in the plates, Rev. Geophys. Space Phys., 17, 981-1019, 1979.

Richter, C.F., Elementary Seismology, W.H. Freeman and Company, San Francisco, 768 pages, 1958.

Strehlau, J., A discussion of the depth extent of rupture in large continental earthquakes, Earthquake Source Mechanics, Geophysical Monograph 37 (Maurice Ewing 6), A.G.U., 131-145, 1986.

Thatcher, W., Nonlinear strain buildup and the earthquakes cycle on the San Andreas fault, J. Geophys. Res., 88, 5893-5902, 1983.

Vogfjord, K.S. and C.A. Langston, The Meckering earthquake of October 14, 1968: A possible downward propagating rupture, submitted to <u>Bull. Seism. Soc. Am.</u>, 1987.

Zoback, M.L. and M. Zoback, State of stress in the conterminous United States, <u>J. Geophys. Res.</u>, <u>85</u>, 6113-6156, 1980.

Table 1

Velocity Models

Model	Vp (km/sec)	Vs (km/sec)	Density (gm/cc)	Layer Thickness (km)
Mathur(1974)[1]	5.54	3.20	2.38	0.5
	6.13	3.54	2.78	9.5
	6.70	3.87	2.94	7.0
	7.49	4.32	3.10	25.0
	8.39	4.84	3.45	-
Drummond and Mohamed(1986)[2]	6.10	3.52	2.78	3.0
	6.15	3.55	2.78	3.0
	6.20	3.58	2.80	3.0
	6.25	3.61	2.80	2.0
	6.35	3.67	2.85	2.0
	6.45	3.72	2.90	4.0
	6.55	3.78	2.92	5.0
	6.65	3.84	2.94	3.5
	6.75	3.90	2.95	4.5
	6.95	4.01	2.95	1.0
	7.25	4.19	2.95	1.0
	7.55	4.36	3.00	1.0
	7.85	4.53	3.10	1.0
	8.20	4.73	3.20	1.0
	8.40	4.85	3.30	-

[1]: The top layer was inferred from observed Rg dispersion and was not given in the original reference. Assumed Q_p and Q_s for all layers is 1000 and 500, respectively.

[2]: Model layers approximate linear gradients for the P-wave velocity structure described by Drummond and Mohamed(1986). Shear wave velocities and densities were assumed.

Table 2

Meckering Foreshock and Aftershock Data

Date	P Time U.T.	S-P Time (sec)	Dist. (km)	Rg/S	sP-P Time (sec)	Maximum Rg Depth (km)	sP Depth (km)	M1
Foreshocks								
10/03/68	03:03:11	--	--	--	0.5	--	2.0	-
10/03/68	03:18:09	-	-	-	0.5	-	2.0	-
10/03/68	03:55:46	-	-	-	0.5	-	2.0	-
10/03/68	04:49:43	9.7	82	5.3	0.5	3	2.0	3.
10/03/68	05:24:30	9.7	82	4.7	<0.4	3	<1.7	3.
10/03/68	21.55:07	9.7	82	5.0	0.4	3	1.7	2.
10/13/68	18:35:28	10.0	85	4.8	0.4	3	1.7	2.
10/13/68	22:51:43.6	9.6	81	-	0.4	-	1.7	3.
10/13/68	23:02:38	9.7	82	4.7	-	3	-	2.
10/13/68	23:13:41.5	9.8	83	5.0	0.4	3	1.7	2.
10/14/68	00:04:59	9.5	81	4.7	-	3	<1	3.
Aftershocks								
10/14/68	03:14:57	9.0	76	2.3	0.5	6	2.0	3.0
10/14/68	04:48:20	10.5	89	0.9	-	6	<1	3.
10/14/68	05:05:06	9.0	76	1.3	-	6	<1	2.7
10/14/68	05:36:26	10.0	85	3.9	0.7	3	2.6	3.
10/14/68	06:01:07	9.2	78	1.4	0.5	6	2.0	3.2
10/14/68	06:17:21	9.5	81	0.5	1.0	6	3.8	3.3
10/14/68	07:38:42	8.5	72	11.6	-	2	<1	3.6
10/14/68	08:00:05	9.0	76	2.7	-	6	<1	3.0
10/14/68	08:04:45	8.0	68	-	2.	-	7.6	2.8
10/14/68	08:18:32	10.0	85	9.3	-	2	<1	3.6
10/14/68	08:20:35	8.0	68	8.0	-	3	<1	3.0
10/14/68	08:38:27	10.0	85	1.8	1.3	6	4.9	3.0
10/14/68	08:47:12	10.5	89	0.8	-	6	-	3.4
10/15/68	06:08:32	8.2	69	22.0	-	<1	<1	3.6
10/15/68	06:31:23.5	9.0	76	3.2	0.6	6	2.3	3.5
10/15/68	07:25:19.5	8.0	68	8.7	-	3	-	2.7
10/15/68	07:41:38.5	8.0	68	10.7	-	2	-	2.8
10/15/68	12:46:31	-	-	-	-	-	<1	-
10/15/68	16:07:26	8.5	72	17.7	-	1	-	3.0
10/15/68	16:44:11.5	8?	(68)	10.5	-	2	-	2.6
10/15/68	18:16:23.5	9.4	80	1.7	-	6	<1	2.9
10/16/68	00:55:23.2	9.0	76	--	1.5	-	5.7	-
10/16/68	02:56:04	9.0	76	5.8	-	3	<1	3.4
10/16/68	08:24:40	10.0	85	1.1	1.2	6	4.5	3.4
10/16/68	08:34:10.4	8.5	72	19.7	-	<1	<1	3.4
10/16/68	09:53:46	8.9	75	12.0	-	2	<1	3.2
10/16/68	12:12:06.8	10.0	85	1.0	1.1	6	4.2	2.8
10/16/68	12:45:26.5	11.0	94	1.5	-	6	-	2.8
10/16/68	23:14:55	10.5	89	9.7	-	2	-	3.4
10/21/68	02:16:36.5	9.8	83	1.7	0.9	6	3.4	2.6

10/21/68	18:35:42	9.0	76	2.9	0.7	6	2.6	2.7
10/22/68	01:04:18.5	10.0	85	-	1.8	-	7.0	-
10/29/68	04:12:59	11.0	94	8.6	-	2	-	3.1
10/29/68	06:39:58	7.5	63	5.1	-	4	-	3.2
11/04/68	03:43:40	8.5	72	1.5	1.2	6	4.5	3.2
11/04/68	04:25:00.5	10.0	85	11.4	-	2	-	3.5
11/04/68	07:37:44	11.0	94	12.7	0.7	1	2.6	3.7
11/04/68	14:45:	nodal P	-	10.0	-	2	-	-
11/05/68	01:20:	nodal P	-	11.5	-	2	-	-
11/07/68	21:32:17	8.0	68	8.3	-	3	-	2.8
11/09/68	11:07:45.5	9.5	81	-	0.5(?)	-	2.0(?)	-
11/09/68	15:57:37.5	8.5	72	4.0	-	5	<1	2.7
11/10/68	00:37:26	11.0	94	>7.8	-	2	-	3.2
12/08/68	12:28:57	10.0	85	13.3	-	1	<1	3.9
12/08/68	14:24:54	8?	(68)	>15	-	1	<1	2.8
12/09/68	01:04:54	7.5?	(63)	24.5	-	<1	<1	3.2
12/18/68	08:19:16.5	9.5	81	1.2	1.0	6	4.0	2.9
03/10/70	06:00:46.5	10.5	89	6.4	-	3	<1	3.2

41

—

Figure Captions

Figure 1: Sketch map of the Meckering area showing epicenters of earthquakes in the SW Australian seismic zone, the Meckering fault scarp, and location of Mundaring (MUN) station. Map was modified after Figure 1 of Denham et al (1980).

Figure 2: Two aftershocks of 14 October (see Table 2) recorded on the WWSSN short-period system at MUN. Maximum ground motion for the vertical (Z), East-West (E), and North-South (N) components is normalized and given in microns for each trace. Major phases are denoted by P, S, and Rg. Most events have large Rg phases evident on the vertical components as shown by the 7:38 event. In contrast, the 8:38 event has a poorly developed Rg phase in addition to a complex P wave.

Figure 3: Short-period vertical component wave forms from six aftershocks of 14 October (Table 2) showing the variability of relative amplitudes among the major arrivals.

Figure 4: Synthetic seismograms for the four fundamental terms needed to construct a general moment tensor point source. VSS, VDS, CLVD, and ISO denote vertical strike-slip, vertical dip-slip, compensated linear vector dipole, and isotropic sources, respectively.

Distance to the receiver is 80 km and seismograms are shown as a function of source depth, H. The wavenumber integration technique was used calculate these synthetics for the Mathur(1974) model of Table 1. They include the short-period WWSSN instrument response and a Brune(1970) time function with a corner frequency of 1 hz. Amplitude is in cm for an assumed source moment of 10^{20} dyn cm. Note the existence of large Rg phases for sources at depths of 2 km and less compared to P and S phases. Rg is not well developed for deeper sources. Also note the existence of sP which separates from the first arriving P as source depth increases. The isotropic source does not show sP since this source does not generate S waves.

Figure 5: The effect of range on wave forms. A vertical strike-slip (VSS) source at 4 km depth is assumed. Model parameters are the same as those used in Figure 4.

Figure 6: Maximum Rg/S ratio plotted as a function of source depth. Curves are shown for ranges of 60, 70, 80, and 90 km. Note that large Rg/S ratios of 10 or more imply shallow source depths of less than 2 km. However, small Rg/S ratios may also be produced for sources less than 2 km depth because of source radiation pattern effects. These curves are used to estimate maximum allowable source depths from the Rg data.

Figure 7: The effect of crustal model on expected P wave forms.
Column A shows a profile of P waves computed using
generalized ray theory and the Mathur(1974) model.
Range is given in kilometers. Source depth is 6 km.
A CLVD source is assumed since it is likely that many
Meckering events are caused by thrusting; a CLVD seis-
mogram can be interpreted as being excited by a 45
degree dipping thrust fault seen at 45 degrees azi-
muth. Column B shows a profile of synthetic seismo-
grams again computed using generalized ray theory but
assuming the Drummond and Mohamed(1986) model. Note
that the relative amplitudes of sP and P depend on
range and the type of crustal model in detail but sP
is always prominent. At ranges of 90 and 100 km the
Drummond and Mohamed model produces a triplication due
to the high velocity gradient at the Moho. This
causes prominent Moho turning phases like sPm. There
is little evidence for this triplication in the data
although there are few events seen at distances
greater than 90 km.

Figure 8: Observed short-period vertical component wave forms
for six foreshocks. Amplitude is in microns for maxi-
mum displacement. The large excursions in the data
for the 23:02 and 23:13 events after the Rg phases are
from the effect of minute marks which were digitized.
Aside from different signal to noise ratios which
principally depend on the size of each event, note the

similarities in wave form between the foreshocks.
This implies that the events probably had similar
hypocenters and source mechanisms.

Figure 9: Observed P wave forms for eleven foreshocks (see Table
2). High amplitude P wave forms (e.g., 3:03 and 00:04
events) were difficult to digitize and are represented
mainly by the peaks and troughs of the observed seis-
mogram. The peak indicated by the arrow on the 3:55 P
wave was truncated on the record since it went off-
scale although it is likely that it was similar to the
P waves of the previous two events. The arrows indi-
cate the interpretation of a wave form feature associ-
ated with sP (see Figure 10). Based on interpretation
of sP to obtain source depth, the foreshock sequence
initiated with events at about 2 km depth. The fore-
shock just before the main event at 00:04 shows a wave
form characteristic of a source less than 1.0 km in
depth.

Figure 10: Synthetic seismograms computed using generalized ray
theory and the Drummond and Mohamed model (Table 1) to
show the effect of source depth on P and sP interfer-
ence. The synthetics were constructed with the short-
period WWSSN instrument response and a Brune(1970)
time function with a corner frequency of 2 hz. A CLVD
source was assumed although the wave form for a VSS
source is similar. Amplitude is arbitrary on the fig-

ure. The two arrows show a wave form feature which depends on the time separation of P and sP. This time interval between peaks was used to estimate depth when interpreting the observed P wave forms of Figure 9. Note how the P wave for a source at 0.5 km shows a simple, compact wave form similar to the P wave form of the 00:04 event of Figure 9. The interference of P and sP for slightly larger source depths produces the distinctive double P pulse seen for P waves from the other aftershocks.

Figure 11: Aftershock P wave forms for events of 14 October. Each event can be identified by its P arrival time (e.g., 7:38) and the P wave is scaled to maximum amplitude. These wave forms are arranged to show the effect of source depth where the shallowest sources are in the upper left and the deepest in the lower right. The arrows show the interpretation of sP which was used to determine source depth. All wave forms were digitized from the vertical component except for the 5:36 event P wave. The east-west component was used for this event because of microseismic noise obscuring the P arrival on the vertical. Note the interpretation of sP which separates from the first arrival P wave with increasing source depth. The 8:04 event was the deepest event found showing no Rg phase and a large differential sP-P time implying a source depth of 7.6 km.

Figure 12: Aftershock P wave forms for events of 15 October, 16 October, and 21 October. The events are arranged in chronological order from top to bottom and left column to right column. All wave forms are from the vertical component. The arrows show the interpretation of sP which was used to determine source depth.

Figure 13: Aftershock P wave forms for events of 22 October, 29 October, 4 November, 7 November, 9 November, 8 December, 9 December, 18 December, 10 March 1970. Same scheme as Figure 12.

Figure 14: Histogram of the number of foreshocks and aftershocks as a function of source depth determined from Rg/S ratios. The Rg/S method maximizes the inferred source depth as discussed in the text.

Figure 15: Histogram of the number of foreshocks and aftershocks as a function of source depth determined from sP-P times. Note the rapid decrease of event numbers with source depth.
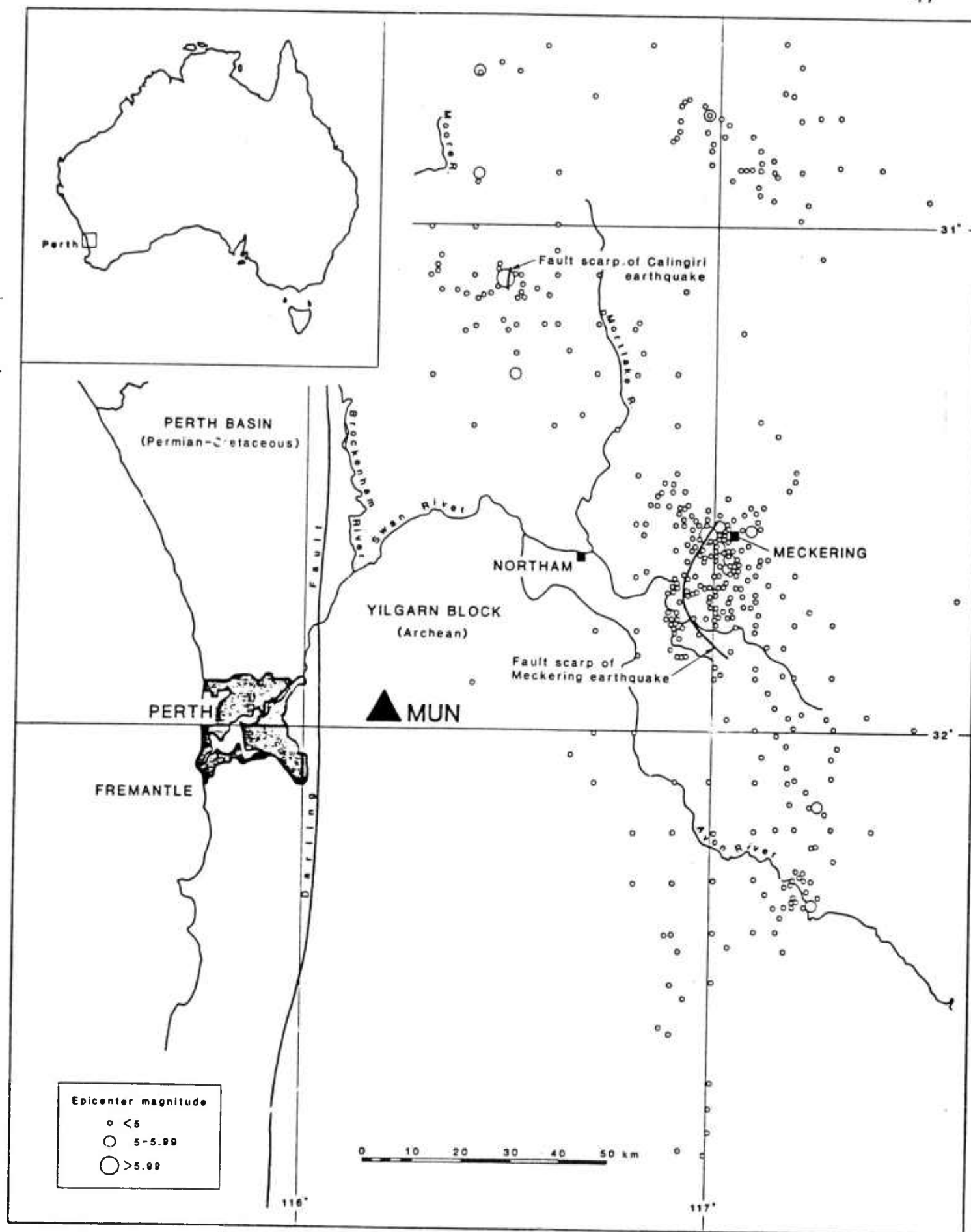
Figure 1
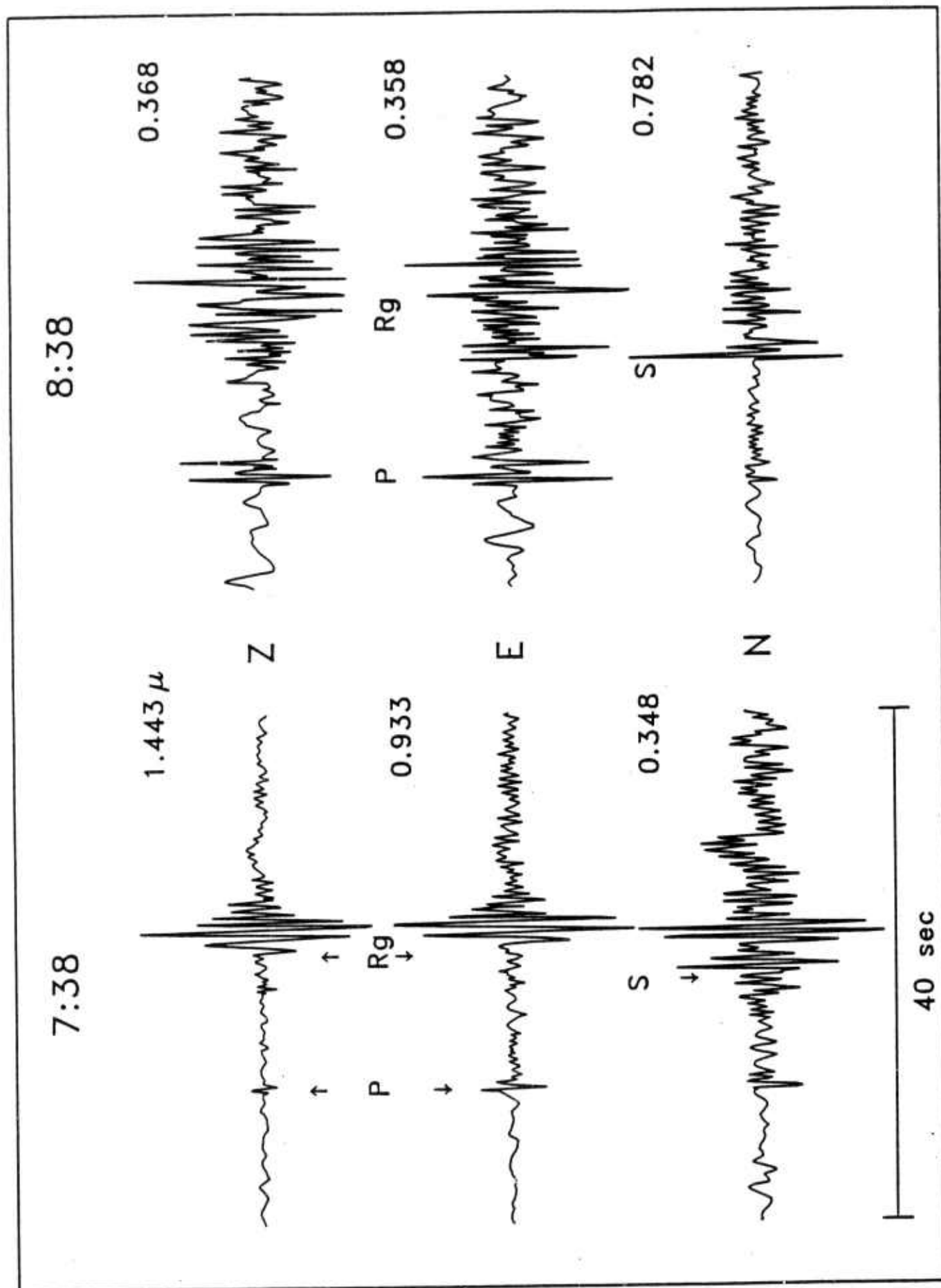
Figure 2

SHORT—PERIOD VERTICAL WAVEFORMS
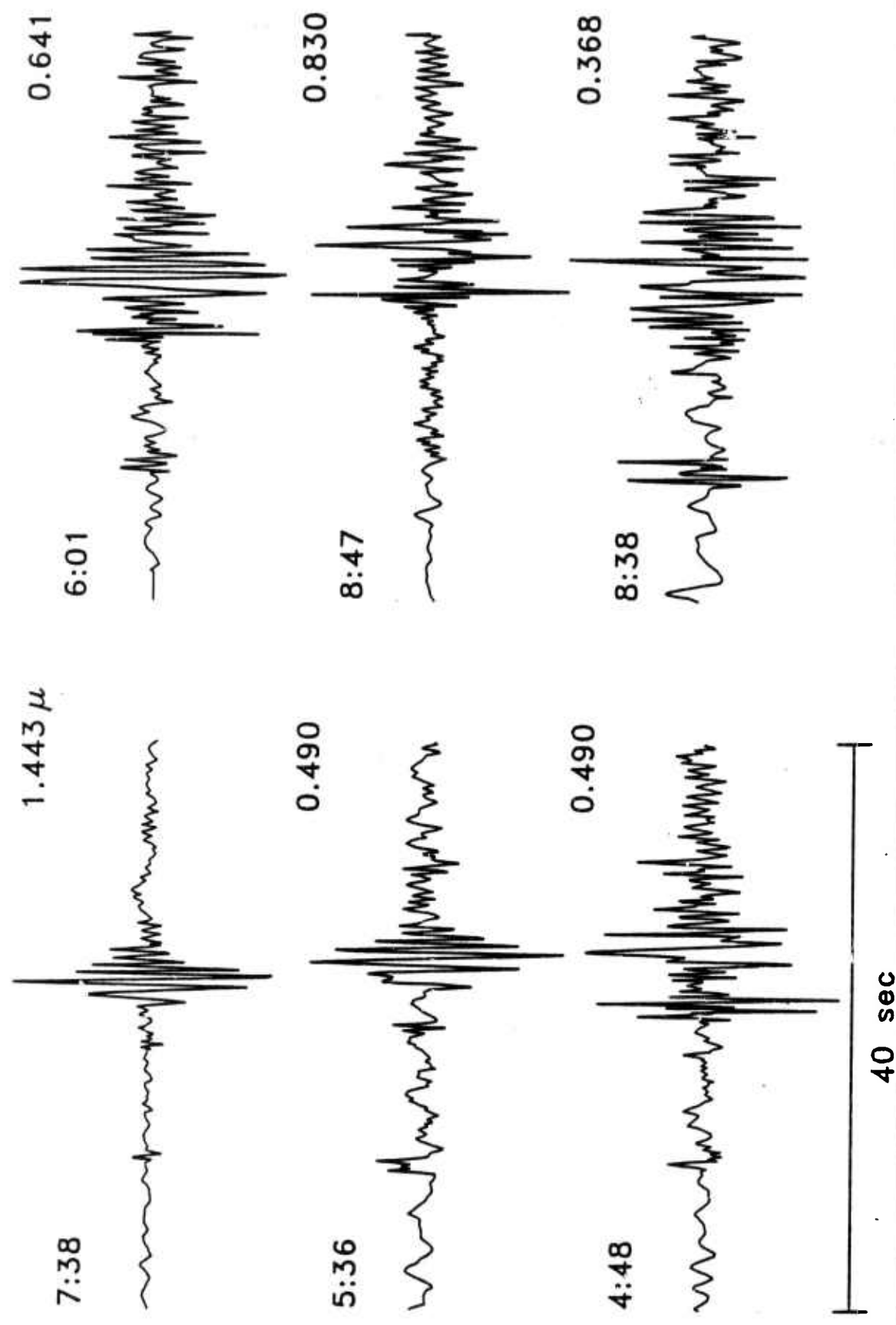
Figure 3
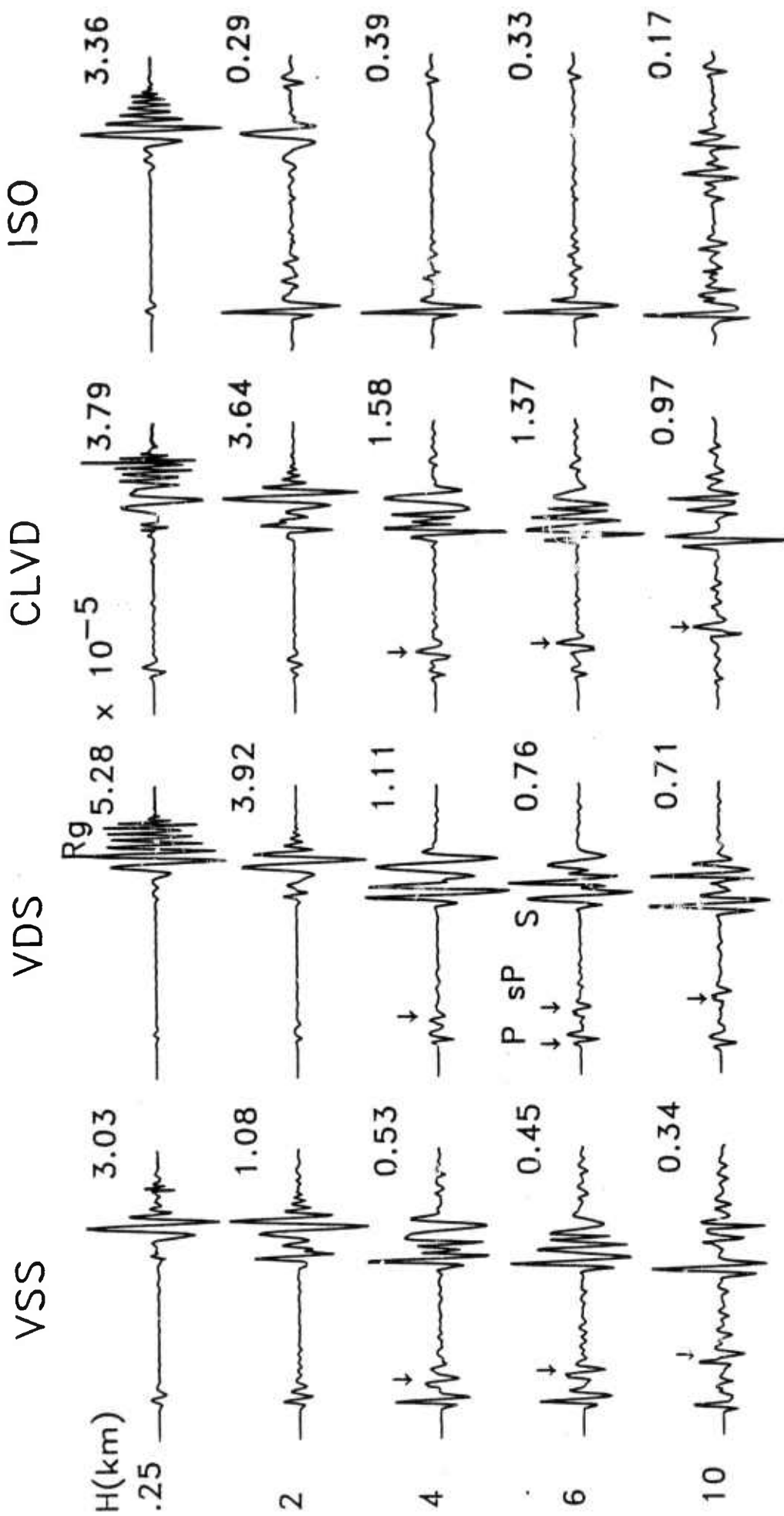
Figure 4
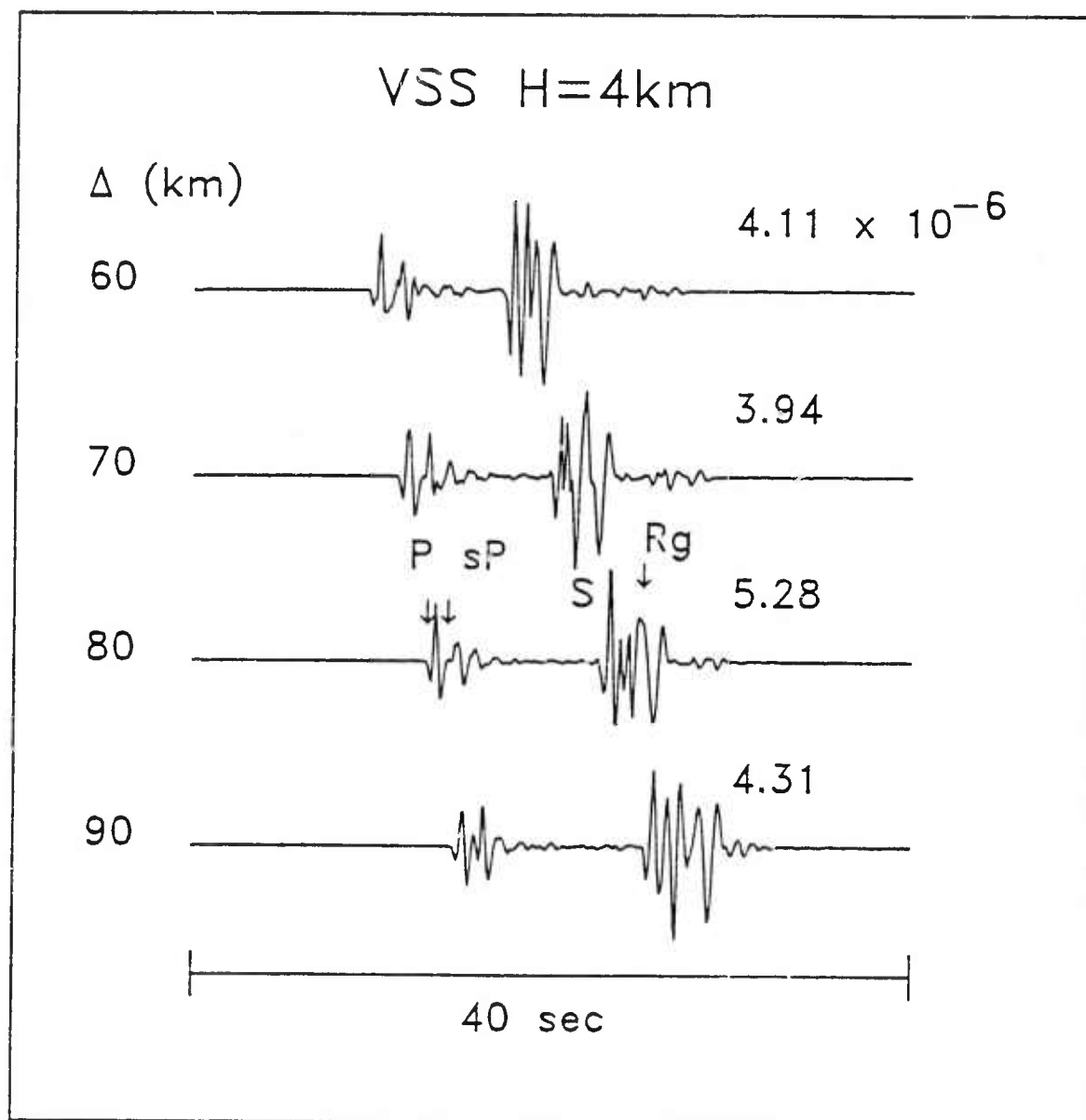
Figure 5
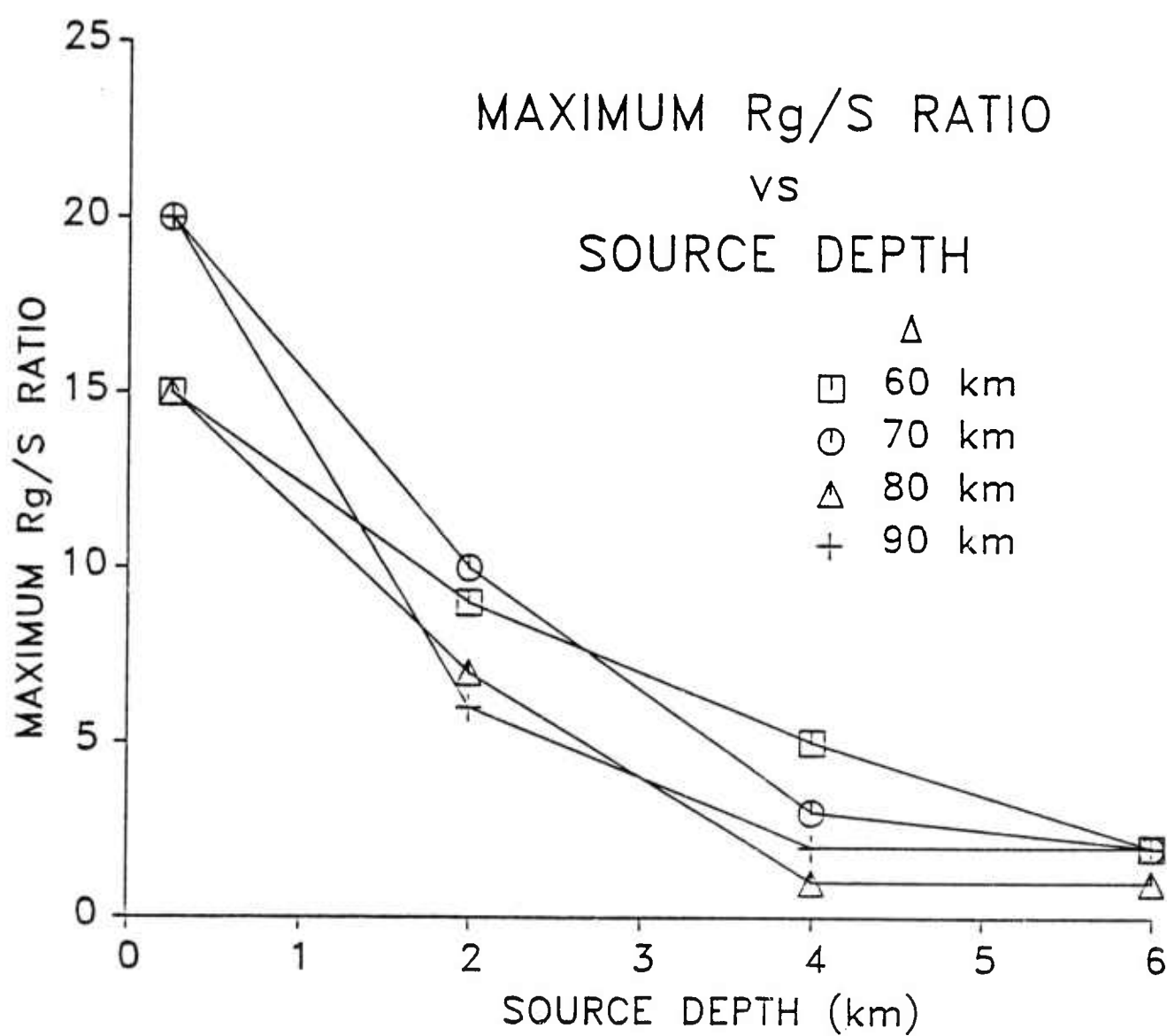
Figure 6
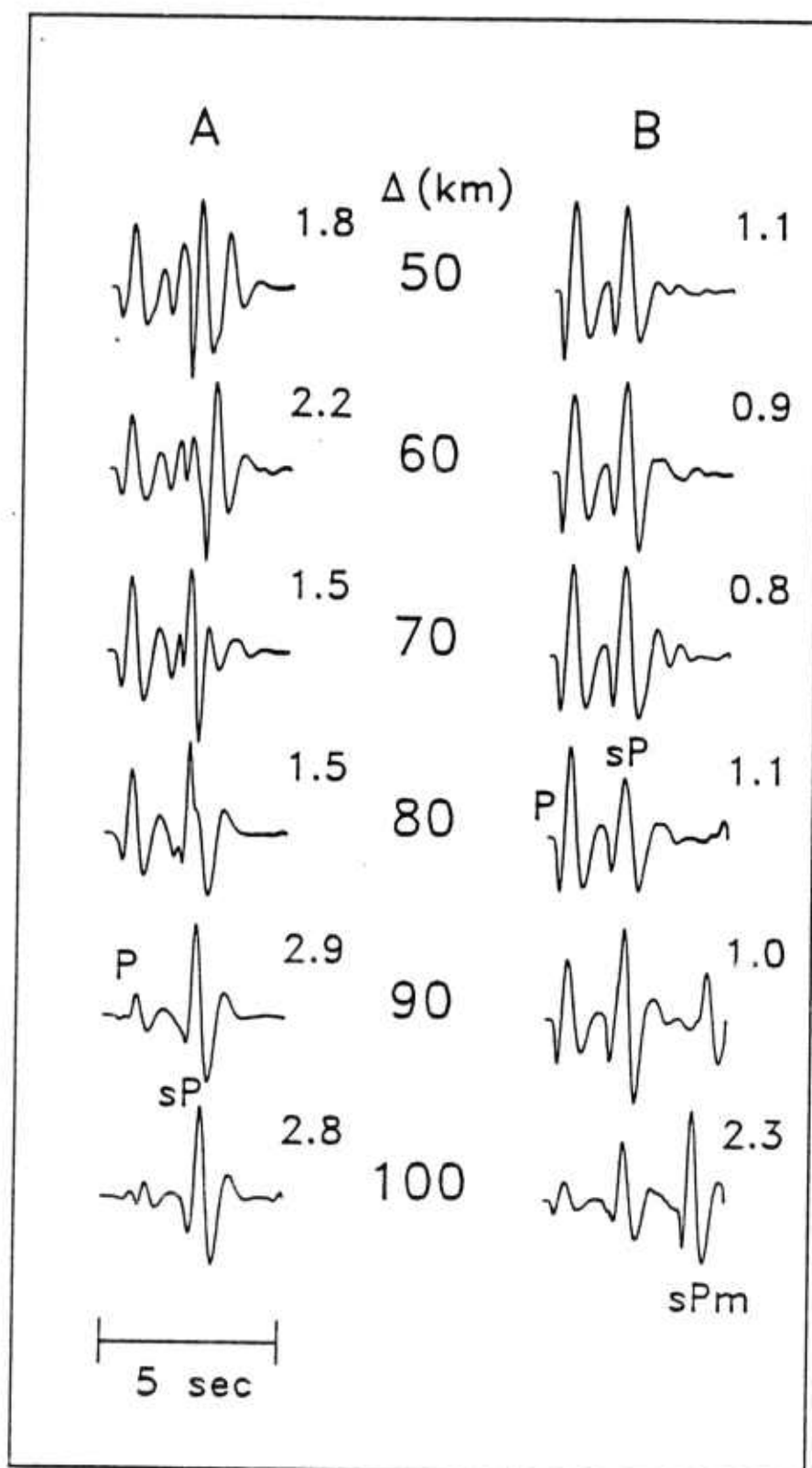
Figure 7

FORESHOCK VERTICAL WAVEFORMS
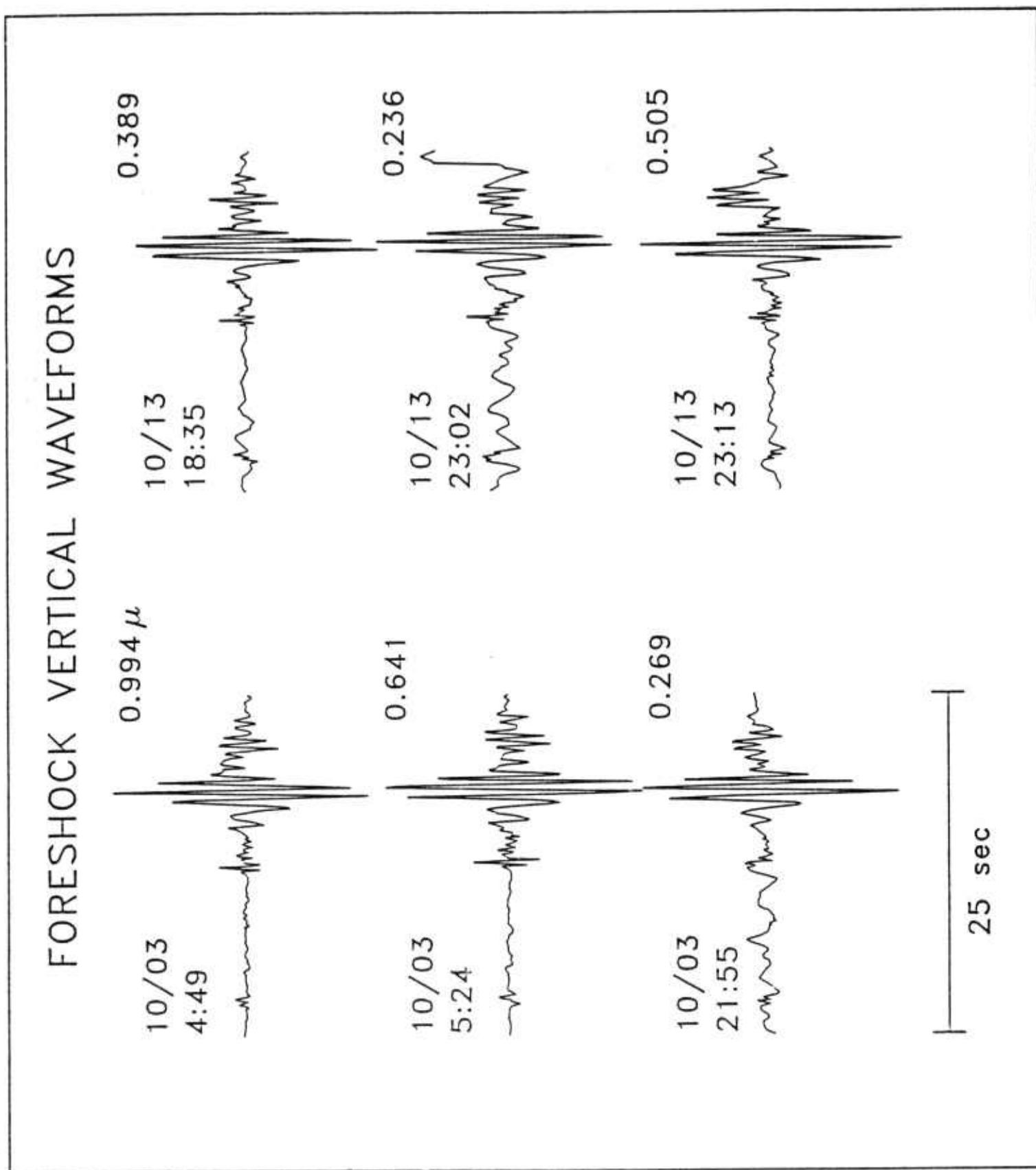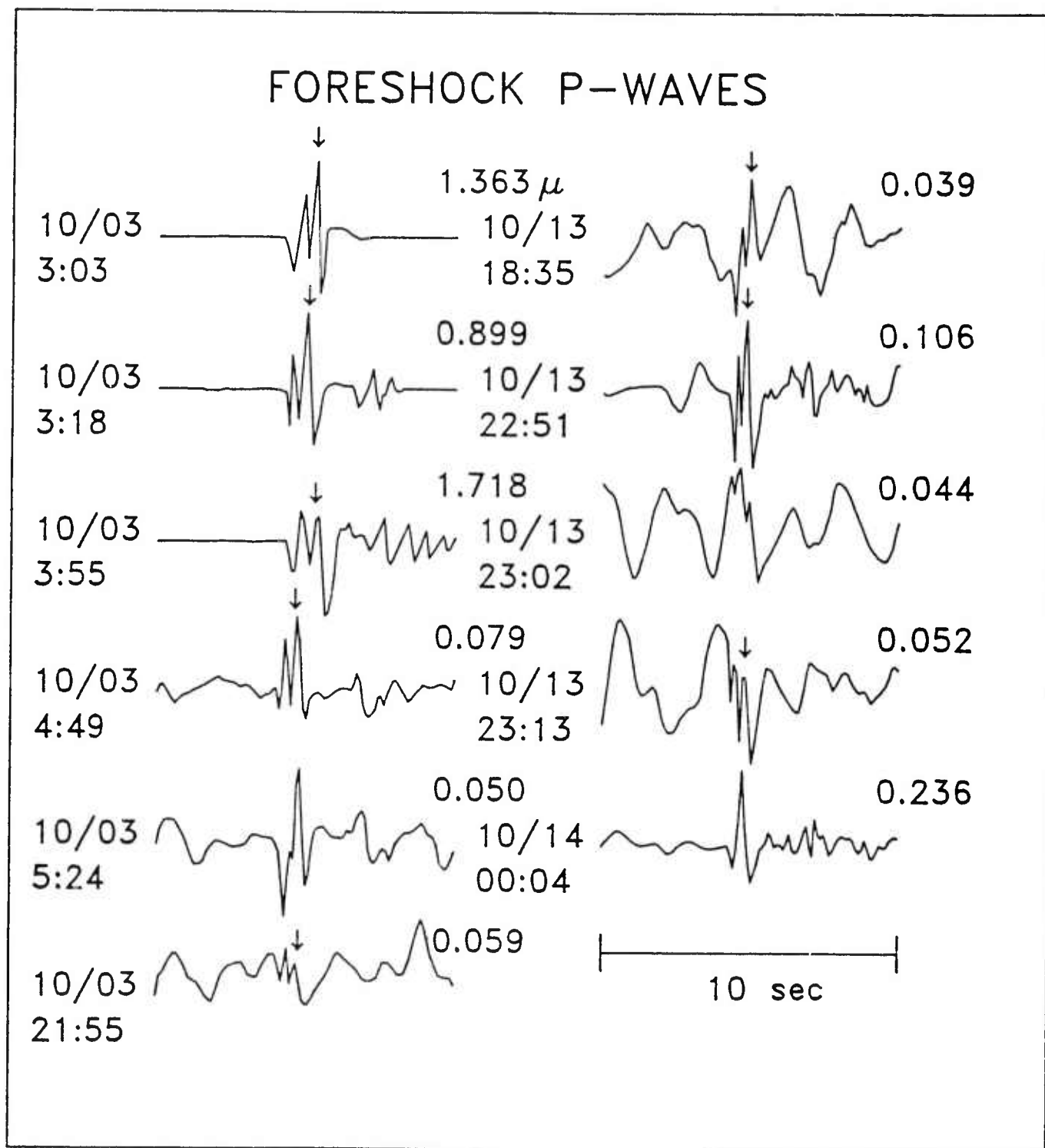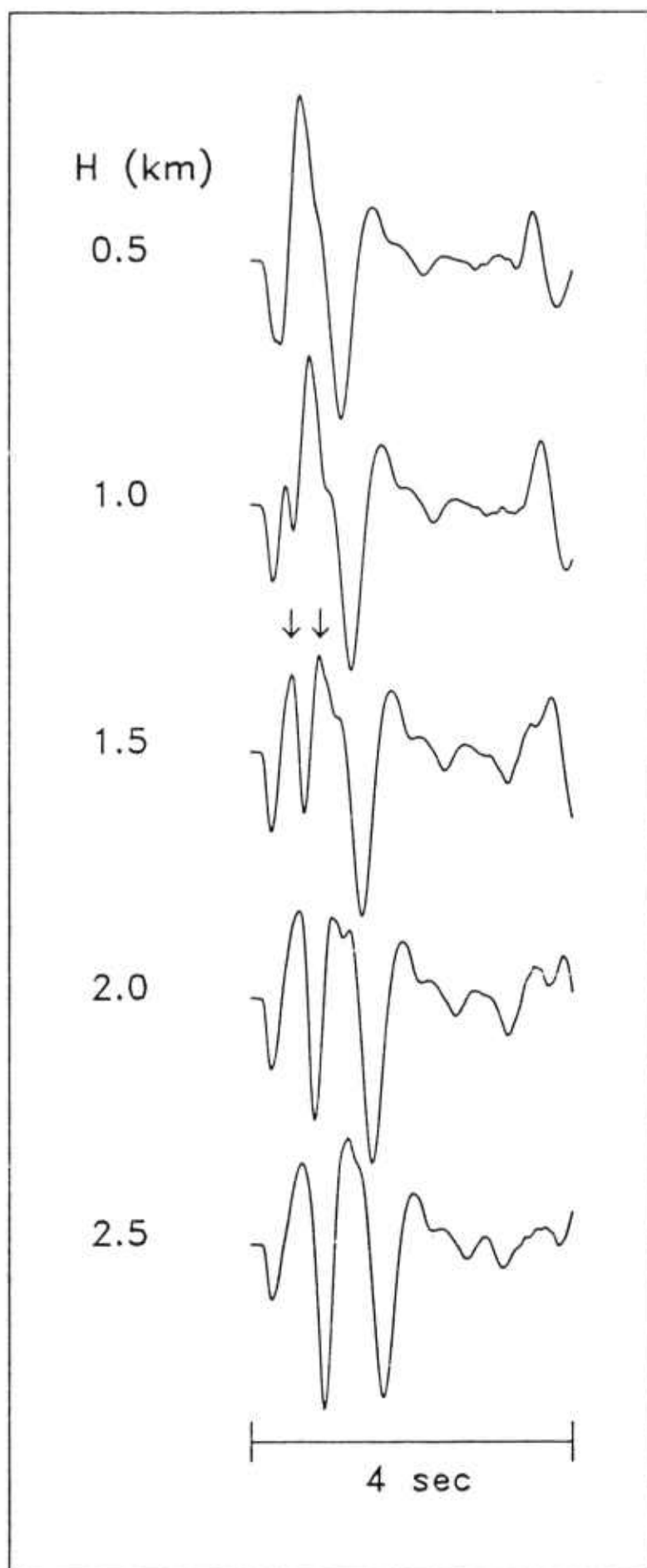
Figure 8

FORESHOCK P-WAVES
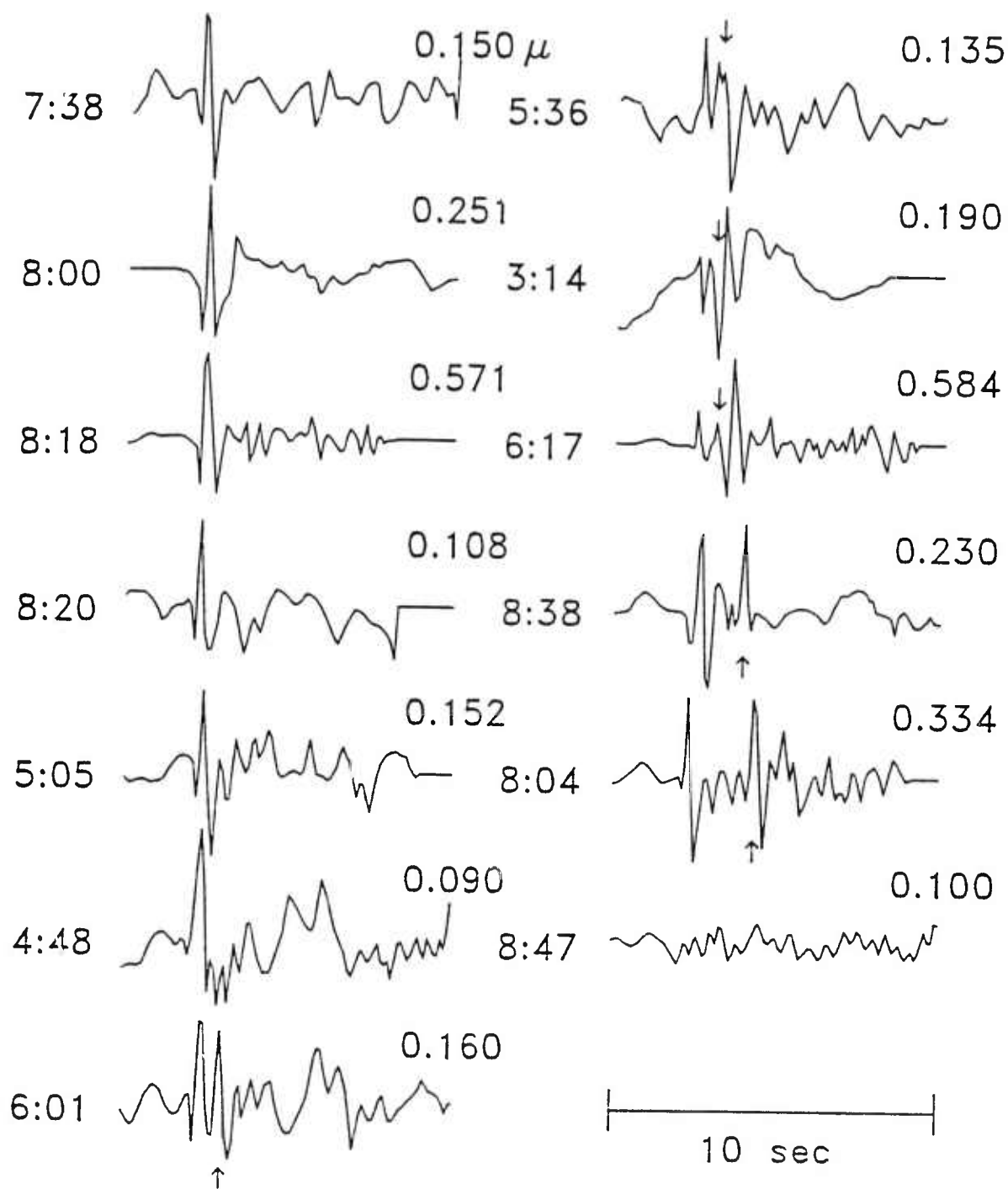
Figure 9

Figure 10

Figure 11

AFTERSHOCK P-WAVES

Figure 12

AFTERSHOCK P-WAVES

Figure 13

NUMBER OF EVENTS
vs
SOURCE DEPTH
from Rg

Figure 14

NUMBER OF EVENTS
vs
SOURCE DEPTH
from sP
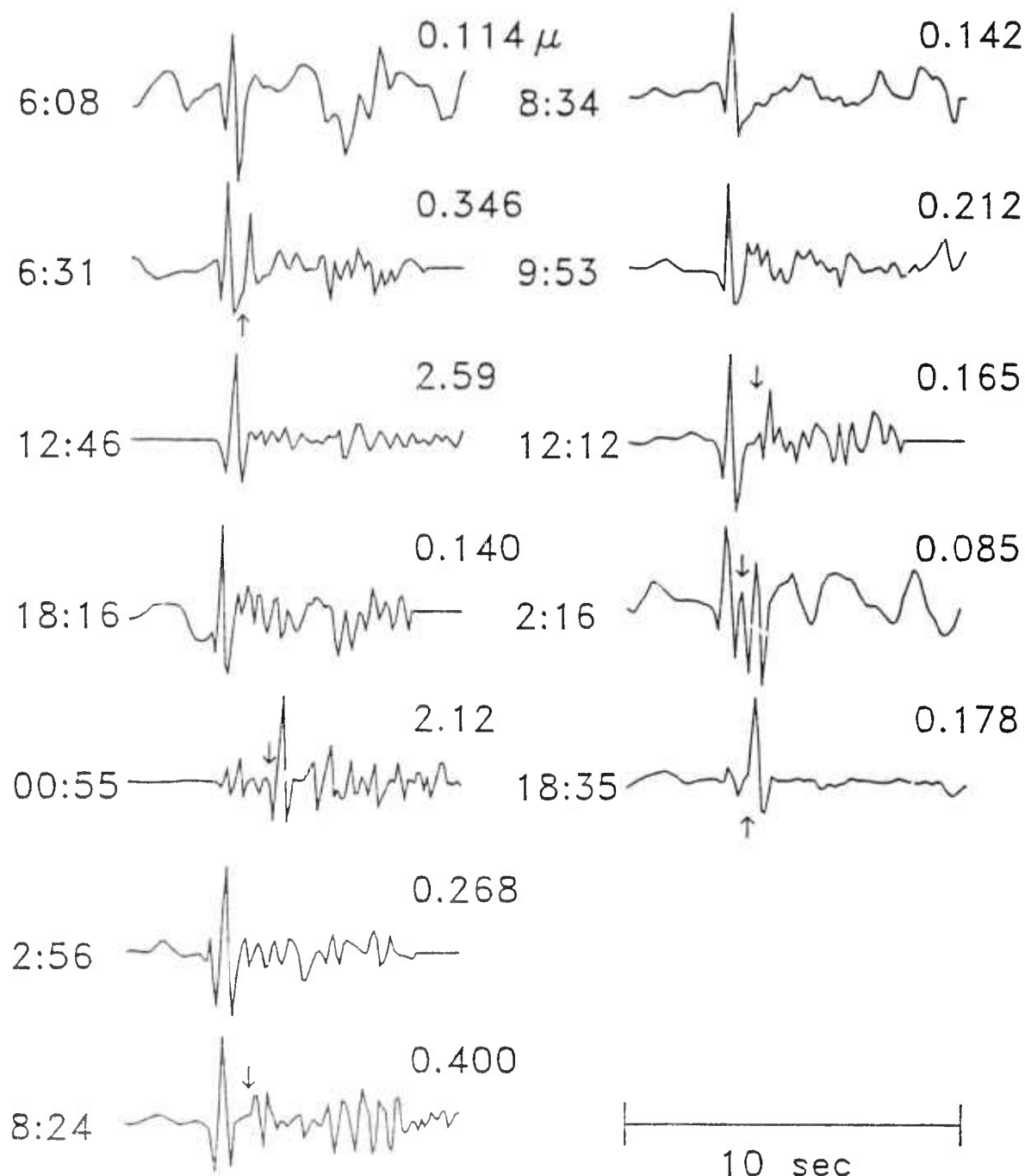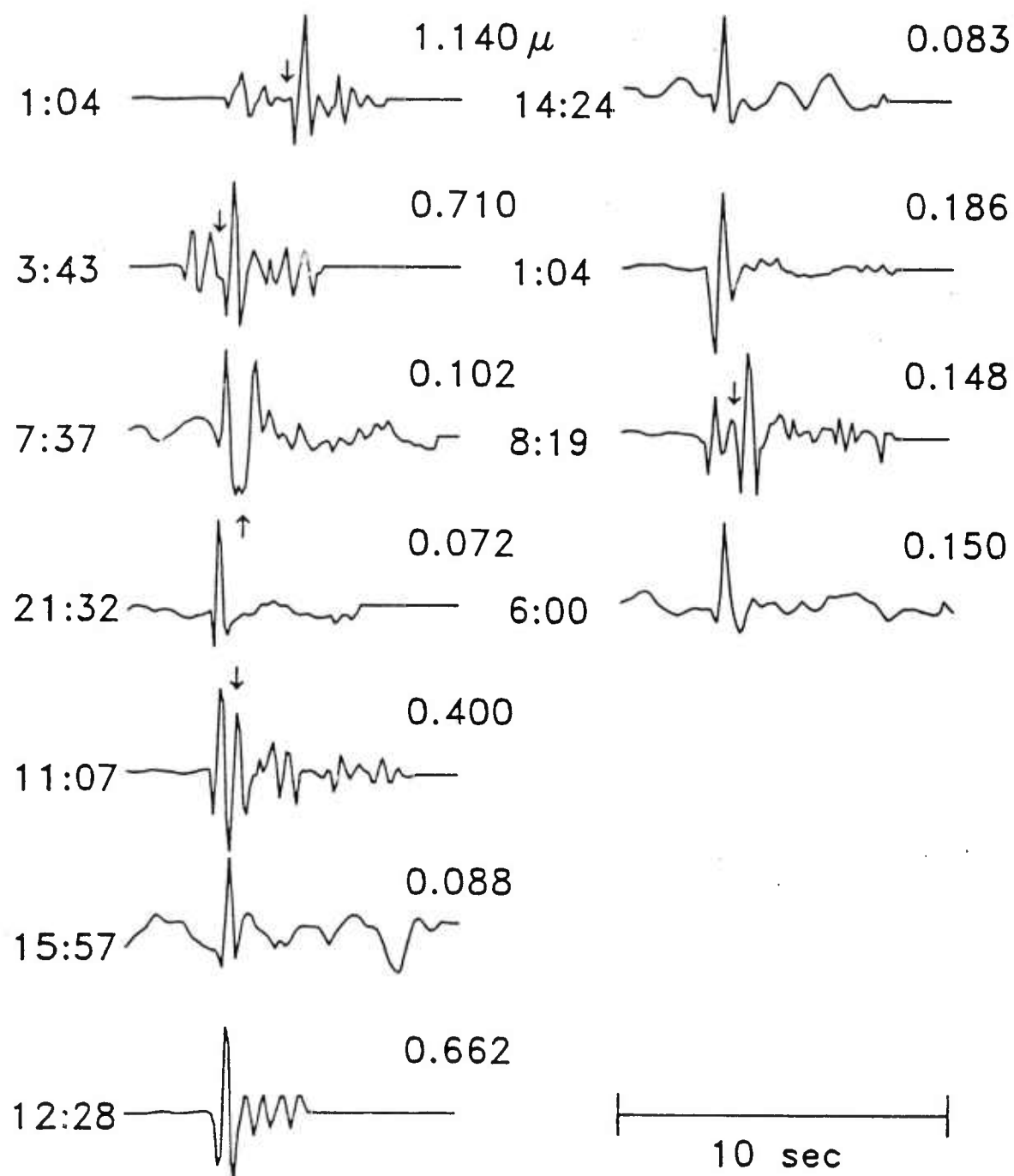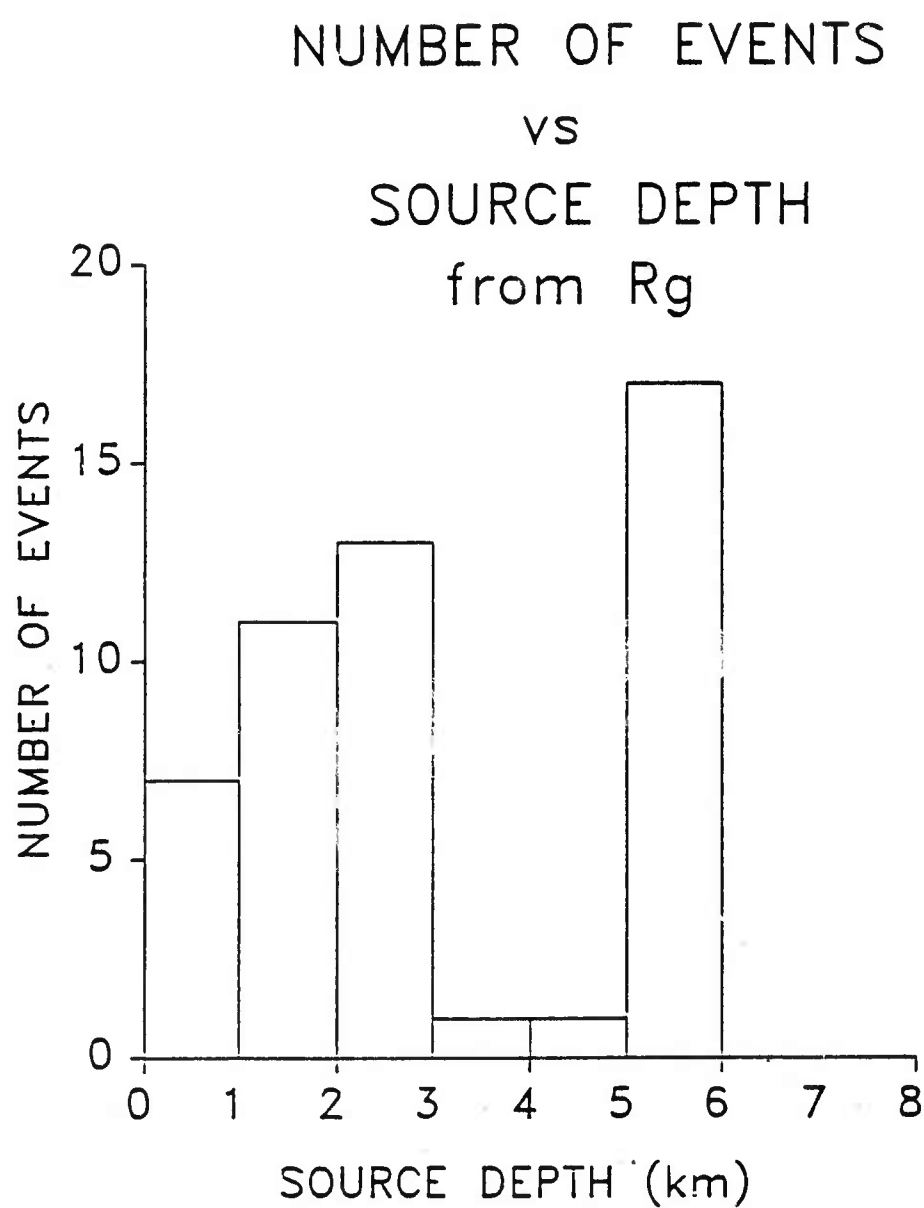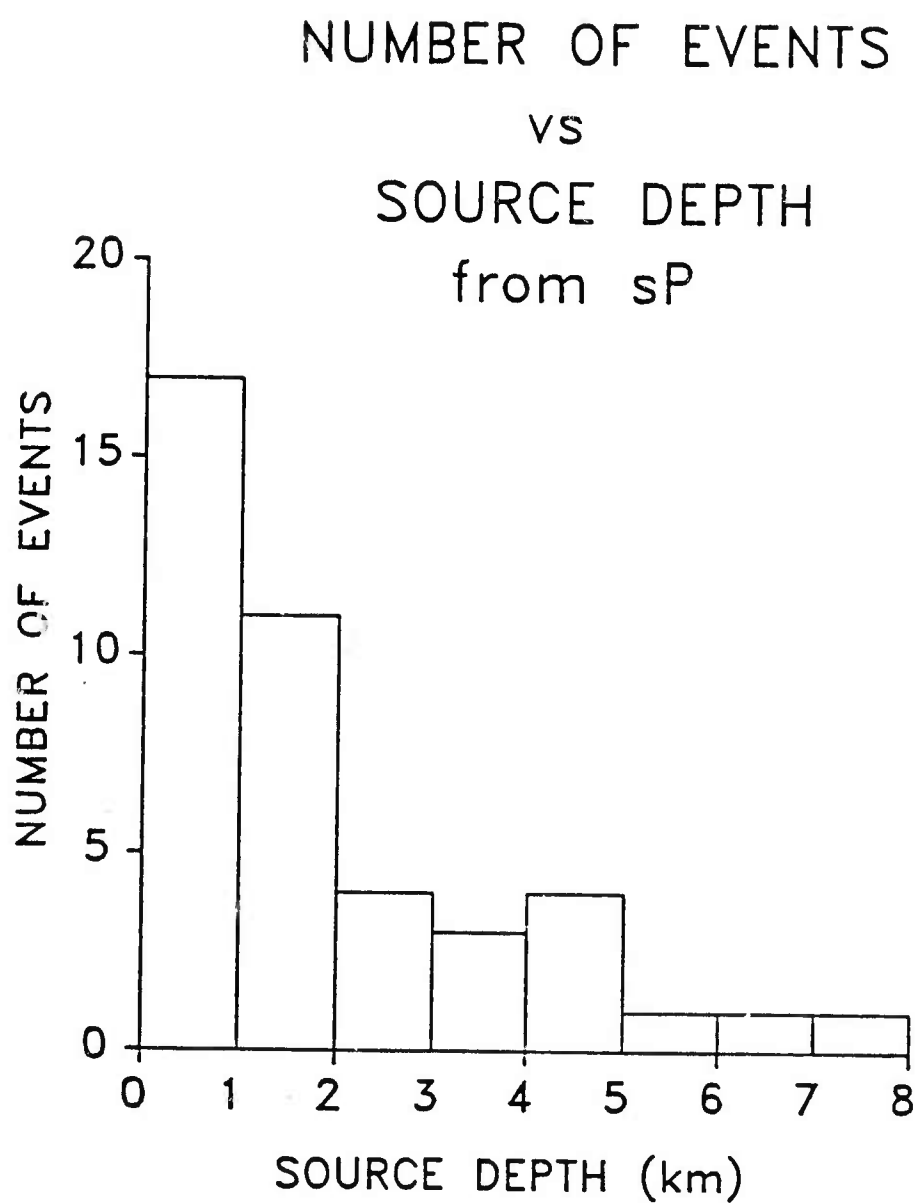
Figure 15

SECTION 2

The Pennsylvania State University

The Graduate School

College of Earth and Mineral Sciences

Aspects of Regional Short-Period Wave Propagation:
A Study of the December 1967 Koyna Earthqukes,
Maharashstra, India

A paper in

Geophysics

by

David J. Alves

Submitted in Partial Fulfillment
of the Requirements
for the Degree of

Master of Science

May 1987

David J. Alves

ABSTRACT

Short-period regional waveforms from thirteen reservoir induced events (magnitude ≈ 3.0) recorded during December 1967 at the WWSSN station, Poona (POO), India, were modeled to investigate event source parameters such as source depth, location, and mechanism as well as regional wave propagation in the vicinity of the Koyna reservoir. Generalized ray theory and wavenumber integration techniques were used in constructing synthetic seismograms for multilayered structure models at distances of 110 to 150 km and source depths of 2, 5, 10, and 15 km. It was determined that an upper layer corresponding to the Deccan Trap basalts was necessary to duplicate the observed waveforms and that the crustal wave propagation effects overwhelm most source effects in this distance range. All source depths were inferred to be less than 10 km and were qualitatively estimated by the time duration of the S waves and characteristic S and sS arrivals. The presence of short-period surface waves was found to indicate source depths of less than than 5 km for some events. The character of the P and S waves is controlled by post-critical Moho reflections interfering with direct and head waves. Thus, detailed wave propagation effects directly related to source orientation and depth tend to be obscured and affected by unknowns in crustal velocity structure.

I. INTRODUCTION

In 1962 a dam was built on the Koyna River in the western part of India creating the Shivagi Sagar Lake, a man-made reservoir (Figure 1). The dam was built on what was thought to be one of the most aseismic Precambrian blocks in the world (Guha et al.,1971), but soon after the completion of the dam, seismic activity in the area began to increase dramatically. Since the formation of the reservoir thousands of earthquakes have been recorded (Guha et al.,1970; Guha et al.,1974; Gupta et al.,1980), the largest of which was the magnitude 6.4 event of December 10, 1967 that killed 200 people, injured thousands, destroyed villages, and was felt as far away as 700 km (Narain and Gupta,1968).

Over the years there has been a great deal of dispute over the exact location, depth, fault mechanism, and cause of the events in the Koyna area. Several studies using different geophysical methods have been made (Guha et al.,1971; Gupta et al.,1972; Dube et al.,1973; Guha et al.,1974; Athavale,1975; Gupta and Combs,1976; Langston,1976,1981; Rastogi and Talwani,1980; Langston and Franco-Spera,1985) but a clear understanding of the origin and cause of these intraplate events is still a matter of debate. In view of the continuing earthquake activity in the Koyna region, accurate locations, depths, and mechanisms are needed for these events because this knowledge is vital

to determining the geological relationships and perhaps the cause of this reservoir induced seismicity. The solution to this problem is important because the more we understand about induced seismicity the better we can avoid the destruction caused by these "man-made" events in the future.

Due to the sparse station coverage, the shallow source depth, and the small magnitude of most of the events in the Koyna area, accurate determination of detailed source parameters has been very difficult. In this study, thirteen events that occurred in December 1967 are examined to see if some of the problems in determining accurate source parameters that have been encountered in the past can be overcome through the study of the regional short-period wave propagation. If aspects of the regional wave propagation are understood, the analysis of the source parameters of the smaller events may be possible. In order to do this, it must be determined what aspects of the seismogram are controlled by source and what aspects are controlled by earth structure. To answer this, the nature of the seismogram at local and regional distances and the factors that control its character must be addressed.

The nature of the short-period, regionally-recorded seismogram is usually complicated because the recorded waveforms are shaped by a complex interaction of seismic source with the crustal structure. The near-source, near-receiver, and most of all, the regional structure between the source and receiver all affect the character of the

seismogram. It is these complicated effects caused by the regional variation in the crustal structure which usually outweigh the source effects and control the character of the regional seismogram. Due to these variations, the regional seismogram is made up of a variety of diffraction effects such as head waves, critical and post-critical reflections, and surface waves. Unlike long-period studies, where knowledge of the gross earth structure is sufficient, short-period studies require finer structural detail to place meaningful constraints on the source parameters.

The events that are studied were selected because the relative simplicity of the short-period waveforms suggested that there is a simple earth structure that could be easily modeled, and hence source details could be inferred from the signal information. Even though the events are small, approximately magnitude 3.0, and insignificant in terms of strain and energy release, they provide the same information as the larger events in the Koyna area as to the nature of faulting, rupture depth, and location. Also, since there are so many small events, the redundancy of the wave propagation information might be used to advantage in identifying specific major regional wave phases.

In this study, wave propagation effects from many small events recorded at a single station are examined. The effectiveness of using a single station to obtain useful seismic information for some data sets has been demonstrated by Langston (1979,1987) and this study was motivated along

similar lines. The earthquakes were recorded at the station POO, located 120 km north of the Koyna Dam at Poona, India. At this range, POO is able to record small events which are not recorded at stations at teleseismic distances. POO, a WWSSN station, has had a very sensitive short period seismograph in operation since the early 1950's (Guha et al.,1971) and is just 5° off azimuth from due north of the dam site. Since the location of POO is almost directly north of these events, the horizontal components there are nearly naturally polarized into radial (north-south) and tangential (east-west) directions.

Synthetic seismograms utilizing previously determined velocity structures were computed using two different methods, a generalized ray theory and a wavenumber integration technique, to model the wave propagation and event source characteristics of the events in the Koyna Dam area. It will be shown that with knowledge of regional wave propagation even short-period data recorded at a single station can be used to constrain some source parameters of small earthquakes. The identification of the major regional body wave phases and the existence of surface waves are used to constrain source depth to within a few kilometers, as well as infer source mechanism and event distance for all the events studied. The simple velocity structure and its effect on wave propagation at ranges of 110-150 km makes the determination of these source parameters possible.

The method used in this study was also applied to an

explosion source along with the earthquake sources. In
doing this it was determined that possibilities exist for
the discrimination between natural events and nuclear tests.
Through the identification of the source parameters the
likelihood of a nuclear source could be eliminated by
constraining rupture depths to >10 km or by locating events
to be in areas unsuited for underground testing (e.g.
Dahlman and Israelson,1977). In addition the method can be
used in regions where limited seismic station coverage
renders other seismological methods of identification
ineffective.

II. DATA PROCESSING

Microfiche copies of all the available WWSSN short- and
long-period records for the month of December 1967 recorded
at the Poona, India station, POO, were obtained from the
National Geophysical and Solar Terrestrial Data Center
EDS/NOAA in Boulder, Colorado. Contained within this data
set were both foreshocks and aftershocks of the December 10
mainshock. These events were too small to be recorded on
the long-period system so only short-period seismograms were
studied.

For an event to be selected for digitization it had to
be on scale and be free of signal interference from adjacent
events. These problems were encountered many times since
there were numerous events distributed over a large range in

magnitude. The events that were finally picked for digitization were digitized from peak to peak at irregular intervals. The digitizing was done in this manner because the short-period seismogram varies quickly from peak to peak and may in fact only be visible at the peak of the waveforms. Other difficulties in digitizing included picking out the peaks of the P waves due to the fact that the background noise was nearly the same size as the P wave amplitude in most cases. Also, due to the compressed time scale the closeness of S wave peaks made it hard to tell which peak was next in the continuous signal.

Once digitized, a magnification correction was applied to the data and it was interpolated to a uniform .1 second interval between points. The final interpolated results for the three components of the thirteen events chosen for the study are illustrated in Figures 2.1, 2.2, and 2.3.

III. CRUSTAL STRUCTURE OF KOYNA REGION

Because of the previous aseismic nature and seemingly simple geology of the area, the geology and tectonics of the Koyna region have not been extensively studied and, therefore, are only partially known. The Koyna Reservoir is located a few kilometers east of the Western Ghats, a 1000m west-facing escarpment which acts as the continental divide for Peninsular India (Snow, 1974). The most prominent lithological unit in the area is the Deccan Trap basalts

(Figure 1). The Deccan Plateau is supported by 500,000 km^2 of these Late Cretaceous to Paleocene age volcanics (Auden,1975). The basalts are believed to be the thickest at their western edge, thin eastward (Narain,1973) and cover a granitic basement (Snow,1974; Kaila et al.,1981). The Koyna Dam is thought to be over a basement high with the basalts 6-7 km deep at the coast, thinning to 1 km at Koyna, and then thickening slightly to about 3 km eastward (Snow,1974). Supporting this is a negative gravity anomaly in the vicinity of the dam. In general, the area is relatively simple geologically and it is very surprising that so much seismic activity is concentrated in this shield area. For finer regional detail of the geologic setting the reader is referred to Snow (1974).

Many authors have suggested different crustal models of the Koyna area (Dube et al.,1973; Gupta et al.,1980; Rastogi and Talwani,1980; Kaila,1981; Bhattacharya,1981; Srivastava et al.,1984) obtained from seismic reflection studies, surface wave dispersion, body wave travel times, etc. although many similarities exist among them. Since this study is concerned with short-period regional wave propagation, it is very important to select the model that is closest to the actual crustal structure because variations may make significant differences in the computed waveforms.

The structure model that was finally chosen was a four-layer model, model A (Table 1), proposed by Dube (1986).

Dube obtained his crustal model from the body wave travel
times of forty Koyna earthquakes (mag ≥ 4.0). Although the
study lacks the exactness of explosion studies like those of
Kaila et al. (1979) and Srivastava et al. (1984), it is,
however, the more appropriate model for this study. Since
the Dube study used information from stations distributed in
azimuth in the Deccan Trap area and immediate vicinity, it
gives a more representative indication of the regional
structure than the others studies whose information
represented only a few localized profiles near the dam. The
Dube model is also supported by similar results from the
surface wave dispersion study of Bhattacharya (1981), but
Dube's model was selected because it incorporated the work
of Tandon (1973) and included an upper layer corresponding
to the Deccan Trap basalts. This upper layer will prove
significant in affecting the short-period waveforms even
though it is very thin. It's significance will be tested by
calculating synthetics for a three-layer model, model B
(Table 1), without the upper basaltic trap layer, and
comparing them to the synthetics using the four-layer, trap
model.

IV. SYNTHETIC SEISMOGRAMS

THEORY

To investigate the effects of regional structure on the
propagation of seismic waves a method of computing synthetic

seismograms which adequately model the observed regional seismograms is required. In this study two such techniques are used, generalized ray theory and wavenumber integration. The synthetics generated are used to study regional wave propagation and to delineate source and structure characteristics contained within the seismogram.

The first of the two techniques to be discussed is the generalized ray theory or Cagnaird de-Hoop method for creating synthetic seismograms. The details of this method are described in Helmberger and Harkrider (1978) for the complete linear response to an arbitrarily oriented, point shear dislocation in elastic, layered media. The advantages of this method are that the calculations are done in the time domain and that it offers insight into individual ray responses. This is possible because each ray that is calculated follows a specific ray path from source to receiver. Because of this, responses from individual rays can be isolated, thus enabling specific arrivals to be separated and identified on the synthetic seismogram. These arrivals in turn, can be used to help identify corresponding arrivals on the real seismograms. Figure 3 gives an example of how the ray paths are described in the generalized ray method where each layer segment can be assigned to be a P, SV, or SH wave depending on the type of arrivals that are to be modeled and studied. Figure 3 also describes the ray paths of the important ray arrivals for structures modeled in this study (Table 1). On both the synthetic and real

seismograms the numbers provide a convenient way of referring to specific arrivals whose ray paths correspond to those in figure 3.

The second of the two methods to be used is a wavenumber integration technique. This approach differs from the generalized ray theory method in that the calculations are done in the frequency domain where an integration over horizontal wavenumber or slowness is performed. This in theory allows a "complete" solution to be calculated resulting in a synthetic seismogram with all the possible ray responses such as multiple reflections and mode conversions included. For the generalized ray method to match this result, an infinite number of rays would have to be specified. The theory behind the wavenumber technique is described in Apsel (1979) and Barker (1984), so only a brief overview of the method will be presented here.

The scalar potential wave equation in cylindrical coordinates is solved in the frequency domain using the equations

$$\bar{\Phi}(r,\theta,z;\omega) = \sum_l A(l\theta) \int_0^\infty \Phi_l(z;k,\omega) J_l(kr)\, dk$$

$$\bar{\Psi}(r,\theta,z;\omega) = \sum_l A(l\theta) \int_0^\infty \Psi_l(z;k,\omega) J_l(kr)\, dk \qquad (1)$$

$$\bar{\chi}(r,\theta,z;\omega) = \sum_l A(l\theta) \int_0^\infty \chi_l(z;k,\omega) J_l(kr)\, dk$$

where $\bar{\Phi}$, $\bar{\Psi}$, and $\bar{\chi}$, represent the P, SV, and SH potentials respectively. A represents the azimuthally dependent terms

of the horizontal radiation pattern from the source. Φ_l, Ψ_l, and X_l, are the vertically dependent terms and are solved by a propagator matrix technique described in Barker (1984). J_l is an ordinary Bessel function of order l and k is the wavenumber in the horizontal direction r, while ω represents the angular frequency. The computational methods involved in solving equation 1 are elaborated in detail in Apsel (1979) and Barker (1984). For the wavenumber integration synthetics, 256 frequency samples were computed over an interval in ray parameter from .1 to .4 sec/km. These were inverse Fourier transformed to 512 time points at .1 sec sampling.

Once the solutions were calculated for both methods, the source time function and instrument response were convolved with them to construct the final synthetic. In all the synthetics generated in this study the source time function was a trapezoid with sides of .1, .1, .1 second duration. The short period WWSSN instrument response of Burdick (1977) was also used.

PROCEDURE

The technique used in generating the synthetic seismograms discussed in this paper, unless otherwise stated, was the wavenumber integration technique. The generalized ray method was used to interpret certain aspects of wave propagation brought out by the wavenumber integration technique. In other words, generalized ray

theory computations were used to examine particular rays to help identify the individual phases seen in both the wavenumber synthetics and the real events. The synthetic seismograms were presented in this manner because the wavenumber synthetics contained all arrivals and it would be very tedious to get generalized ray calculations of similar quality and content. This method was made practical by the John Von Neumann Computer Center's Cyber 205 supercomputer which allowed the very involved and time consuming wavenumber calculations to be performed in a reasonable amount of time.

Synthetics were calculated using the two models described in Table 1. The wavenumber technique was used to calculate seismograms for source depths of 2, 5, 10, and 15 km at receiver distances of 110, 120, 130, 140, and 150 km for both model A and model B. For model A, Figures 4.1-4.5 show an example of depth plots and figures 5.1-5.5 show an example of distance plots for different source mechanisms; the vertical, radial, and tangential components are shown in each case.

The distances for the synthetics were selected because the Koyna Dam is 120 km away from Poo and most of the regional seismicity was found to have occurred within 20 km of the reservoir (Figure 1) (Guha et al.,1970; Guha et al.,1971; Guha et al.,1974; Gupta et al.,1980; Rastogi and Talwani,1980). This is important because locating the events in question within 20 km of the Koyna Dam implies

that the wave propagation involved in all the events is
through the same crustal structure. The source depths for
the synthetic calculations were selected because previous
investigations (Guha et al., 1970; Dube et al.1973; Guha et
al.,1974; Guha et al.,1971; Rastogi and Talwani,1980;
Langston,1985) all suggest that the events in the Koyna Dam
area had originated at shallow source depths.

RESULTS

The synthetic seismograms generated by the wavenumber
integration technique will now be examined to see what
general observations can be made about them. By making
these general observations, source and structure effects are
identified in hope of making similar identifications in the
real events when they are compared. Wave propagation
aspects of the synthetics that will be discussed relate to
source depth, event distance, source mechanism, and model or
earth structure effects. The plots that will be analyzed
are those generated from model A, the four-layer structure.

The seismograms in this study are characterized by
relatively small P wave arrivals followed by a larger set of
S waves arriving 14-18 seconds after the initial P (Figures
4.1-4.5). At the shallower depths, surface waves arrive ≈10
seconds after the first S arrival on the radial and vertical
components and ≈7 seconds after the S arrival on the
tangential component. Surface waves on the vertical and
radial components are identified as Rayleigh waves from

their velocity and retrograde motion. These waves are
designated Rg because they are short-period fundamental-mode
Rayleigh waves which travel over a short continental path
and exhibit normal dispersion (Bath,1975). On the
tangential component the surface waves are identified as
Love waves which, in this case, are the fundamental-mode
transverse waves that travel in the Deccan Trap wave guide
at velocities approaching the S velocity (Bath,1975).

The first aspect of the synthetic plots to be examined
is the effect of varying source depth on the generated
waveforms (Figures 4.1-4.5). The most striking observation
is the rapid decay of the surface wave amplitude as the
source depth increases. At a source depth of 2 km the
surface waves are the largest amplitude waves on the trace
but are just barely identifiable at 5 km and non-existent at
a source depth of 10 km. A depth effect is also seen in the
P and S waves where the duration of the arrivals get
increasingly longer as the source depth increases. As the
source gets deeper the time differential between the first
and last major arrival gets greater causing the signal
duration to lengthen. The reason for this behavior is shown
with the help of Figure 3. The last major arrival, ray #7,
is a surface reflection and a source depth increase would
lengthen its travel time to the surface and therefore, to
the receiver. The first arrival, on the other hand, changes
from the direct ray, ray #1, to a higher velocity earlier
head wave arrival as the depth increases.

Another thing to note is the characteristic and distinctive nature of the major S wave peaks for different source depths. These major S wave arrivals are identified by numbers in Figures 4.1-4.5. Specific major arrivals can be seen moving apart as the depth increases. This is particularly apparent in rays #4 and #7 on the VSS and CLVD radial traces in Figures 4.3 and 4.4 and in rays #4, #6, and #7 on the VSS and VDS tangential traces in Figure 4.5. The behavior of these peaks, that are easily identifiable with the help of generalized ray theory will be a key factor in determining the depth and distance of the real events.

One last thing to note is the lack of any systematic amplitude change in the body waves that can be established as a function of depth. This is explained by the fact that the maximum amplitude depends so much on largest S wave peak which is very sensitive to angles of incidence and constructive and destructive interference of arrivals caused by structure effects at this distance.

The next aspect to be discussed is the effect of event distance on the synthetic waveforms which is most useful for determining event locations (Figures 5.1-5.5). Unfortunately, only estimates on event distance and not location can be made, because with these data from only a single station, event azimuth cannot be accurately determined. S-P times, the time difference between the initial P and S arrivals, are an effective way of determining event distances. The S-P times as seen in

figures 5.1-5.5 range from 14 seconds at 110 km to 18.5
seconds at 150 km. The initial P and S times were selected
from the vertical and tangential components respectively.
S-P times determined in a similar fashion will be used in
estimating the distances of the real events.

Another significant aspect is again, the variation of
the S wave peak amplitude. One cause of this variation is
evident in the S wave portion of the vertical and tangential
components (Figure 6). Here the interaction between ray #6
and ray #4 plays an important role in shaping the S
waveform. As the distance increases the order of the
arrivals changes from #6 arriving before #4, at 110-120 km,
to simultaneous arrivals, at 130 km, to #4 arriving before
#6, at 140-150 km. This wave propagation effect of
constructive and destructive interference significantly
alters the relative S wave amplitudes and character of the S
waves on these components.

A different type of distance effect can also be seen in
the S wave portion of the seismograms. The timing of
post-critical reflections alters the nature of the traces.
Impressive changes in arrival #7, the surface-to-Moho
reflection, are evident, changing from a small pre-critical
arrival at 120 km to a large post-critical reflection at a
distance of 130 km (Figure 7).

When the variation in source mechanism is examined it
must be kept in mind that the information to be gained is
very limited. Due to the fact that only pure VSS, VDS,

CLVD, and explosion sources are calculated at a single station and azimuth, only major differences will be of any use when analyzing the real events. At first glance, the only characteristic that stands out is the fact that the amplitudes of the radial S waves are smaller than the vertical S waves for VDS mechanism by a factor of three. In comparison, the ratio of the vertical to radial S waves is about one for the VSS and CLVD mechanisms. The variation in source radiation pattern, which has a profound affect on the seismic waveforms, causes these changes in amplitude.

The explosion source shown in Figures 4.2 and 4.4, even though not directly relevant to the Koyna earthquakes, is still useful in showing wave propagation effects for consider tion of nuclear discrimination problems. Since the explosion source generates no S wave, it is also useful for examining possible P to S conversions. As seen in Figures 4.2 and 4.4, P to S conversions (arriving at approximately the same time as the S arrivals on the other mechanisms) do not have a profound effect on the character of the seismogram. Even at a source depth of 2 km the major P to S conversion is an order of magnitude smaller than the corresponding S waves of the other mechanisms. The same is true for the surface waves.

The final aspect of the synthetic seismograms to be examined is earth structure effects which are model dependent. To do this, model A and model B synthetics are compared. The most noticeable difference in seismograms

calculated from model B (Table 1) is that they have a total lack of long-duration surface waves even at a source depth of 2 km (Figures 8.1-8.3). This effect is caused by the change in arrival time of the surface waves due to the existence of the Trap layer in model A. The Rg wave (Figures 8.1-8.2) travels at ~ 3.0 km/sec in model B but at only ~ 2.4 km/sec in model A. At a distance of 120 km this causes the model B Rg wave to arrive only 3 sec after the direct S while the model A Rg wave arrives 12 sec after the initial S. Thus, model B surface waves interfere with S reflections arriving shortly after the direct S arrival, while model A surface waves are clearly visible on the trace, arriving long after the major S reflections. The same is true of the Love waves in Figure 8.3. This upper layer also has the effect of dispersing the surface waves due to the wave guide it provides.

Model B seismograms are less complicated in terms of general appearance than those of model A because there is less reverberation in the structure with fewer layers. Also in the three-layer model, the radial P waves and vertical SV waves are large while the opposite is true for the four-layer model. This occurs because the upper trap layer on the four-layer model acts to decrease the angle of incidence of the incoming waves. Thus, the P waves are larger in the vertical direction and the SV waves are larger in the radial direction, since SV motion is orthogonal to the P wave motion. Another difference is the distance where

the rays turn from pre-critical to post-critical reflections. In Figure 8.1, the surface to Moho arrival is post-critical at 120 km in model B (ray #5), but is not in model A (ray #7). These are examples of how slight changes in the velocity structure can drastically affect the seismograms.

V. COMPARISON OF THE SYNTHETICS TO THE OBSERVATIONS

Using the general behavior of the synthetics as discussed earlier, comparisons with the real data can now be made to see what can be learned about these events. In identifying characteristics of the real events it must be pointed out that the extent to which they are constrained is limited to the scale on which the synthetics are generated. In other words, since the depths are calculated at 2, 5, 10, and 15 km and the distances in 10 km intervals, constraining depths and distances to within a few kilometers could be difficult because of these gaps in the parameters. The problems with determining location and source mechanism of the events has already been touched upon in previous sections, and because of these, the distances and fault mechanisms will be only discussed in a general way when applied to the real event descriptions.

Identifying depth and structure effects in the real events on the other hand, seems to be slightly more promising since the synthetics effectively mimic the S wave

behavior of the real events. These effects can be
constrained with single station data with a greater degree
of confidence than other effects. P wave information will
not be used because the very low signal to noise ratio
obscures any useful phase information that could have been
gained from it. It should be understood, however, that many
of the source parameter interpretations are very subjective,
because structure effects seem to dominate the waveforms.
This coupled with the background noise and unknowns in
crustal velocity structure makes exact identification of
arrivals on the real seismograms difficult.

Some event depth determinations are possible due to the
presence of surface waves. Looking at the real events it is
easy to see in Figures 2.1 and 2.2 that events 5, 6, 9, and
13 have Rg waves associated with them and in Figure 2.3 that
events 1, 5, 9, and 13 have Love waves associated with them.
The presence of these surface waves indicates a shallow
source depth, less than 5 km. This was shown in the
synthetics (Figures 4.1-4.5) where the surface waves were
significant at a source depth of 2 km but were very small by
the time the source was 5 km in depth. The shallowness of
these real events has the effect of making the usually
distinctive S wave arrivals disappear and merge with the
surface waves to form a long train of arrivals where phase
identification is lost.

The distinctive S wave pattern of peaks that is so
prevalent in the data can also be used as a depth indicator,

if the specific phase identifications are to be believed.
Depth determinations are possible due to the success of
using the known S arrivals on the synthetic seismograms to
identify specific S arrivals on the real seismograms. The
major S arrivals are identified by running generalized ray
models for the rays specified in Figure 3. From these major
arrivals it is hoped that a depth indicator can be found,
but only certain pairs of ray paths can give a reliable
indication of depth. One of the rays must travel down to an
interface while the other in the pair travels upward to an
interface, before reflecting downward. The difference in
the arrival times gives an indication of depth, the greater
the time differential between these reflectors the deeper
the source.

Of the three components the radial component is the
most promising for identifying depth phases (Figure 2.2).
The S wave portion of the radial component is the simplest
of the three with only two arrivals that stand out,
identified as #4 and #7. This is fortunate because this
pair of rays is a combination that fits the criteria for a
depth determination, with #4 going down to the Moho while
ray #7 travels upward to the surface before reflecting down
to the Moho. The S wave portion on the radial component of
events 1, 2, 3, 4, 7, 8, 10, 11, and 12 (Figure 2.2) looks
remarkably similar to the VSS synthetics generated at a
distance of 120 km (Figure 7). In the synthetics at a
distance of 120 km and depths of 5 and 10 km, the #4 and #7

arrivals can be seen moving apart as the depth increases.
This effect is illustrated in Figure 9 where the real events
are put in order of increasing depth based on the synthetics
of 2, 5, 10, and 15 km source depths, assuming these phase
identifications are correct.   The arrival times of both rays
#4 and #7 were corroborated to some degree by the vertical
and tangential components as well.

The VSS synthetics are shown because the real events
seem to resemble that type of mechanism more than any of the
others which were synthesized.   This is consistent with many
of the mechanism determinations previously reported (Guha et
al.,1970; Guha et al.,1974; Langston,1976; Rastogi and
Talwani,1980; Langston,1981) which show that strike-slip
faulting is common in the area.   The strike-slip mechanism
is also supported by the amplitude of the S waves seen in
the real events.   The S wave amplitude is much greater than
the P wave amplitude and dominates the character of the
seismogram.   This was seen in the VSS, but not in the VDS
synthetics (Figures 4.1-4.5).

The events shown in Figure 9 seem to have occurred at
distances of less than 130 km because of the small amplitude
of ray #7 compared to the large amplitude of ray #4.   This
amplitude variation was discussed in the synthetic results
section and is shown in Figure 7 where the surface to Moho
reflection changes from of small amplitude arrival at 120 km
to a large amplitude post-critical reflection at 130 km.
The S-P times of the real events also indicate distances of

less than 130 km. The S-P times for the real events range
from 14 to 17 seconds. When compared to the synthetics this
indicates event distances between 110 and 130 km.

In comparing the results from the two models (Figures
8.1-8.3), it is determined that model A is the superior
model, thus making the trap layer an important ingredient in
characterizing regional wave propagation of the Koyna area.
Many differences in the synthetics generated for the two
models make it clear that model A is the better model. The
first of which is that there are surface waves present in
some of the real events. Their long duration and timing
cannot be duplicated in the three-layer model, even at a
source depth of 2 km, but is duplicated by the four-layer
model with the addition of the trap layer. The longer
duration of the surface waves in the real events could be a
result of dispersion or reflecting and scattering of waves
by lateral heterogeneity in the trap layer.

There are also more detailed features in the observed
data which are duplicated more effectively with model A than
with model B. The surface-to-Moho reflection is
post-critical at 120 km in model B (Figure 8.1) but not in
model A. This tends to support model A because the real
events do not show a large arrival at that time and the
events are in that distance range. The amplitude ratios of
P to SV waves on the vertical and radial components also
agree more with model A. The P wave radial-to-vertical
amplitude ratio is much greater for the three-layer model

than the four-layer model or the real events (Figures 8.1-8.2). The reason for this difference was explained earlier by the angle of incidence of the rays being changed by the addition of the trap layer. This makes the ratio of the radial and vertical P waves about one, similar to the real events (Figures 2.1-2.2). Also, the radial component of the trapless model has no distinct identifiable phases, unlike the real events and model A synthetics in which the radial component has the most easily identifiable and distinct arrivals. On the tangential component model B has a very large first S arrival, in fact the largest arrival on the trace. This large arrival is contrary to what is seen in the model A synthetics and the real events where the first S arrival is very small and is sometimes lost in the noise. These factors all contribute to the conclusion that the trap layer plays an important role in regional wave propagation in the Koyna area.

VI. DISCUSSION AND CONCLUSIONS

From the comparison of the synthetics to the real events it can be seen that the wavenumber integration technique does a satisfactory job of effectively reproducing the the simplistic waveforms first noticed in the real events. The results from generalized ray theory confirm that the structure in the Koyna area is relatively simple due to the fact that by specifying just seven rays, the

resulting synthetics can sufficiently duplicate the S wave character of the real events (Figure 6). From the synthetics generated by the two methods, aspects of the regional wave propagation were identified. The major regional phases were identified and from these it was determined that many interesting wave effects occur at this distance of 110-130 km. From these, source and structure properties of the thirteen Koyna events were determined.

Model A was found to be the superior model for the Koyna area because the trap layer plays a major role in influencing regional wave propagation. It is important that with the addition of the fourth layer, surface waves could be generated at shallow depths because the existence of Rg and Love waves in some of the real events. The post-critical timing of the surface-to-Moho reflection and the P to S amplitude ratios of the synthetics also resemble the real events more effectively with the addition of the trap layer.

Of the source parameters examined, depth was probably the best constrained for these events. The depths of all thirteen events studied were determined to be less than 10 km. Supporting this conclusion is the existence of short-period surface waves. Rg waves in events 5, 6, 9, and 13 and Love waves in events 1, 5, 9, and 13, indicating that these events occurred at depths of less than 5 km. This makes them the shallowest of the events studied. The rest of the events, 2, 3, 4, 7, 8, 10, 11, and 12 were found to

be shallower than 10 km based on the Moho reflection (ray
#4) and the surface to Moho reflection (ray #7) which were
found to be the two large, easily identifiable arrivals on
the radial component of the seismograms (Figure 9). The
time between the two arrivals increases as the source depth
increases and it can be seen that the time differential
between them is consistent with depths shallower than 10 km.

Also contributing to the depth determination is the
character of the major S wave arrivals on the vertical and
tangential components. The interaction between the #4 and
#6 ray arrivals and the #7 arrival make up the S wave
character of these two components. At the distances in
question, ~ 120 to 130 km, the real events resemble the
synthetics at 5 and 10 km in depth rather than the 15 km
case. The duration of the P and S waves, as well as the
time separation among the major S wave arrivals, was too
great at a source depth of 15 km. The P waves were used
only for determining the event first arrival and duration.

As for other source parameters such as location and
source mechanism, very few conclusions can be drawn but some
observations can be made. The source radiation pattern and
unknowns in velocity gradients control the amplitude and
character of the distinctive S wave peaks. Large changes in
relative amplitudes can occur just because radiation pattern
differences in up and downgoing rays. Varying the
post-critical timing and constructive and destructive
interference of the waves are examples of how the complex

interaction between radiation pattern and crustal structure
can affect relative amplitudes. Another general observation
is that the synthetics calculated with VSS fault mechanism
created seismograms with waveforms most like those observed
in the real events. This is consistent with past mechanism
determinations in the the area, but again is only the most
general of observations since there is only a single station
and only four fault mechanisms calculated. Some of the
problems in determining location have been already
discussed, but it was observed that the real events
resembled the synthetics generated for a distance of 110 to
130 km which is the approximate distance from Poona to the
Koyna dam. S-P times also agreed with distance estimates in
this range.

From the synthetics it was seen that the simplistic
waveforms in the real events were easily duplicated. The
major waveforms which make up the events have been
identified resulting in the discovery of many interesting
regional wave propagation effects. It was shown that the
small events (≈ magnitude 3) are generally shallow in depth,
less than 10 km, have some strike-slip characteristics, and
that the Deccan trap layer was essential to modeling these
short period effects. The need for more data from short-
period seismic stations in the area is apparent, for without
these data, fault mechanisms and event locations of these
small events are not able to be found with any degree of
confidence. If the synthetic modeling and wave propagation

information from this study are combined with information
from other stations in the area, much more could be learned
about the nature of the event source parameters. This would
help increase the knowledge of the geologic and tectonic
relationships of these reservoir induced events from which
some of the causes could eventually be determined.

REFERENCES

Apsel, R. (1979). Dynamic Green's functions for layered media and applications to boundary value problems, Ph.D. Thesis, University of California, San Diego, La Jolla, California, 349 pages.

Athavale, R.N. (1975). Induced seepage along a coast parallel system of faults as possible cause of the Koyna earthquakes, Bull. Seis. Soc. Am., 65, 183-191.

Auden, J.B. (1975). Seismicity associated with the Koyna Reservoir, Maharashtra, Prepared for the Government of India by the United Nations Educational, Scientific and Cultural Organization (Unesco), Paris, Serial No. FMR/SC/GEO/75/135.

Barker, J.S. (1984). A seismological analysis of the May 1980 Mammoth Lakes, California, earthquakes, Ph.D. Thesis, Pennsylvania State University, University Park, Pennsylvania, 279 pages.

Bath, M. (1975). Short-period Rayleigh waves from near-surface events, Phys. Earth Plant. Interiors, 10, 369-376.

Bhattacharya, S.N. (1981). Observation and inversion of surface wave group velocities across central India, Bull. Seim. Soc. Am., 71, 1489-1501.

Burdick, L.J. (1977). Broad-band seismic studies of body waves, Ph.D. Thesis, California Institute of Technology, Pasadena, California, 151 pages.

Dahlman, O. and H. Israelson (1977). Monitoring Underground Nuclear Explosions, Elsevier, Amsterdam-Oxford-New York, 440 pages.

Dube, R.K., J.C. Bhayana, and H.M. Chaudhury (1973). Crustal structure of the Peninsular India, Pure Appl. Geophys., 109, 1717-1727.

Dube, R.K. (1986). Relocation of the Koyna earthquakes with a new velocity model, Bull. Seism. Soc. Am., 76, 395-407.

Guha, S.K., P.D. Gosavi, M.M. Varma, S.P. Agarwal, J.G. Padale, and S.C. Marwadi (1970). Recent seismic disturbances in the Shivajisagar Lake area of the Koyna Hydroelectric project, Maharashtra, India, Report of the Central Water and Power Research Station, Poona, India.

Guha, S.K., P.D. Gosavi, J.G. Padale, and S.C. Marwadi (1971). An earthquake cluster at Koyna, <u>Bull. Seism. Soc. Am.</u>, 61, 297-315.

Guha, S.K., P.D. Gosavi, K. Nand, J.G. Padale, and S.C. Meradi (1974). Koyna earthquakes (October 1963 to December 1973), Report of the Central Water and Power Research Station, Poona, India, 340 pp.

Gupta, H.K., B.K. Rastogi, and H. Narain (1972). Some discriminatory characteristics of earthquakes near Kariba, Kramasta and Koyna artificial lakes, <u>Bull. Seis. Soc. Am.</u>, 62, 493-507.

Gupta, H.K. and J. Combs (1976). Continued seismic activity at the Koyna reservoir site, India, <u>Eng. Geol.</u>, 10, 307-313.

Gupta, H.K., C.V. Rama Krishna Rao, B.K. Rastogi, and S.C. Bhatia (1980). An investigation of earthquakes in Koyna region, Maharashtra, for the period October 1973 through December 1976, <u>Bull. Seism. Soc. Am.</u>, 70, 1833-1847.

Helmberger, D.V. and D.G. Harkrider (1978). Modeling earthquakes with generalized ray theory, in <u>Proc. of IUTAM Symposium: Modern problems in elastic wave propagation</u>, J. Miklowitz and J. Achenback, eds., John Wiley and Sons, New York.

Kaila, K.L., P.R. Reddy, M.M. Dixit and M.A. Lazarenko (1981). Deep crustal structure at Koyna, Maharashtra, indicated by deep seismic soundings, <u>Jour. Geol. Soc. India</u>, 22, 1-16.

Langston, C.A. (1976). A body wave inversion of the Koyna, India, earthquake of December 10, 1967, and some implications for body wave focal mechanisms, <u>J. Geophys. Res.</u>, 81, 2517-2529.

Langston, C.A. (1979). A single-station fault-plane solution method, <u>Geophys. Res. Letters</u>, 6, 41-44.

Langston, C.A. (1981). Source inversion of seismic waveforms: the Koyna, India, earthquakes of 13 September 1967, <u>Bull. Seism. Soc. Am.</u>, 71, 1-24.

Langston, C.A. and M. Franco-Spera (1985). Modeling of the Koyna, India, aftershock of 12 December 1967, <u>Bull. Seis. Soc. Am.</u>, 75, 651-660.

Langston, C.A. (1987). Depth of faulting during the 1968 Meckering, Australia, earthquake sequence determined

from wave form analysis of local seismograms, submitted to _J. Geophys. Res._

Narain, H. and H. Gupta (1968). Koyna earthquake, _Nature_, 217, 1138-1139.

Narain, H. (1973). Crustal structure of the Indian subcontinent, _Tectonophysics_, 20, 249-260.

Rastogi, B.K. and P. Talwani (1980). Relocation of Koyna earthquakes, _Bull. Seism. Soc. Am._, 70, 1849-1868.

Snow, D.T. (1974). The hydraulic, geomorphic and tectonic setting of man-made earthquakes, _Final Tech. Rept. U.S. Geol. Surv. Contract_, 73pp.

Srivastava, H.N., R.K. Verma, G.S. Verma, and H.M. Chaudhury (1984). Crustal structure of the Koyna region using explosion data from deep seismic sounding, _Tectonophysics_, 110, 61-72.

Tandon, A.N. (1973). Average thickness of the Deccan Trap between Bombay and Koyna from dispersion of short period love waves, _Pure Appl. Geophys._, 109, 1693-1699.

TABLE 1

MODEL A
Four-Layer Model Structure Parameters

```
******************************************************************
```

Vp (km/sec)	Vs (km/sec)	Density (g/cc)	Thickness (km)	QP[1]	QS[1]
4.60	2.65	2.60	1.2	1000	500
5.78	3.34	2.70	20.0	1000	500
6.58	3.80	2.90	18.8	1000	500
8.19	4.73	3.20	H.S.	1000	500

```
******************************************************************
```

MODEL B
Three-Layer Model Structure Parameters

```
******************************************************************
```

Vp (km/sec)	Vs (km/sec)	Density (g/cc)	Thickness (km)	QP[1]	QS[1]
5.78	3.34	2.70	20.0	1000	500
6.58	3.80	2.90	18.8	1000	500
8.19	4.73	3.20	H.S.	1000	500

```
******************************************************************
```

[1] Attenuation not used in generalized ray calculations
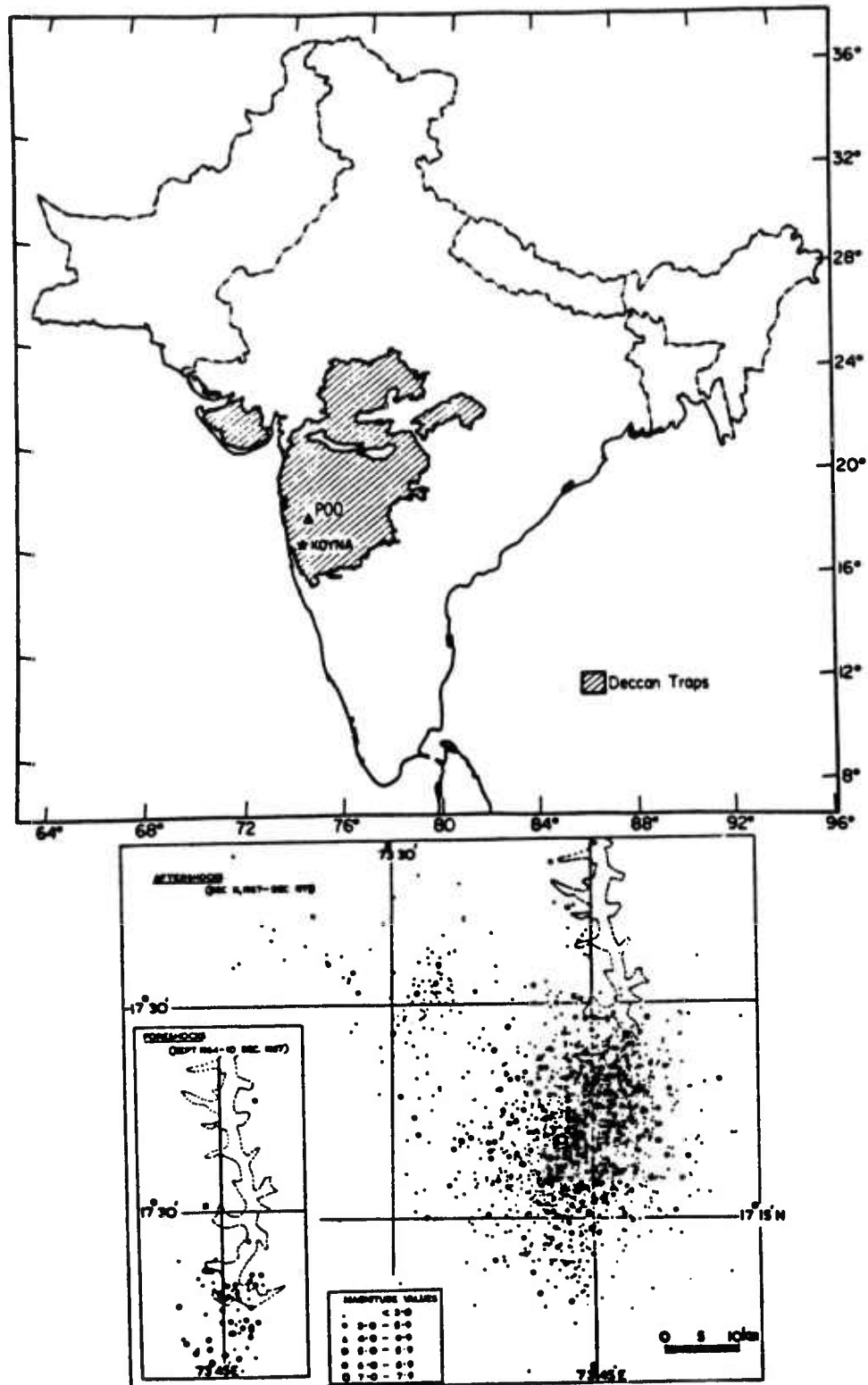
Figure 1 (Top) Index map showing extent of Deccan Traps and source and station locations (after Langston, 1981). (Bottom) Expanded view of star showing Shivagi Sagar Lake and associated seismicity (after Guha et al.,1974).
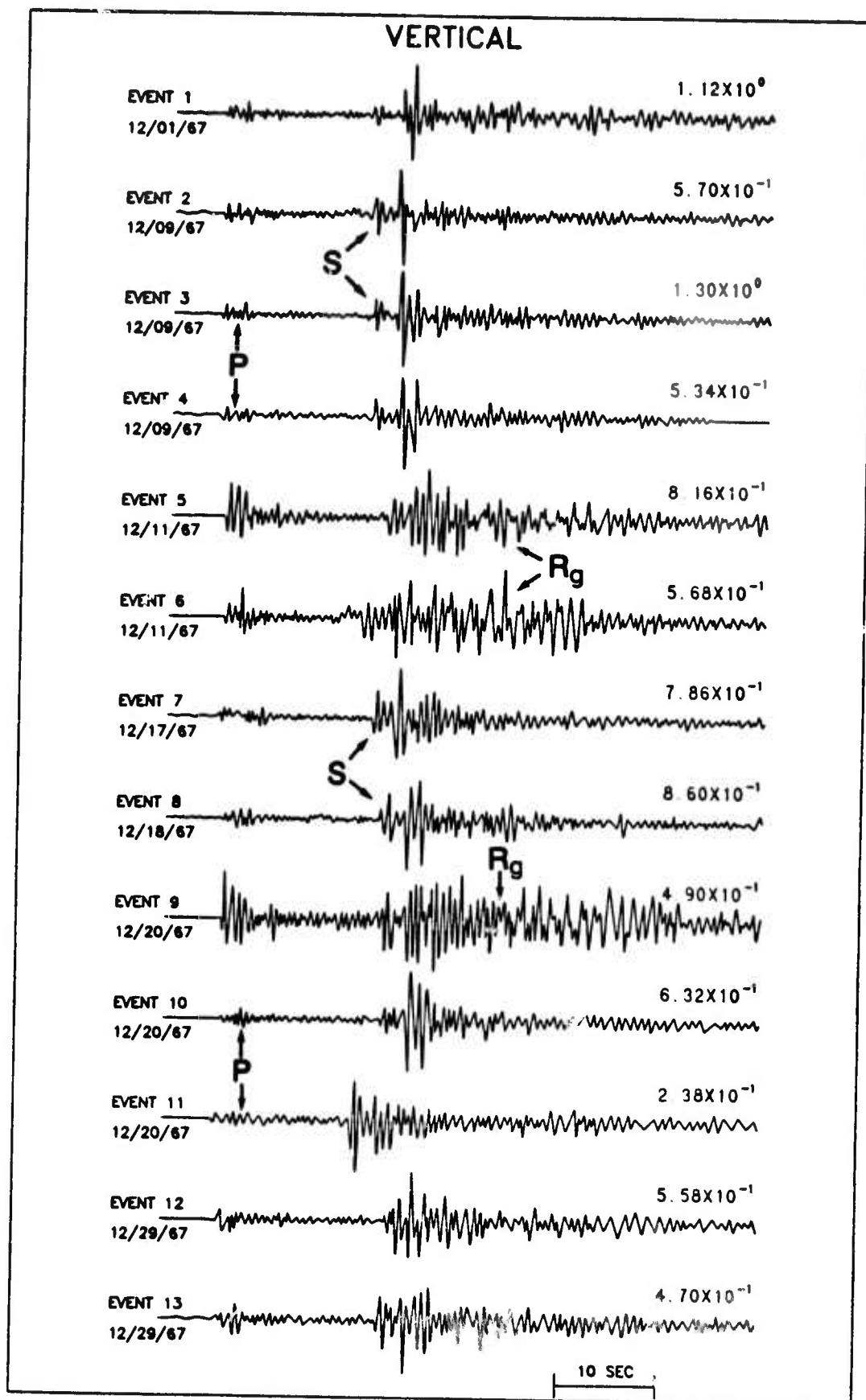
Figure 2.1 Vertical component of the thirteen digitized Koyna events of December 1967 recorded at POO. Major phases are denoted by P, S and Rg. Amplitudes are normalized and given in microns.
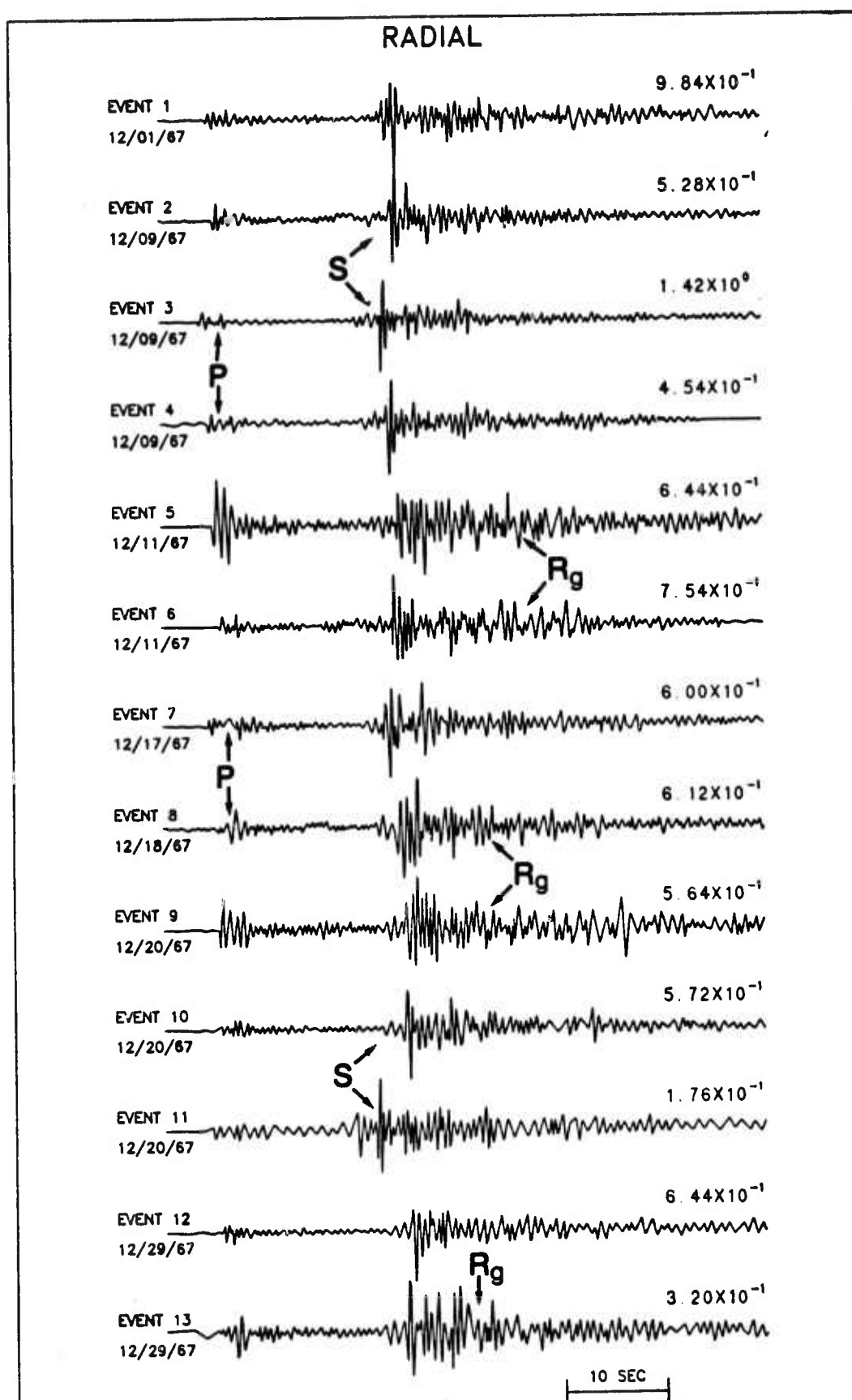
Figure 2.2 Radial component of the thirteen digitized Koyna events
of December 1967 recorded at POO. Major phases are
denoted by P, S and Rg. Amplitudes are normalized and
given in microns.
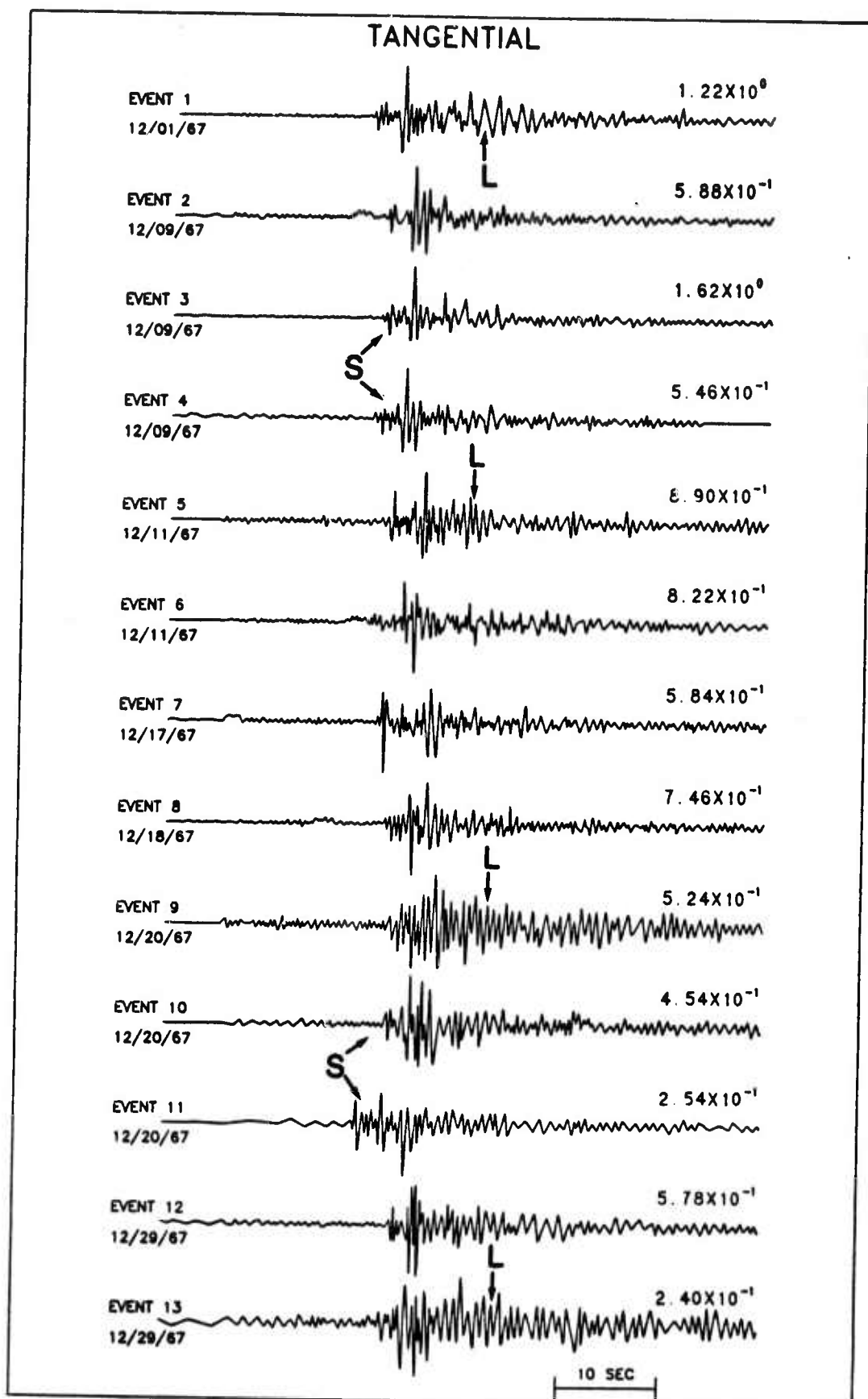
Figure 2.3   Tangential component of the thirteen digitized Koyna events of December 1967 recorded at POO.   Major phases are denoted by S and L (Love).   Amplitudes are normalized and given in microns.
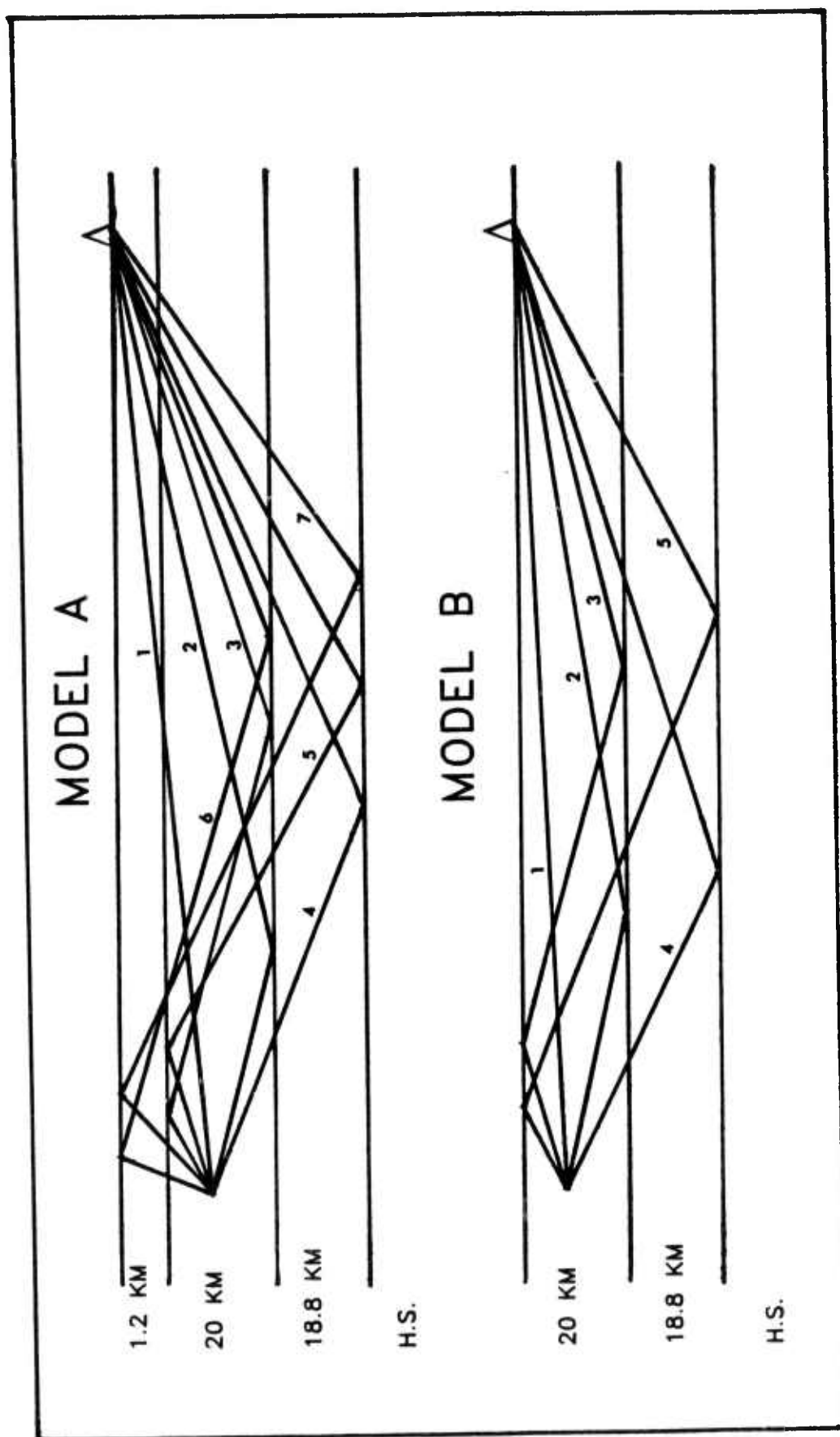
Figure 3 Ray paths of the major arrivals generated from the synthetics for the structures described in Table 1.
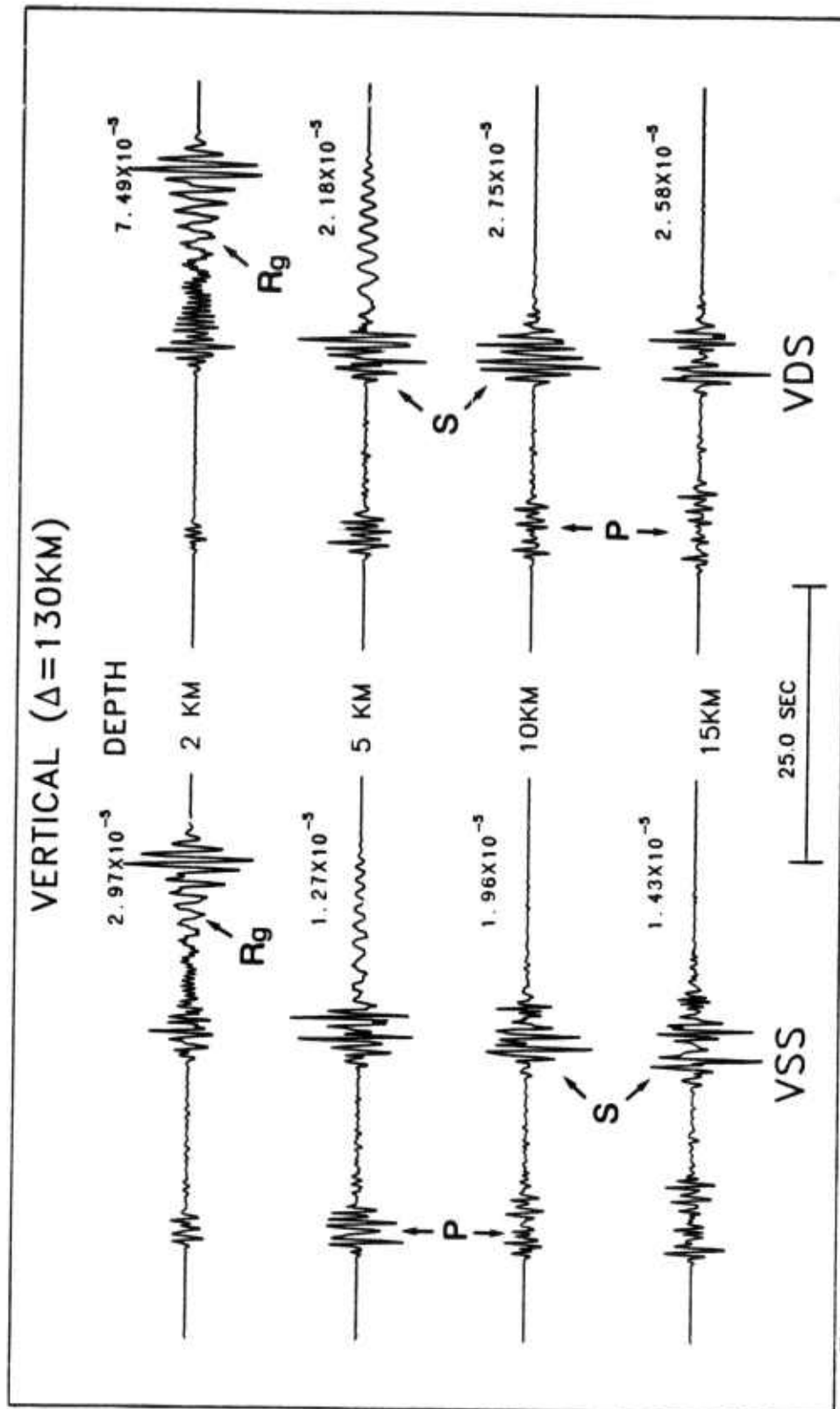
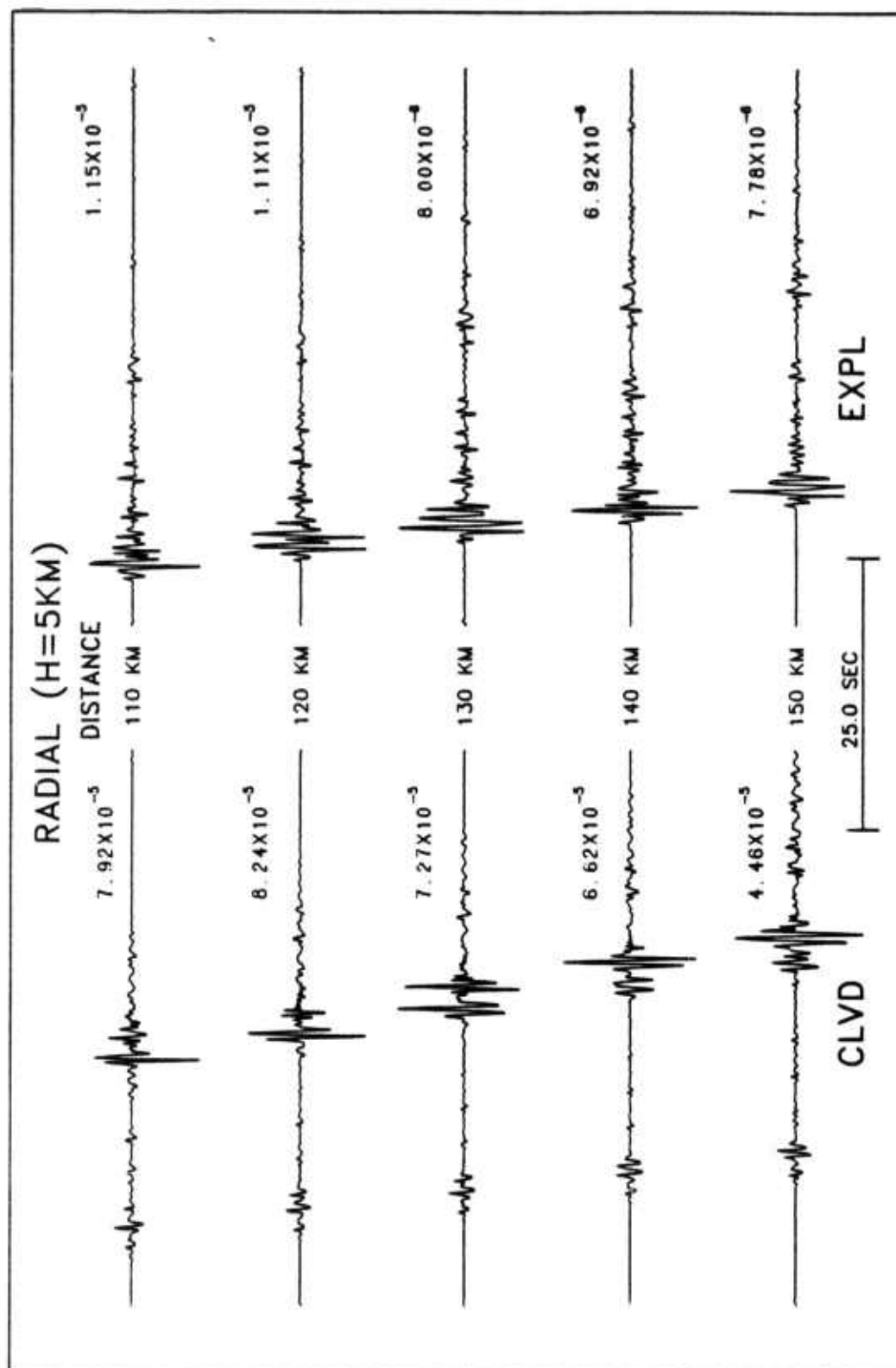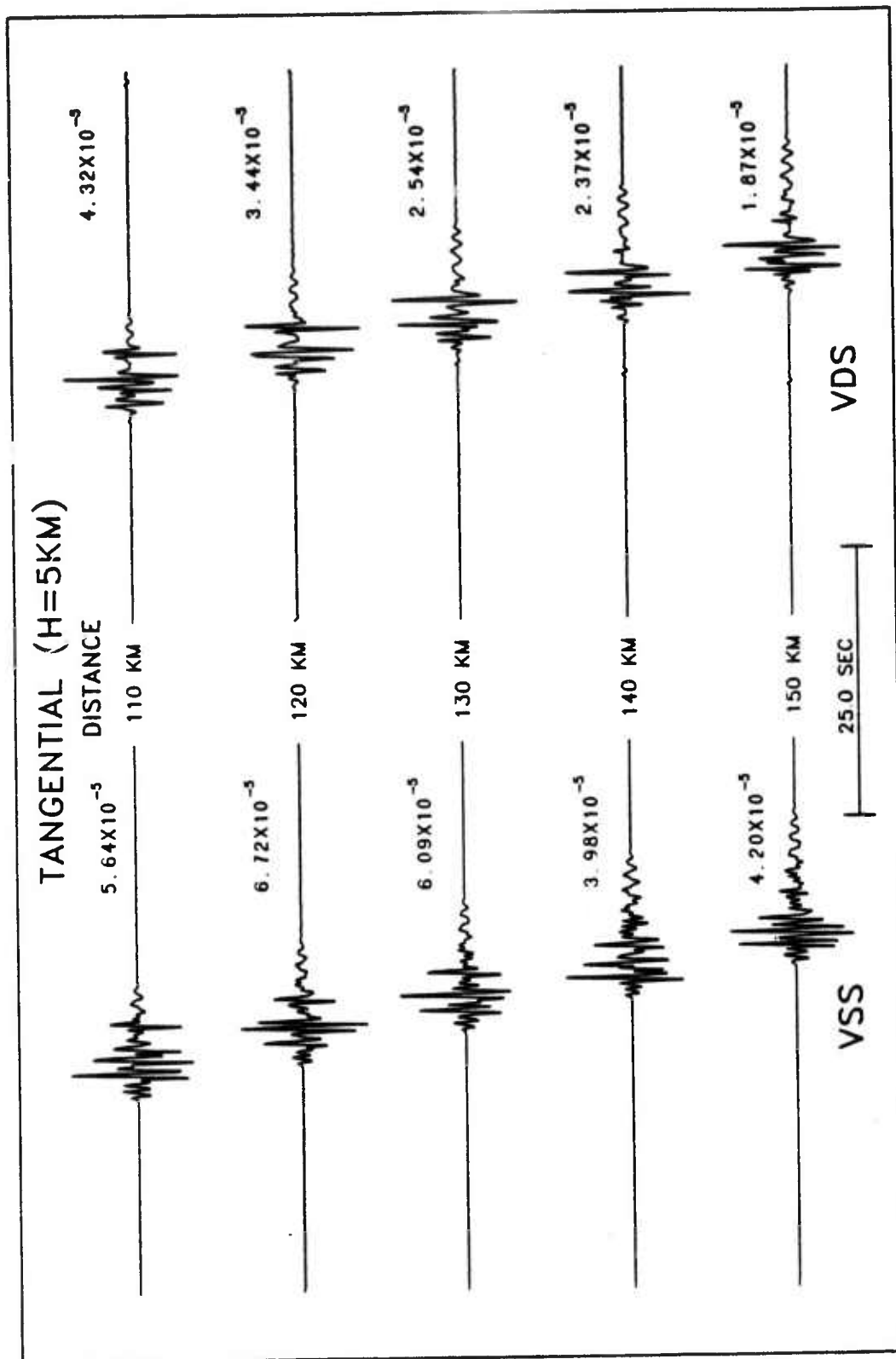Figure 4.1 Synthetics created using Model A showing waveform variation with depth of vertical component for vertical strike-slip (VSS) and vertical dip-slip (VDS) source mechanisms. Note the S wave character and the presence of surface waves at 2 km depth. Major phases are indicated as P, S and Rg. Amplitude is in cm for an assumed seismic moment of 20 dyn cm for all synthetics generated.
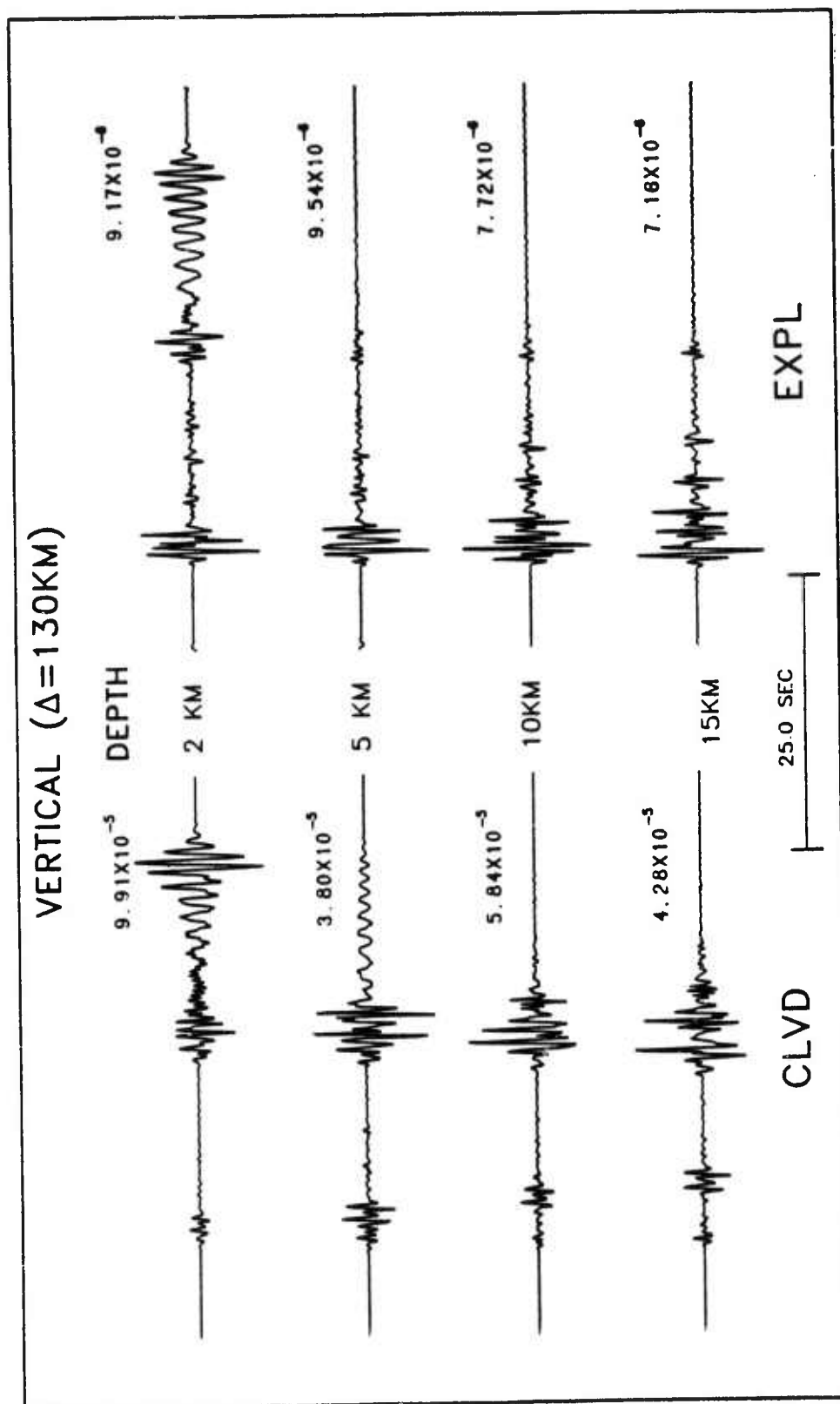
Figure 4.2 Synthetics created using Model A showing waveform variation with depth of vertical component for compensated linear vector dipole (CLVD) and explosion (EXPL) source mechanisms. Note the S wave character and the presence of surface waves at 2 km depth.
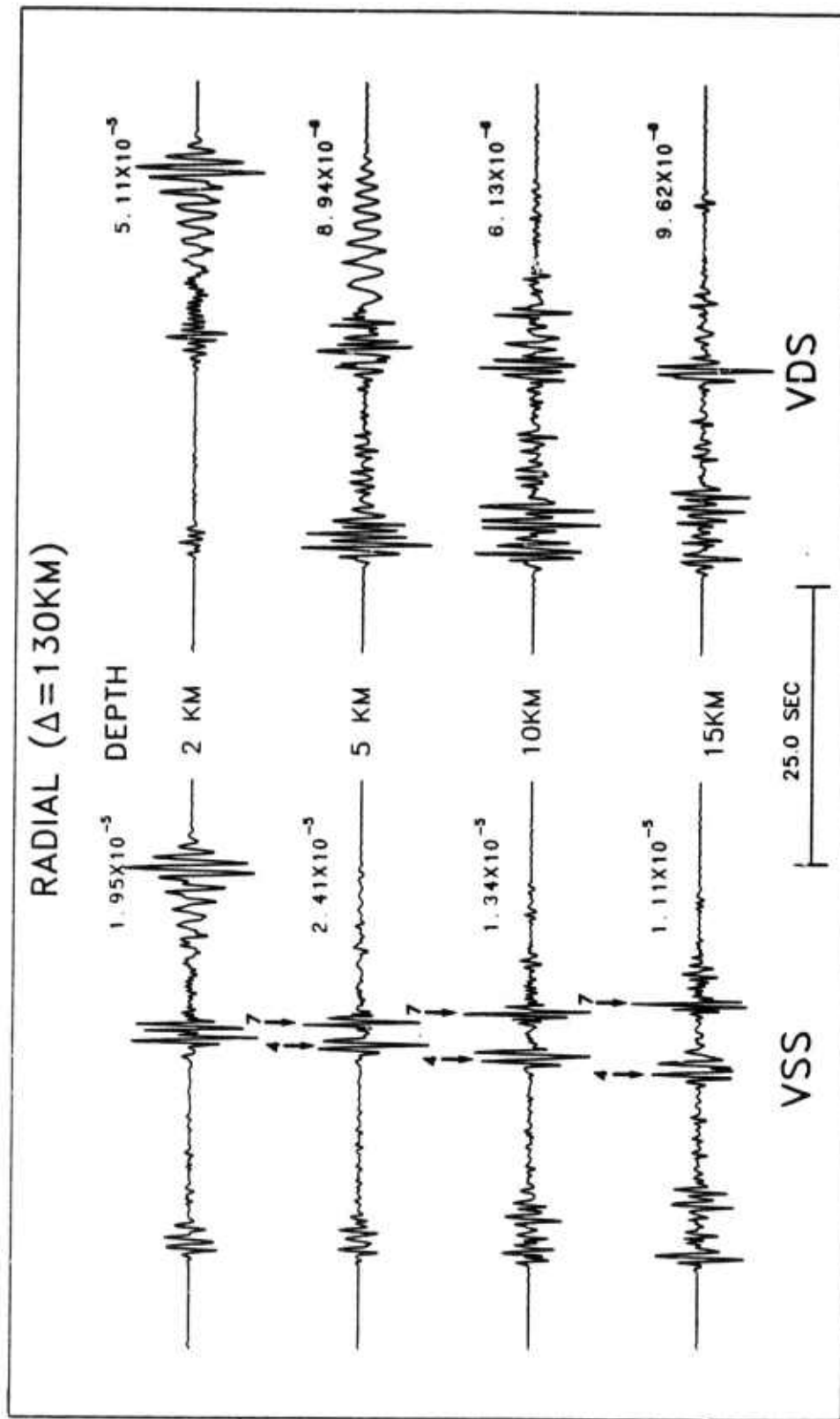
Figure 4.3 Synthetics created using Model A showing waveform variation with depth of radial component for vertical strike-slip (VSS) and vertical dip-slip (VDS) source mechanisms. Note the S wave character and the presence of surface waves at 2 km depth.
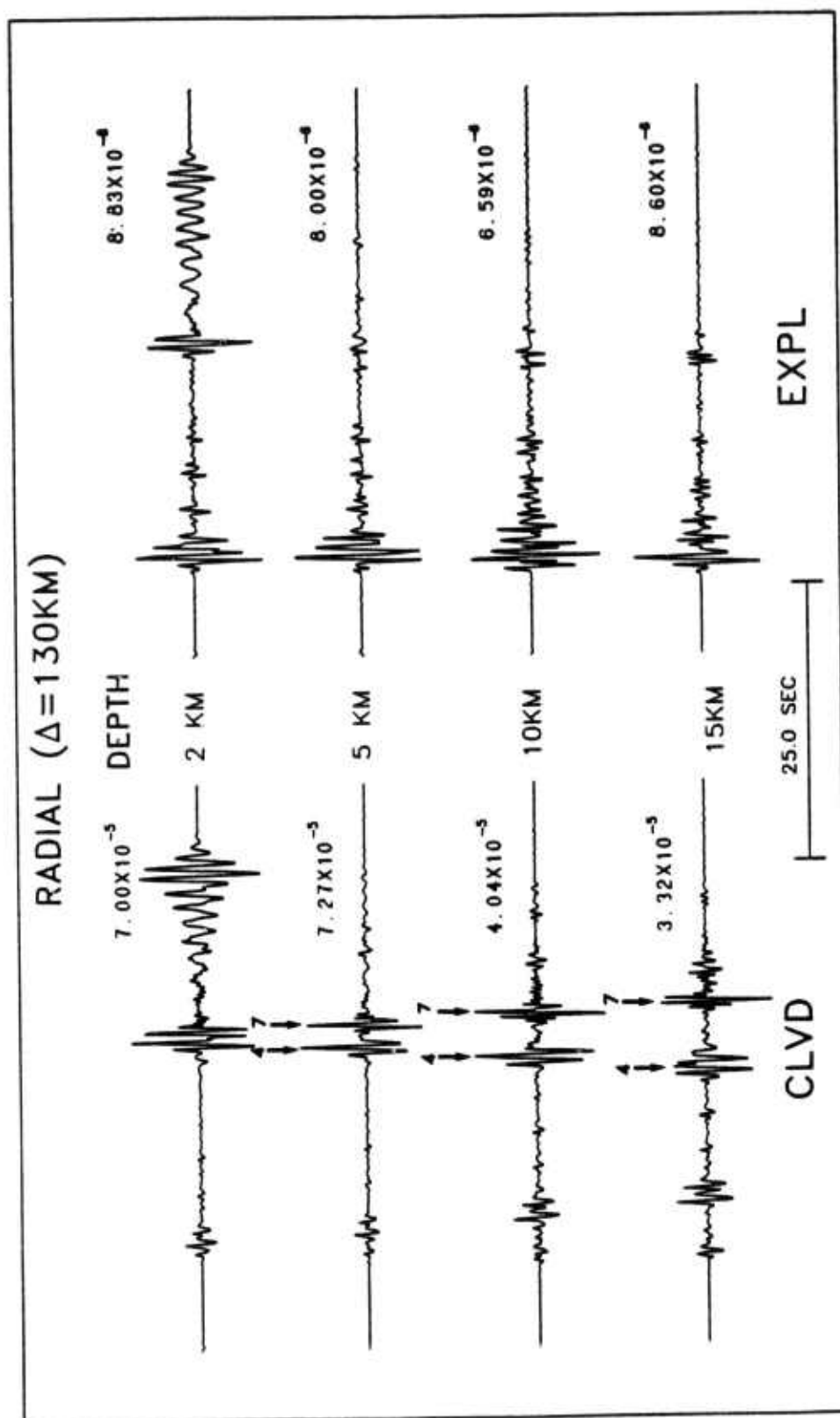
Figure 4.4 Synthetics created using Model A showing waveform variation with depth of radial component for compensated linear vector dipole (CLVD) and explosion (EXPL) source mechanisms. Note the S wave character and the presence of surface waves at 2 km depth.
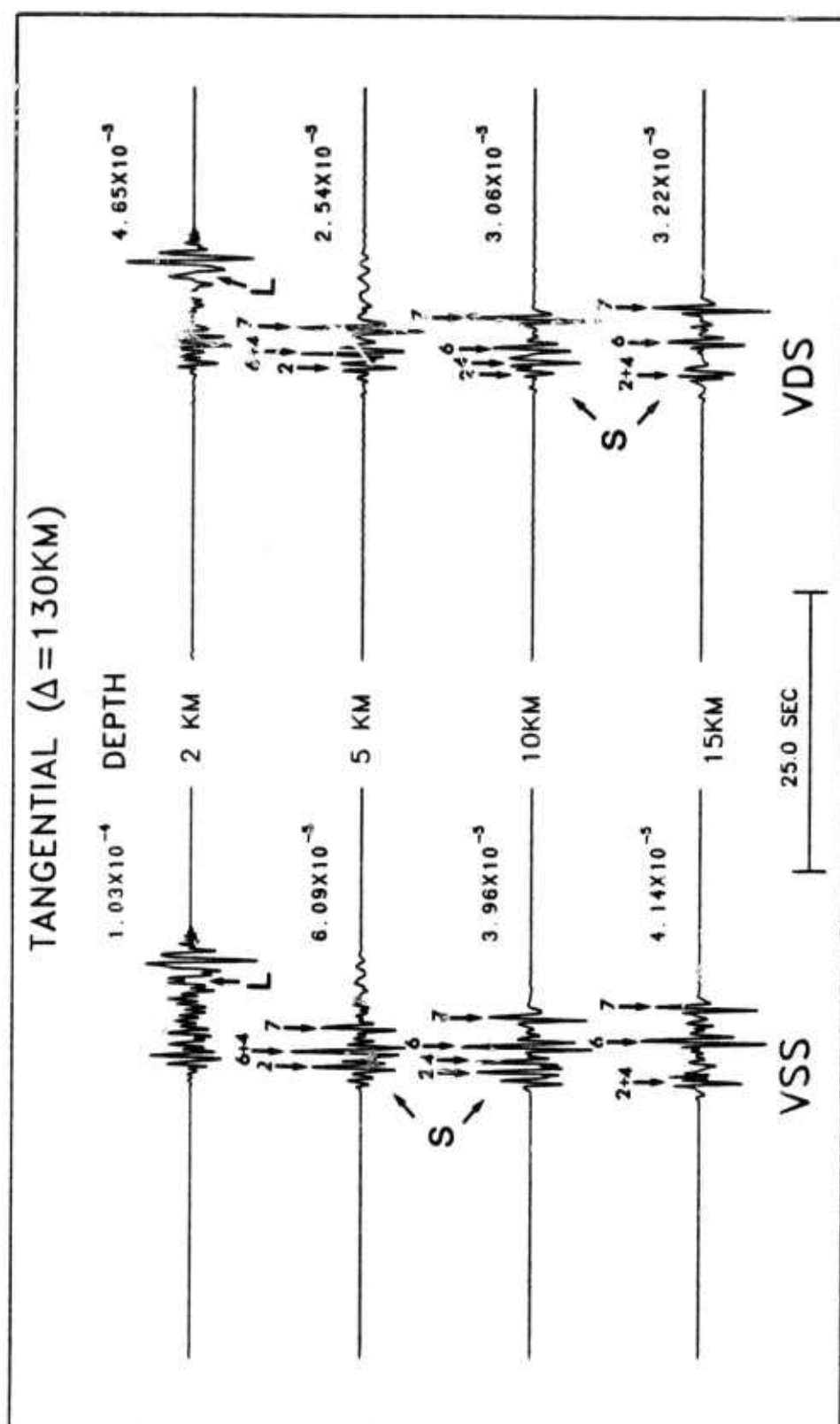
Figure 4.5 Synthetics created using Model A showing waveform variation with depth of tangential component for vertical strike-slip (VSS) and vertical dip-slip (VDS) source mechanisms. Note the S wave character and the presence of surface waves at 2 km depth. Major phases are indicated by P, S and L (Love).
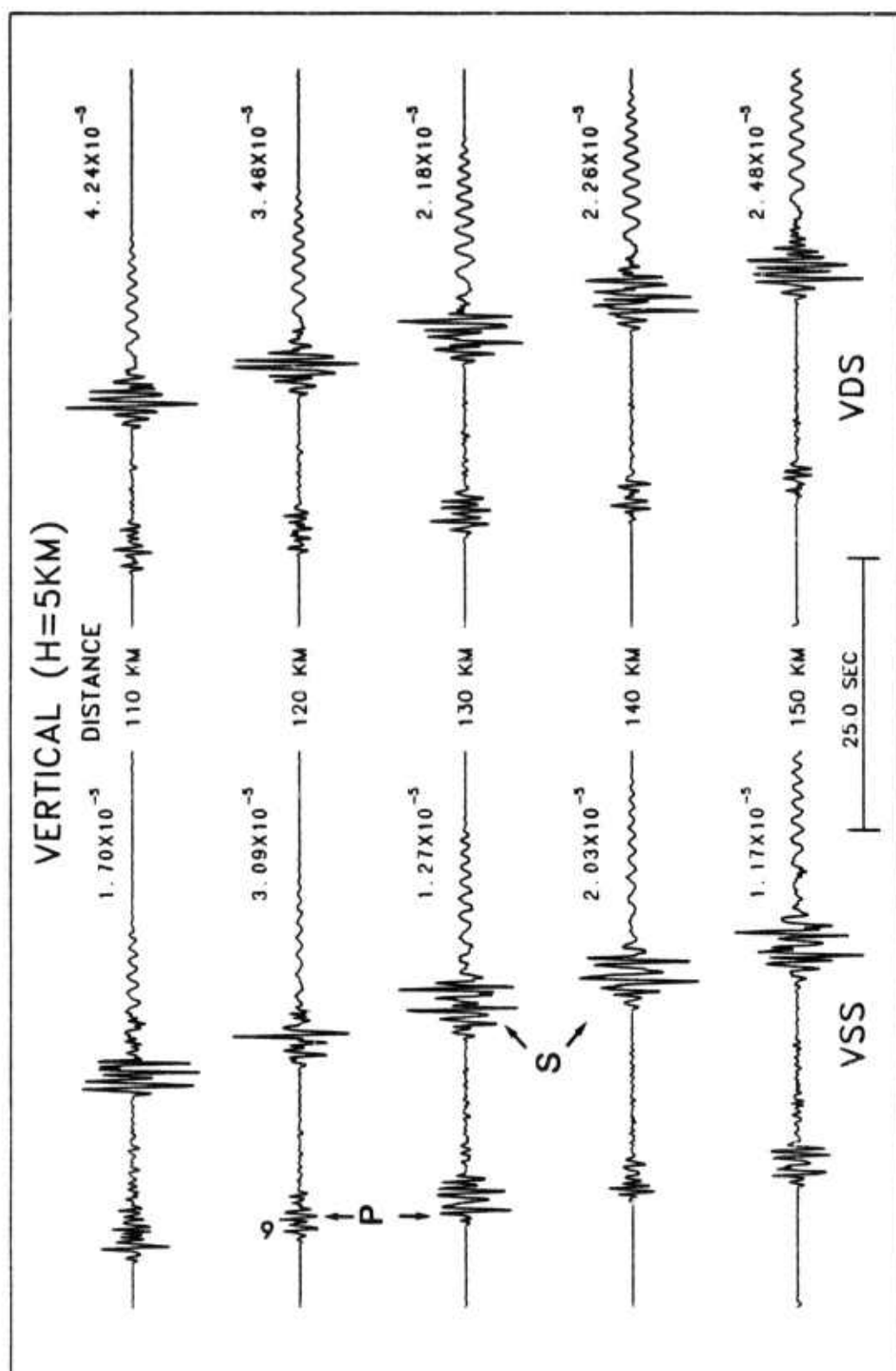
Figure 5.1 Synthetics created using Model A showing waveform variation with distance of vertical component for vertical strike-slip (VSS) and vertical dip-slip (VDS) source mechanisms. P and S wave phases are indicated.
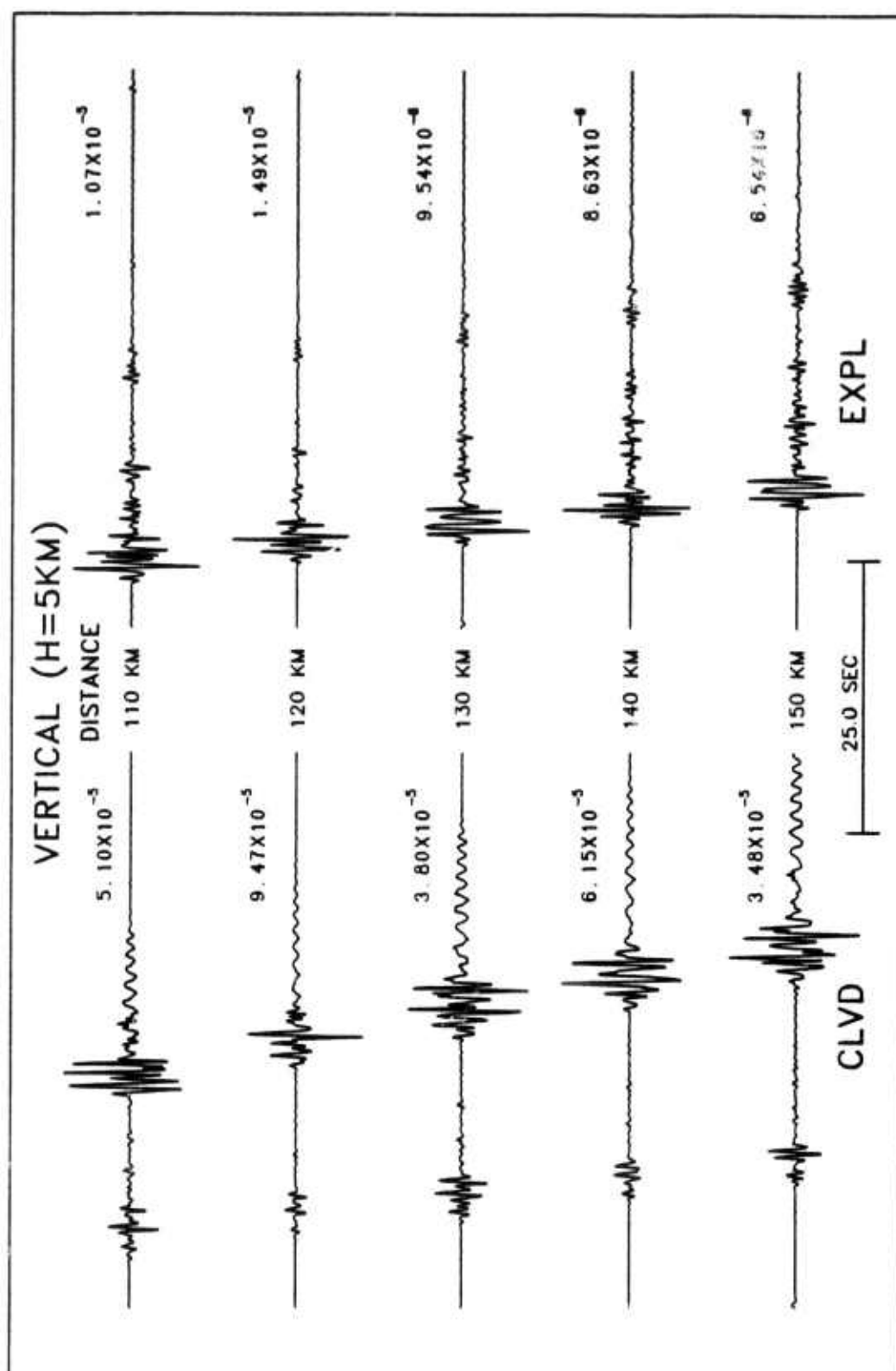
Figure 5.2 Synthetics created using Model A showing waveform variation with distance of vertical component for compensated linear vector dipole (CLVD) and explosion (EXPL) source mechanisms.
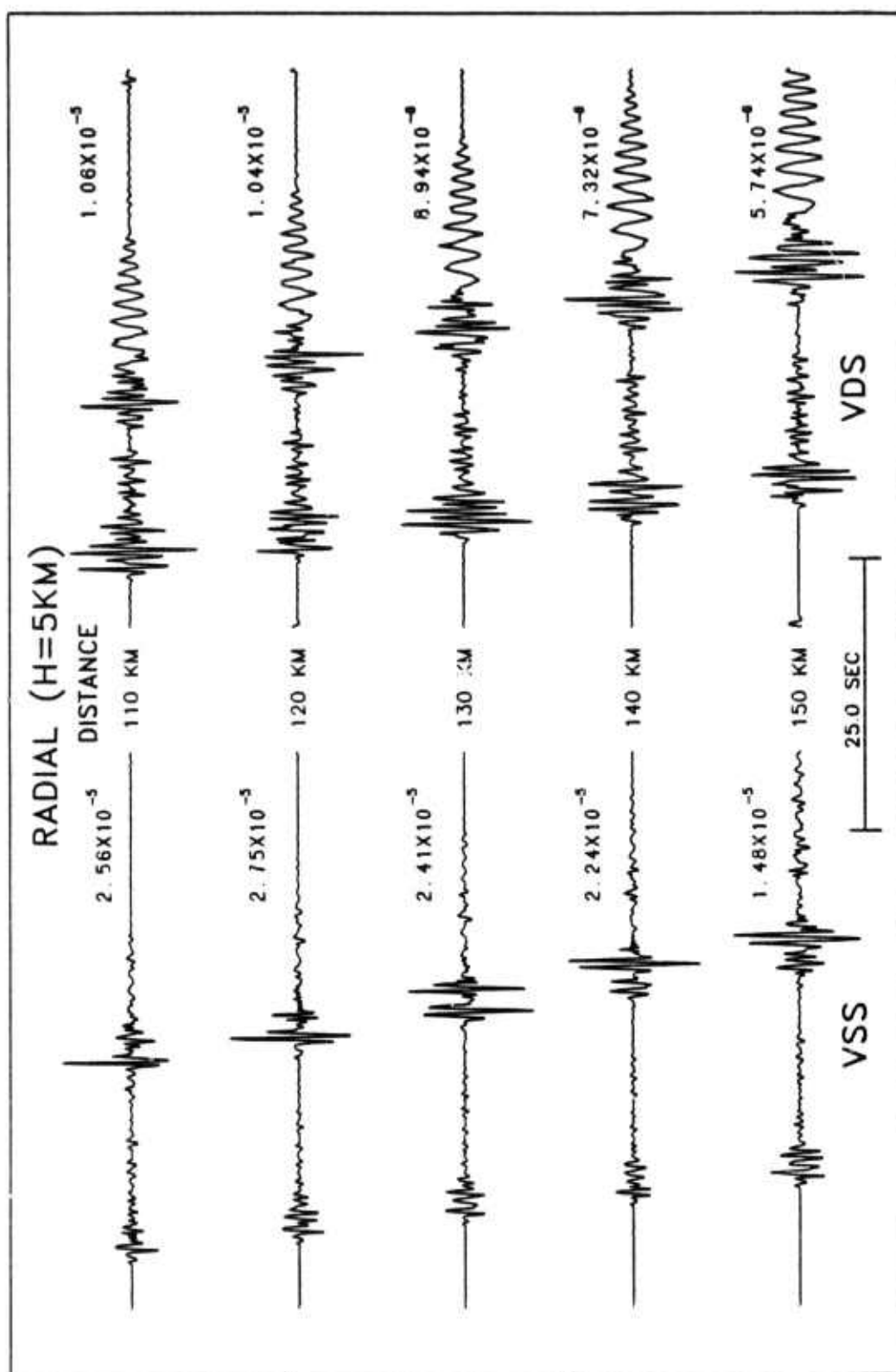
Figure 5.3 Synthetics created using Model A showing waveform variation with distance of radial component for vertical strike-slip (VSS) and vertical dip-slip (VDS) source mechanisms.

Figure 5.4 Synthetics created using Model A showing waveform variation with distance of radial component for compensated linear vector dipole (CLVD) and explosion (EXPL) source mechanisms.

Figure 5.5 Synthetics created using Model A showing waveform variation with distance of tangential component for vertical strike-slip (VSS) and vertical dip-slip (VDS) source mechanisms.
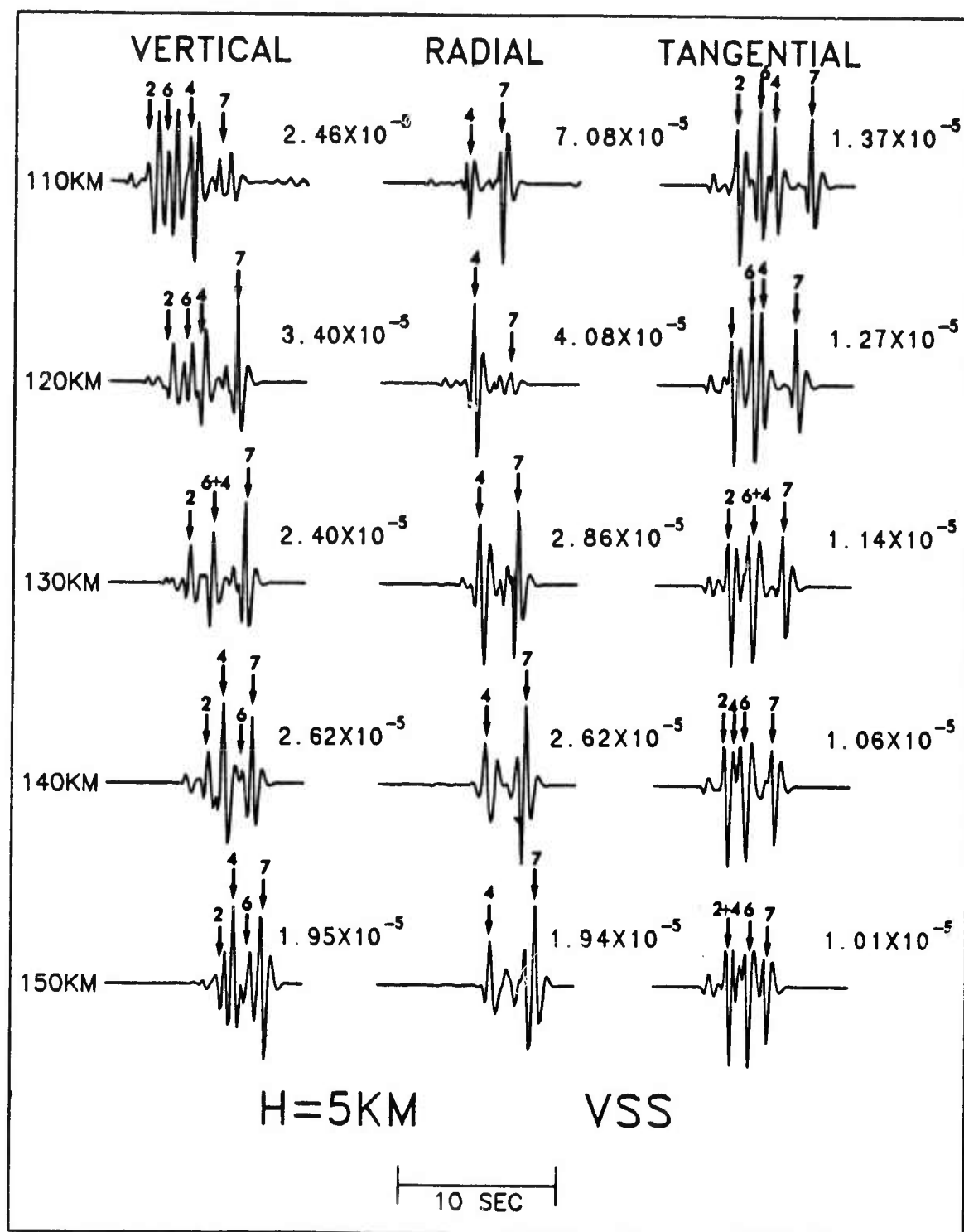
Figure 6 Generalized ray synthetics illustrating the complex interaction of rays #4 and #6 as a function of distance. Note the similarities to the wavenumber synthetics and the real events even though only seven ray paths, as shown in Figure 3, are specified.
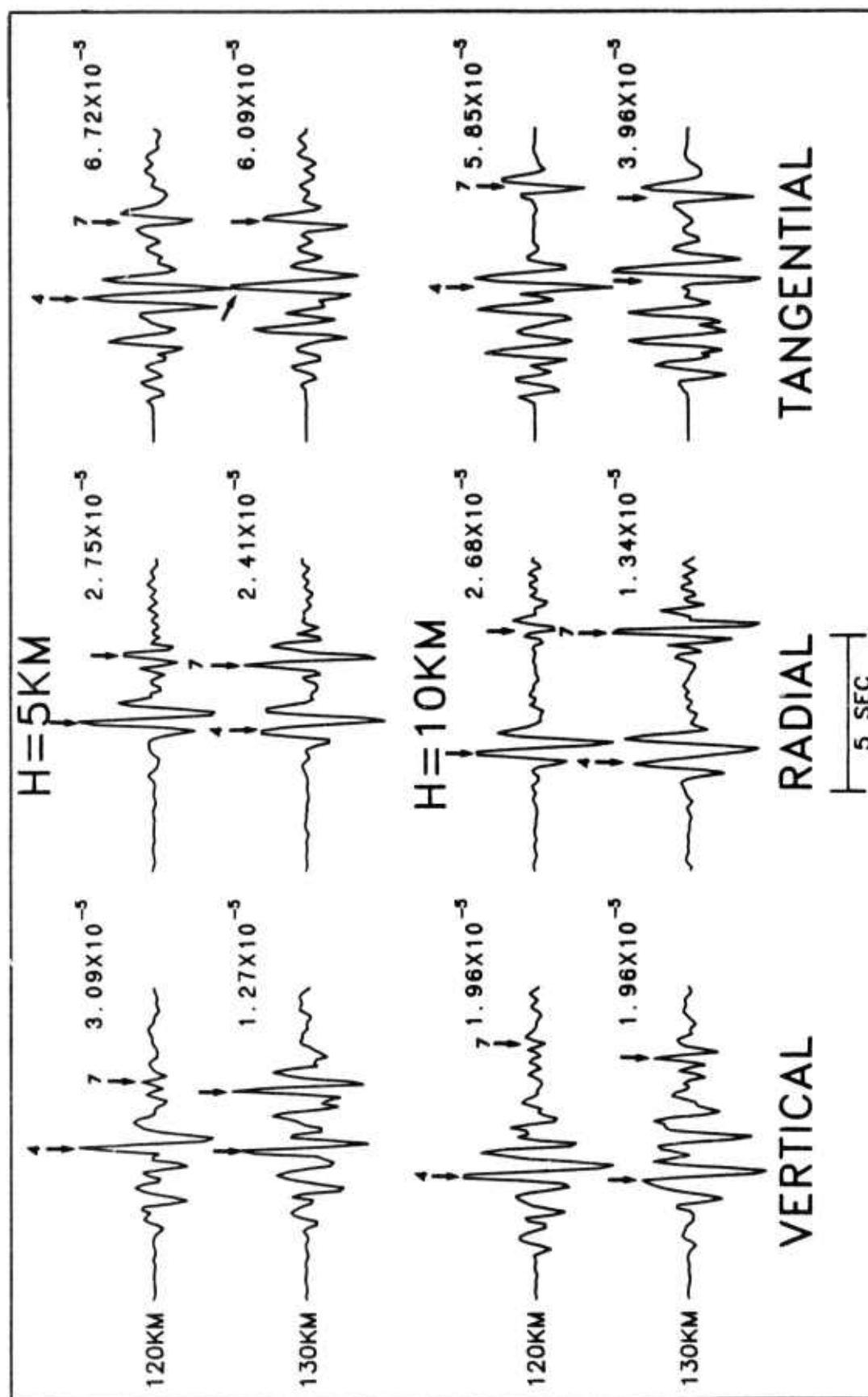
Figure 7 S-wave section of vertical strike-slip synthetics illustrating the relative amplitude increase of ray #7 with respect to ray #4 as ray #7 becomes a post critical reflection.
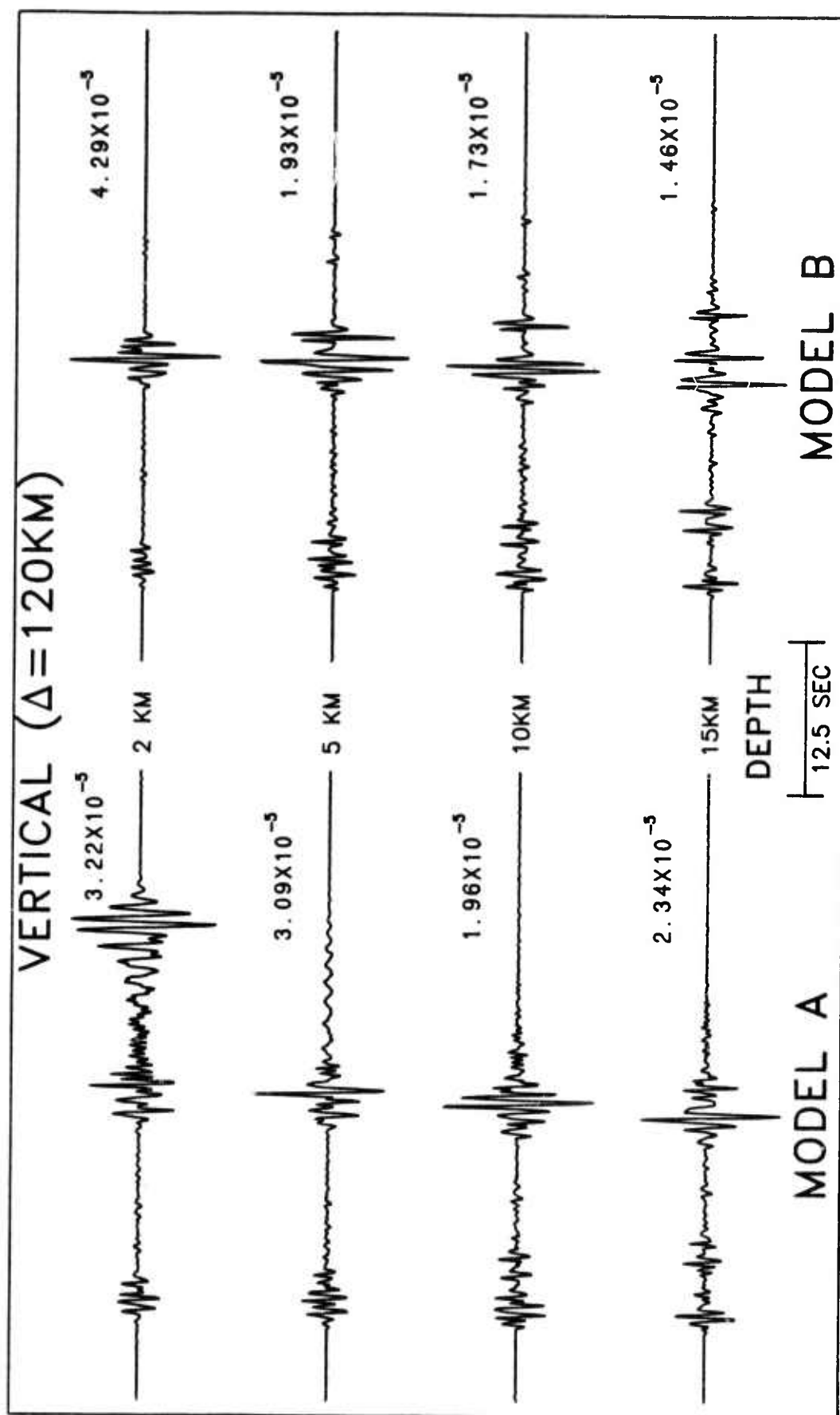
Figure 8.1 Comparison of Model A and Model B vertical-component synthetics (VSS mechanism).

114
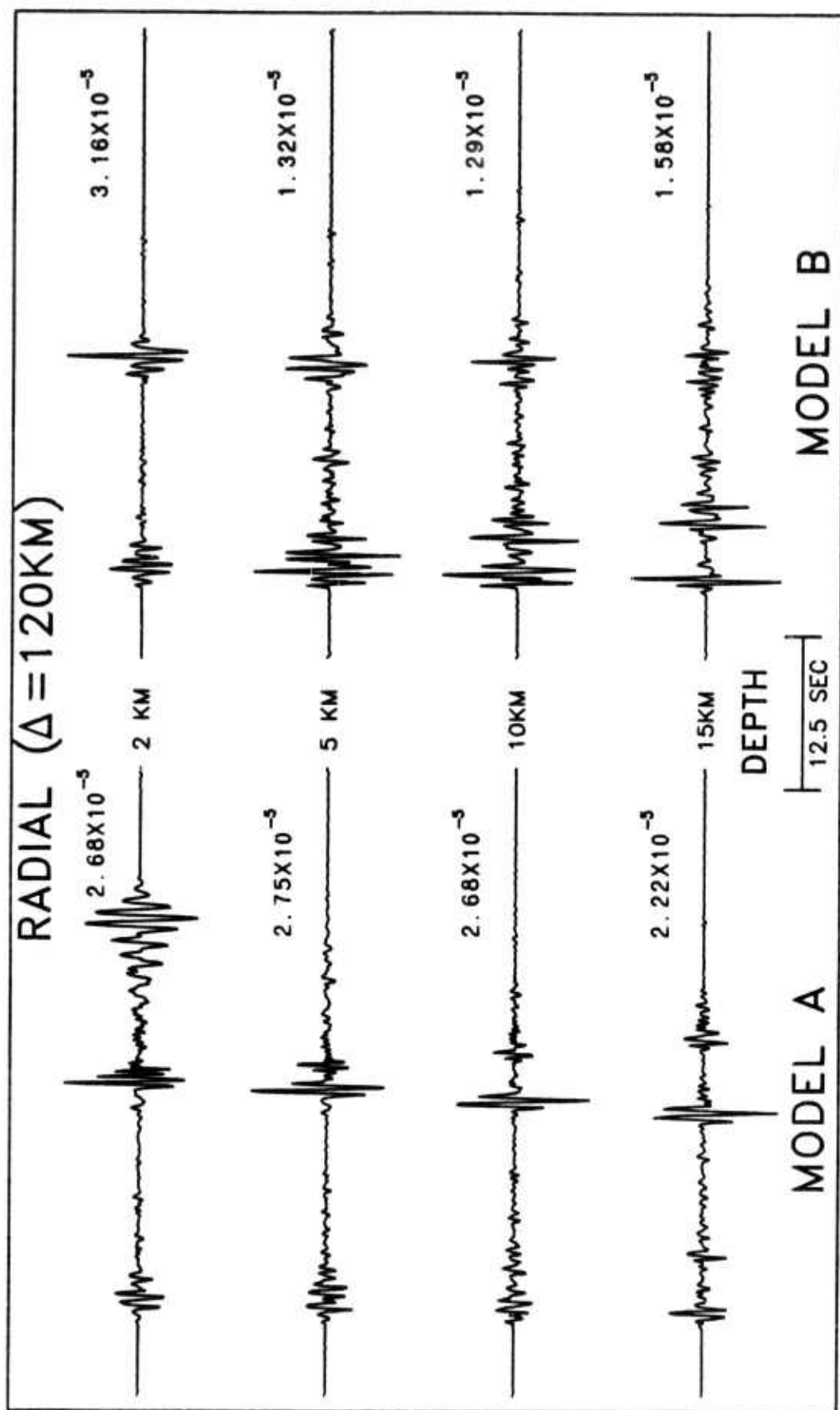
Figure 8.2 Comparison of Model A and Model B radial-component synthetics (VSS mechanism).
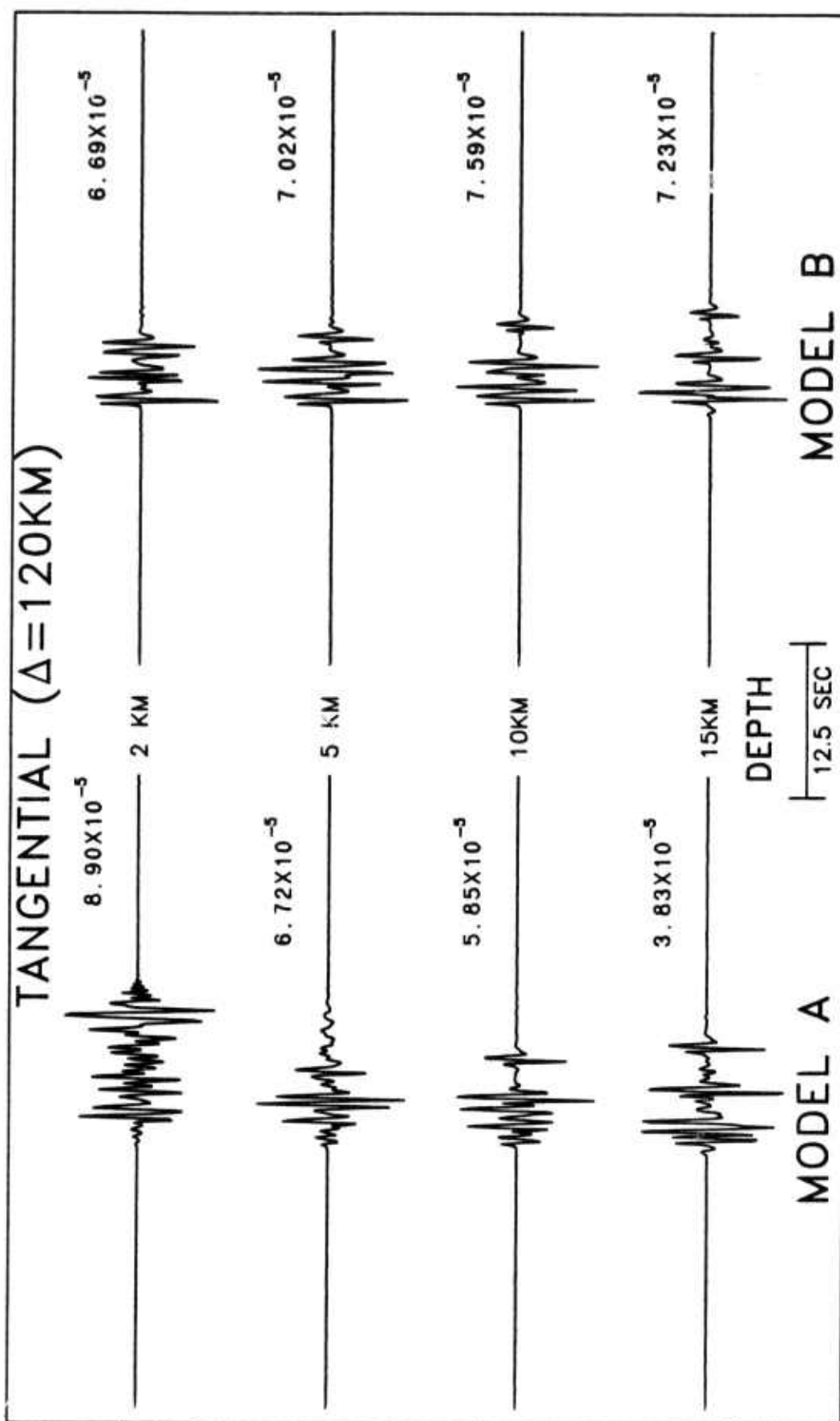
Figure 8.3 Comparison of Model A and Model B tangential-component synthetics (VSS mechanism).
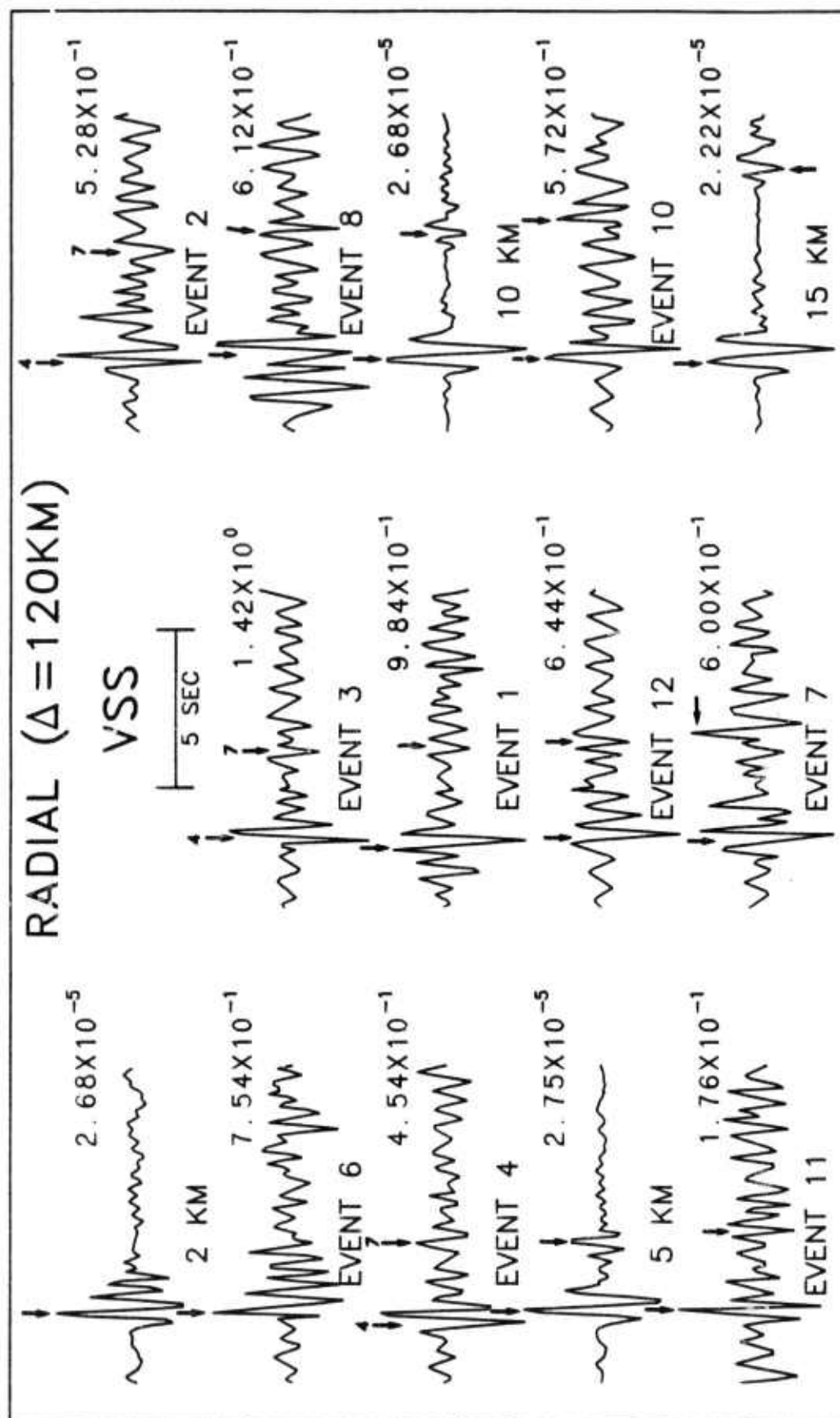
Figure 9 Radial component of both synthetic and real events as a function of increasing source depth. Depth is determined by the separation of S and sS arrivals (rays #4 and #7).

SECTION 3

RADIATION CHARACTERISTICS OF ELASTODYNAMIC LINE SOURCES BURIED IN LAYERED MEDIA WITH PERIODIC INTERFACES. I - SH WAVE ANALYSIS

Vijay K. Varadan[+], Akhlesh Lakhtakia[+], Vasundara V. Varadan[+] & Charles A. Langston[*]

[+]*Laboratory for Electromagnetic and Acoustic Research*
Department of Engineering Science and Mechanics
[*]*Department of Geosciences*
The Pennsylvania State University
UNIVERSITY PARK, PA 16802

ABSTRACT

Using the T-matrix, or the extended boundary condition, method the solution for a class of problems involving an SH line source in an elastic waveguide is determined. The boundaries of the waveguide may be periodically corrugated and the waveguide may be embedded between elastic media. Numerical results are given for a seismically interesting case of wave propagation in a one-layer crustal model over a mantle half-space with a corrugated free surface representing the Basin and Range topography in the Western United States. Analysis of the scattered fields at the surface, and of the fields radiated into the halfspace, shows complicated field behavior, even with sinusoidal free surface corrugation. These results are directly applicable to regional wave propagation and scattering.

INTRODUCTION

Scattering is known to be a general characteristic of seismic wave propagation and undoubtedly, it plays a large part in the observational interpretations of Q and the mechanism of anelastic attenuation. Scattering in short-period regional phases, such as L_g and P_g, is very important in interpretations of the seismic source spectrum and radiation pattern discrimination between small explosions and earthquakes. For example, transverse L_g motion is nearly always observed from explosion sources, yet a purely isotropic source should excite far-field motion only in the vertical plane. Either the source is not isotropic, which would imply some common form of tectonic release, or, more likely, transverse motion is due to the scattering by the geometric irregularities of the crustal waveguide. Source spectrum estimates from these phases rely on the assumption of a white spectrum for propagation effects to yield interpretations of seismic moment and corner frequency, but as yet, this assumption has not been tested for validity; scattering must play a role in shaping the seismic spectrum of these phases.

At present there are no practical numerical techniques to compute the far-field displacement in even simple models of structures containing irregular boundaries. Although techniques which incorporate plane-layered elastic structure models have been very useful in routine computations and data interpretations, these methods are inacapable of rigorously addressing even the simplest of laterally heterogeneous structures. Methods are needed to extend these computations of plane layered structure to include, as a first perturbation, the effect of changing boundary geometry. The method presented in this paper is developed for geometries of two dimensions and SH line sources. It represents a necessary first step in dealing with waveguide scattering due to heterogeneous boundaries and will be extended to geophysically interesting point source problems in the near future. Nevertheless, even this relatively simple problem yields insight into scattering mechanisms present in the crustal waveguide.

We will utilize the extended boundary condition method, also known as the T-matrix method [Waterman, 1975], to investigate the radiation characteristics of a source embedded in a material plate bounded on the top by a traction-free surface, and on the bottom by a homogeneous half-space. Both surfaces can be taken to be periodically rough in the theory to be developed here, but for the sake of simplicity, we shall take the lower one to be planar. Discrete mode representation of the fields involved will be used to solve the radiation

problem. Because of the relative simplicity of SH wave propagation, the features of this technique are more clearly displayed without the complicating effects of coupling between P and SV wave fields. Hence, in this paper we are interested only in the radiation characteristics of a SH-wave line source, while P-SV line sources are treated in a companion paper [Varadan et al., 1986].

Several interesting problems can immediately be examined from the theoretical treatment presented. As an example, both interfaces can be made bimaterial, thereby allowing one to consider the radiation characteristics of a line source within a leaky parallel-plate waveguide. Another problem of interest would be to have both interfaces impermeable, which could be used to study the radiation characteristics of a line source in a non-leaky waveguide of varying cross-section. Yet another possibility would to be to replace the line source by any other source, provided a plane wave spectral decomposition of the field radiated by it is possible [Lakhtakia et al., 1985a]. Thus, it can be concluded that the theory presented is versatile enough to be of use in solving problems in several areas of research.

THEORETICAL DEVELOPMENT

Consider a SH-wave line source which is embedded at a point r_p in between two non-intersecting surfaces S_a and S_b whose mean planes are parallel to the x axis. While S_a is specified by the function $y = h(x) > y_p$ with $h(x)$ possessing a finite differential coefficient and having a period L in its argument, i.e., $h(x \pm L) = h(x)$; for the sake of simplicity we consider the surface S_b to be the plane $y = -d < y_p$. The surface S_a is assumed to be traction-free; the elastic medium in between the surfaces has a shear modulus of μ and density ρ, while the homogeneous half-space below S_b is characterised by μ' and ρ'. In what follows the ratio $\mu'/\mu = q$, $k = \omega[\rho/\mu]^{1/2}$ and $K = \omega[\rho'/\mu']^{1/2}$; an $\exp[-i\omega t]$ harmonic time dependence has been assumed; i and j represent the x- and the y-directed unit vectors, respectively; and the scalar w represents z-directed displacement fields.

On applying Huyghens' principle to the region enclosed between S_a and S_b in the manner of Waterman [1975] and Bostrom [1980], we find that the total field

$$w(r) = w^i(r) + (1/4i)\int_{S_b} ds_0\, n_b(r_0) \cdot \left[H_0(k|r - r_0|)\,\nabla_0 w_b(r_0) - w_b(r_0)\,\nabla_0 H_0(k|r - r_0|)\right]$$

$$+ (1/4i)\int_{S_a} ds_0\, n_a(r_0) \cdot \left[w_a(r_0)\,\nabla_0 H_0(k|r - r_0|)\right], \text{ if } h(x) > y > -d \qquad (1a)$$

for all r in between S_a and S_b, while

$$0 = w^i(r) + (1/4i) \int_{S_b} ds_0 \, n_b(r_0) \cdot \left[H_0(k|r - r_0|) \nabla_0 w_b(r_0) - w_b(r_0) \nabla_0 H_0(k|r - r_0|) \right]$$

$$+ (1/4i) \int_{S_a} ds_0 \, n_a(r_0) \cdot \left[w_a(r_0) \nabla_0 H_0(k|r - r_0|) \right], \quad y > h(x) \text{ or } y < -d \qquad (1b)$$

if r is either above S_a or below S_b. The unit vectors n_a and n_b are normal to S_a and S_b, respectively, and must contain +y-directed components; w_a is the field on the -y side of the surface S_a, while w_b is the field on the +y side of the surface S_b; and $H_0(k|r - r_0|) = H_0^{(1)}(k|r - r_0|)$, the cylindrical Hankel function of zeroth order and first kind, is the free space Green's function for two dimensional problems. Parenthetically, we mention here that the last equation is called the *extinction theorem* which forms the cornerstone of the extended boundary condition method.

Because of the periodicity inherent in the problem, the zero h-order Hankel function possesses the plane wave spectral (Bloch-Fourier) representation [Waterman, 1975],

$$H_0(k|r - r_0|) = (1/\pi) \int_{-\pi/L}^{\pi/L} d\alpha \, D_\alpha \sum_{|n| \le \infty} \left\{ \exp[ik_n^{\pm}(\alpha) \cdot (r - r_0)] \right\}/\beta_n(\alpha), \qquad (2)$$

where

$$k_n^{\pm}(\alpha) = (\alpha + 2\pi n/L)x \pm \beta_n(\alpha)y; \quad \beta_n(\alpha) = +\sqrt{\{k^2 - (\alpha + 2\pi n/L)^2\}}, \qquad (3a,b)$$

$$1/D_\alpha = 1 + \delta(\alpha - \pi/L) + \delta(\alpha + \pi/L), \qquad (3c)$$

with the superscript "+" (resp. "-") holding for $j \cdot r > j \cdot r_0$ (resp. $j \cdot r < j \cdot r_0$); $\delta(\alpha - \alpha')$ is the Dirac delta. The source field w^i is the field radiated by the line source located at r_p, as if all space were filled by the medium occupying the region between the two surfaces, and is given by [Bowman *et al.*, 1969]

$$w^i(r) = (1/4i) H_0(k|r - r_p|). \qquad (4)$$

This field can also be decomposed into a continuum of planewaves as

$$w^i(r) = (1/4i\pi) \int_{-\pi/L}^{\pi/L} d\alpha \, D_\alpha \sum_{|n| \le \infty} \left\{ \exp[ik_n^{\pm}(\alpha) \cdot (r - r_p)] \right\}/\beta_n(\alpha), \qquad (5)$$

Now, we successively choose r, first above S_a and then below S_b in (1b), and substitute the aforementioned representations (2) and (5). Further simplification of the two resulting equations is afforded by enforcing the orthogonality of planewaves over two plane surfaces, to get

$$0 = \exp[-ik_n^{\pm}(\alpha) \cdot r_p] + \int_{S_b} ds_0 \, n_b(r_0) \cdot \left\{ \nabla_0 w_b(r_0) \right\} \exp[-ik_n^{\pm}(\alpha) \cdot r_0]$$

$$- \int_{S_b} ds_0 \, w_b(r_0) \, n_b(r_0) \cdot \nabla_0 \left\{ \exp[-ik_n^{\pm}(\alpha) \cdot r_0] \right\}$$

$$+ \int_{S_a} ds_0 \, w_a(r_0) \, n_a(r_0) \cdot \nabla_0 \left\{ \exp[-ik_n^{\pm}(\alpha) \cdot r_0] \right\}, \forall \alpha : |\alpha| \le \pi/L, \forall n. \qquad (6a,b)$$

In deriving (6b), this orthogonality was enforced over the *plane* surface S_b, but to get (6a) that was done over

the plane surface S_{a+} which is the plane $y = \max[h(x)]$. It should be noted that the second enforcement of orthogonality is not over the actual surface S_a but over a surface which is just above it: this procedure is in complete accord with the limiting principle of the extended boundary condition method [Waterman, 1971; Waterman; 1975; Barber and Yeh, 1975] and need not be commented upon here in any detail.

Next, the boundary conditions,

$$w_b(r) = w_2(r); \quad j \cdot \nabla w_b(r) = q \, j \cdot \nabla w_2(r) \, ; \, r \in S_b \tag{7}$$

where w_2 is the field radiated by the line source in the medium below S_b, are substituted in (6a,b), along with the needed plane wave spectral representation for w_2:

$$w_2(r) = (1/4i\pi) \, _{-\pi/L}\!\int^{\pi/L} d\alpha \sum_{|n| \leq \infty} \{A_n(\alpha)\exp[iK_n^-(\alpha) \cdot r]\}/\gamma_n(\alpha), \tag{8a}$$

where

$$K_n^{\pm}(\alpha) = (\alpha + 2\pi n/L) \, i \pm \gamma_n(\alpha) \, j; \quad \gamma_n(\alpha) = +\sqrt{\{K^2 - (\alpha + 2\pi n/L)^2\}}, \tag{8b}$$

The Bloch-Fourier expansion used by Waterman [1975] for w_a is not used here; instead a Fourier expansion [Masel et al., 1975] is also susbstituted in (6a,b). This expansion for w_a is given by

$$w_a(r) = (1/4i\pi) \, _{-\pi/L}\!\int^{\pi/L} d\alpha \sum_{|n| \leq \infty} \{B_n(\alpha)\exp[i(\alpha + 2\pi n/L)x]\}/\beta_n(\alpha). \tag{9}$$

The use of $\exp[i(\alpha + 2\pi n/L)x]$ in (9) instead of $\exp[ik_n^{\pm}(\alpha) \cdot r]$ facilitates calculations involving periodic surfaces, as has been noted by Goodman [1977] by bypassing the Rayleigh hypothesis [Millar, 1973; Lakhtakia et al., 1985b]: surfaces S_a of maximum slopes upto about 1.5 can be treated with ease.

As a result of these substitutions, (6a,b) can be finally simplified into the matrix equations

$$0 = 2\exp[-ik_n^{\pm}(\alpha) \cdot r_p] + A_n(\alpha)[-q \pm \beta_n(\alpha)/\gamma_n(\alpha)] \exp[id(\pm\beta_n(\alpha) + \gamma_n(\alpha)]$$

$$- \sum_{|m| \leq \infty} [\pm B_m(\alpha)/\beta_n(\alpha)\beta_m(\alpha)] \cdot [\beta_n^2(\alpha) + (\alpha + 2\pi n/L)(2\pi/L)(n-m)] \, \aleph_{nm}^{\pm}(\alpha),$$

$$\forall n : |n| \leq \infty, \forall \alpha : |\alpha| \leq \pi/L \tag{10a,b}$$

where the integrals

$$\aleph_{nm}^{\pm}(\alpha) = (1/L) \, _{-L/2}\!\int^{L/2} dx \, \exp[-i(n-m)2\pi x/L] \, \exp[-i\{\pm\beta_n(\alpha)h(x)\}]. \tag{11}$$

In particular, if the surface S_a is the sinusoid

$$h(x) = a + b \sin(2\pi x/L), \tag{12a}$$

then

$$\aleph_{nm}^{\pm}(\alpha) = \exp[-i\{\pm a\beta_n(\alpha)\}] \, J_{n-m}[-\{\pm b\beta_n(\alpha)\}], \tag{12b}$$

with $J_n[\cdot]$ being the cylindrical Bessel function of order n. The twin sets of matrix equations (10a,b) can be solved very easily, and the coefficients $A_m(\alpha)$ and $B_m(\alpha)$ computed for each α.

DISCUSSION AND NUMERICAL RESULTS

In presenting the data computed using the present method, however, we shall confine ourselves to the surface S_a being given by (12a) and S_b being the plane $y = -d$. Throughout this section now we shall keep $a = d = L$, $\rho = 2700$ kg m^{-3} and $\mu = 3.3075 \times 10^{10}$ N m^{-2}; the line source is placed at $r_p = (0,0)$. Of necessity, the sets of equations (10a,b) have to be terminated at some $|m|, |n| = N$, it being made sure that convergence is achieved at some value of N for each α. This is done by ensuring that the unitarity parameter [Lakhtakia et al., 1985b] for each α

$$\sum_{|m| < N} \left| A_m(\alpha) / 4\pi \, \gamma_m(\alpha) \right|^2 Re\{\gamma_m(\alpha)\} \tag{13}$$

converges to within a tolerance limit of 0.1% as N increases. Simultaneously, it is also ensured that $A_m(\alpha)$ and $B_m(\alpha)$ converge satisfactorily as well. If, in addition, a sufficiently large number (91, here) of α's are chosen in the range $|\alpha| \leq \pi/L$, it is reasonable to expect that a satisfactorily converged solution for the total problem has been obtained. This is because the various α's in this domain do not interact with each other owing to the periodicity of the problem. It may be mentioned here that values of N no larger than 13 turned out to be adequate for the calculations presented in this section.

The calculation of the far-zone radiated field in the region below S_b is quite straightforward. If, for a given m and α, $\gamma_m(\alpha)$ be real positive, then at an angle $\theta = \tan^{-1}\{\alpha/\gamma_m(\alpha)\}$ with respect to the y-axis, the radiated field

$$w_2(r,\theta) \rightarrow \left\{ A_m(\alpha)/4\pi i \gamma_m(\alpha) \right\} \exp[iK_m^-(\alpha) \cdot r] \text{ as } Kr \rightarrow \infty. \tag{14}$$

Shown in Figs. 1 and 2 are these radiation amplitudes, $\left| A_m(\alpha)/4\pi i \gamma_m(\alpha) \right|$ as functions of the angle $\theta = \sin^{-1}(\alpha + 2\pi m/L)$, $|\alpha + 2\pi m/L| \leq K$, $|m| \leq \infty$, for roughness $b/L = 0.10$ at the normalised frequencies kL = 5.0 and 10.0. The medium below S_b has a density $\rho' = 3200$ kg m^{-3} and a shear modulus $\mu' = 6.48 \times 10^{10}$ N m^{-2}. The chosen values for the densities and the shear moduli correspond to shear wave velocities of 3500 and 4500 m s^{-1}, appropriate for a one-layer continental crust model. Normalized frequencies used correspond to shear waves of periods 10 and 5 s, respectively. The corrugation period, L, is equal to the mean crustal thickness, and

the choices for the corrugation amplitude are based on the average wavelength of the topography encountered in the Basin and Range province of the western United States. Thus, $b/L = 0.1$ corresponds to topography with 3 km amplitude and 30 km wavelength. The examples show wave propagation for waves with wavelengths shorter than the topography and appropriate for intermediate period seismic data.

Two points need to be noted here. Firstly, the use of $\exp[i(\alpha + 2\pi n/L)x]$ in (9) instead of $\exp[ik_n^\pm(\alpha) \cdot r]$ has allowed us to compute for roughnesses $b/L > 0.072$, the classic Rayleigh limit [Millar, 1973; Lakhtakia et al., 1985c] for surface scattering problems. This has been established by several authors [e.g., Masel et al., 1975; Goodman, 1977; Cain et al., 1986] to whom the interested reader is referred. Secondly, the computed amplitudes are somewhat asymmetrical about $\theta = 0^{\scriptscriptstyle\text{II}}$. This is because the upper surface is asymmetrical about the location of the line source, due to the former's specification as $y = a + b \sin(2\pi x/L)$.

An important characteristic of Figs. 1 and 2 is the presence of sharp extrema in the radiation pattern plots. Not counting the traction-free surface S_a, for the moment, these extrema can occur for at least two reasons. Firstly, the presence of the Brewster anomaly [Weeks, 1964], whenever

$$\alpha + 2\pi n/L = K\left\{[q^2 - (k/K)^2]/[q^2 - 1]\right\}^{-1/2}, \ |n| = 0,1,2,3 \ldots, \tag{15}$$

for a given α and n, is such that $\beta_n(\alpha)$ is real positive, maximizes transmission across a planar bimaterial interface. Also, if $\alpha + 2\pi n/L = \pm K$, then a reflectionless anomaly [Cain et al., 1986] appears for a planar bimaterial interface.

In order to consider yet another reason for the extrema in these figures, let us consider, first, a planar S_a. When the two waves $\exp[ik_n^\pm(\alpha) \cdot (r - r_p)]$ launched by the line source first arrive at S_b, their phases differ by $2a\beta_n(\alpha)$. If $2a\beta_n(\alpha)$ is equal to an odd multiple of $\pm\pi$ they interefere destructively, but if $2a\beta_n(\alpha)$ is an even multiple of $\pm\pi$ then constructive intereference takes place. Consequently, minima and maxima may occur. For example, when $b/L = 0$ in Fig. 2, a minimum is recorded in the radiation pattern when $\theta = 25.5^{\scriptscriptstyle\text{II}}$, $\alpha/K = 0.4297745$ and $2a\beta_0(\alpha) = 3\pi$. When the upper surface becomes periodically rough, such simple arguments do not explain all the possible extrema [Lakhtakia et al., 1985a]. It may be surmised, however, that the mutual intereference of the $n \neq 0$ modes in (10a,b) makes the field in the region between S_a and S_b very complicated, giving rise to an extremely complex radiation pattern. Due to periodicity, nevertheless, a very clearcut extremum occurs whenever $\alpha + 2\pi n/L$ equals either $\pm k$ or $\pm K$. Such an extremum is called the Rayleigh-Wood anomaly

and has been discussed elsewhere [Waterman, 1975; Goodman, 1977; Lakhtakia *et al.*, 1985a] in greater detail.

In Fig. 3 is shown the radiation pattern when (A) q = 1.9591837 and K = (7/9)k, and (B) q = 1 and k = K. Both plots are at a normalised frequency kL = 15 when b/L = 0.15. To be noted is the significant complexity of the plot in Fig. 3(A) when compared with that in Fig. 3(B). In the latter case the media on either side of the surface S_b are identical, which means that the extrema due to the back-and-forth bouncing of the waves in between S_a and S_b are no longer there.

An important quantity measured for seismological applications is the field w_a induced on S_a. Shown in Fig. 4 are the computed values of the magnitude of w_a at locations x/L = ±1, ±10 and ±50 as the normalized frequency increases from kL = 10 to kL = 30 in steps of 0.2; the other parameters are b/L = 0.10, q = 1.9591837 and K = (7/9)k. Equation (9) was used to calculate w_a with a 31 - point Gauss-Legendre quadrature implemented for the integral over α. The asymmetry in these computations, again, is due to the fact that S_a is asymmetric with respect to the line source. Although the plots are very complicated, generally speaking it appears that w_a decreases somewhat as kL increases. Furthermore, there is some indication of a trend for w_a to decrease as the location |x| on S_a is increased.

In conclusion, the examples shown in this paper have been oriented towards intermediate and short-period seismic wave propagation in contentinental crustal structures. Application to seismic observations and calculation of synthetic seismograms is deferred for later work. The important result is that this technique makes such studies feasible. The method is most efficient for long wavelength interactions, but is not practically restricted until very high normalized frequencies are attained. The limitation on interface corrugation is topography, and not the Rayleigh ansatz of representing each surface field by Bloch-Fourier expansions. Although a SH line source has been considered, the formalism is amenable to P-SV line sources [Varadan *et al.*, 1986] and point sources as well.

ACKNOWLEDGEMENTS

REFERENCES

Barber, P.W. and C. Yeh (1975). Scattering of electromagnetic waves by arbitrary shaped dielectric bodies, *Appl. Opt.*, 14, 2864.

Bostrom, A. (1980). Transmission and reflection of acoustic waves by an obstacle in a waveguide, *Wave Motion*, 2, 167.

Bowman, J.J., T.B.A. Senior and P.L.E. Uslenghi (1969). *Electromagnetic and Acoustic Scattering by Simple Shapes*, Amsterdam: North-Holland.

Cain, W.N., V.K. Varadan, V.V. Varadan and A. Lakhtakia (1986). Reflection and transmission characteristics of a slab with periodically varying surfaces, *IEEE Trans. Antennas Propagat.*, 34, 000 (in press).

Goodman, F.O. (1977). Scattering of atoms by a stationary sinusoidal hard wall: Rigorous treatment in $(n+1)$ dimensions and comparison with the Rayleigh method, *J. Chem. Phys.*, 66, 976.

Lakhtakia, A., V.K. Varadan and V.V. Varadan (1985a). The acoustic response of a periodically rough elastic plate (ice) in contact with water, *ASME J. Appl. Mech.*, 52, 144.

Lakhtakia, A., V.K. Varadan and V.V. Varadan (1985b). A T-matrix approach for EM scattering by a perfectly conducting periodic surface, *Proc. IEEE*, 73, 1238.

Lakhtakia, A., V.K. Varadan and V.V. Varadan (1985c). On the acoustic response of a deeply-corrugated periodic surface -- A hybrid T-matrix approach, *J. Acoust. Soc. Am.*, 78, 2100.

Masel, R.I., R.P. Merrill and W.H. Miller (1975). Quantum scattering from a sinusoidal hard wall: Atomic diffraction from solid surfaces, *Phys. Rev. B*, 12, 5545.

Millar, R.F. (1973). The Rayleigh hypothesis and a related least - squares solution to scattering problems for periodic surfaces and other scatterers, *Rad. Sci.*, 8, 785.

Varadan, V.K., A. Lakhtakia, V.V. Varadan and C. A. Langston (1986). Radiation characteristics of elastodynamic line sources buried in layered media with periodic interfaces. II - P and SV wave analysis, *Bull. Seismol. Soc. Am.* (submitted).

Waterman, P.C. (1971). Symmetry, unitarity, and geometry in electromagnetic scattering, *Phys. Rev. D*, 3, 825.

Waterman, P.C. (1975). Scattering by periodic surfaces, *J. Acoust. Soc. Am.*, 57, 791.

Weeks, W.L. (1964). *Electromagnetic Theory for Engineering Applications*, New York: Wiley.
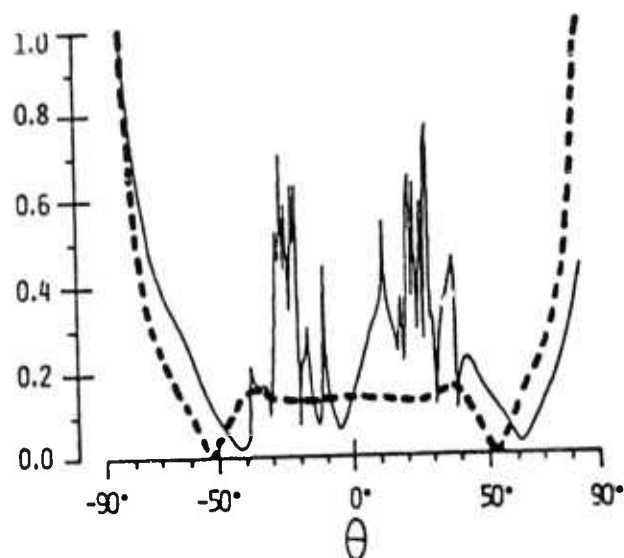
Fig.1 Normalized field amplitude as a function of θ, the angular displacement from the y-axis, in the medium below S_b due to a line source located at $r_p = (0,0)$. The surface S_a is $y = L\{1 + (0.10) \sin(2\pi x/L)\}$, while the surface S_b is the plane $y = -L$. The relevant parameters are $kL = 5.0$, $q = 1.9591837$, and $K = (7/9)k$. For comparison, the dashed line shows the same calculations for $b/L = 0$. To get the actual amplitude, multiply the values read from the graph by 0.126033 for $b/L = 0$, and by 0.102563 for $b/L = 0.10$.
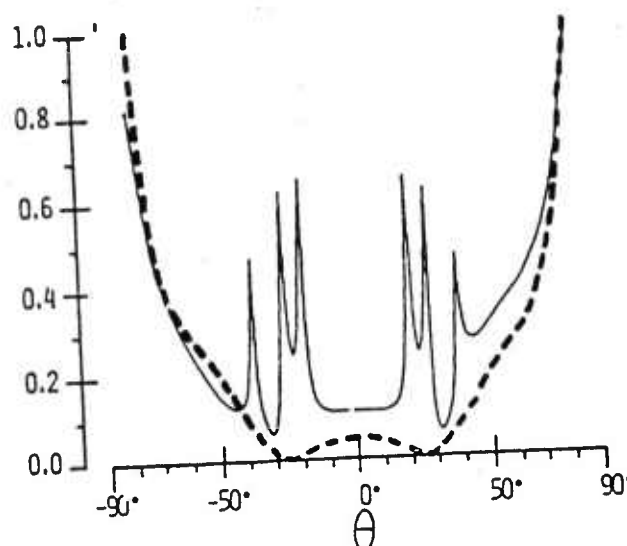
Fig.2 Same as Fig. 2, except kL = 10.0. To get the actual amplitude, multiply the values read from the graph by 0.0866611 for b/L = 0, and by 0.0442079 for b/L = 0.10.

Fig.3 Normalized field amplitude as a function of θ, the angular displacement from the y-axis, in the medium below S_b due to a line source located at r_p = (0,0). The surface S_a is y = L{1 + 0.15 sin(2πx/L)}, while the surface S_b is the plane y = - L. The normalized frequency kL = 15.0, while (A) q = 1.9591837, K = (7/9)k, and (B) q = 1.0 and K = k. To get the actual amplitude, multiply the values read from (A) by 0.027005, and from (B) by 0.0864508.
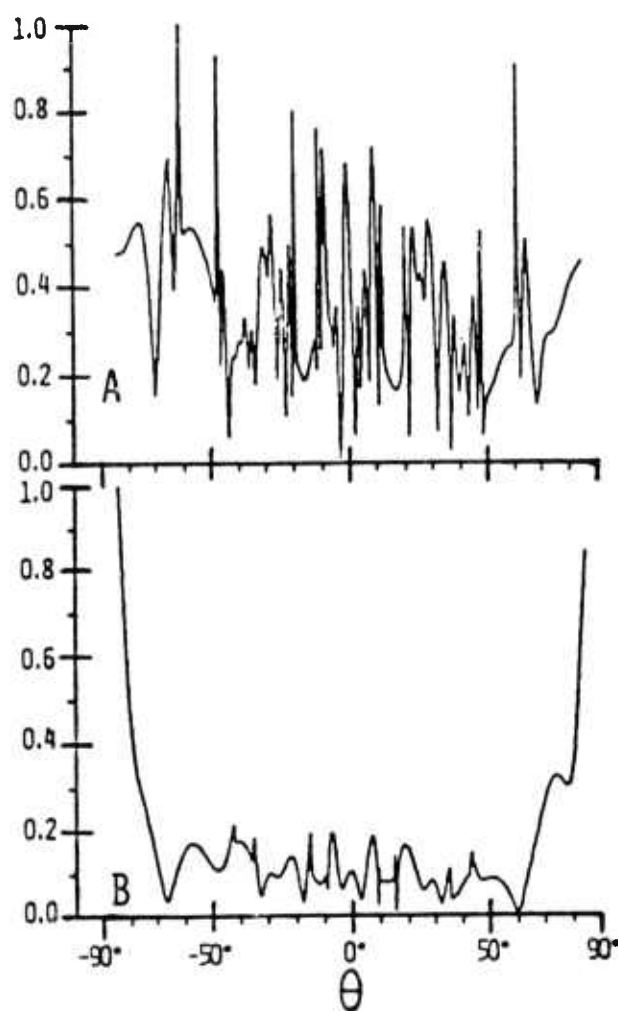
Fig.4 Magnitude of w_a computed at locations x on S_a, due to a line source located at r_p = (0,0), as a function of the normalized frequency kL. The surface S_a is y = L{1 + 0.10 sin(2πx/L)}, while the surface S_b is the plane y = - L. The other relevant parameters are q = 1.9591837, and K = (7/9)k. (A) x = ± L, (B) x = ± 10L, (C) x = ± 50L.
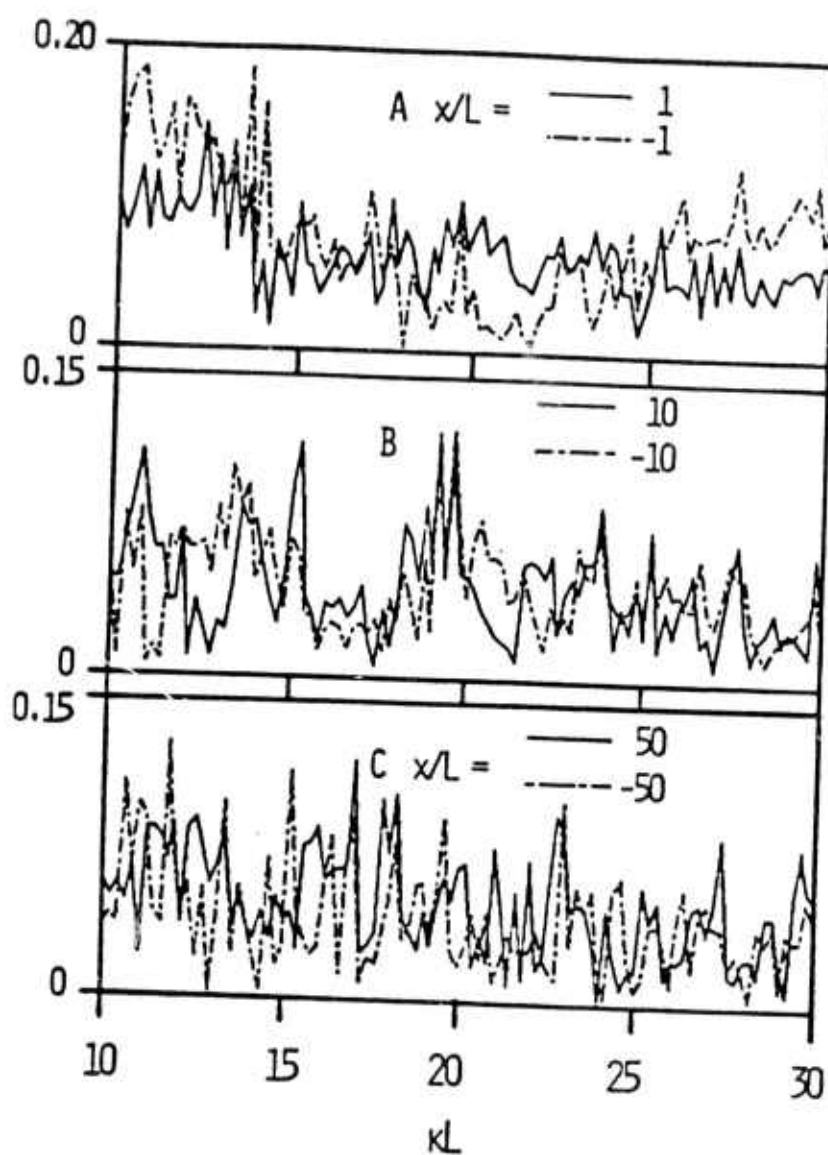
RADIATION CHARACTERISTICS OF ELASTODYNAMIC LINE SOURCES BURIED IN LAYERED MEDIA WITH PERIODIC INTERFACES. II - P AND SV WAVE ANALYSIS

Vijay K. Varadan[+], Akhlesh Lakhtakia[+], Vasundara V. Varadan[+] and Charles A. Langston[*]

[+]Laboratory for Electromagnetic and Acoustic Research,
Department of Engineering Science and Mechanics
[*]Department of Geosciences
The Pennsylvania State University,
UNIVERSITY PARK, PA 16802.

ABSTRACT

A method for determining the elastodynamic (P and SV waves) radiation characteristics of finite-size sources buried in horizontally layered media, having periodically corrugated interfaces, is described. In particular, the example problem chosen to illustrate the procedure is as follows: a solid plate lies on top of an solid half-space; the solid-solid interface has been taken to be planar, but traction-free conditions prevail on the other boundary of the elastic plate, which surface is also periodically corrugated; and the source has been taken to be an isotropic, P-wave line source located inside the elastic plate. The technique presented utilizes the planewave spectral decomposition of the relevant fields within the framework of the extended boundary condition, or the T-matrix, method. Since the T-matrix method is a matrix approach, it is very attractive computationally, and is certainly more tractable than a method based on the direct solution of the integral equations involved in the scattering problem. Numerical results are given to delineate the various features of the field diffracted into the elastic half-space, as well as those of the displacement field induced on the traction-free boundary of the elastic plate. The specific example examined is directly related to regional wave propagation in a continental crustal waveguide.

INTRODUCTION

In the companion paper [Varadan *et al.*, 1986], a method was developed to treat the scattering of the radiated fields of a SH-wave line source embedded in a two-dimensional elastic waveguide bounded by corrugated interfaces, which can lie either between elastic media, or have homogeneous boundary conditions prescribed on either or both of the interfaces. Problems of this type are important in various fields such as, noise control, meteorology, as well as seismology.

In this paper, we utilize the extended boundary condition, or the T-matrix, method [Waterman, 1975] to treat the problem of P- and SV- wave propagation in a waveguide excited by a line source. This is a necessary extension of the technique to treat problems involving seismic wave propagation at regional and teleseismic distances where the effect of waveguide imperfections is of great interest. A motivation for obtaining this solution is to understand crustal waveguide scattering of regional waves, such as L_g and P_g excited by nuclear explosions.

A simple scattering arrangement is chosen: a solid plate lies on top of an elastic (solid) half-space. The solid-solid interface has been taken to be planar, but traction-free conditions prevail on the other boundary of the elastic plate, which surface is also periodically corrugated; and the source has been taken to be an isotropic, P wave line source located inside the elastic plate. The parameters and dimensions of the model chosen here are motivated by the geophysically interesting situation of a continental crust over a mantle half-space. The corrugations of the free surface simulate the topography of the Basin and Range province of the western United States, as has been alluded to in the companion paper [Varadan *et al.*, 1986]. It should be noted that such a simple scattering geometry merely exemplifies more complicated arrangements: there can be several elastic (solid or fluid) plates atop each other; some or all of the various interfaces can be periodically rough; and the choice of the source can be purely arbitrary, provide the field radiated by it can be expressed [Clemmow, 1956] in terms of a planewave spectrum, discrete or continuous.

The method of solution proposed here is not an extension of the one used elsewhere by us [Lakhtakia *et al.*, 1985a], where all relevant fields were expanded in terms of a discrete planewave spectral representation, the T-matrix of each interface was separately computed, and the inter-surface distance was taken into account using co-ordinate transfer [Cain *et al.*, 1986] or planewave propagation matrices. Instead, here the extinction theorem of the extended boundary condition method [Waterman, 1975; Barber and Yeh, 1975] is applied to elastic plate

and the relevant fields are decomposed into a continuous planewave spectrum. The resulting theoretical treatment is then converted into a set of matix equations, which can then be solved on a digital computer. This process gives rise to a more compact formulation as compared to that which could be obtained using the method of Lakhtakia *et al.* [1985a]. Numerical results are given to delineate the various features of the field diffracted into the elastic half-space, as well as those of the displacement field induced on the traction-free boundary of the elastic plate.

PRELIMINARIES AND NOTATION

Shown in Fig. 1 is a schematic of the problem to be solved here. The stress-free boundary condition prevails on Γ_a, which surface is determined by the relationship $y = h(x) > 0$, $-\infty < x < \infty$, where h is single valued and has a period L in its argument, i.e., $h(x) = h(x + L)$. On the other hand, the surface Γ_b is taken to be the planar interface $y = -d < 0$, $-\infty < x < \infty$, and the two surfaces, thus may never meet. Interposed in between the two surfaces is a homogeneous, isotropic, perfectly elastic solid of density ρ and Lame constants λ and μ, while the semi-infinite region below Γ_b is occupied by a similar elastic solid whose constants are ρ', λ' and μ'. Furthermore, a source is embedded at the location r_p, chosen such that $h(x) > y_p > -d$, $\forall x$. It is the aim of this paper to obtain the field present in the primed medium below Γ_b due to this source.

Two-dimensional wave propagation in elastic media is characterized by two types of wave motion: the longitudinal or P wave and the vertically-polarized shear or SV wave. In general mode conversion between P and SV waves takes place at boundaries; hence, it is necessary to consider the two wave types simultaneously. In what follows a combination of vector and tensor notation will be used, and which will be developed along with the theory. The position vector r can be interchangeably represented as either (x, y) or (r_1, r_2). Greek subscripts (except κ) are to be only assigned values of 1 and 2, while the summation convention holds for repeated Greek subscripts. An exponential time dependence $\exp[-i\omega t]$ is implicit in this treatment.

Particularly with reference to the unprimed medium, the *displacement* and the *stress* Green's tensors, denoted by $\underline{G}(r - r_o)$ and $\underline{T}(r - r_o)$, respectively, together satisfy the differential relations [Achenbach, 1973]:

$$\partial_\beta T_{\alpha\beta\gamma} + \rho\omega^2 G_{\alpha\gamma} = -\delta_{\alpha\gamma}\delta(r - r_o), \tag{1a}$$

$$T_{\alpha\beta\gamma} = \lambda\delta_{\alpha\beta}\partial_\xi G_{\xi\gamma} + \mu[\partial_\beta G_{\alpha\gamma} + \partial_\alpha G_{\beta\gamma}], \tag{1b}$$

with both $\underline{G}$ and $\underline{T}$ also satisfying suitable radiation conditions [Tan, 1975] as well as the Floquet conditions

[Lakhtakia *et al.*, 1984b] due to the periodicity of Γ_a. These Green's tensors are represented as:

$$G_{\alpha\gamma}(r - r_0) = \pi/L \int_{-\pi/L}^{\pi/L} d\kappa \ D_\kappa \ G_{\alpha\gamma}(\kappa, r, r_0), \tag{2a}$$

$$T_{\alpha\beta\gamma}(r - r_0) = \pi/L \int_{-\pi/L}^{\pi/L} d\kappa \ D_\kappa \ T_{\alpha\beta\gamma}(\kappa, r, r_0). \tag{2b}$$

where

$$1/D_\kappa = 1 + \delta(\kappa - \pi/L) + \delta(\kappa + \pi/L), \tag{2c}$$

and the basic variable κ varies from $-\pi/L$ to π/L along the real line, and $\delta(\kappa - \kappa')$ being the Dirac delta. For the solid medium with density ρ and Lame constants λ and μ, pertinent to the present problem, the following quantities are now defined:

$$\kappa_n = \kappa + 2\pi n/L, \quad n \in [0, \pm 1, \pm 2, \pm 3, ...], \tag{3a}$$

$$\pi_n = +\sqrt{[k_p^2 - \kappa_n^2]}; \quad \sigma_n = +\sqrt{[k_s^2 - \kappa_n^2]}, \tag{3b}$$

$$P_n^\pm = x\kappa_n \pm y\pi_n = xP_{1n}^\pm + yP_{2n}^\pm; \quad S_n^\pm = x\kappa_n \pm y\sigma_n = xS_{1n}^\pm + yS_{2n}^\pm, \tag{3c}$$

$$k_p = \omega/c_p \ ; c_p = [(\lambda + 2\mu)/\rho]^{1/2}, \tag{3d}$$

$$k_s = \omega/c_s \ ; c_s = [\mu/\rho]^{1/2}. \tag{3f}$$

Associated with each κ are also the various free-space Green's functions, $G_{\alpha\gamma}(\kappa, r, r_0)$ and $T_{\alpha\beta\gamma}(\kappa, r, r_0)$. The free-space *displacement* Green's function can be most easily set down as [Lakhtakia *et al.*, 1984b]:

$$G_{\alpha\gamma}(\kappa, r, r_0) = \sum_n (ik_s^2/2\rho\omega^2\sigma_n L) \ U_{\alpha n}^{s\pm} \ U_{\gamma m}^{s\pm} \ \exp[iS_n^\pm \cdot (r - r_0)] +$$
$$+ \sum_n (ik_p^2/2\rho\omega^2\pi_n L) \ U_{\alpha n}^{P\pm} \ U_{\gamma m}^{P\pm} \ \exp[iP_n^\pm \cdot (r - r_0)], \tag{4}$$

where

$$U_{\alpha n}^{P\pm} = (1/k_p) \ P_{\alpha n}^\pm, \quad U_{\alpha n}^{s\pm} = (1/k_s) \ \varepsilon_{\alpha\beta} \ S_{\beta n}^\pm, \tag{5a,b}$$

$\varepsilon_{\alpha\beta}$ is an unit antisymmetric tensor, and the superscript '+' (resp. '-') is to be used if $y > y_0$ (resp. $y < y_0$). Corresponding to this $G_{\alpha\gamma}(\kappa, r, r_0)$ is the *stress* Green's function given by [Lakhtakia *et al.*, 1984b]

$$T_{\alpha\beta\gamma}(\kappa, r, r_0) = \sum_n (ik_s^2/2\rho\omega^2\sigma_n L) \ U_{\gamma m}^{s\pm} \ T_{\alpha\beta n}^{s\pm} \ \exp[iS_n^\pm \cdot (r - r_0)] +$$
$$+ \sum_n (ik_p^2/2\rho\omega^2\pi_n L) \ U_{\gamma m}^{P\pm} \ T_{\alpha\beta n}^{P\pm} \ \exp[iP_n^\pm \cdot (r - r_0)], \tag{6}$$

where

$$T_{\alpha\beta n}^{P\pm} = ik_p [\lambda\delta_{\alpha\beta} + 2\mu \ U_{\alpha n}^{P\pm} \ U_{\beta n}^{P\pm}], \tag{7a}$$

$$T_{\alpha\beta n}^{s\pm} = i\mu [S_{\alpha n}^{s\pm} \ U_{\beta n}^{s\pm} + S_{\beta n}^{s\pm} \ U_{\alpha n}^{s\pm}]. \tag{7b}$$

It should be noted that κ is implicit in the definitions (3), (5) and (87; moreover, by putting primes on the various quantities defined above (except κ), those quantities can be made to refer to the primed medium below

Γ_b.

APPLICATION OF THE EXTINCTION THEOREM

The application of Huyghens' principle to the field in the unprimed medium enclosed in between Γ_a and Γ_b leads to [Waterman, 1975; Varadan et al., 1986]:

$$u_\gamma^i(r) = -\int_{\Gamma_b} ds_0 \left[T_{\alpha\beta\gamma}(r-r_0) u_{b\alpha}(r_0) + G_{\alpha\gamma}(r-r_0) \tau_{b\alpha\beta}(r_0) \right] n_{b\beta}(r_0)$$
$$+ \int_{\Gamma_a} ds_0 \left[T_{\alpha\beta\gamma}(r-r_0) u_{a\alpha}(r_0) \right] n_{a\beta}(r_0) \tag{8}$$

where r must lie either above Γ_a or below Γ_b; and the slash across the integral sign indicates that the integration takes place on one period of the relevant surface, i.e., over the range $-L/2 \le x_0 \le L/2$. This equation, called the *extinction theorem*, forms the bedrock of the extended boundary condition method, and will be utilized in this section to solve for the present problem. Here, the boundary condition on Γ_a has been taken into account already; n_a and n_b, respectively, are the unit normals on Γ_a and Γ_b; u_b and τ_b are the displacement vector and the stress tensor induced on the +y side of Γ_b; and u_a is the displacement vector induced on the -y side of Γ_a.

The field radiated by the source, embedded between Γ_a and Γ_b, in (8) is u^i which may be decided upon at this stage for later ease. Any arbitrary source can be taken into account; and its radiated field should be expressed in a continuous plane wave spectrum [Clemmow, 1956] to be substituted in (8). For the sake of illustration, as stated earlier, here a P wave line source located at r_p is considered: its radiated field is given by

$$u^i(r) = (1/k_p) \nabla H_0(k_p |r - r_p|), \tag{9}$$

where $H_0(\cdot) = H_0^{(1)}(\cdot)$ is the zeroth-order cylindrical Hankel function of the first kind. But the Hankel function can be expanded in a spectrum of plane waves as [Varadan et al., 1986]:

$$H_0(k_p |r - r_p|) = (1/\pi) \int_{-\pi/L}^{\pi/L} d\kappa \ D_\kappa \sum_n \exp[iP_n^\pm(\kappa) \cdot (r - r_p)]/\pi_n(\kappa) \tag{10a}$$

with the aid of the definitions of the previous section. The superscript '+' (resp. '-') is to be used in (11) if $y > y_p$ (resp. $y < y_p$). Hence, the radiated displacement field is given by

$$u_\gamma^i(r) = (1/\pi) \int_{-\pi/L}^{\pi/L} d\kappa \ D_\kappa \sum_n U_{\gamma n}^{P\pm} \exp[iP_n^\pm(\kappa) \cdot (r - r_p)]/\pi_n(\kappa) \tag{10b}$$

Substitution of (2a,b) and (10b) in (8) gives rise to the relation

$$(1/\pi) \sum_n U_{\gamma n}^{P\pm} \exp[iP_n^\pm(\kappa) \cdot (r - r_p)]/\pi_n(\kappa) = \int_{\Gamma_a} ds_0 \left[T_{\alpha\beta\gamma}(\kappa,r,r_0) u_{a\alpha}(\kappa,r_0) \right] n_{a\beta}(r_0)$$
$$- \int_{\Gamma_b} ds_0 \left[T_{\alpha\beta\gamma}(\kappa,r,r_0) u_{b\alpha}(\kappa,r_0) + G_{\alpha\gamma}(\kappa,r,r_0) \tau_{b\alpha\beta}(\kappa,r_0) \right] n_{b\beta}(r_0); \ \forall \kappa : |\kappa| \le \pi/L, \tag{11a}$$

after eliminating the integral on κ, and defining the surface quantities involved in (11a) in the form

$$u_{a\alpha}(r) = \,_{-\pi/L}\!\int^{\pi/L} d\kappa \; u_{a\alpha}(\kappa,r), \tag{11b}$$

etc. Finally, the limiting principle [Waterman, 1971; Waterman, 1975; Barber and Yeh, 1975] of the T-matrix method has to be employed. Expansions (4) and (6) are substituted in (11a) and inner products of (11a) are taken, with $\exp[-iP_n^{\pm}(\kappa) \cdot r]$ and $\exp[-i\omega_n^{\pm}(\kappa) \cdot r]$, over the domain $|x| \le L/2$ on both the surfaces Γ_{a+} and Γ_b (see Fig. 1). Of the four inner products thus taken, those over Γ_b are straightforward and need no explanation. But the reason for taking the inner products over Γ_{a+}, rather than on Γ_a, can best be explained by the concept of analytic continuation put forth by Waterman [1971; 1975] and to which the interested reader is referred.

As a result of the foregoing manipulations, the twin relations of (11a) simplify to the four equations,

$$\exp[-iP_n^{\pm}(\kappa) \cdot r_p] = C_p \oint_{\Gamma_a} ds_0 \; T_{\alpha\beta n}{}^{p\pm} u_{a\alpha}(\kappa,r_0) \; n_{a\beta}(r_0) \exp[-iP_n^{\pm}(\kappa) \cdot r_0]$$
$$- C_p \oint_{\Gamma_b} ds_0 \left[T_{\alpha\beta n}{}^{p\pm} u_{b\alpha}(\kappa,r_0) + U_{\alpha n}{}^{p\pm} \tau_{b\alpha\beta}(\kappa,r_0) \right] n_{b\beta}(r_0) \exp[-iP_n^{\pm}(\kappa) \cdot r_0];$$
$$\forall \kappa : |\kappa| \le \pi/L, \; \forall n : |n| \le \infty, \tag{12a,b}$$

and

$$0 = C_s \oint_{\Gamma_a} ds_0 \; T_{\alpha\beta n}{}^{s\pm} u_{a\alpha}(\kappa,r_0) \; n_{a\beta}(r_0) \exp[-iS_n^{\pm}(\kappa) \cdot r_0]$$
$$- C_s \oint_{\Gamma_b} ds_0 \left[T_{\alpha\beta n}{}^{s\pm} u_{b\alpha}(\kappa,r_0) + U_{\alpha n}{}^{s\pm} \tau_{b\alpha\beta}(\kappa,r_0) \right] n_{b\beta}(r_0) \exp[-S_n^{\pm}(\kappa) \cdot r_0];$$
$$\forall \kappa : |\kappa| \le \pi/L, \; \forall n : |n| \le \infty, \tag{12c,d}$$

where

$$C_p = i\pi \, k_p{}^2/2\rho\omega^2 L, \qquad C_s = i\pi \, k_s{}^2/2\rho\omega^2 L. \tag{13a,b}$$

These four equations suffice to solve for the fields induced on the two boundaries, and are a direct consequence of the application of the extinction theorem. Their solution can be attempted using the integral equation methods [e.g., Fokkema, 1979] but, instead, here the four equations grouped together as (12) will be converted into a system of matrix equations after using the boundary conditions on Γ_b.

THE MATRIX EQUATIONS

In (12) the boundary conditions

$$\tau_{b\alpha\beta}(\kappa,r) \, n_{b\beta}(r) = \tau'_{\alpha\beta}(\kappa,r) \, n_{b\beta}(r), \quad u_{b\alpha}(\kappa,r) = u'_{\alpha}(\kappa,r); \; r \in \Gamma_b, \tag{14}$$

appropriate for the solid-solid interface should be substituted, with u' and τ' being the displacement vector and the stress tensor, respectively, of the field radiated into the region below Γ_b. The plane wave spectral decomposition of these two quantities is given by

$$\tau'_{\alpha\beta}(r) = {}_{-\pi/L}\!\int^{\pi/L} d\kappa \ \tau'_{\alpha\beta}(\kappa,r), \quad u'_{\alpha}(r) = {}_{-\pi/L}\!\int^{\pi/L} d\kappa \ u'_{\alpha}(\kappa,r); \ y \le -d, \tag{15}$$

where,

$$u'_{\alpha}(\kappa,r) = \sum_m \left\{ A_m^P(\kappa) \, U'_{\alpha m}^{P-} \, \exp[iP'^{-}_m(\kappa) \cdot r] + A_m^S(\kappa) \, U'_{\alpha m}^{S-} \, \exp[iS'^{-}_m(\kappa) \cdot r] \right\}, \tag{16a}$$

$$\tau'_{\alpha\beta}(\kappa,r) = \sum_m \left\{ A_m^P(\kappa) \, T_{\alpha\beta m}^{P-} \, \exp[iP'^{-}_m(\kappa) \cdot r] + A_m^S(\kappa) \, \Gamma_{\alpha\beta m}^{S-} \, \exp[iS'^{-}_m(\kappa) \cdot r] \right\}. \tag{16b}$$

Finally, as regards the displacement vector on Γ_a, it can be expanded in terms of the Fourier-Bloch waves [Waterman, 1975; Lakhtakia *et al.*, 1984b] as:

$$u_{a\alpha}(\kappa,r) = \sum_m \left\{ B_m^P(\kappa) \, U_{\alpha m}^{P+} \exp[iP_m^+(\kappa) \cdot r] + B_m^S(\kappa) \, U_{\alpha m}^{S+} \exp[iS_m^+(\kappa) \cdot r] \right\}, r \in \Gamma_a. \tag{17}$$

Substitution, now, of (14), (16) and (17) in (12) leads to a system of matrix equations, which can be compactly set down as:

$$\forall \kappa : |\kappa| \le \pi/L, \ \forall n : |n| \le \infty,$$

$$
\begin{aligned}
\exp[-iP_n^{\pm}(\kappa) \cdot r_p] \ =\ & C_p \sum_m \left\{ B_m^P \, T_{\alpha\beta n}^{P\pm} \, U_{\alpha m}^{P+} \textstyle\oint_{\Gamma a} ds \ n_{a\beta}(r) \exp[-iP_n^{\pm} \cdot r] \exp[iP_m^+ \cdot r] \right\} \\
& + C_p \sum_m \left\{ B_m^S \, T_{\alpha\beta n}^{P\pm} \, U_{\alpha m}^{S+} \textstyle\oint_{\Gamma a} ds \ n_{a\beta}(r) \exp[-iP_n^{\pm} \cdot r] \exp[iS_m^+ \cdot r] \right\} \\
& - C_p \sum_m \left\{ A_m^P \left[T_{\alpha\beta n}^{P\pm} U'_{\alpha m}^{P-} + T_{\alpha\beta m}^{P-} U_{\alpha n}^{P\pm} \right] \cdot \right. \\
& \hspace{3cm} \left. {}^{\bullet}\textstyle\oint_{\Gamma b} ds \ n_{b\beta}(r) \exp[-iP_n^{\pm} \cdot r] \exp[iP'^{-}_m \cdot r] \right\} \\
& - C_p \sum_m \left\{ A_m^S \left[T_{\alpha\beta n}^{P\pm} U'_{\alpha m}^{S-} + T_{\alpha\beta m}^{S-} U_{\alpha n}^{P\pm} \right] \cdot \right. \\
& \hspace{3cm} \left. {}^{\bullet}\textstyle\oint_{\Gamma b} ds \ n_{b\beta}(r) \exp[-iP_n^{\pm} \cdot r] \exp[iS'^{-}_m \cdot r] \right\}
\end{aligned} \tag{18a,b}
$$

and

$$
\begin{aligned}
0 \ =\ & - C_s \sum_m \left\{ B_m^P \, T_{\alpha\beta n}^{S\pm} \, U_{\alpha m}^{P+} \textstyle\oint_{\Gamma a} ds \ n_{a\beta}(r) \exp[-iS_n^{\pm} \cdot r] \exp[iP_m^+ \cdot r] \right\} \\
& + C_s \sum_m \left\{ B_m^S \, T_{\alpha\beta n}^{S\pm} \, U_{\alpha m}^{S+} \textstyle\oint_{\Gamma a} ds \ n_{a\beta}(r) \exp[-iS_n^{\pm} \cdot r] \exp[iS_m^+ \cdot r] \right\} \\
& - C_s \sum_m \left\{ {}_{\cdot} \cdot{}_m^P \left[T_{\alpha\beta n}^{S\pm} U'_{\alpha m}^{P-} + T_{\alpha\beta m}^{P-} U_{\alpha n}^{S\pm} \right] \cdot \right. \\
& \hspace{3cm} \left. {}^{\bullet}\textstyle\oint_{\Gamma b} ds \ n_{b\beta}(r) \exp[-iS_n^{\pm} \cdot r] \exp[iP'^{-}_m \cdot r] \right\} \\
& - C_s \sum_m \left\{ A_m^S \left[T_{\alpha\beta n}^{S\pm} U'_{\alpha m}^{S-} + T_{\alpha\beta m}^{S-} U_{\alpha n}^{S\pm} \right] \cdot \right. \\
& \hspace{3cm} \left. {}^{\bullet}\textstyle\oint_{\Gamma b} ds \ n_{b\beta}(r) \exp[-iS_n^{\pm} \cdot r] \exp[iS'^{-}_m \cdot r] \right\}
\end{aligned} \tag{18c,d}
$$

Further simplification by putting in the geometry of the two surfaces gives rise to the four equations:

$$\forall \kappa : |\kappa| \le \pi/L, \ \forall n : |n| \le \infty,$$

$$
\begin{aligned}
\exp[-iP_n^{\pm}(\kappa) \cdot r_p] \ =\ & C_p \sum_m \left\{ B_m^P \, T_{\alpha\beta n}^{P\pm} \, U_{\alpha m}^{P+} \ \aleph_{\beta n m}^{\pm}(\pi_n, \pi_m) \right\} \\
& + C_p \sum_m \left\{ B_m^S \, T_{\alpha\beta n}^{P\pm} \, U_{\alpha m}^{S+} \ \aleph_{\beta n m}^{\pm}(\pi_n, \sigma_m) \right\} \\
& - L C_p \, A_n^P \left[T_{\alpha 2 n}^{P\pm} U'_{\alpha n}^{P-} + T_{\alpha 2 n}^{P-} U_{\alpha n}^{P\pm} \right] \exp[i(\pm \pi_n + \pi'_n)d]
\end{aligned}
$$

$$- LC_p A_n{}^S \left[T_{\alpha 2n}{}^{P\pm} U'_{\alpha n}{}^{S-} + T_{\alpha 2n}{}^{S-} U_{\alpha n}{}^{P\pm}\right] \exp[i(\pm\pi_n + \sigma'_n)d], \tag{19a,b}$$

and

$$\begin{aligned}
0 \quad &= C_s \sum_m \left\{ B_m{}^P \, T_{\alpha\beta n}{}^{S\pm} U_{\alpha m}{}^{P+} \, \aleph_{\beta nm}{}^{\pm}(\sigma_n, \pi_m) \right\} \\
&+ C_s \sum_m \left\{ B_m{}^S \, T_{\alpha\beta n}{}^{S\pm} U_{\alpha m}{}^{S+} \, \aleph_{\beta nm}{}^{\pm}(\sigma_n, \sigma_m) \right\} \\
&- LC_s A_n{}^P \left[T_{\alpha 2n}{}^{S\pm} U'_{\alpha n}{}^{P-} + T_{\alpha 2n}{}^{P-} U_{\alpha n}{}^{S\pm}\right] \exp[i(\pm\sigma_n + \pi'_n)d] \\
&- LC_s A_n{}^S \left[T_{\alpha 2n}{}^{S\pm} U'_{\alpha n}{}^{S-} + T_{\alpha 2n}{}^{S-} U_{\alpha n}{}^{S\pm}\right] \exp[i(\pm\sigma_n + \sigma'_{ri})d],
\end{aligned} \tag{19c,d}$$

where the integrals,

$$\aleph_{1nm}{}^{\pm}(q, Q) = (2\pi/L) \left[(n-m)/(\pm q - Q)\right] \aleph_{2nm}{}^{\pm}(q, Q), \tag{20a}$$

and

$$\aleph_{2nm}{}^{\pm}(q, Q) = \int_{-L/2}^{L/2} dx \, \exp[-i2(n-m)\pi x/L] \, \exp[-i(\pm q - Q)h(x)]. \tag{20b}$$

If the traction-free surface Γ_a be sinusoidal, i.e.,

$$h(x) = a - b \cos(2\pi x/L), \tag{21a}$$

then the integral (20b) can be evaluated in terms of the cylindrical Bessel functions $J_n(\cdot)$ as

$$\aleph_{2nm}{}^{\pm}(q,Q) = i^{|n-m|} L \, \exp[-i(\pm q - Q)a] \, J_{|n-m|}([\pm q - Q]b), \tag{21b}$$

with $\aleph_{1nm}{}^{\pm}(q, Q)$ still defined as in (20a); the only special case arises for $q = Q$, when

$$\aleph_{2nm}{}^{+}(q, q) = L \, \delta_{nm}; \quad \aleph_{1nm}{}^{+}(q, q) = -i\pi b \, [\delta_{n,m+1} - \delta_{n,m-1}], \tag{21c,d}$$

$\delta_{n,m}$ being the Kronecker delta.

DISCUSSION AND NUMERICAL RESULTS

Of necessity, the system of equations in (19) has to be truncated at some $|m|, |n| = N$, for each κ, care being taken however to ensure that convergence is achieved at some value of N. This is done by ensuring that the unitarity parameter [Lakhtakia et al., 1985b] for each κ,

$$\sum_m (\lambda' + 2\mu') \, |A_m{}^P(\kappa)|^2 \, Re\{\pi'_m(\kappa)\} + \mu'|A_m{}^S(\kappa)|^2 \, Re\{\sigma'_m(\kappa)\} \tag{22}$$

converges to within a preset tolerance of $\pm 0.1\%$ as N is increased. Simultaneously, the various field coefficients $A_m{}^{P,S}$ and $B_m{}^{P,S}$ should also converge within similar error bounds.

It should be noted that if $\pi_m(\kappa)$ for a given m and κ be real positive then at an angle $\theta = \tan^{-1}\{\kappa/\pi_m(\kappa)\}$ with respect to the y-axis, the P wave component of the radiated field in the medium below Γ_b,

$$u'_\alpha(r) \to A_m{}^P(\kappa) \, U'_{\alpha m}{}^{P-}(\kappa) \, \exp[-iP'_m{}^{-}(\kappa) \cdot r] \text{ as } k'_p r \to \infty; \tag{23a}$$

likewise, if $\sigma_m(\kappa)$ for a given m and κ be real positive then at an angle $\theta = \tan^{-1}\{\kappa/\sigma_m(\kappa)\}$ with respect to the y-axis, the *SV wave* component of the radiated field in the medium below Γ_b,

$$u'_\alpha(r) \to A_m{}^S(\kappa)\, U'_{\alpha m}{}^{S-}(\kappa)\, \exp[-iS'_m{}^-(\kappa) \cdot r] \text{ as } k'_s r \to \infty. \tag{23b}$$

The computation of the far-zone radiated field in that half-space, therefore, is very straightforward.

In the calculations to be presented in this section, the surface Γ_a has been chosen to be the sinusoid $y = a - b\cos(2\pi x/L)$ while the lower surface is the plane $y = -d$. The material parameters of the medium enclosed by the two surfaces are $c_p = 3500$ m s^{-1}, $c_s = 6000$ m s^{-1} and $\rho = 2700$ kg m^{-3}; the P-wave line source is located at the origin, i.e., $r_p = (0,0)$. Because of the symmetry of the two surfaces about the line source location, both the P and the SV radiation patterns, as $y \to -\infty$, are symmetric about the y axis. It may be mentioned here that the calculation of the radiation patterns was carried out at each frequency in Figs. 2 - 7 by discretizing the range $|\kappa| \leq \pi/L$ into 91 equi-spaced values of κ; matrices of order not exceeding 44 (i.e., $N \leq 5$) were used to achieve convergent results on a DEC VAX 11/730 minicomputer.

Shown in Fig. 2 are the far zone radiation amplitudes as functions of θ, the angle made with the -y axis, at the normalized frequencies $k_p L = 5.0$, 7.5 and 10.0. The homogeneous half-space below Γ_b has the parameters $c'_p = 4500$ m s^{-1}, $c'_s = 8000$ m s^{-1} and $\rho' = 3200$ kg m^{-3}; while $b/L = 0.05$ and $a/L = d/L = 1.0$. These calculations are repeated in Fig. 3, but for $b/L = 0.0$. In comparing these two figures, one prominent feature stands out. The radiated SV wave amplitude is essentially non-zero only for the range $|\theta| < 50$ deg in Fig. 3 when the upper surface is plane, whereas the same amplitude is trivially non-vanishing for the entire range $|\theta| \leq 90$ deg. Of course, for $\theta = 0$ deg, no SV radiated wave can exist [Achenbach, 1973] in the present context. Furthermore, all plots in Figs. 2 and 3 depict the presence of sharp discontinuities, or anomalies, which have to be accounted for and understood. Lastly, the number of anomalies increases as the frequency does; this last observation can, however, be explained in a simple manner as follows: As the frequency increases, then for each $\kappa : |\kappa| \leq \pi/L$, there are more $\kappa_n(\kappa)$ for which $\pi_n(\kappa)$, $\sigma_n(\kappa)$, $\pi'_n(\kappa)$, and/or $\sigma'_n(\kappa)$ become positive real. This implies that an increasingly larger number of the components, of the planewave decompositions of the various fields involved, change from being evanescent in the $\pm y$ directions to being propagating. As that happens, the radiated energy has to be distributed among more and more propagating waves, giving rise to the increase in the number of the anomalies.

In order, however, to understand the first two features of these two figures mentioned above, calculations

for several test cases were carried out. In Fig. 4, the radiation amplitudes at $k_pL = 7.5$ are plotted for $(a+d)/L =$ 2.0, $b/L = 0.05$, $c'_p = 4500$ m s^{-1}, $c'_s = 8000$ m s^{-1} and $\rho' = 3200$ kg m^{-3}; the separation between the line source and Γ_b assumes two values: (a) $d/L = 1.0$, and (b) $d/L = 1.5$. In Fig. 5 the calculations of Fig. 4 are repeated, but for $c'_p = c_p$, $c'_s = c_s$ and $\rho' = \rho$. Finally, the computations of Figs. 4 and 5 were re-done for $b/L = 0.0$, and the resulting radiation patterns are shown in Figs. 6 and 7, respectively. Thus, all relevant combinations of the material properties and the geometry of Γ_a have been used in Figs. 4 - 7 to enable one to explain the features mentioned above.

With reference to Fig. 7, first, the simplest of these four sets of calculations ($\pi_n = \pi'_n$, etc.), consider a P wave, with a wave vector $P_n^+(\kappa)$, launched by the source and which hits the *plane* surface Γ_a. As a result, a SV wave with the wave vector $\delta_{mn} S_m^-(\kappa)$ is excited. Because of Fresnel's laws [Lakhtakia *et al.*, 1984b; Lakhtakia *et al*, 1985a], this SV wave propagates downward at an angle θ, where

$$|\theta| = \sin^{-1} \{c_s |P_{1n}^+(\kappa)|\} \tag{24}$$

with respect to the -y axis. If, however, $|P_{1n}^+(\kappa)| \geq k_p$, then that P wave carries no energy in the +y direction: consequently, the SV waves propagating downwards at angles $|\theta| > \sin^{-1} \{c_s/c_p\} = 35.7$ deg may not transport any energy in the -y direction. It is conjectured, therefore, that is the reason why the SV wave amplitudes in Fig. 7 quickly become negligible around this limiting angle. (In Figs. 3 and 6, the corresponding limit will be around $|\theta| = \sin^{-1} \{c'_s/c_p\} = 48.6$ deg.) When, however, Γ_a is periodically corrugated, as in Figs. 2 and 5, the launched P wave with the wave vector $P_n^+(\kappa)$ excites *all* SV waves with wave vectors $S_m^-(\kappa)$, and $S'_m^-(\kappa)$, thereby extending the angular spread of the SV wave radiation pattern.

Considering Fig. 7, again, it is known [Achenbach, 1973] that a Rayleigh surface wave can propagate on the traction-free Γ_a with a x-directed wavenumber $\pm k_R$ given by

$$k_R = k_s \cdot [1+\nu] \cdot [0.862 + 1.14\nu]^{-1}; \, 0 \leq \nu \leq 0.5, \tag{25a}$$

where ν, the Poisson's ratio, is defined as

$$2\nu = [(c_p/c_s)^2 - 2] \cdot [(c_p/c_s)^2 - 1]^{-1}. \tag{25b}$$

Again, if attention is fixed upon any $\kappa : |\kappa| \leq \pi/L$, for which a certain $\kappa_n(\kappa)$ equals $\pm k_R$, then the excitation of the surface wave on Γ_a will exhibit itself in the radiation patterns as an anomaly. This is what happens for $\pm\theta = 37.069$ deg, when $\kappa_{\pm 1}(k_s \sin\theta)$ equals $\pm k_R$, and the spikes in the SV radiation patterns in Fig. 7 exhibit this phenomenon. Using the methods outlined by Lakhtakia *et al.* [1984b; 1985a], several of the anomalies in Fgis.

2 - 6 may also be shown to be attributed to the excitation of the Rayleigh surface waves on Γ_a.

Finally, and again with reference to Fig. 7, it is seen that the P-wave radiation pattern records several broadened extrema. The reason for these is as follows: The P wave with spatial dependence $\exp[iP_n^+(\kappa)\cdot(r - r_p)]$ hits Γ_a and is reflected back, partly as a P wave, with a change of phase, say $\left\{\xi_n(\kappa)\cdot\exp[iP_n^-(\kappa)\cdot r]\cdot\exp[-iP_n^+(\kappa)\cdot r_p]\cdot\exp[i2a\pi_n(\kappa)]\right\}$; it then interferes with the P wave having the spatial dependence $\exp[iP_n^-(\kappa)\cdot(r - r_p)]$ which also has been launched by the line source. The extrema of the function $\left\{\xi_n(\kappa)\exp[-iP_n^+(\kappa)\cdot r_p]\exp[i2a\pi_n(\kappa)] + \exp[-iP_n^-(\kappa)\cdot r_p]\right\}$, therefore, cause the broadened extrema of the P-wave radiation patterns in Fig. 7. When Γ_a is periodically corrugated, as in Fig. 5, these extrema become more numerous and sharper, since each P wave incident on Γ_a is reflected back, partly, as an ensemble of P waves with spatial dependences $\xi_{nm}(\kappa)\exp[iP_m^-(\kappa)\cdot r]\exp[-iP_n^+(\kappa)\cdot r_p]\exp[ia\pi_n(\kappa)]\exp[ia\pi_m(\kappa)]$. A further increase in the numbers of such extrema comes in if Γ_b is a bimaterial interface, as in Figs. 2 - 4, and 6, when similar arguments hold for the multiply reflected P and SV waves inside the unprimed medium. In addition, because of the involvement of factors like $\exp[ia\pi_n(\kappa)]$ and $\exp[id\pi_n(\kappa)]$, etc., the dependence of these extrema is sensitive to the location y_p of the line source, as may be observed by comparing the two P-wave radiation patterns in Fig. 7.

Comparison of Figs. 5 and 7 reveals yet another class of anomalies peculiar to periodic surfaces. If, for instance, for a given κ, $\pi_n(\kappa) = 0$ then the corresponding P wave is in a limbo: it is neither propagating nor evanescent; but even a slight alteration of the frequency could make it of either type, thereby causing a redistribution of energy among the surviving propagating waves. (Of course, this redistribution occurs only if any of the refracting surfaces is periodically corrugated.) An SV wave would have such an instability if its $\sigma_n(\kappa)$ = 0. This instability is called the Rayleigh-Wood anomaly, and a reasonable description, pertinent to the present problem, is given elsewhere [Lakhtakia et al., 1984b; 1985a]. Suffice it will to state here that if any one member of the four sets of quantities, $\pi_n(\kappa)$, $\sigma_n(\kappa)$, $\pi'_n(\kappa)$, and $\sigma'_n(\kappa)$, happens to vanish, then a sharp Rayleigh-Wood anomaly can be observed in the radiation patterns. As a numerical example, a Rayleigh-Wood anomaly occurs in the P-wave radiation patterns of Fig. 5 at $\theta = \pm 9.3$ deg when $\kappa_{\pm 1}(k_p|\sin\theta|) = \pm k_p$, which is also reflected in the SV radiation patterns at $\theta = \pm 5.4$ deg. Likewise, at $-\theta = \pm 42.5$ deg when $\kappa_{\pm 2}(k_p|\sin\theta|) = \pm k_p$, which is also reflected in the SV radiation patterns at $-\theta = \pm 23.2$ deg. Also, at $-\theta = \pm 27.8$ deg, $\kappa_{\pm 3}(k_s|\sin\theta|) = \pm k_s$, showing an anomaly in the SV radiation pattern. There are no such anomalies in Fig. 7

where the upper surface was taken to be planar. Not all of such anomalies are very prominent, and some may have indeed been missed because of the discretization of the range of κ for ease in calculations.

Finally, the last identifiable reason for some of the various anomalies to exist, when Γ_b is a bimaterial interface, is the excitation of a Stoneley wave [Cagniard *et al.*, 1962; Yamaguchi and Sato, 1955; Phynney, 1961] on Γ_b. A Stoneley wave is a non-dispersive surface wave which propagates on a solid-solid interface; it decays as $y^{-1/2}$ away from the interface, and its x-directed wavenumber can have two roots which are not necessarily real nor on the proper Riemann surface. If, however, for a $\kappa : |\kappa| \leq \pi/L$, there exists a *real* $\kappa_n(\kappa)$ which satisfies the condition

$$0 = \kappa_n^2 \left[\kappa_n^2 - (1/2)\omega^2(\rho'-\rho)/(\mu'-\mu)\right]^2 + \pi_n \sigma_n \left[\kappa_n^2 - (1/2)\omega^2\rho'/(\mu'-\mu)\right]^2 +$$
$$+ \pi'_n \sigma'_n \left[\kappa_n^2 + (1/2)\omega^2\rho/(\mu'-\mu)\right]^2 + \left[\pi_n \sigma_n + \pi'_n \sigma'_n\right] (1/4)\omega^2\rho \, \rho'/(\mu'-\mu)^2 + \pi_n\sigma_n\pi'_n\sigma'_n \, \kappa_n^2,$$

$$(26)$$

then a Stoneley wave will be excited for that κ, and its effect can be observed in the P-wave radiation pattern at $\theta = \pm\sin^{-1}(\kappa/k'_p)$, and in the SV-wave radiation pattern at $\theta = \pm\sin^{-1}(\kappa/k'_s)$. The subject of Stoneley waves is, and has been, in itself meritorious of extensive attention, for which reason we shall not discuss it any further here.

Having gone through, qualitatively, the various reasons for the occurrence of anomalies in the radiation patterns, the characteristics of the displacement field excited on the traction-free surface Γ_a remain to be investigated. This is an important field, very often being measured, particularly, in seismological studies. Shown in Fig. 8 are the plots of the two components of u_a versus $\pm x/L$ when the line source is located at $r_p = (0,0)$ and the normalized frequency $k_p L = 7.5$. The wave velocities in, and the densities of, the two media are the same as in Fig. 2; $a/L = d/L = 1.0$; and $b/L = 0.05$. In Fig. 9, these same quantities are re-plotted but for $b/L = 0.0$ so that Γ_a is flat. The highlight of these figures is the extreme variability of the components of u_a. In particular, when Γ_a is flat, then bunching of data seems to occur, with some evidence of quasi-periodicity, as may be seen by the repetition of similar (not necessarily, the same) features in Fig. 9. In Fig. 8, on the other hand, the periodicity of Γ_a creates additional anomalies due to inter-modal interactions; hence, the data variability is enhanced, and the bunching is diffused. Incidently, the computations of u_a were carried out by a 63-point Gauss-Legendre quadrature integration [Abramowitz and Stegun, 1972] for the integral over $\kappa : |\kappa| \leq \pi/L$ in (19), and considering upto $n = \pm 5$ for each κ, keeping, of course, in mind that the computations for each κ converged satisfactorily.

In order to investigate the characteristic feature of Figs. 8 and 9, the incident field was modified to

$$u^i(r) = (1/k_p)[\nabla H_0(k_p r)] \cdot \delta(\kappa), \tag{27}$$

so that it simply contains a longitudinal wave which has only a y-directed component of displacement. Corresponding to Figs. 8 and 9, respectively, Figs. 10 and 11 show the computed values of u_a versus $\pm x/L$. It should be noted that, in Fig. 11, u_{a1} is identically zero and u_{a2} is constant for all x, as should be the case when Γ_a is flat. But the periodicity of Γ_a in Fig. 10 has generated a generally non-zero u_{a1}, which is about one-fourth in magnitude of u_{a2}. The displacement fields, in addition, are perfectly periodic in Fig. 8 (data was computed in Figs. 8 - 15 at intervals $\Delta x/L = 0.04$).

Then, in Figs 12 and 13, respectively, the data of Figs. 8 and 9 was re-computed, but with the incident field modified to

$$u^i(r) = (1/k_p)[\nabla H_0(k_p r)] \cdot \sum_{|n| \le \infty} \delta(\kappa - 2n\pi/L), \tag{28}$$

so as to include the higher-order modes associated with $\kappa = 0$ in the calculations for Figs. 8 and 9. With this change, neither u_{a1} is zero nor u_{a2} is constant in Fig. 13; in fact, u_{a1} is generally higher in magnitude than u_{a2}. This latter observation also holds for Fig. 12 where Γ_a is periodically corrugated. In either figure, u_a is also perfectly periodic with respect to x/L: the periodic profiles of its components, however, are more complicated than those shown in Figs. 10 and 11.

Finally in this series of calculations, Figs. 14 and 15 show the computed values of u_a when the incident field is modified to

$$u^i(r) = (1/k_p)[\nabla H_0(k_p r)] \cdot \sum_{|n| \le \infty} \{\delta(\kappa - 1 - 2n\pi/L) + \delta(\kappa + 1 - 2n\pi/L)\}, \tag{29}$$

in order to consider a non-zero value of κ : $|\kappa| \le \pi/L$. It is clear from both of these figures that the plots of u_a are certainly more complicated than those of the previous four figures. Bunching is apparent in all of the plots, the most dramatic occurrence being in the graph of u_{a1} in Fig. 15 which is not unlike an amplitude-modulated sinusoid so familiar to students of radio communication. As expected by now, bunching is more diffused in Fig. 14 due to the presence of inter-modal interactions when Γ_a is periodically corrugated.

Thus, it appears that any non-zero value of κ in the field expansion (12) creates the data bunching in Figs. 8 and 9. This becomes even more accentuated when contributions from all κ : $|\kappa| \le \pi/L$ and corresponding modes $\kappa_n(\kappa)$, $|n| \le \infty$, are added up; a further effect due to the diffraction from the periodicity of Γ_a (or Γ_b) serves only to diffuse the bunching. Furthermore, since the P-wave line source, by itself, is an isotropic radiator, in u^i

are present all spatial frequencies ($\kappa : |\kappa| \leq \infty$) [Goodman, 1968], having the same amplitude but differing in phase when starting out from r_p. Therefore, in the present context, there is no likelihood that u_a will eventually decay down uniformly for some relatively small values of $\pm x/L$ on Γ_a, as can be observed from the range $|x/L| \leq$ 100.0 of Figs. 8 and 9. Parenthetically, it is noted here that were the line source to be an uni-directional radiator, radiating out both P and SV waves, then u_a would decay down uniformly to some mean value (zero or otherwise) at some reasonably small values of $\pm x/L$. This conclusion has been drawn also by Fokkema [1979] for the case when the media on either side of Γ_b are identical.

The last data set computed is shown in Figs. 16 and 17 where $|u_{a1}|$ and $|u_{a2}|$, respectively, have been plotted against the normalized frequency $k_p L$ for some selected locations $\pm x/L$ on Γ_a. The wave velocities in, and the densities of, the two media involved are the same as in Fig. 2; and Γ_a is either sinusoidally corrugated ($b/L = 0.05$) or flat ($b/L = 0.0$). At $x = 0$, u_{a1} is identically zero, for which reason the latter has not been plotted in Fig. 16. From these graphs it is observed that generally u_a decreases in magnitude as $|x/L|$ and $k_p L$ become quite large. This is not surprising, and for the following reason: at any location r, the incident field u^i of Eq. (9) possesses variations of the kind $|r - r_p|^{-1}$, $|r - r_p|^{-2}$, $|r - r_p|^{-3}$,..... When r is far away from the source location r_p, then the only pertinent variation of u^i is $|r - r_p|^{-1}$, the field magnitude decaying inversely with the distance $|r - r_p|$. But when r gets closer to r_p, then the higher order variations also become significant, and the field amplitude can become quite large [Lakhtakia and Iskander, 1983; Lakhtakia et al., 1984a]. This means that although the line source radiates a fixed amount of power, at larger distances from it, its radiated field can be quite small, while close to it, the field magnitude can be very high. Furthermore, the near-zone (i.e., the zone in which the higher-order variations of the incident field are significant) has a larger expanse when the frequency is small, and vice versa. Hence, the observation just made from Figs. 16 and 17.

In conclusion, a method based on the extended boundary condition method has been described here to compute the radiation characteristics of an elastodynamic, isotropic line source embedded in layered media with periodically varying interfaces. Since it is a matrix approach, it is computationally more tractable than a procedure involving the solution of integral equations. Although the specific problem solved here is quite simple, it is an effective example of a wide class of problems, and the presented approach can be used with profit for solving them. Because of the specific expansion (17) used for the surface field on Γ_a, one limitation of this method is that the maximum slopes of the corrugated interfaces may not exceed 0.448. This limitation is often

called the Rayleigh hypothesis [Millar, 1973] and, though it has been overcome for the simpler, scalar scattering formulations [Lakhtakia *et al.*, 1985b; 1985c; Cain *et al.*, 1986; Varadan *et al.*, 1986], efforts still need to be directed for the elastodynamic problems so as to be able to handle more deeply corrugated surfaces. A number of numerical results have also been shown here to illustrate the specific features of the radiation problem. Again, with the help of this procedure, it is hoped that a wide variety of radiation phenomena can be explained or understood.

REFERENCES

Abramowitz, M. and I.A. Stegun (1972). *Handbook of Mathematical Functions*, New York: Dover.

Achenbach, J.D. (1973). *Wave Propagation in Elastic Solids* Amsterdam: North-Holland.

Barber, P.W. and C. Yeh (1975). Scattering of electromagnetic waves by arbitrary shaped dielectric bodies, *Appl. Opt.*, 14, 2864.

Cagniard, L., E.A. Flinn and C.H. Dix (1962). *Reflection and Refraction of Progressive Seismic Waves*, New York: McGraw-Hill.

Cain, W.N., V.K. Varadan, V.V. Varadan and A. Lakhtakia (1986). Reflection and transmission characteristics of a slab with periodically varying surfaces, *IEEE Trans. Antennas Propagat.*, 34, 000 (in press).

Clemmow, P.C. (1956). *The Plane Wave Spectrum Representation of Electromagnetic Fields*, New York: Pergamon.

Fokkema, J.T. (1979). *Reflection and transmission of time-harmonic elastic waves by the periodic interface between two elastic media*, Ph.D. thesis, Delft University of Technology, Delft, The Netherlands.

Goodman, J.W. (1968). *Introduction to Fourier Optics*, New York: McGraw-Hill.

Lakhtakia, A. and M.F. Iskander (1983). Scattering and absorption characteristics of lossy dielectric objects exposed to the near fields of aperture sources, *IEEE Trans. Antennas Propagat.*, 31, 111.

Lakhtakia, A., N. Sitaram, V.K. Varadan and V.V. Varadan (1984a). Post-resonance scattering by lossy dielectric biological targets: Point dipole sources, *Innovation Technol. Biol. Med.* (Lille, France), 5, 417.

Lakhtakia, A., V.K. Varadan, V.V. Varadan and D.J.N. Wall (1984b). The T-matrix approach for scattering by a traction-free periodic surface, *J. Acoust. Soc. Am.*, 76, 1839.

Lakhtakia, A., V.K. Varadan and V.V. Varadan (1985a). The acoustic response of a periodically rough elastic plate (ice) in contact with water, *ASME J. Appl. Mech.*, 52, 144.

Lakhtakia, A., V.K. Varadan and V.V. Varadan (1985b). A T-matrix approach for EM scattering by a perfectly conducting periodic surface, *Proc. IEEE*, 73, 1238.

Lakhtakia, A., V.K. Varadan and V.V. Varadan (1985c). On the acoustic response of a deeply-corrugated periodic surface -- A hybrid T-matrix approach, *J. Acoust. Soc. Am.*, 78, 2100.

Millar, R.F. (1973). The Rayleigh hypothesis and a related least - squares solution to scattering problems for periodic surfaces and other scatterers, *Rad. Sci.*, 8, 785.

Phynney, R.A. (1961). Propagation of leaking interface waves, *Bull. Seismol. Soc. Am.*, 51, 527.

Tan, T.H. (1975). Far-field radiation characteristics of elastic waves and the elastodynamic radiation condition, *Appl. Sci. Res.*, 31, 363.

Varadan, V.K., A. Lakhtakia, V.V. Varadan and C. A. Langston (1986). Radiation characteristics of elastodynamic line sources buried in layered media with periodic interfaces. I - SH wave analysis, *Bull. Seismol. Soc. Am.* (submitted).

Waterman, P.C. (1971). Symmetry, unitarity, and geometry in electromagnetic scattering, *Phys. Rev. D*, 3, 825.

Waterman, P.C. (1975). Scattering by periodic surfaces, *J.Acoust. Soc. Am.*, 57, 791.

Yamaguchi, R. and Y. Sato (1955). Stoneley wave - Its velocity, orbit and the distribution of amplitude, *Bull. Earthquake Res. Inst.* (Tokyo Univ.), 23, 549.

Fig. 1 Schematic of the problem to be solved.
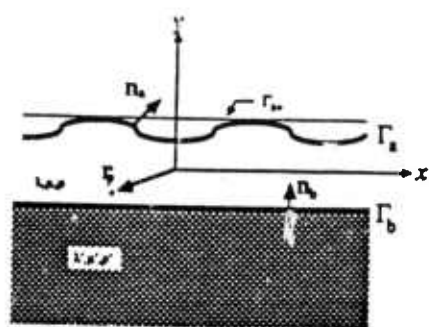
Fig. 2 Far-zone P wave (-•-•-•-) and SV wave (———) radiated amplitudes, in the lower half-space, due to the P-wave line source located at r_p = (0,0). These amplitudes are drawn as functions of θ, $|\theta| \leq 90$ deg, the angle with respect to the -y axis. The surface Γ_a is specified by y = a - b cos($2\pi x/L$) while Γ_b is the plane y = - d. The relevant parameters are c_p = 3500 m s^{-1}, c_s = 6000 m s^{-1}, ρ = 2700 kg m^{-3}, c'_p = 4500 m s^{-1}, c'_s = 8000 m s^{-1} and ρ' = 3200 kg m^{-3}; while a/L = d/L = 1.0 and b/L = 0.05. The normalized frequency (a) k_pL = 5.0, (b) k_pL = 7.5 and (c) k_pL = 10.0.
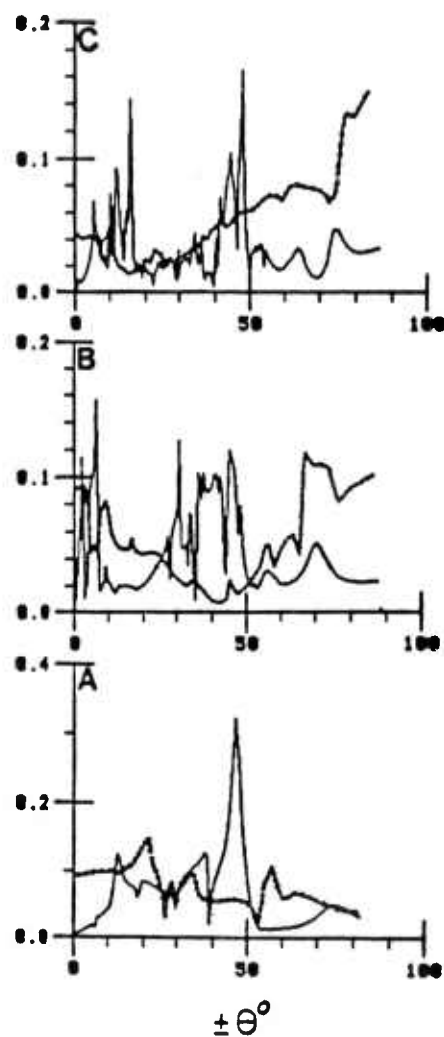
Fig. 3 Same as Fig. 2, except for b/L = 0.0.
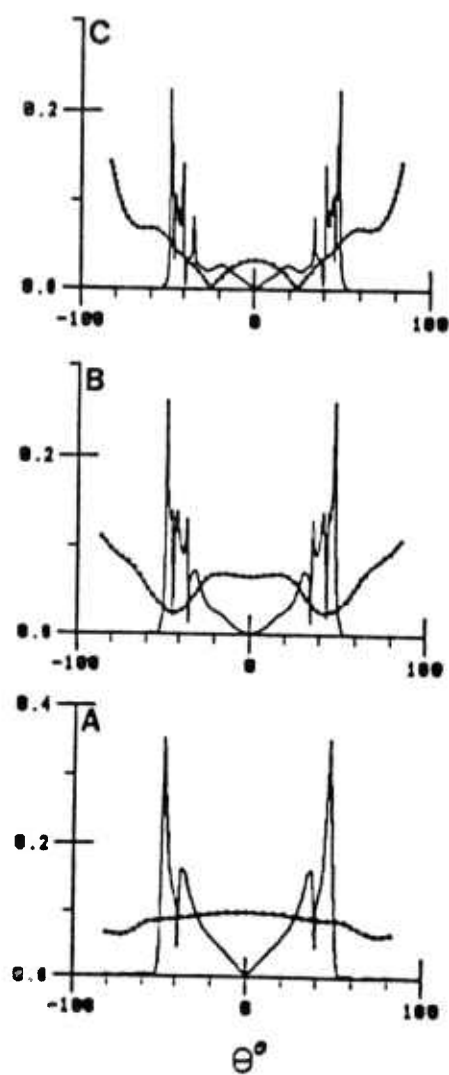
Fig. 4. Far-zone P wave (-•-•-•-) and SV wave (——) radiated amplitudes, in the lower half-space, due to the P-wave line source located at r_p = (0,0). These amplitudes are drawn as functions of θ, |θ| ≤ 90 deg, the angle with respect to the -y axis. The surface Γ_a is specified by y = a - b cos(2πx/L) while Γ_b is the plane y = - d. The relevant parameters are c_p = 3500 m s^{-1}, c_s = 6000 m s^{-1}, ρ = 2700 kg m^{-3}, c'_p = 4500 m s^{-1}, c'_s = 8000 m s^{-1} and ρ' = 3200 kg m^{-3}; while (a+d)/L = 2.0, b/L = 0.05, and the normalized frequency $k_p L$ = 7.5; (a) a/L = 1.0 and (b) a/L = 0.5.
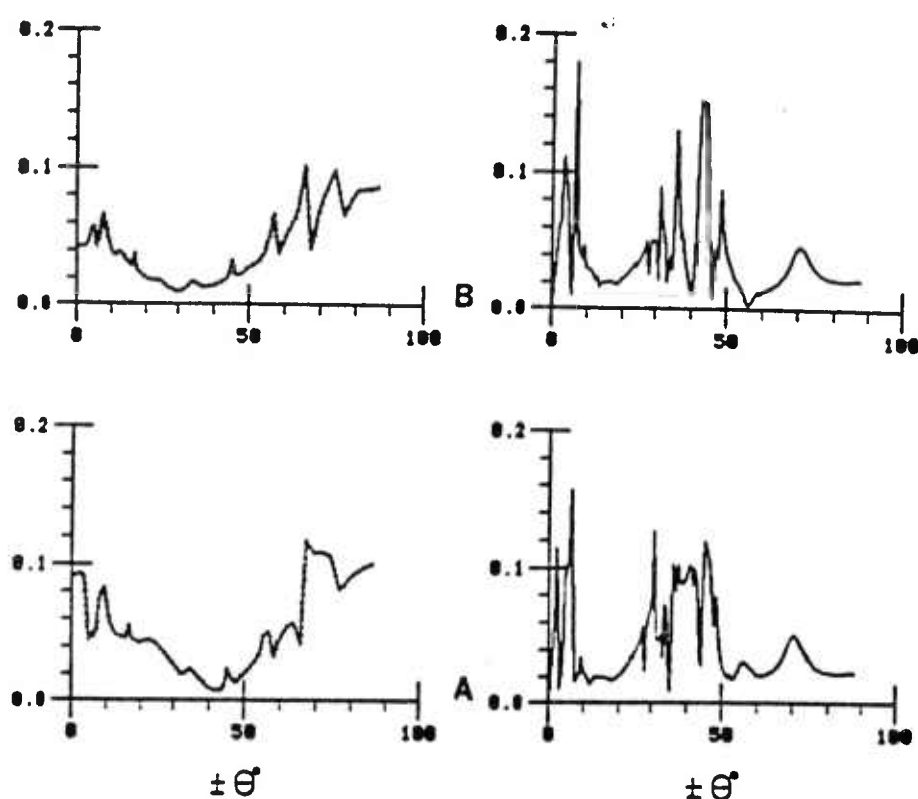
Fig. 5 Same as Fig. 4, except for $c'_p = 3500$ m s^{-1}, $c'_s = 6000$ m s^{-1} and $\rho' = 2700$ kg m^{-3}.
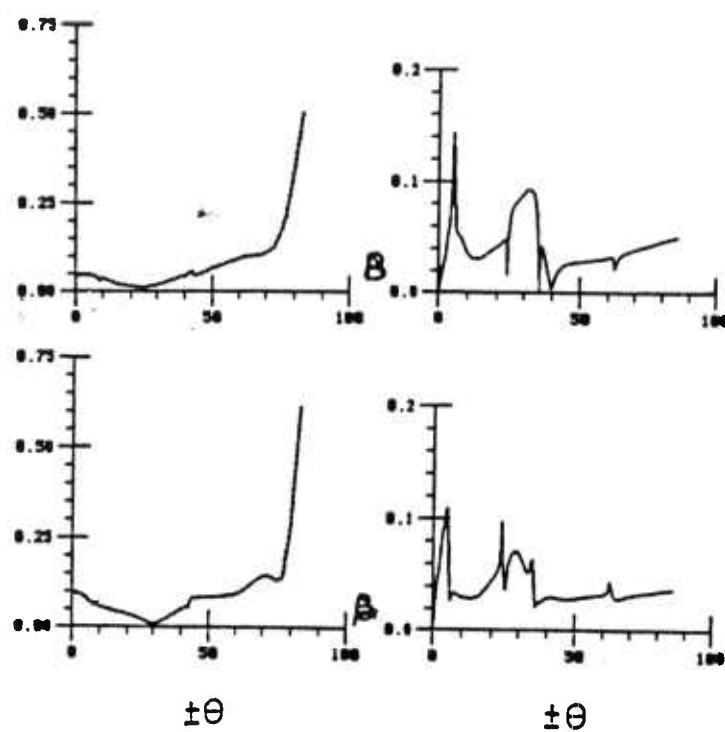
Fig. 6 Same as Fig. 4, except for b/L = 0.0.
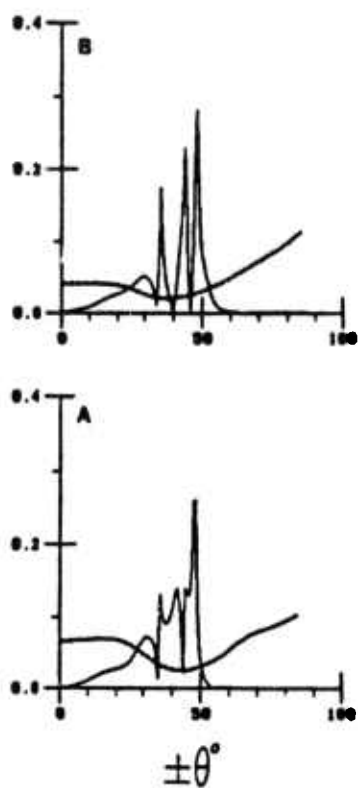
Fig. 7 Same as Fig. 5, except for b/L = 0.0.
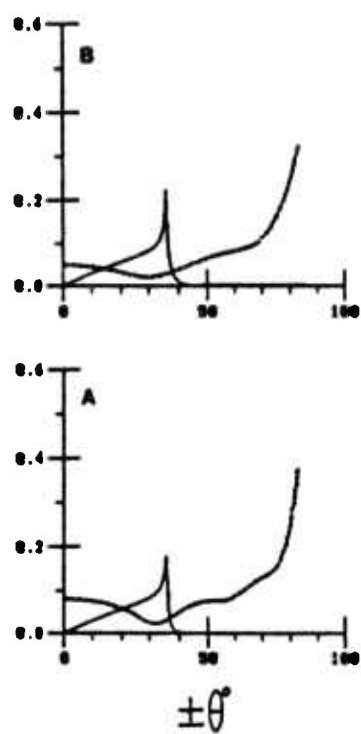
Fig. 8 Computed values of the surface displacement u_a as function of the distance x/L along the sinusoidally corrugated Γ_a. The line source is located at $r_p = (0,0)$; $a/L = d/L = 1.0$; $b/L = 0.05$; and $k_p L = 7.5$. The other relevant parameters are $c_p = 3500$ m s^{-1}, $c_s = 6000$ m s^{-1}, $\rho = 2700$ kg m^{-3}, $c'_p = 4500$ m s^{-1}, $c'_s = 8000$ m s^{-1} and $\rho' = 3200$ kg m^{-3}.
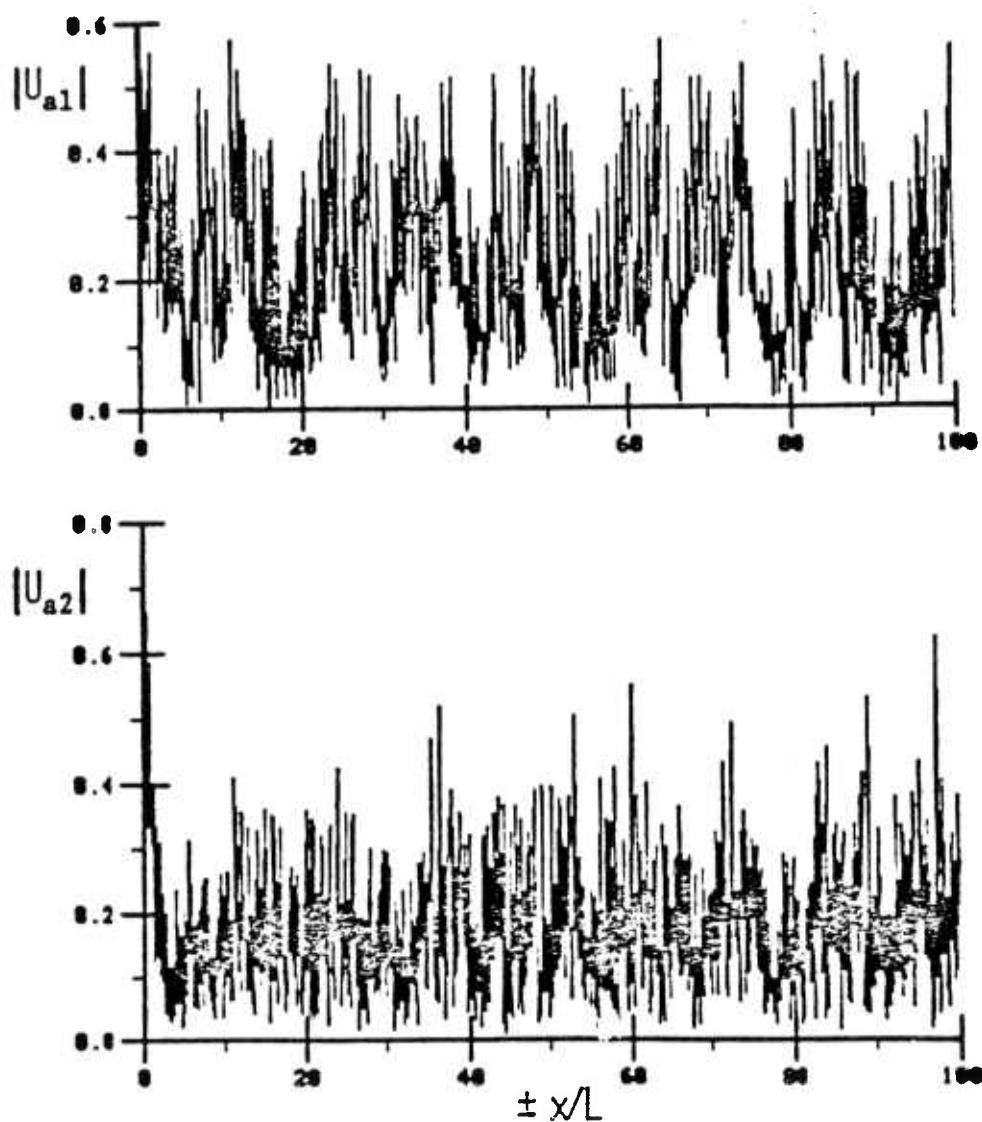
Fig. 9 Same as Fig. 8, except b/L = 0.0.
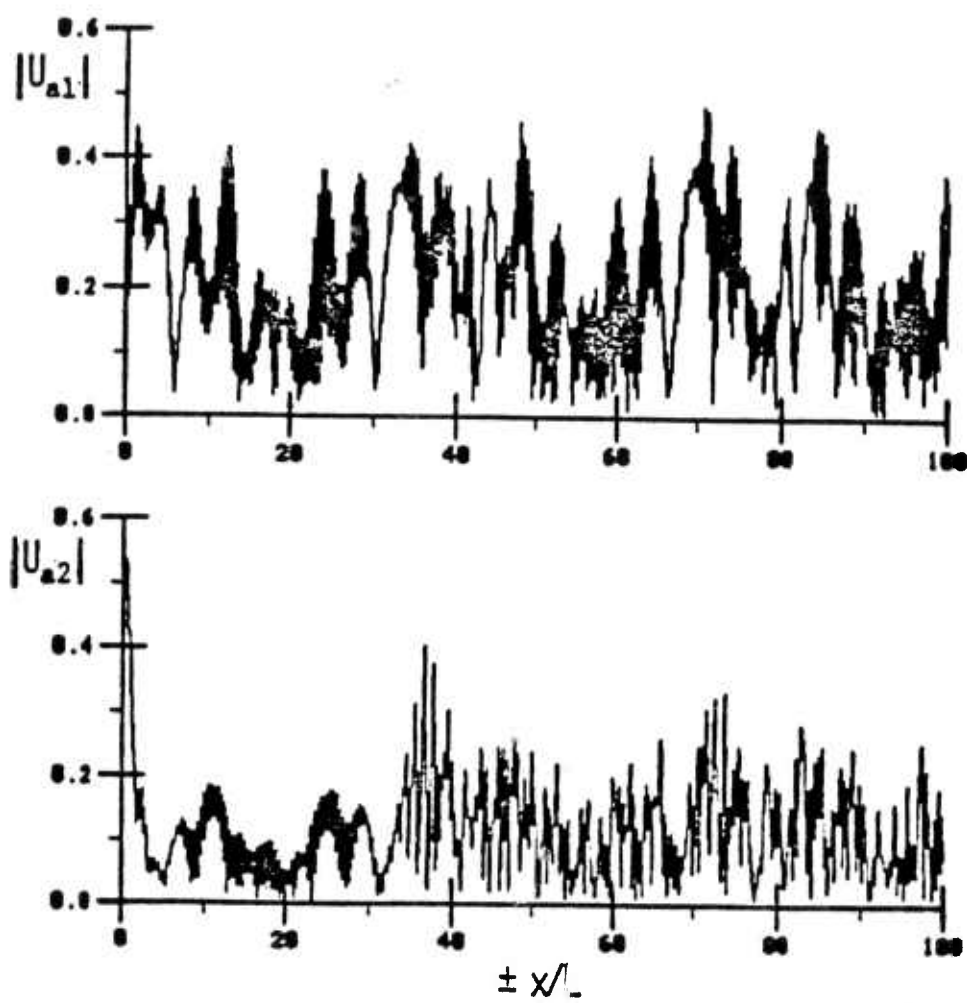
Fig.10 Same as Fig. 8, except Eq. (29) is used in place of Eq. (10) for the incident field.
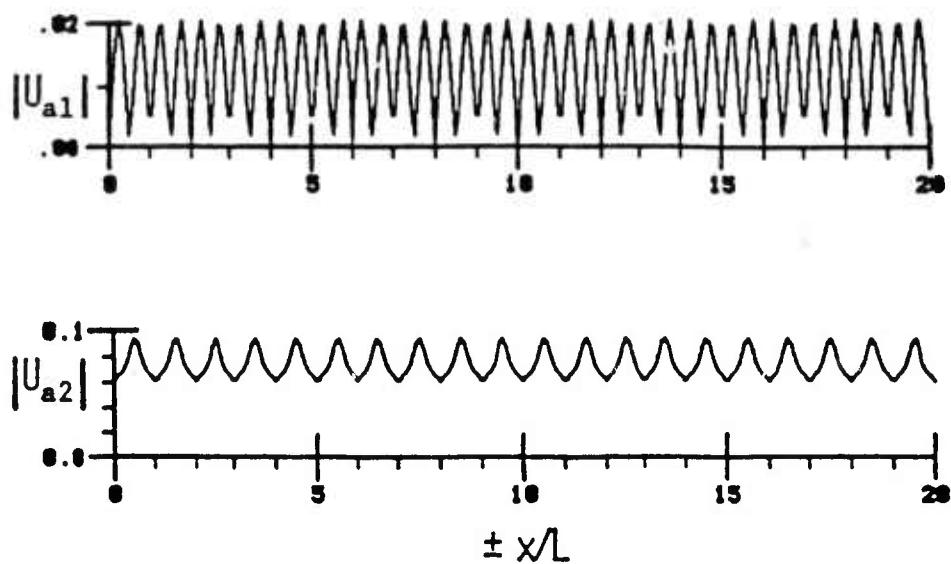
Fig.11 Same as Fig. 9, except Eq. (29) is used in place of Eq. (10) for the incident field.
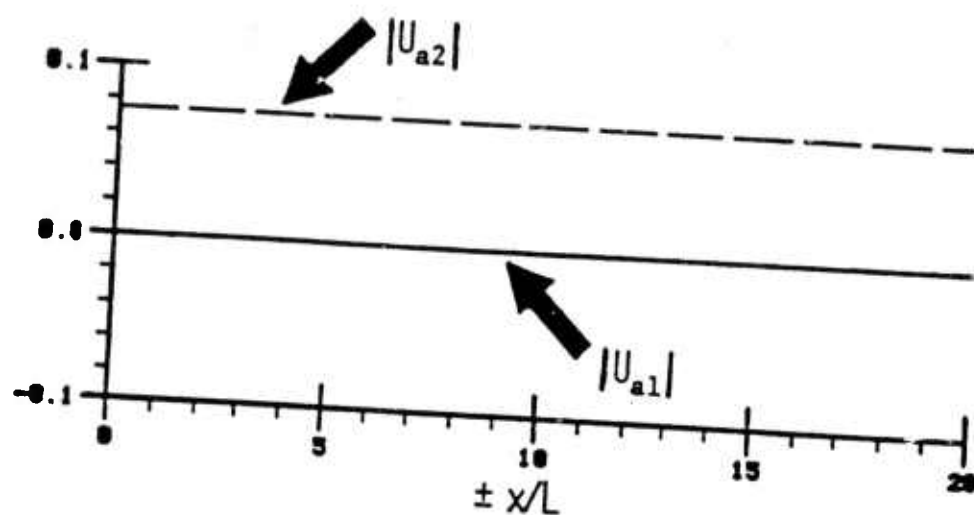
Fig.12 Same as Fig. 8, except Eq. (30) is used in place of Eq. (10) for the incident field.
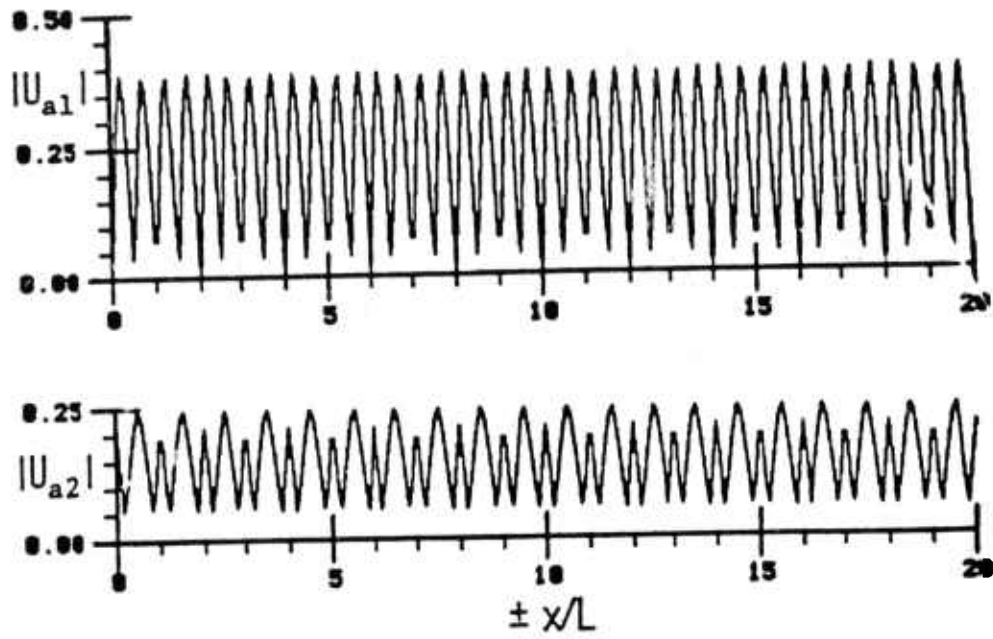
Fig.13 Same as Fig. 9, except Eq. (30) is used in place of Eq. (10) for the incident field.
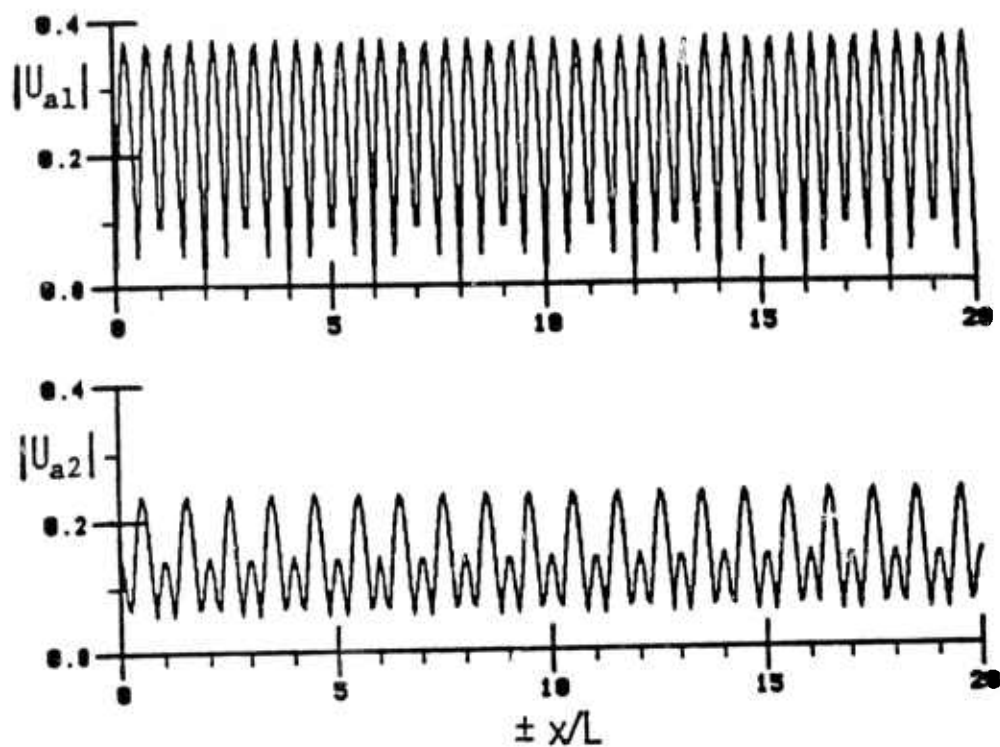
Fig.14 Same as Fig. 8, except Eq. (31) is used in place of Eq. (10) for the incident field.
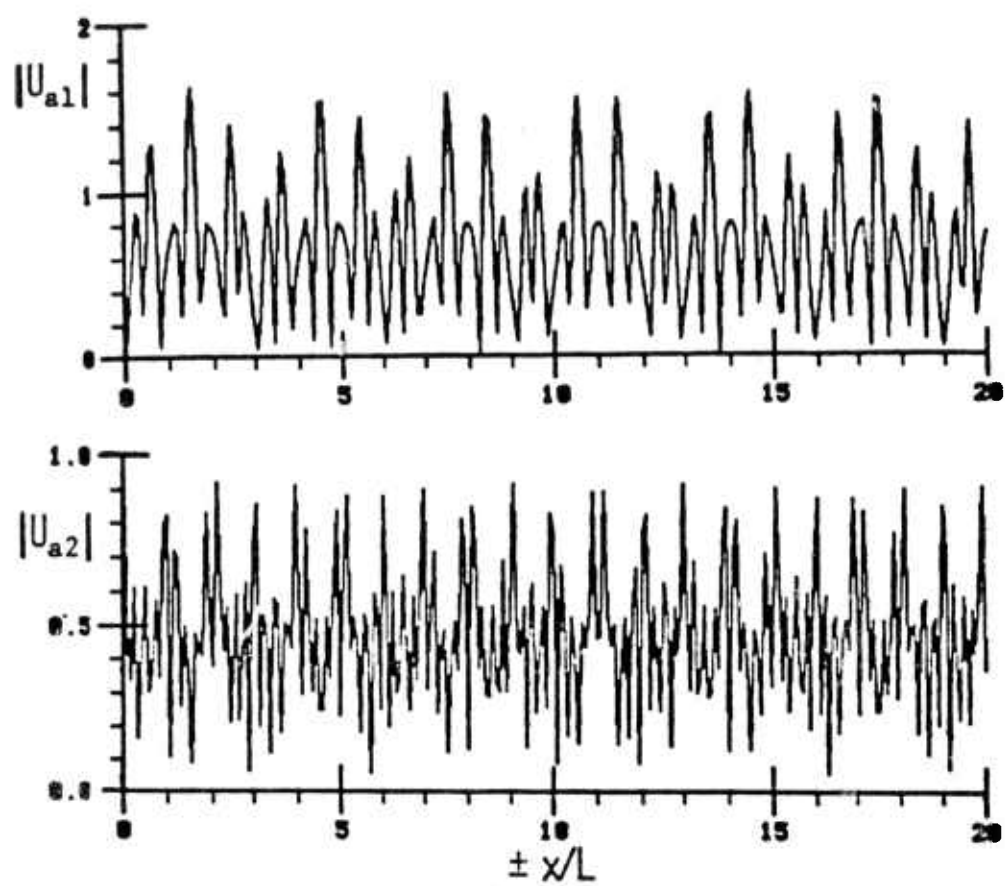
Fig.15 Same as Fig. 9, except Eq. (31) is used in place of Eq. (10) for the incident field.
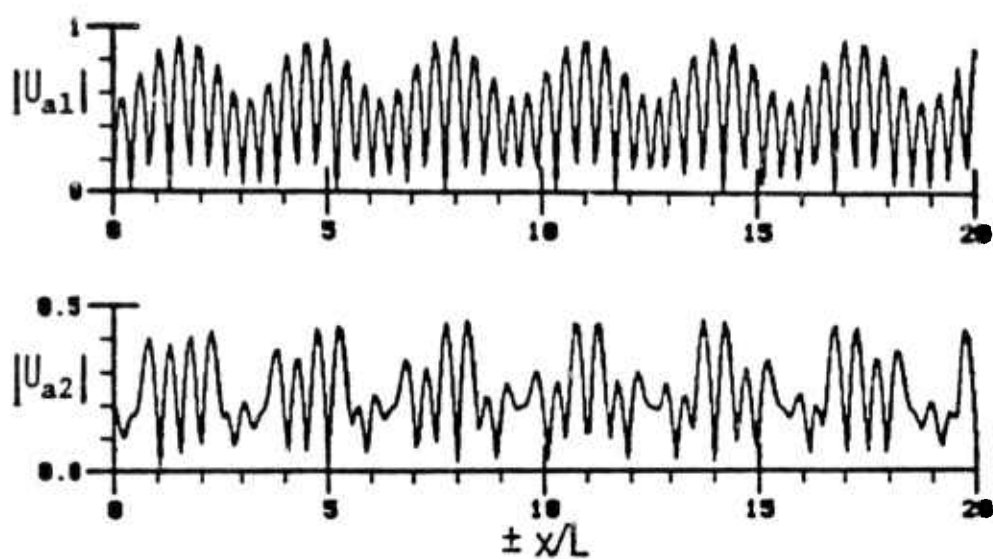
Fig.16 Computed values of the surface displacement component u_{a1} as function of the normalized frequency k_pL at several distances x/L along the sinusoidally corrugated Γ_a. The line source is located at $r_p = (0,0)$; $a/L = d/L = 1.0$; $b/L = 0.05$ (——) and $b/L = 0.0$ (-·-·-·-). The other relevant parameters are $c_p = 3500$ m s^{-1}, $c_s = 6000$ m s^{-1}, $\rho = 2700$ kg m^{-3}, $c'_p = 4500$ m s^{-1}, $c'_s = 8000$ m s^{-1} and $\rho' = 3200$ kg m^{-3}. (a) $x/L = \pm1.0$; (b) $x/L = \pm5.0$; (c) $x/L = \pm10.0$; (d) $x/L = \pm100.0$.
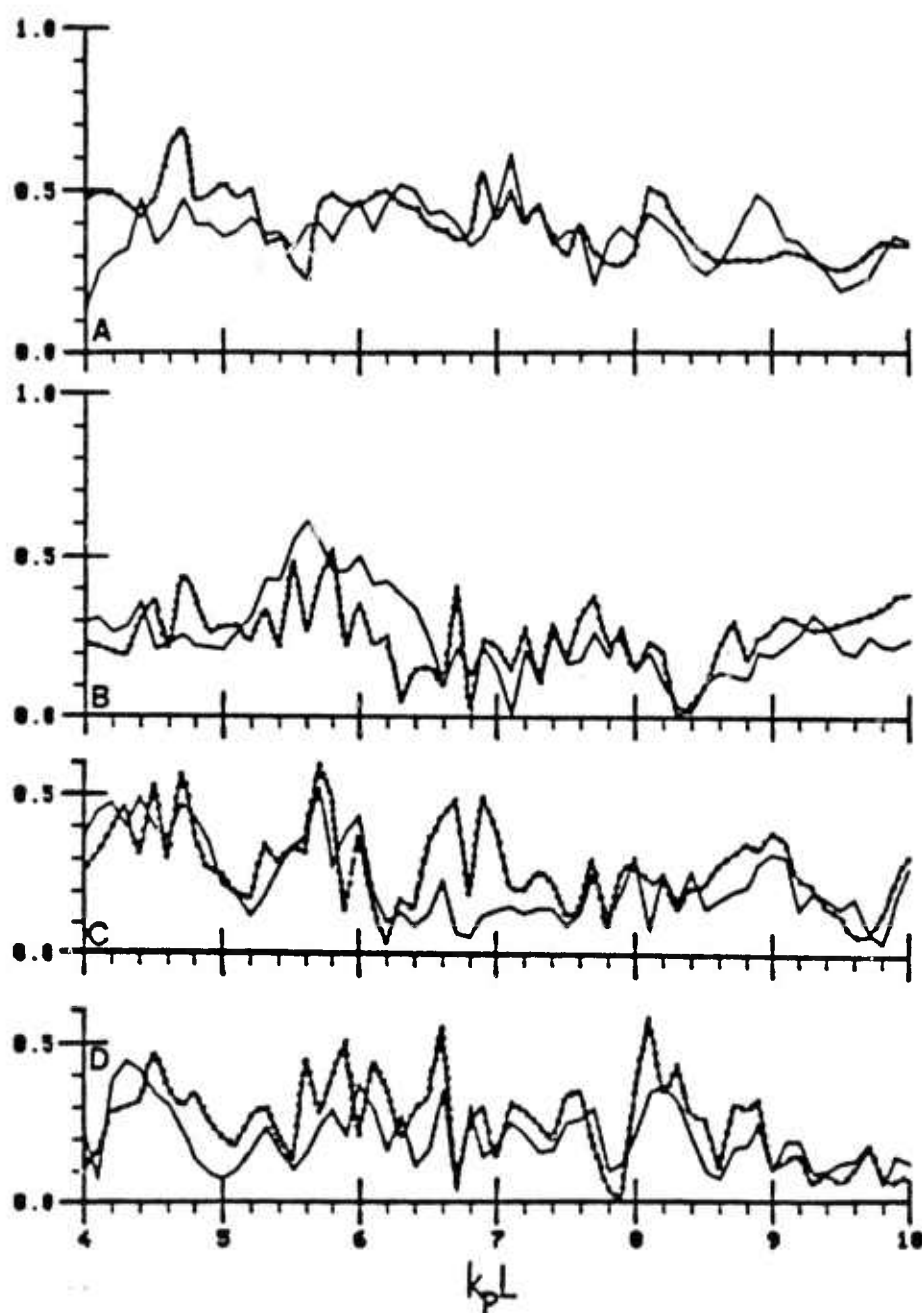
Fig.17 Computed values of the surface displacement component u_{a2} as function of the normalized frequency $k_p L$ at several distances x/L along the sinusoidally corrugated Γ_a. The line source is located at $r_p = (0,0)$; $a/L = d/L = 1.0$; $b/L = 0.05$ (———) and $b/L = 0.0$ (-·-·-·-). The other relevant parameters are $c_p = 3500$ m s^{-1}, $c_s = 6000$ m s^{-1}, $\rho = 2700$ kg m^{-3}, $c'_p = 4500$ m s^{-1}, $c'_s = 8000$ m s^{-1} and $\rho' = 3200$ kg m^{-3}. (a) $x/L = 0.0$; (b) $x/L = \pm 5.0$; (c) $x/L = \pm 10.0$; (d) $x/L = \pm 100.0$.
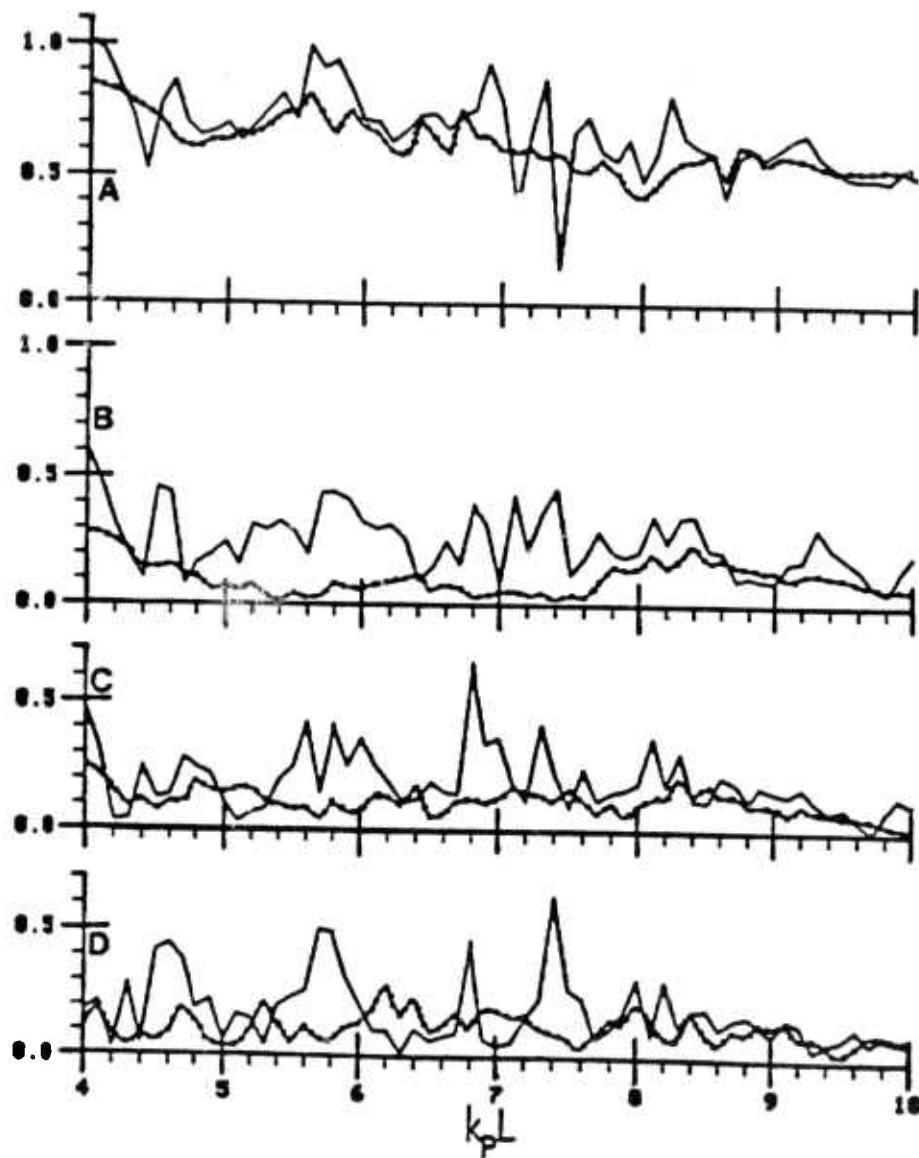
SECTION 5

The Meckering Earthquake of October 14, 1968.

A Possible Downward Propagating Rupture.

by

Kristín S. Vogfjörd and Charles A. Langston

Department of Geosciences

The Pennsylvania State University

University Park, PA 16802

ABSTRACT

Average source parameters of the 1968 Meckering,
Australia earthquake are obtained by the inversion of body
waves. The objectives of the inversion are the elements of
the moment tensor and the source time history. An optimum
source depth of 3 km is determined, but because of source
complexity the point source assumption fails and the moment
tensor obtained at that depth has a large non-double-couple
term, CLVD = 34 %. The source parameters of the major
double-couple are : strike 341^0, dip 37^0, rake 61^0 and
seismic moment 8.2×10^{25} dyne-cm. The source time function
is of approximately 4 seconds duration, with a long rise
time and a sharp fall-off. The fault length is constrained
on the surface by the observed surface break and results
from vertical displacement modeling suggest a width of
approximately 10 km in the middle, assuming a dip of 37^0.
That restricts the entire faulted area to lie above 6 km
depth. Two finite fault models for the earthquake are
presented, with rupture initiating at a point 1) near the
top of the fault and 2) at the bottom of the fault. Both
models produce similar long period synthetics, but based on
the short period waveforms, model 1 is favored. It is
argued that such a rupture process is the most reasonable in
this cold shield region.

I. Introduction

Seismic activity in Australia is low in comparison to all other continents excluding Antarctica. However, several zones of considerable activity have been identified, with earthquakes located mainly within the upper crust (Doyle et al. 1968). One such region is the South West Seismic Zone, a NNW trending belt of seismic activity that cuts across the south west corner of the Australian continent. This seismic zone is in an area of relatively flat topography and is not associated with any major tectonic features, such as a mountain belt or through going faults. It extends across the corner of the Archaean Yilgarn Block, which is the oldest part of the Precambrian shield, and crosses the enormous dip-slip Darling Fault that marks the shield's western boundary (Doyle et al., 1968). No earthquakes have been observed on the Darling Fault, which apparently has been inactive since the Pliocene (Doyle, 1971). A map of the area is shown in Figure 1. There is some geophysical evidence that indicates changes in crustal structure across the Seismic Zone. Bouguer gravity contours trend parallel to it, with gravity increasing towards the shield boundary (Haxby et al., 1983). Seismic crustal studies reveal the existence of a high velocity basal layer, possibly eclogite under the south west corner of the shield. This layer which is confined to the Yilgarn Block thickens towards the shield boundary, where the crust becomes abnormally thick (Mathur,

1974 ; Drummond, 1979). Most of the seismicity in the region is of low magnitude, yet two of Australia's largest earthquakes were located within this seismic zone. One occured in 1941 and was located in the northern part of the zone, the other was the Meckering earthquake, which occured on October 14, 1968.

The Meckering earthquake was a moderate-sized intraplate event with a surface wave magnitude of 6.8 and a very shallow source depth, 1 km as determined by the USCGS. The epicenter was located near the small town of Meckering which was destroyed in the earthquake (Everingham et al., 1969). This event is of special interest because of its location in Archaean shield within the South West Seismic Zone. Also it is one of a few intraplate earthquakes known to be accompanied by large scale surface thrust faulting. The near semicircular appearance of the fault scarp is also quite unusual. The surface faulting accompanying the earthquake and its aftershocks extends over a 200 km^2 area which is largely covered by several meters of sand and clay. Faulting is not exposed in the underlying bedrock which consists mainly of deeply weathered granite and gneiss (Gordon, 1971). The largest fault is the Meckering fault, a 37 km long arcuate fault scarp (see Figure 1) concave to the east and dipping about 40^0 inward (Gordon, 1971). This fault was not shown on any structural maps of the region, prior to the earthquake. However, Gordon and Lewis (1980) report findings of iron stained fault breccia on the fault,

and during the mapping of the fault scarp a correlation was noted between the fault trace and frequent quartz scatter, or iron-rich reddish soil. This they interpreted as indications of a preexisting fault. The displacement on the fault is in the reverse-dextral sense with the eastern side uplifted and thrust over the western side. It is greatest near the middle and decreases towards the ends. The measured throw in the middle is about 2 m, the heave about 2.4 m, and the dextral movement about 1.5 m (Gordon, 1971).

Stress measurements made in the area after the earthquake, at depths less than 10 m (Denham et al., 1980) indicate a high level of horizontal compressive stress in the upper crust, with the average direction of maximum principal stress about N77E. The lowest compressional stress was measured near the earthquake's epicenter, approximately 40 bars and increased with distance away from it, up to approximately 230 bars 90 km north of Meckering. This large horizontal compressive stress is the probable cause of the earthquake and assuming that the difference in stress is due to the stress relieved by the earthquake, it would imply a stress drop of about 100 bars. The dominance of compression observed in the Australian continent can be generated by plate tectonic forces acting on the Indian-Australian plate (Cloetingh and Wortel, 1985). However, the compressional direction predicted for Western Australia does not agree with the observed direction, which may therefore be caused by regional effects. The proximity

to the continental margin, which has experienced several kilometers of normal offset along the Darling Fault, may be an influence.

The objective of this study is to gain some insight into the stress condition existing in the upper crust of the Precambrian shield. The state of stress can be deduced from the source mechanism of the Meckering earthquake, which is determined by use of seismic and static uplift data. A linearized inversion of body waves is performed to obtain a moment tensor and time function for the event, then the measured ground displacement is modeled by elastic dislocation theory to obtain some information about fault dimensions, dip and displacement. Finally, forward modeling is attempted using finite-fault dislocation models. Results from two different fault models are presented.

Previous work on this earthquake includes a first motion body wave study by Fitch et al. (1973) to obtain a double-couple solution. They favored reverse-sinistral motion on a fault plane striking 332° and dipping 68°W, with a seismic moment of 6.1×10^{25} dyne-cm. This is not consistent with the dip and reverse-dextral displacement indicated by the surface rupture. A small foreshock with a different mechanism that occured about 3.5 seconds before the main shock may have affected their results such that first arrivals at some stations were incorrectly chosen. This study offers an improvement to their results by providing a focal mechanism that is in better agreement with

the observed surface displacement.

II. Body Wave Inversions

Long and short period seismograms from WWSSN stations in the teleseismic range were digitized for the purpose of this study. The strong interference evident at the beginning of these records suggests a very shallow source depth, $\leq$ 7 km. The long period seismograms were used to obtain the moment tensor and source time function for the earthquake, by applying an iterative, generalized inversion procedure, which is described in Langston (1981) and Barker and Langston (1982). Short period seismograms were not included in the inversion. The data chosen for the inversion consisted of 20 P and 5 SH waves with distance distribution in the teleseismic range. The azimuthal coverage was deficient in southern azimuths. These data were sampled at 1 sample per second and windowed to include about 16 seconds after the P wave onset and about 20 seconds after the SH wave onset.

Green's functions for a point source with step dislocation in a plane-layered medium were calculated at several different source depths by the ray theory method of Langston and Helmberger (1975). A three layered crustal model was used, based on the results of Mathur's (1974) seismic and gravity study in South West Australia. The

model is presented in Table 1. Responses from 73 P rays and
18 SH rays, which included all significant arrivals within
the first 30 seconds were calculated and summed up. The
responses were then convolved with the WWSSN 15-100
instrument response, and an attenuation operator with $t^* =$
1.0 for P waves and $t^* = 4.0$ for S waves. The source time
function was parameterized as a series of weighted boxcars,
each of 1 second duration.

Inversions for the moment tensor and six time function
elements were performed with the source at 2 km intervals in
the depth range of 1 - 7 km. Five iterations were performed
at each depth but convergence was usually obtained within
three. In this study, the parameters were not weighted and
the covariance matrix for the data was assumed to be the
identity matrix. A cut-off value specifying the maximum
allowable variance of the parameter changes was set to be
0.3. With that choice, all parameters were well resolved
and a unique solution obtained. The condition numbers for
the inversions were between 60 and 100.

The final moment tensor is decomposed into a major
double-couple, which is the average of the maximum and
minimum principal components and a remainder, which is the
compensated linear vector dipole, or CLVD. The relative
size of the CLVD can be a measure of the complexity of the
source, although a large CLVD component can also be an
indication of deficiencies in the model. Other indicators
of the performance of the inversion are the RMS error, which

measures the fit of the synthetics to the data, and the least squares error which is a measure of the quality of the inversion. Figure 2 a) shows the variation of the CLVD with depth. It is quite large at all depths, although it decreases rapidly as the source depth approaches the surface. Figure 2 b) shows the change in RMS error with source depth and in Figure 2 c), the variation of the least squares error with depth is shown. Although resolution is not good, especially in the RMS error, they both have minima at 3km depth.

Incorrect assumptions made in calculating the Green's functions, such as source depth and the value of t^* can be compensated by changes in the source time function, to produce the same synthetics. An error in t^* is compensated by the length of the source function, and deviations from the correct source depth add complications to the source function. The simplest time function therefore corresponds to the best estimate of the source depth (Christensen and Ruff, 1985). The inversion time functions for various source depths are plotted in Figure 3, where the simplest time functions result from the 3 km and 5 km source depths, and the deepest source at 6.9 km produces a periodically oscillating time function, indicating that the actual source depth has been exceeded. These results combined with the minima in the least squares and the RMS error indicate a source depth of approximately 3 km. The duration of the time function was not known in advance, so in order to avoid

truncating it the number of boxcar elements inverted was greater than necessary. The last elements may therefore be attributed to noise in the data, leaving approximately a 4 second long triangular time function with a long rise time and a sharp fall-off.

The inverted P and SH waveforms and the resulting synthetics for a source depth of 3 km are plotted in Figures 4 and 5, respectively. The waveforms are normalized to their maximum amplitude, which is shown to the right of each trace (in microns). The synthetics show a good fit at most stations, both in amplitude and overall waveform shape within the inversion window for P and SH waves alike. Large later arrivals, which are mainly crustal reverberations are not as well matched. The amplitudes of these arrivals in the synthetics are generally too small. The first P arrival is compressional at all stations except WIN, PRE and BUL, where it is nodal, but the model does not predict these correctly since the synthetics have a compressional first motion at these stations. However, the first motion of the synthetic SH wave at PRE is correctly predicted. The small foreshock, visible in some of the P wave seismograms approximately 3.5 seconds before the arrival of the main shock, is not within the inversion window and therefore does not show up in the synthetics.

Stations with large amplitudes had a higher importance in the inversion and were therefore preferentially fit by the synthetics; weighting the data equalized the importance,

but that did not change the results significantly. Weighting
the time function elements by a factor of 0.01 relative to
the moment tensor elements lowered the condition number
below 10, but produced the same results as before.

The moment tensor obtained in the inversion for a 3 km
source depth, along with the time function elements and the
standard error (σ) of the parameter changes is given in
Table 2. The nodal surfaces of the moment tensor and its
major double-couple are plotted on a lower hemisphere equal
area projection in Figures 4 and 5 , for P and SH waves,
respectively. First motion polarities of the inverted
waveforms and the principal axes of the moment tensor are
also shown on the same plots. The pressure axis is almost
horizontal and directed east-west (Az = 271^0), the same
direction as that obtained in the first motion study (Fitch
et al., 1973), and in fair agreement with the N 77^0 E
direction obtained from stress measurements (Denham et al.,
1980). The seismic moment, determined by dividing the
modulus of the moment tensor by $\sqrt{2}$ is 8.52 x 10^{25} dyne-cm
and the fault parameters of the major double-couple are :
strike (θ) = 340.7^0, dip (δ) = 36.7^0 and rake (λ) = 61.2^0.
The directional variation of the pressure axis with source
depth is very little, but there is no constraint on the
plunge of the intermediate and tension axes at 5 and 7 km
source depths. To decrease the orientational variations in
those two axes at depths below 3 km, the data can be
weighted to equalize the importance of the seismograms. The

orientations thus obtained are better constrained and give a near vertical tension axis.

The large non-double-couple term in the moment tensor indicates that the assumed point source model may be inadequate for determining the source mechanism, and a finite-sized source allowing rupture on a non-planar fault might have to be incorporated to explain the radiation pattern completely. In fact, the surface rupture strongly suggests a moment tensor with a changing source orientation. Lateral heterogeneity of the source region can also disturb the radiation pattern, so the proximity of the source area to the shield boundary where major lateral discontinuities occur is also of some concern. Therefore, the assumption of a homogeneous plane-layered source structure is likely to be the cause of some error in the solution, especially at stations in western azimuths.

III. The surface displacement

The surface deformation caused by the earthquake can be used to place some constraints on the fault's dimensions and dip. The static data available are presented in Figure 6 and consist of throw measurements on the fault scarp, and uplift measurements obtained from relevelling surveys of pipelines and the road to Meckering (Gordon, 1971). Also shown are the contours of equal uplift, which for lack of

data are estimated away from the fault scarp. The uplift is greatest near the middle of the fault, about 2 m and decreases towards the ends.

The surface displacement can be modeled by the use of static, elastic dislocation theory, where theoretical displacements are calculated by assuming a rectangular fault, embedded in an elastic half-space, and having constant displacement over the entire fault area. The expressions for the displacement fields resulting from strike-slip and dip-slip faults are given in indefinite integral form by Mansinha et al. (1971). The desired surface displacement is obtained by evaluating these expressions on the surface. The vertical surface displacement, calculated along the profile AA' in Figure 6 is compared to the contoured uplift, and the projection of the road uplift on AA'. The fault is assumed to be 20 km long, centered where the profile cuts across the fault scarp and striking perpendicular to AA'; length is defined as the horizontal dimension of the fault and width as the dimension down-dip. The uplift along the profile is not sensitive to variations in the fault length, so the correct assumption of length is not critical. The contribution of strike-slip motion to the vertical displacement along AA' is negligible, so a pure dip-slip can be safely assumed. With a dip of 37^0 to the east the best fit to the data is obtained with a dip-slip of 3.8 m and a fault width of 9.5 km. The calculated uplift fits the data reasonably well, as shown in

Figure 7.

The dip is not perfectly constrained by the data, but the true average dip must be close to the assumed value, because a greater fault dip would cause the negative displacements on the downthrown side to become more negative, and a smaller dip would have the same effect on the negative displacement on the eastern side. This is demonstrated in Figure 8, where the vertical displacements resulting from greater and lesser fault dips are plotted. The displacement is not constant on the fault and the dip may not be constant either, but the sparse dataset does not justify refinements of the theoretical model in order to fit the data in more detail. Therefore, these results indicate an actual fault width of approximately 10 km and an average dip of about 37^0 to the east. This places a depth constraint on the fault, namely that the faulted surface lies above 6 km. The fault length is constrained on the surface by the length of the surface break.

The seismic moment can be estimated from the slip and the fault dimensions, by use of,

$$M_0 = \mu \, U \, A$$

where μ is the rigidity, U is the average slip and A is the fault area. The slip is greatest in the middle and decreases towards the ends, so the average slip is about 2 m. With $\mu = 3.5 \times 10^{11}$ dyne/cm^2 and A = 200 km^2, the

resulting moment is 14×10^{25} dyne-cm which is nearly two
times the value obtained from the body wave inversion. This
difference suggests that roughly half of the energy released
in the earthquake excited the body waves and the rest may
have been released by slow slip on the fault after the
initial rupture phase, and or by the aftershocks.
Overestimated fault area can also be a factor. Using a
relation from Kanamori and Anderson (1975) for the stress
drop on a shallow dip-slip fault,

$$\Delta\sigma \approx \mu\ U\ /\ W$$

where W is the width of the fault, the stress drop is found
to be : $\Delta\sigma \approx 100$ bars. Fitch et al. (1973) obtained a
similar stress drop, although their estimate of displacement
(1.5 m) was too small and they assumed a fault width of only
5 km, which is half the width obtained in this study.

IV.   Finite Fault Models

An attempt was made to produce matching synthetics with
the use of finite fault models. The method, described in
Langston (1978) is identical to the method used to calculate
the Green's functions for the inversion, except for the
calculation of the source time function. A propagating
dislocation source with a given rupture velocity on a finite

fault is assumed. The dislocation at each point on the fault is described by a step function, delayed in time relative to the distance away from the initation of rupture, and the resulting source time function is the integral of the dislocation over the whole fault area. The source time functions thus computed differ for P and S waves, and for up- and downgoing rays from the initial source. Depending on the directivity, some variation with distance and azimuth may also occur in the source functions. In addition to the long period P waveforms used in the inversion, short period P waves were also included in this part of the study.

Because of the foreshock 3.5 seconds before the main shock and the shallow source depth, extreme interference makes it impossible to identify distinct phases in the short period seismograms; the P phase of the main shock is buried in the coda of the foreshock and the P, pP and sP phases all arrive within a short time interval, thus causing the interference and making amplitudes small at the beginning of the records. However, by careful alignment in time of the long period and the short period waveforms, the arrival of the main shock in the short period record can be inferred from its arrival in the long period record. This is demonstrated in Figure 9, where the first arrow indicates the arrival of the foreshock and the second arrow indicates the main shock arrival.

Starting out with the fault parameters of the major double-couple from the inversion and a fault width of 9.5 km

in the middle, as determined by the surface uplift, best
fitting synthetics were calculated by trial and error
procedure. Synthetics were made assuming either a rupture
initiation at a point, or a propagating finite line source.
The parameters allowed to vary were the fault dimensions
(except for its width in the middle), the rupture velocity,
and the initial source depth. All these parameters can
trade off to produce the same synthetics for various
different choices of parameters. The best fitting long
period and short period synthetics were obtained with
rupture initating at a point at 1 km depth and propagating
radially with a rupture velocity of 2.0 km/sec. The
orientation of the near semicircular fault plane, which
extends down to 5.7 km depth is shown in Figure 10. The
long period and short period waveforms produced by this
model are plotted in Figures 11 and 12, respectively. The
overall shape of the long period waveforms is fairly well
fit at all stations, although the first motions at the
stations in western azimuths are not perfectly matched. The
short period waveforms are also surprisingly well fit,
considering that such a simplified model of the fault is
used.

The dominant factors in shaping the short period
synthetics are the source time functions of the up- and
downgoing rays. Due to the slowly increasing fault area and
then the abrupt stopping of rupture, the source time
functions have a long rise time and a sharp fall-off. That

causes the receiver responses to have the largest amplitudes at the end. When the responses due to the P, pP and sP phases are added up they produce the large negative amplitudes denoted by A and B in Figure 12, where A is the backswing of the P response, and B is due to the end of the pP or sP response, depending on which is the dominant one. In eastern azimuths, at stations GUA, AFI, and RAR, the sP phase is the largest, but at all other stations pP has the largest amplitude. The arrivals of these phases are also denoted in the figure. The main features in the short period synthetics that simulate the seismograms so well are therefore caused by the sudden stopping of rupture, and for such a shallow source depth the P, pP and sP phases all arrive within the first second, causing destructive interference and very small amplitudes in the first few seconds. The observed short period seismograms also have small amplitudes within the first seconds, but they are contaminated by the coda of the foreshock, making it impossible to identify specific phases. A few of the short period waveforms are not well matched by the synthetics. These are generally richer in high frequencies, which can be explained by a lesser attenuation along these raypaths.

Small changes in the orientation and dip of the fault might improve the first motion fits in the long period waveforms and would not cause any major changes in the short period waveforms, as long as the source depth and fault dimensions are kept constant.

The fault area of the model is 144 km^2, and the seismic moment is 8.2 x 10^{25} dyne-cm. That gives a displacement of 1.6 m on the fault, which is less than the displacement inferred from the static data.

A second model was also tried to see if matching synthetics could be made with rupture initiating at depth and propagating upwards. The fault was made to approximate the surface break more closely and the rupture was started at a point at 5.2 km depth, at the bottom of the fault, and propagated radially. The orientation of this fault model is shown in Figure 13. The fault was broken into three sections with equal dips of 30^0 but different strikes. The direction of slip was the same on all sections. By trial and error, best fits were obtained with a rupture velocity of 2.7 km/sec and a 30 % higher moment on the middle section than on the other two. The total moment was 8.0 x 10^{25} dyne-cm and the total area was 194 km^2. The corresponding slip on each section is 1.8 m in the middle and 1.0 m on the other two. The long period waveforms produced by this model are plotted in Figure 14. They fit the seismograms fairly well and the fit is as good as for the previous model. However, the short period waveforms, which are plotted in Figure 15 do not fit the seismograms very well, the main reason being that the time functions for the down going rays are too long, so that the backswing from the P arrival is annihilated by the backswing from the surface reflected phases, pP and sP. The time intervals between the arrivals

of P and pP or sP are longer, 1.7 and 2.3 seconds, respectively. Therefore, the interference between the phases is different. However, since the rupture propagates upwards, less energy is carried by the downgoing rays, which automatically makes amplitudes small at the beginning of the synthetics.

The results of this finite fault modeling exercise indicate that the long period waveforms can not resolve the rupture process, since both models produce adequate fits. On the basis of the short period waveforms, although distinct phases can not always be identified in the seismic records, the former model approximates the major features in the records much better and must therefore be preferred. However, the length of the time function can trade off with rupture velocity so the same duration time functions could be obtained at slightly different source depths by allowing the rupture velocity to vary on the fault. The short period records are therefore not deterministic of the exact depth of rupture initiation, but strongly suggest that it started close to the surface on the upper half of the fault plane.

V. Discussion

The orientation of the moment tensor's pressure axis is well constrained by the data, reflecting the east-west horizontal compression dominating in the region. The good

agreement between the pressure axis and the direction of maximum principal stress, the low dip angle of the fault, and the fact that the fault was not shown on any structural map of the region, may suggest that the earthquake was not caused by dislocation on a preexisting fault. However, observations on the fault scarp suggest otherwise (Gordon and Lewis, 1980). Although the strike of the fault is not well determined by the data, the length is constrained by the surface rupture. The dip, which is constrained to within $\pm 10^{0}$ (as demonstrated in Figure 8), and the extent of the surface deformation, constrain the fault dimensions at depth. These factors confine the fault to the uppermost 6 km of the crust.

The large non-double-couple component in the point source solution at 3 km depth is an indication of source complexity. The semicircular surface rupture suggests that it could be due to rupture on a nonplanar fault. Finite fault modeling however, gives the best results when the fault is planar and rupture propagates radially from a point at 1 km depth and reaches a depth of nearly 6 km. This may indicate that even though the fault was not planar, the major part of the energy was radiated from a section of the fault with the orientation of that model. Furthermore, although rupture may not have started at 3 km depth, it may have had a sharp maximum in dislocation there, therefore approximating the point source solution best at that depth.

The implications of the finite fault modeling are

contrary to other previous studies of large thrust events,
such as the Gazli events (Kristy et al., 1980; Hartzell,
1980), The San Fernando (Langston, 1978; Heaton, 1982) and
the New Brunswick events (Choy et al., 1983), where rupture
is proposed to have started at depth and propagated
unilaterally upward, although Langston's (1978) results
indicate initial bilateral rupture. However, all these
events are believed to have occurred on preexisting steeply
dipping faults and they all initiated deeper than the
Meckering earthquake, at depths between 9 and 15 km. Rupture
did not reach the surface in the New Brunswick and the Gazli
events; therefore, the compressive stress near the surface
must be lower in those regions. But most importantly, these
events are located in regions of higher heat flow than in
the South West Australian shield, indicating a hotter crust
and thus causing the brittle-ductile transition zone to be
closer to the surface. The heat flow at Meckering is about
1.2 HFU (Cull and Denham, 1979), while at Gazli and New
Brunswick it is approximately 1.5 HFU, and at San Fernando
it is about 2 HFU (Morgan, 1984).

The different rupture processes are best explained in
terms of a crustal rheology model by Meissner and Strehlau
(1982) and Strehlau (1986); The static frictional strength
of rock in the brittle region of the crust increases with
depth. At some depth, mainly determined by the geothermal
gradient and water content, the various minerals of the rock
start deforming in a ductile manner. Below this transition

zone, in the ductile region, the whole rock matrix yields by aseismic creep and the shear strength decreases drastically with depth.

Compiled stress measurements from various regions (McGarr, 1980; Bamford, 1976) indicate a linear increase in shear stress with depth, but the gradient is less than that of the rock's static frictional strength. Accordingly, the shear stress is generally less than the rock strength over all of the brittle region. In the ductile region however, shear stress and rock strength will eventually become equal and aseismic slip can occur. In areas of medium to high heat flow this occurs at shallow depths and the ductile deformation can build up enough stress in the transition zone above to allow rupture to initiate on a crack and continue upwards to cause an earthquake. The rupture stops when the shear stress becomes smaller than the dynamic frictional strength of the rock. This could be the case for the aforementioned events, which all initiated in or above the transition zone and ruptured upwards. On the other hand, in a cold region such as South West Australia, by assuming a dry lower crust (Meissner and Strehlau, 1982) the transition zone is at approximately 30 km depth. No earthquakes have been observed at that depth in the region, implying a shear stress in the lower crust that is too low to overcome the static frictional strength and cause rupture. However, the measured shear stress at the surface is quite high, about 100 bars (Denham et al., 1980) and

assuming the same linear gradient as before, the shear stress can exceed the frictional strength in a limited depth interval just below the surface. There the stress difference should also be greatest, and decrease with depth. Accordingly, rupture is most likely to initiate near the surface and propagate to some depth before terminating. This model therefore indicates that in the cold shield of Western Australia, the brittle-ductile transition zone is far below the fault area, which lies entirely in the brittle region, and only at shallow depths is the shear stress sufficiently high to cause rupture.

The horizontal compression of the crust in Western Australia does not explain the existence or the location of the Seismic Zone. The driving force for the seismicity could be isostatic movements of the Yilgarn Block, perhaps due to the thickening of the dense basal layer towards the shield boundary. This vertical movement could cause compressive stresses over a limited area at the surface that would add just enough to the regional compressive stress to trigger earthquakes.

VI. Conclusions

A moment tensor solution that describes the average fault mechanism of the Meckering earthquake, has been obtained. The horizontal, east-west direction of the

pressure axis agrees well with the orientation of the maximum principal stress measured in-situ. If the fault was preexisting, this would suggest that the orientation of the stress field has not changed since the original faulting. The fault dimensions are constrained by the extent of surface rupture and uplift, which determine the fault length at the surface and suggest a maximum width of approximately 10 km and an average dip of about 37^0. With this geometry the fault is restricted to the uppermost 6 km of the crust. The rupture process is unresolvable with the long period seismograms, but a shallow initiation point with bilateral rupture is suggested by the short period seismograms. The observed high compressive stress at the surface, and the low regional heat flow, explain the shallow source depth and support that rupture process.

ACKNOWLEDGEMENTS

REFERENCES

Bamford, W.E., 1976. Evolution of stresses in rock masses, as related to compressive strengths and plate tectonics. Investigation of stress in rock, <u>Proc. ISRM Symp. Investigation of Stress in Rock</u>, Sydney, Australia, pp. 63-70.

Bark.r, S.B. and C.A. Langston, 1982. Moment tensor 'nversion of complex earthquakes, <u>Geophys. J. R. astr. Soc.</u>, 68, 777-803.

Choy, L.C., J. Boatwright, J.W. Dewey and S.A. Sipkin, 1983. A Teleseismic Analysis of the New Brunswick Earthquake of January 9, 1982, <u>J. Geophys. Res.</u>, 88, 2199-2212.

Christensen, D.H. and L. Ruff, 1985. Analysis of the trade-off between hypocentral depth and source time function, <u>Bull. Seism. Soc. Am.</u>, 75, 1637-1656

Cloetingh, S. and R. Wortel, 1985. Regional stress field of the Indian plate, <u>Geophys. Res. Lett.</u>, 12, 77-80

Denham, D., L.G. Alexander and G. Worotnicki, 1980. The stress field near the sites of the Meckering (1968) and Calingiri (1970) earthquakes, Western Australia, <u>Tectonophysics</u>, 67, 283-317.

Doyle, H.A., I.B. Everingham and D.J. Sutton, 1968. Seismicity of the Australian continent, <u>J. Geol. Soc. Austral.</u>, 15, 295-312.

Doyle, H.A. 1971. Seismicity and structure in Australia. <u>R. Soc. New Zealand Bull.</u>, 9, 149-152.

Drummond B.J., 1979. A Crustal Profile Across the Archaean Pilbara and Northern Yilgarn Cratons, Northwest Australia, <u>BMR J. Austral. Geol. & Geophys.</u>, 4, 171-189.

Everingham, I.B. and H.A. Doyle, 1969. Thrust fault scarp in the Western Australian shield, <u>Nature</u>, 223, 701-703.

Fitch, J., M.H. Worthington and I.B. Everingham, 1973. Mechanisms of Australian earthquakes and contemporary stress in the Indian Ocean plate, <u>Earth Planet Sci. Lett.</u>, 18, 345-356.

Gordon, F.R., 1971. Faulting during the earthquake at Meckering, Western Australia: 14 October 1968, <u>R. Soc. New Zealand Bull.</u>, 9, 85-93.

Gordon, F.R. and J.D. Lewis, 1980. The Meckering and Calingiri earthquakes, October 1968 and March 1970, <u>Geol. Surv. Western Australia,</u> Bull. 126, 229 pages.

Gordon, F.R. and H.W. Wellman, 1971. A mechanism for the Meckering earthquake, <u>R. Soc. New Zealand Bull.</u>, 9, 95-96.

Hartzell, S., 1980. Faulting Process of the May 17, 1976 Gasli, USSR Earthquake. <u>Bull. Seism. Soc. Am.</u>, 70, 1715-1736.

Haxby, W.F., G.D. Karner, J.L. LaBrecque and J.K. Weissel, 1983. Digital images of combined oceanic and continental data sets and their use in tectonic studies, <u>EOS</u>, 64, 995-1004.

Heaton, T.H., 1982. The 1971 San Fernando Earthquake: A Double Event?, <u>Bull. Seism. Soc. Am.</u>, 72, 2037-2062.

Jackson, D.D., 1972. Interpretation of inaccurate, insufficient and inconsistent data, <u>Geophys. J. R. astr. Soc.</u>, 28, 97-109.

Kanamori, H. and D.L. Anderson, 1975. Theoretical basis of some empirical relations in seismology, <u>Bull. Seism. Soc. Am.</u>, 65, 1073-1095.

Kristy, M.J., L.J. Burdick, and D.W. Simpson, 1980. The Focal Mechanisms of the Gasli, USSR, Earthquakes, <u>Bull. Seism. Soc. Am.</u>, 70, 1737-1750.

Langston, C.A. and D. Helmberger, 1975. A precedure for modeling shallow dislocation sources, <u>Geophys. J. R. astr. Soc.</u>, 42, 117-130.

Langston, C.A., 1978. The February 9, 1971 San Fernando earthquake: a study of source finiteness in tele-seismic body waves, <u>Bull. Seism. Soc. Am.</u>, 68, 1-29.

Langston, C.A., 1981. Source inversion of seismic waveforms: the Koyna, India, earthquakes of 13 September 1967, <u>Bull. Seism. Soc. Am.</u>, 71, 1-24.

Mansinha, L. and D.E. Smylie, 1971. The displacement fields of inclined faults, <u>Bull. Seism. Soc. Am.</u>, 61, 1433-1440.

Mathur, S.P., 1974. Crustal structure in Southwestern Australia from seismic and gravity data, Tectonophysics, 24, 151-182.

McGarr, A., 1980. Some constraints on levels of snear stress in the crust from observations and theory. J. Geophys. Res., 85, 6231-6238.

Meissner, R. and J. Strehlau, 1982. Limits of stresses in continental crusts and their relation to the depth-frequency distribution of shallow earthquakes, Tectonics, 1, 73-89.

Menke, W., 1984. Geophysical Data Analysis: Discrete Inverse Theory, pp 260, Academic Press, Orlando.

Morgan, P., 1984. The thermal structure and thermal evolution of the continental lithosphere, Phys. and Chem. of the Earth, 15, 107-193.

Strehlau, J., 1986. A discussion of the depth extent of rupture in large continental earthquakes, Earthquake Source Mechanics, Geophysical Monograph 37 (Maurice Ewing 6), A.G.U., 131-145.

Wiggins, R.A., 1972. The general linear inverse problem: Implication of surface waves and free oscillations for earth structure, Rev. Geophys. Space Phys, 10, 251-285.

Table 1. - Crustal Model

V_p(km/sec)	V_s(km/sec)	Density (g/cm^3)	Thickness (km)
6.13	3.54	2.78	7.0
6.70	3.87	2.94	7.0
7.49	4.32	3.10	28.0
8.39	4.84	3.45	half-space

Table 2. - Inversion Results

Inversion parameters :	p	$\sigma_{\Delta p}$
MOMENT TENSOR:		
M_{11} x 10^{25} dyne-cm	-3.130	0.143
M_{22} "	8.940	0.310
M_{12} "	-0.005	0.097
M_{13} "	1.150	0.122
M_{23} "	-3.060	0.135
M_O "	8.520	

Pressure axis :
   Azimuth   271°
   Plunge   11.3°

Tension axis :
   Azimuth   4.5°
   Plunge   16.7°

Intermediate axis :
   Azimuth   148°
   Plunge   69.9°

TIME FUNCTION:

S_1	0.128	0.014
S_2	0.262	0.018
S_3	0.345	0.020
S_4	0.139	0.018
S_5	0.088	0.016
S_6	0.038	0.011
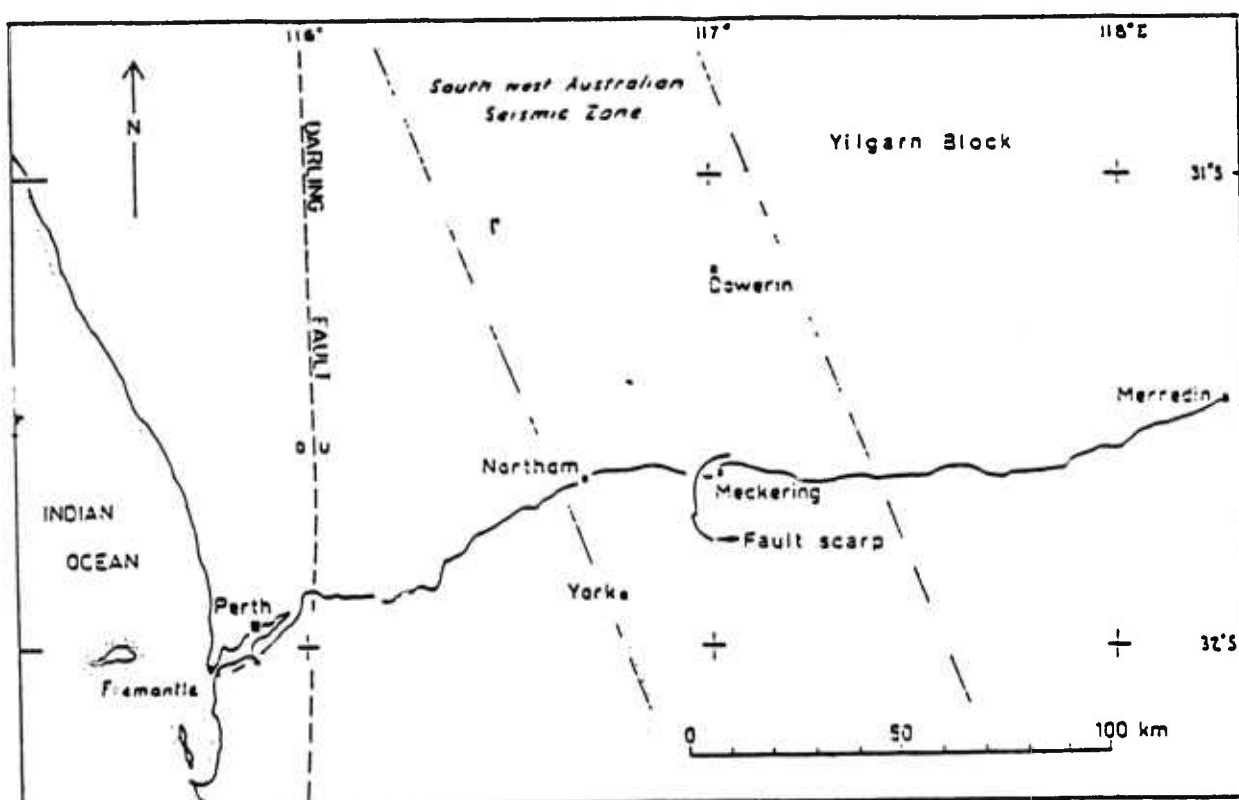
Figure 1. Map of the epicentral area, showing the surface rupture at Meckering (Modified from Gordon, 1971).
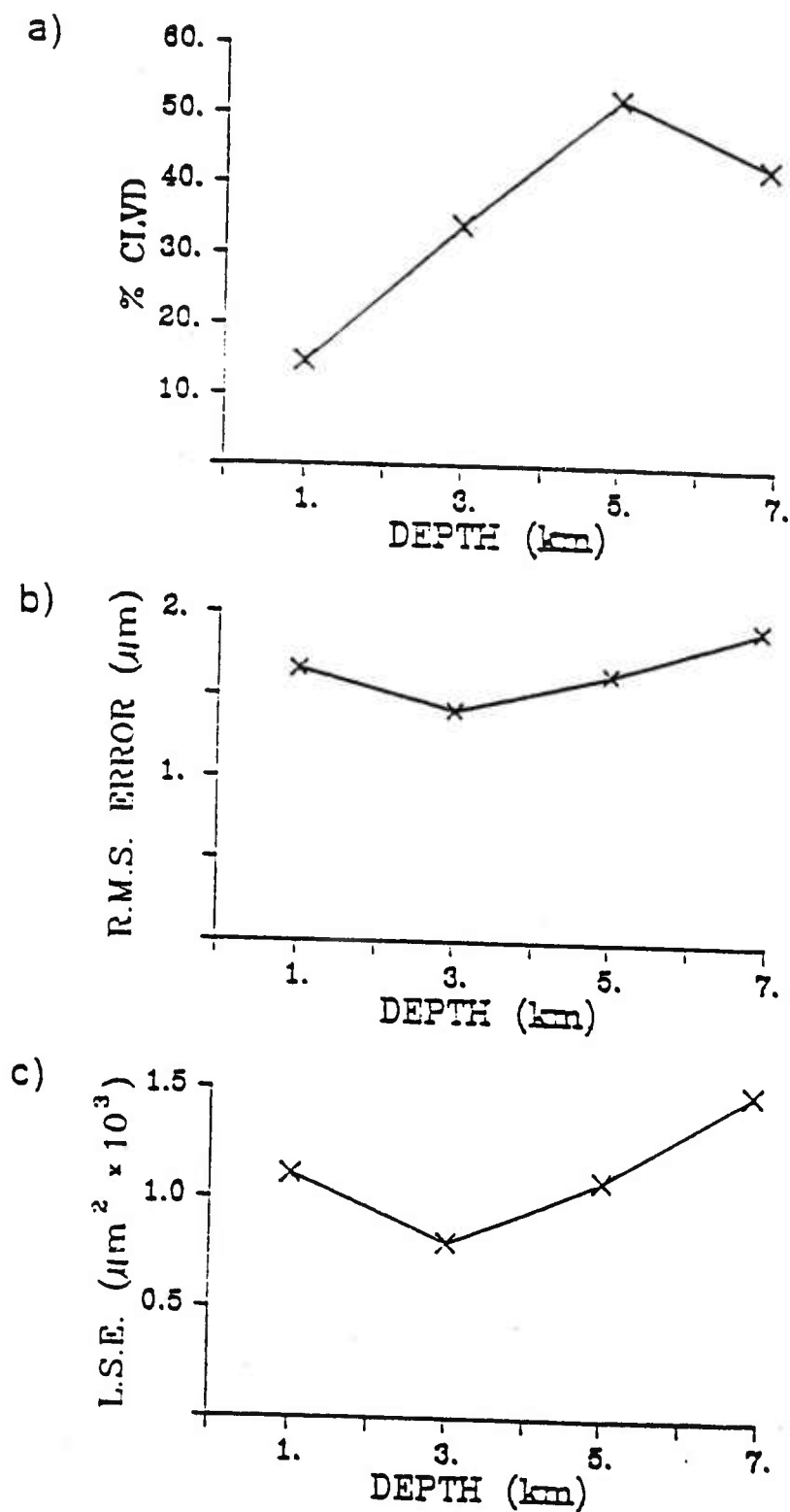
Figure 2. a) Plot of the CLVD as a function of source depth ; b) Plot of the RMS error versus source depth ; c) Plot of the least squares error versus source depth.

INVERSION TIME FUNCTIONS
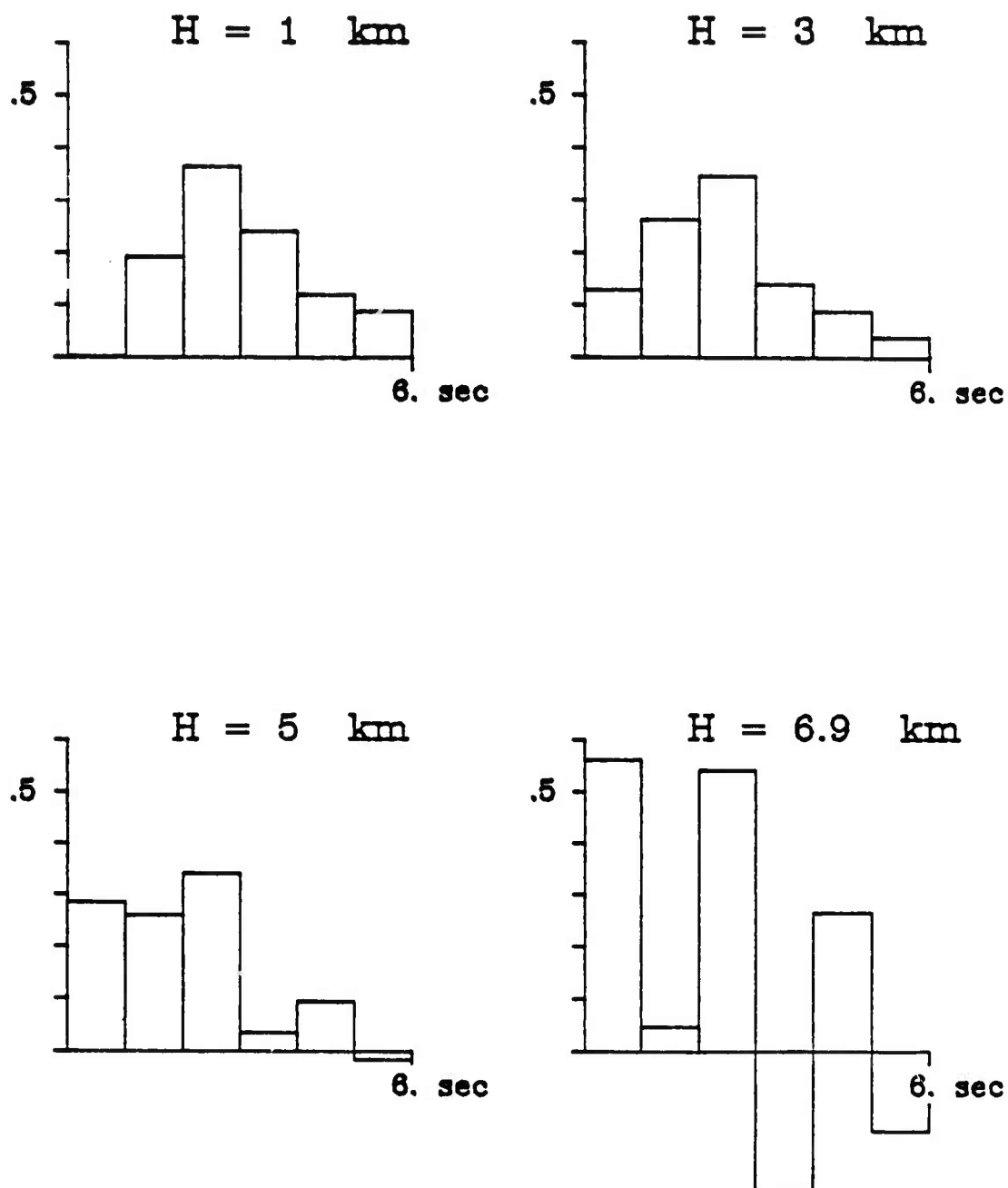
Figure 3. Inversion time functions at various source depths.
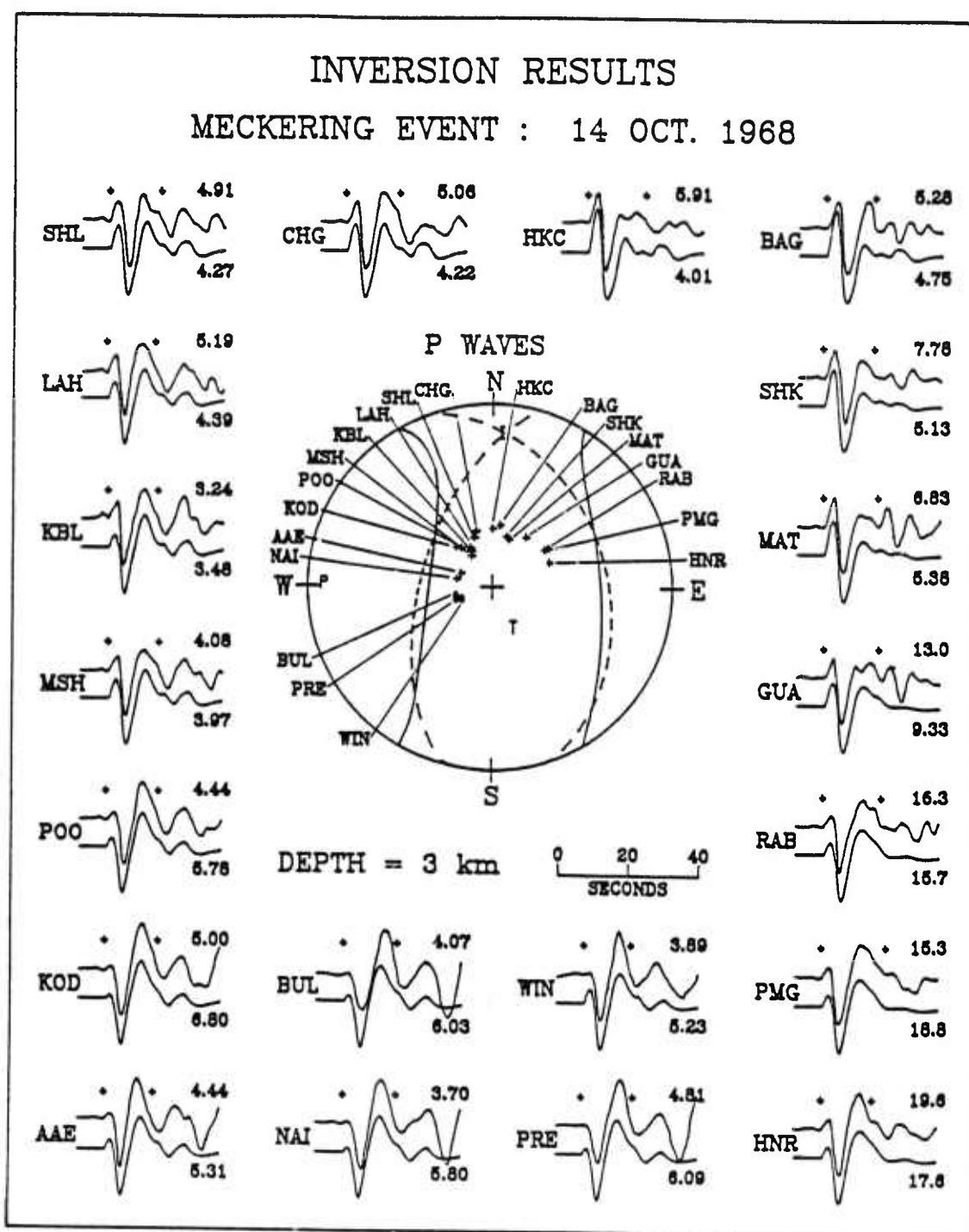
Figure 4. Observed and synthetic P waveforms, same scheme as figure 5, except (+ = compressional first motion ; 0 = nodal ; - = dilatational).
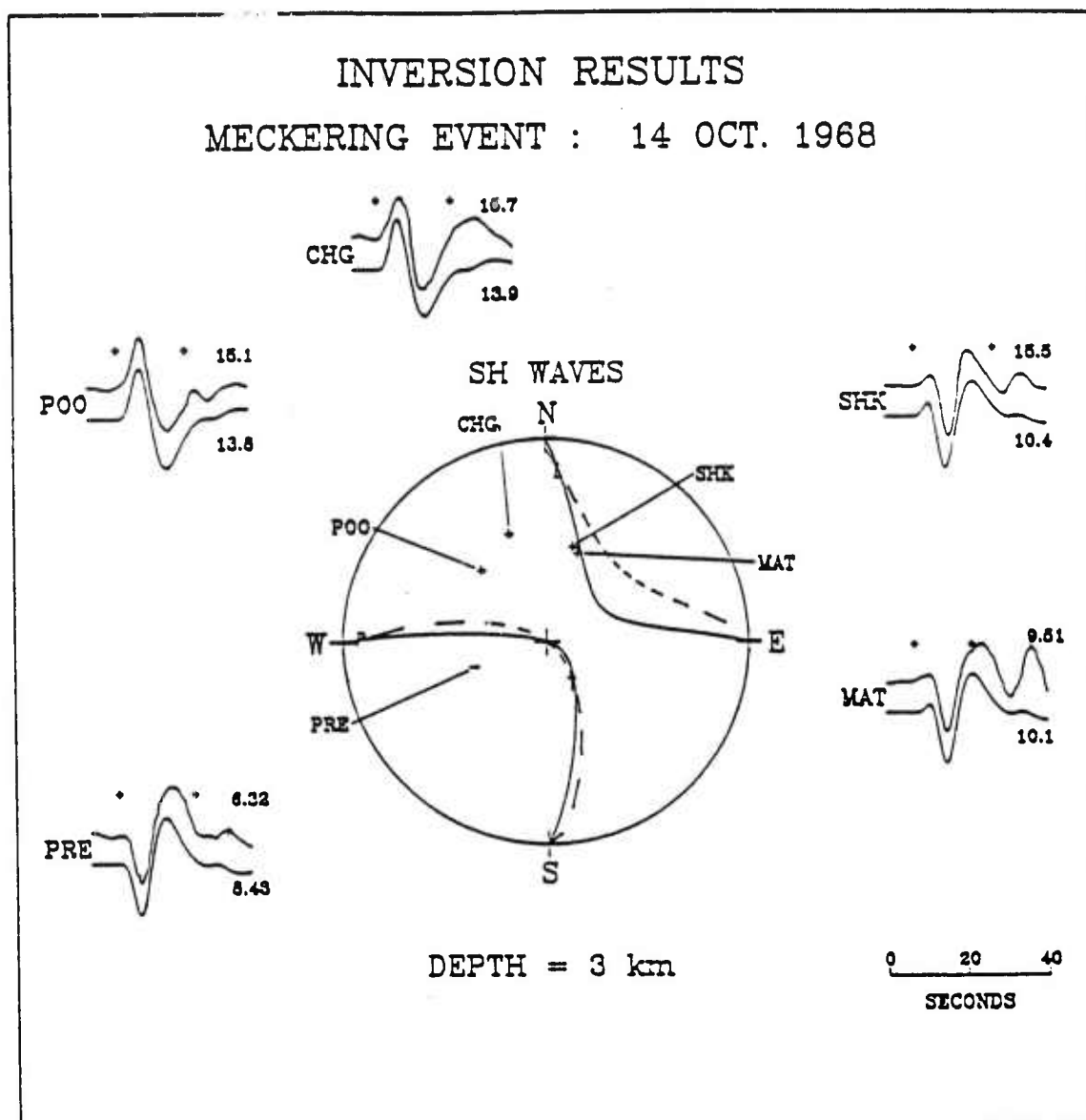
Figure 5. Observed (above) and synthetic (below) SH
waveforms for a 3 km source depth. Waveforms
are normalized to their maximum amplitude, which
is indicated to the right of each trace. The
inversion time windows are indicated by the
arrows. Also shown are lower hemisphere equal-
area projections of the moment tensor nodal
surfaces (solid lines), the nodal planes of its
major double-couple (dashed lines), and the
location and polarities of SH wave first motions
(+ =clockwise ; O =nodal ; - =counterclockwise)
The pressure (P), tension (T) and intermediate
(I) axes are also indicated.
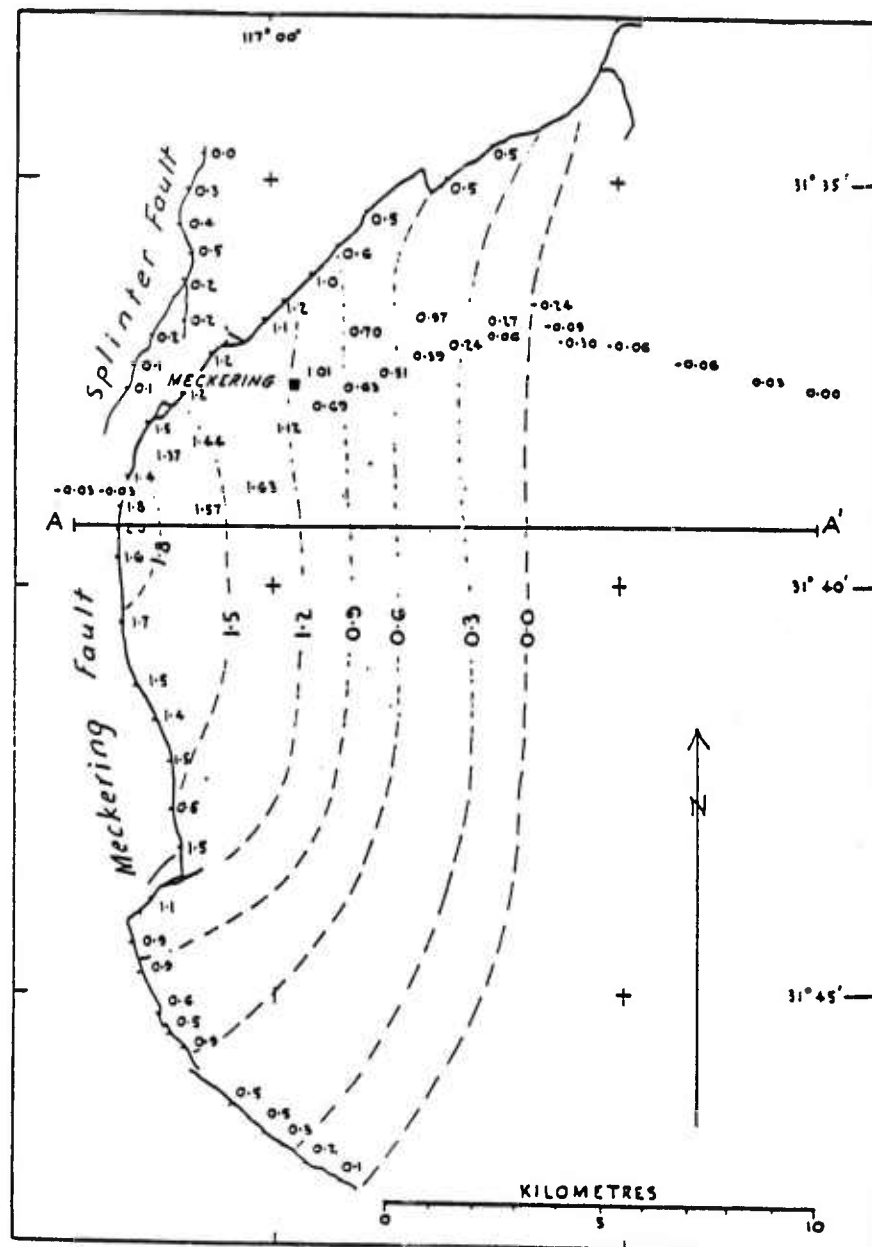
Figure 6. Map showing vertical displacement on the fault
scarp and uplift based on relevelling of a
pipeline and the road from Northam to Meckering
(uplift in meters). The uplift contours are
estimated away from the scarp and the relevelled
lines (Modified from Gordon, 1971).

VERTICAL SURFACE DISPLACEMENT
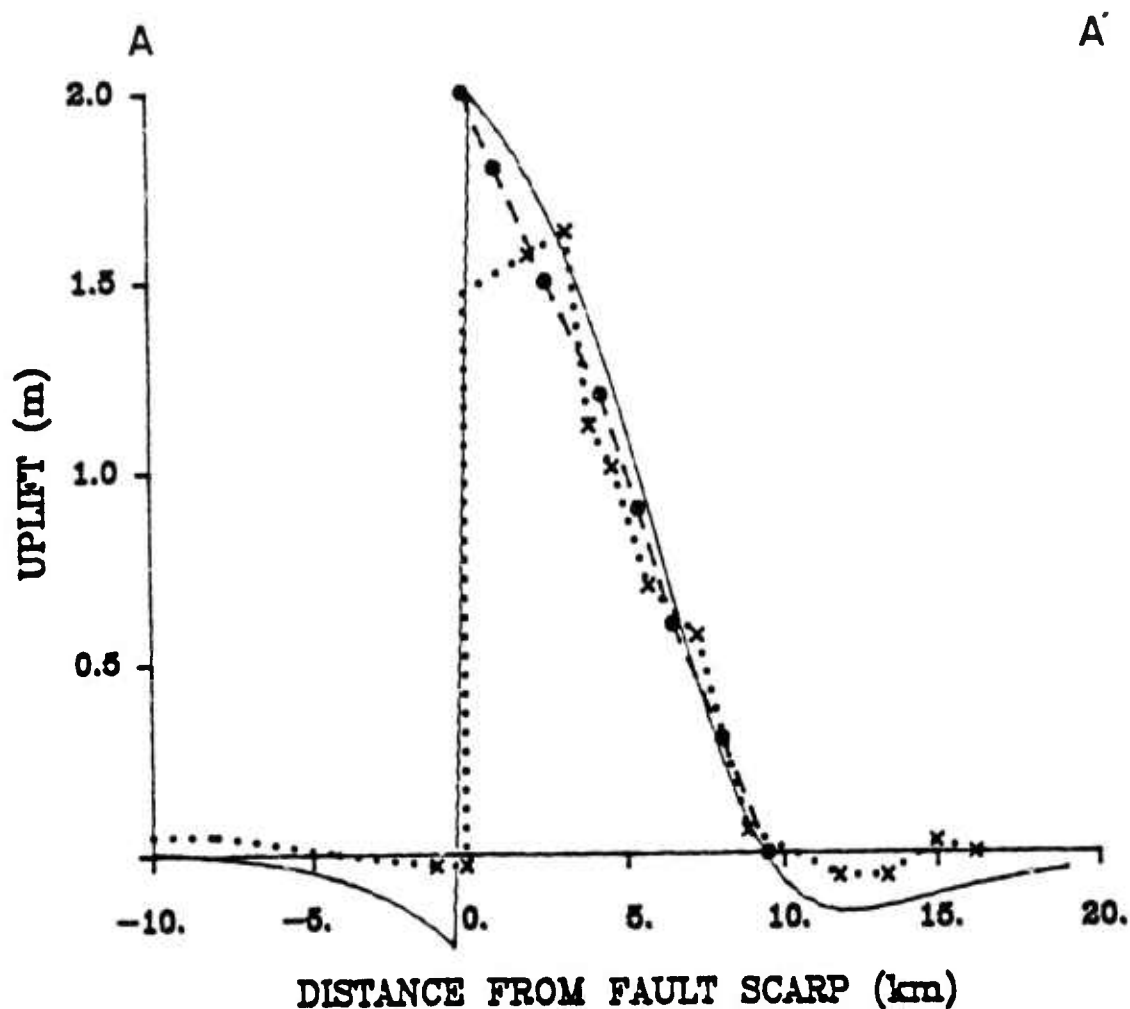
Figure 7. Vertical displacement along the profile AA´, showing : the projection of the uplift on the road (X´s), the contoured uplift (solid circles) and the calculated uplift along the profile (solid line).
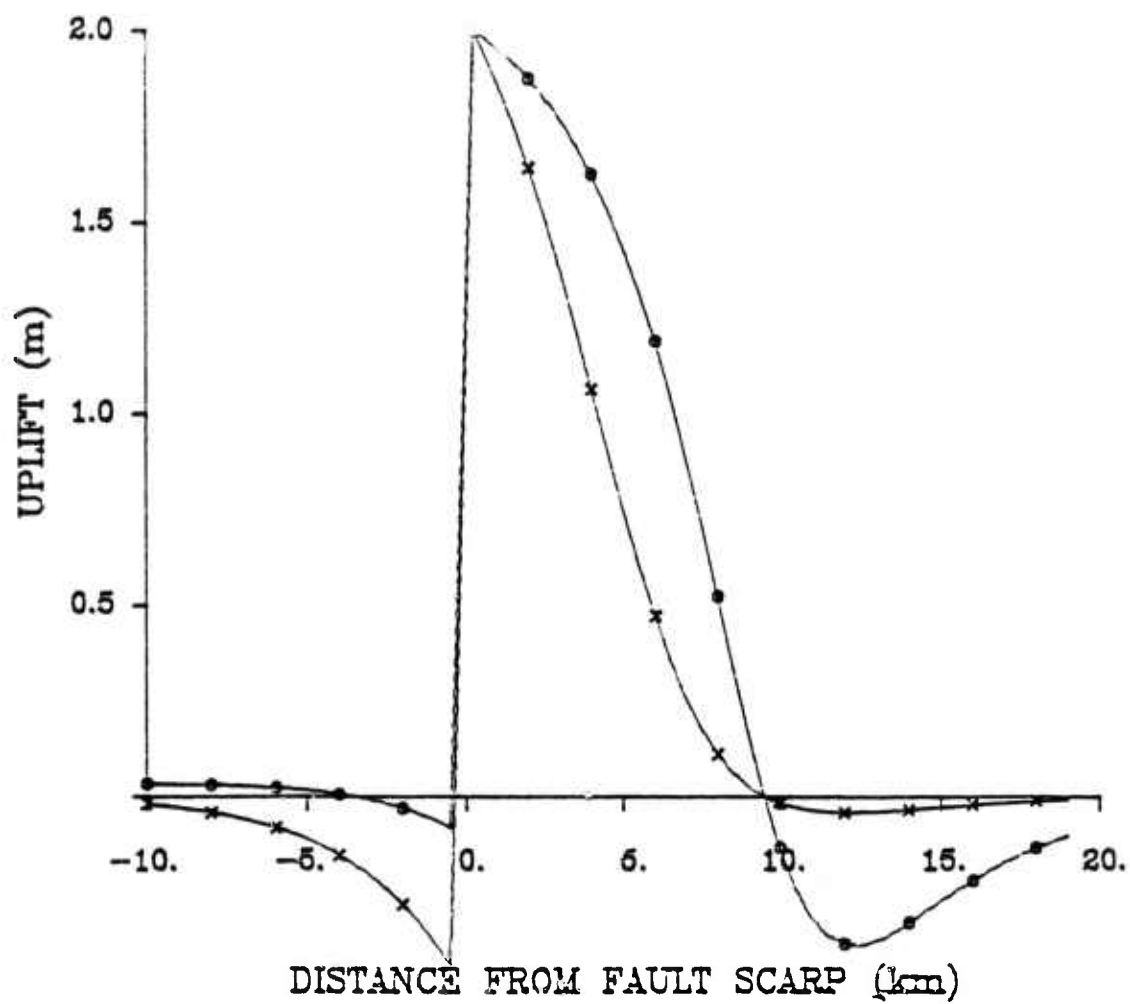
Figure 8. Vertical displacement of a 47° dipping fault
(x's), and a 27° dipping fault (circles).
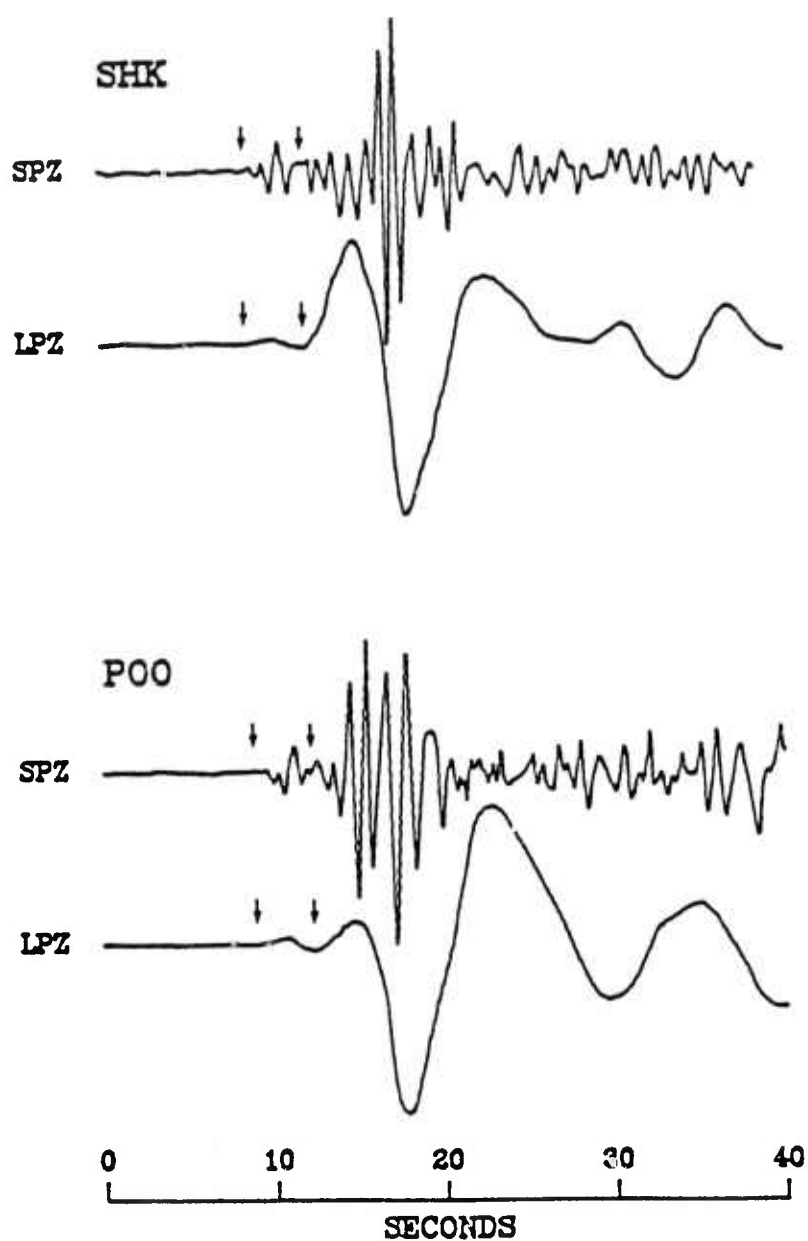
Figure 9. Short period (above) and long period (below) seismograms aligned in time to show arrival times at stations SHK and POO. First arrow marks arrival of the foreshock and second arrow marks the main shock arrival.
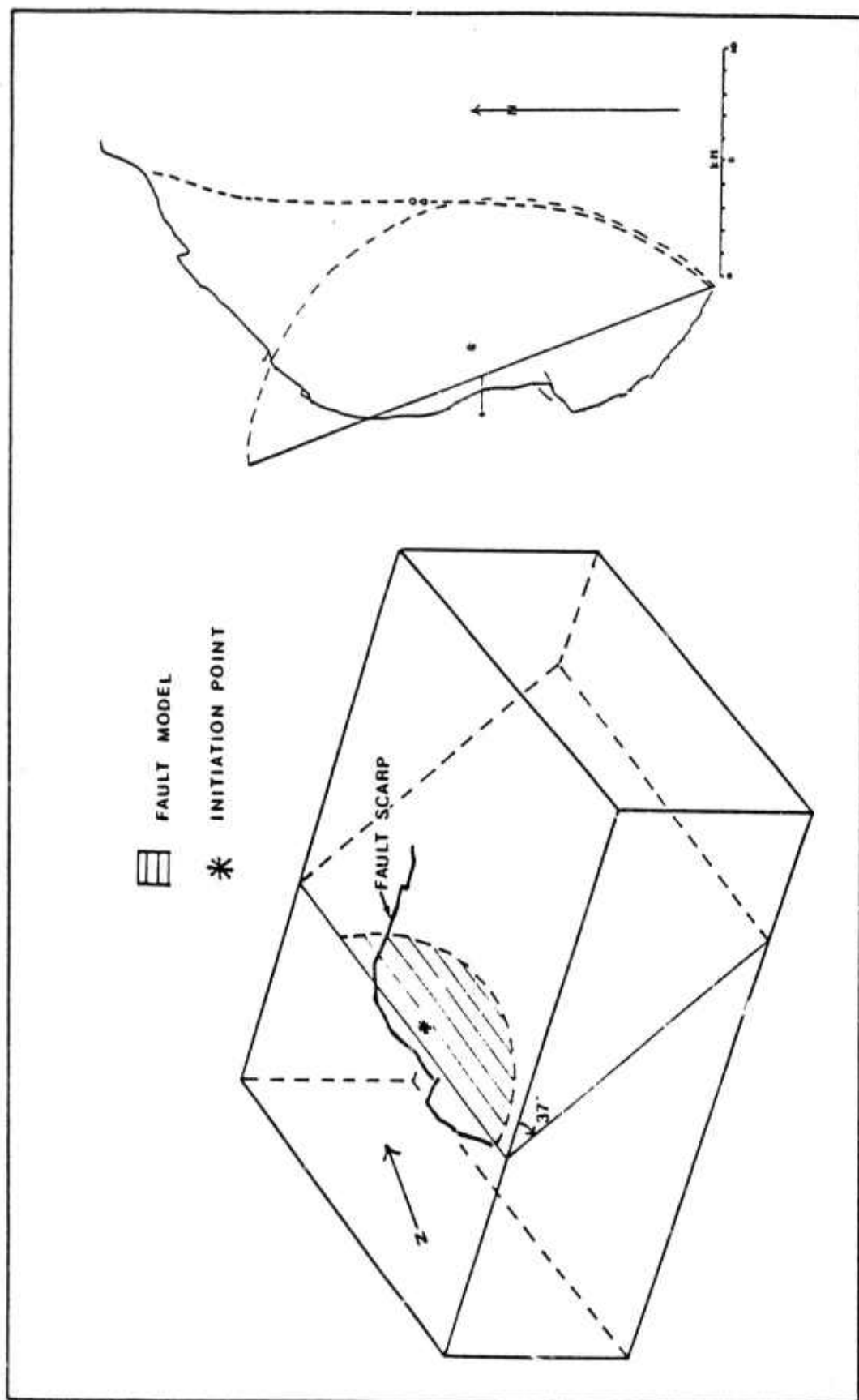
Figure 10. Fault model 1. Arrow on fault plane indicates the direction of slip.
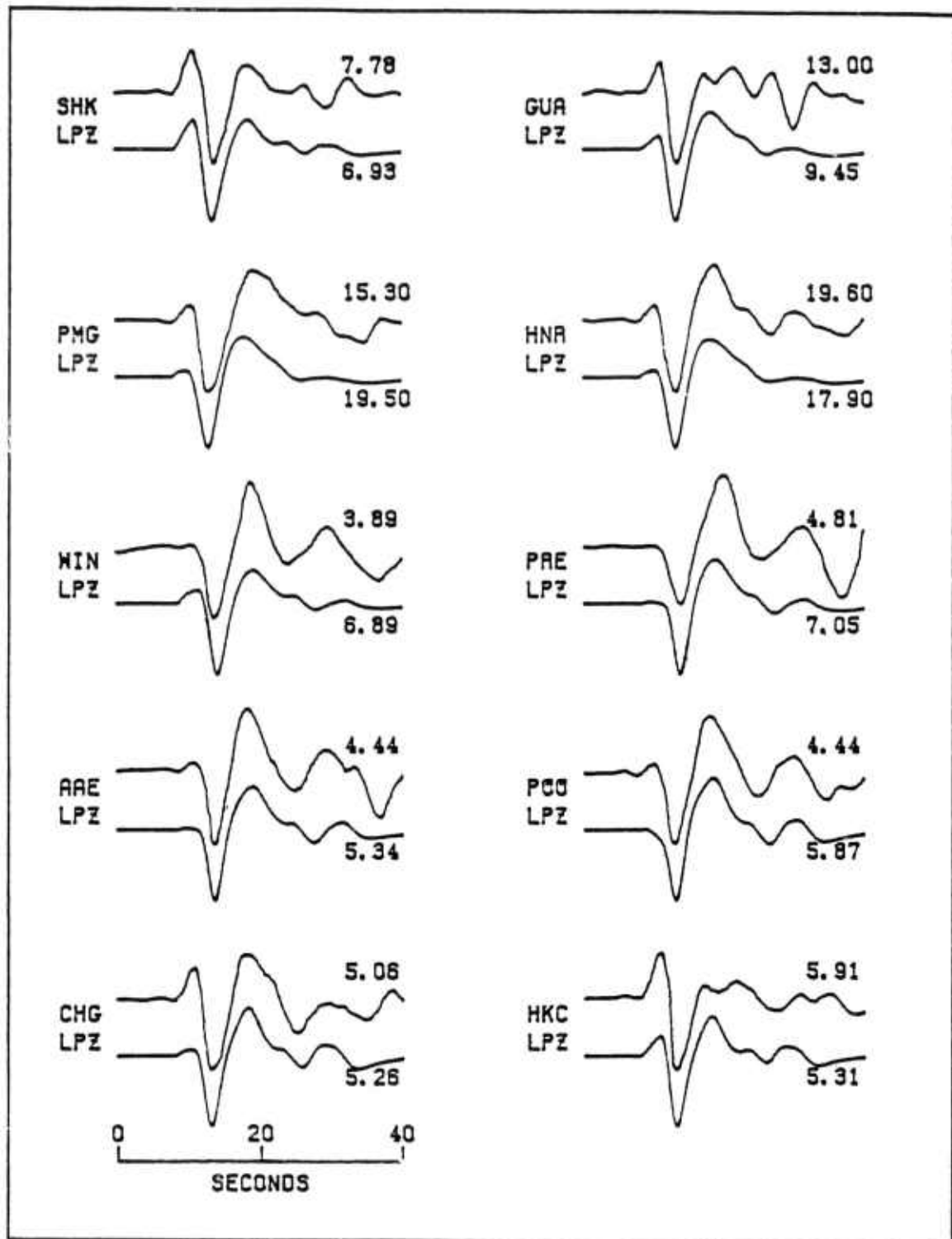
Figure 11. Observed (above) and synthetic (below) long
period P waveforms for model 1, normalized to
their maximum amplitude.
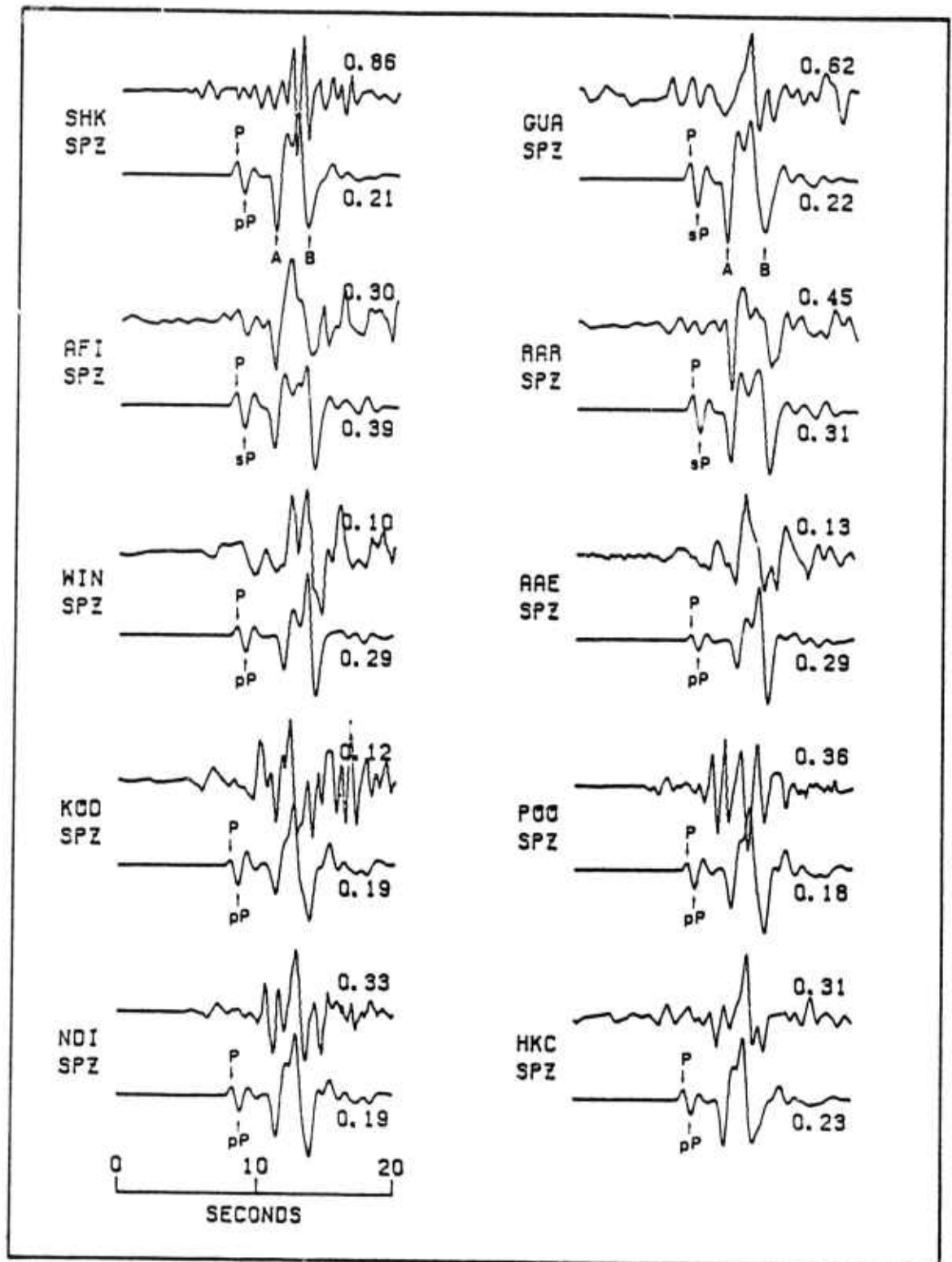
Figure 12. Observed (above) and synthetic (below) short period P waveforms for model 1, normalized to their maximum amplitude. Arrivals of P, pP and sP are indicated.
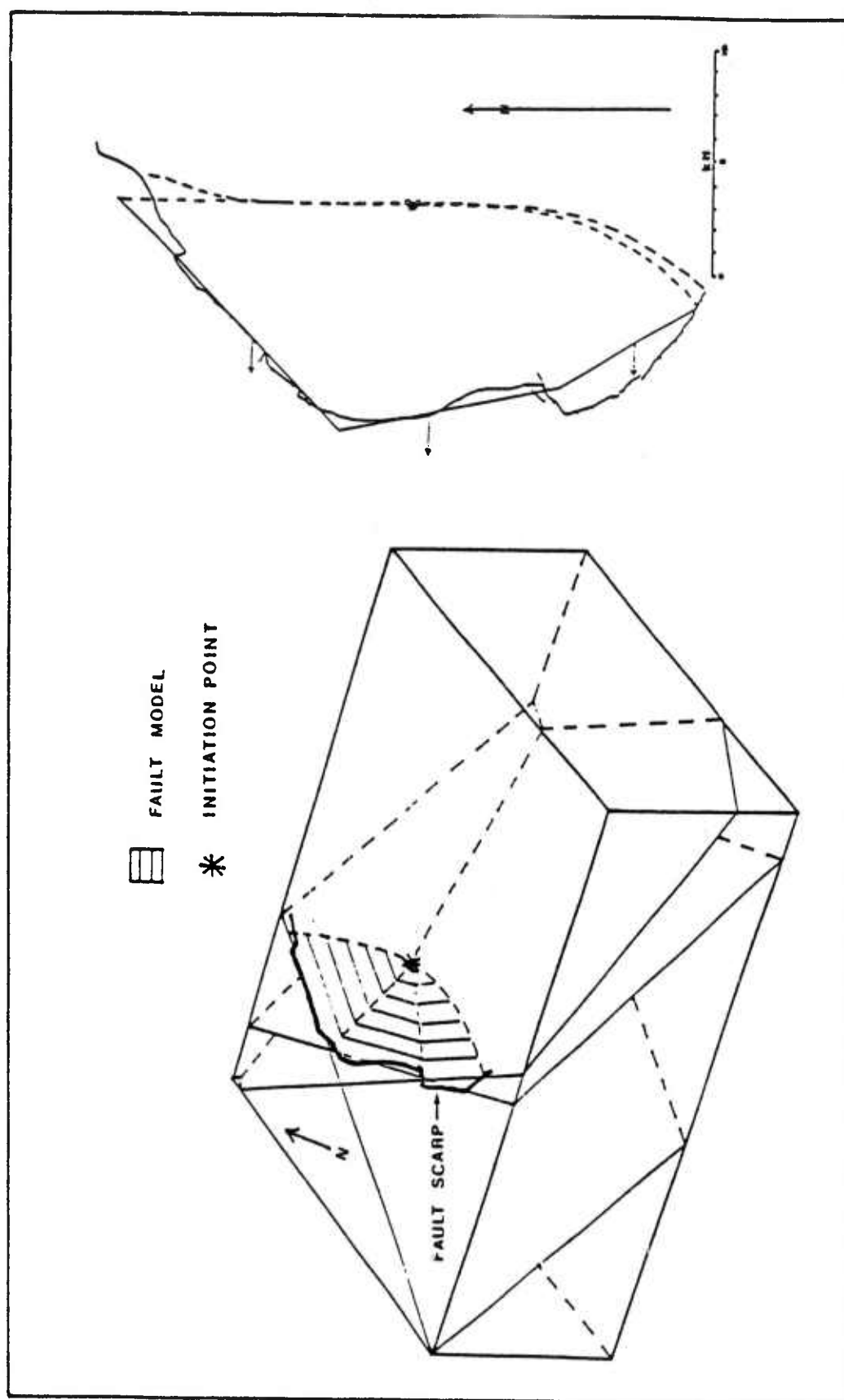
Figure 13. Fault model 2. Arrows on fault sections indicate the direction of slip.
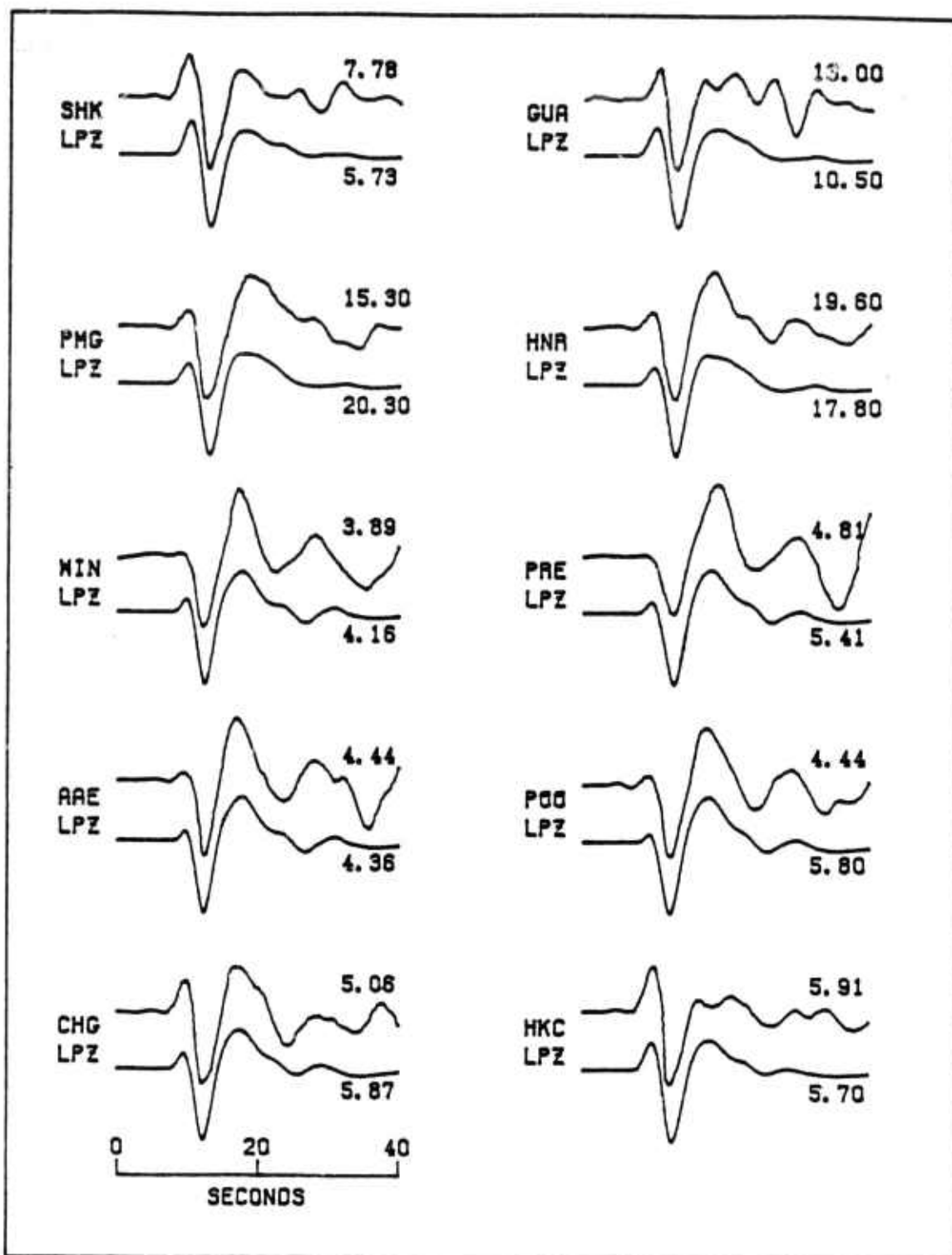
Figure 14. Observed (above) and synthetic (below) long
period P waveforms for model 2.
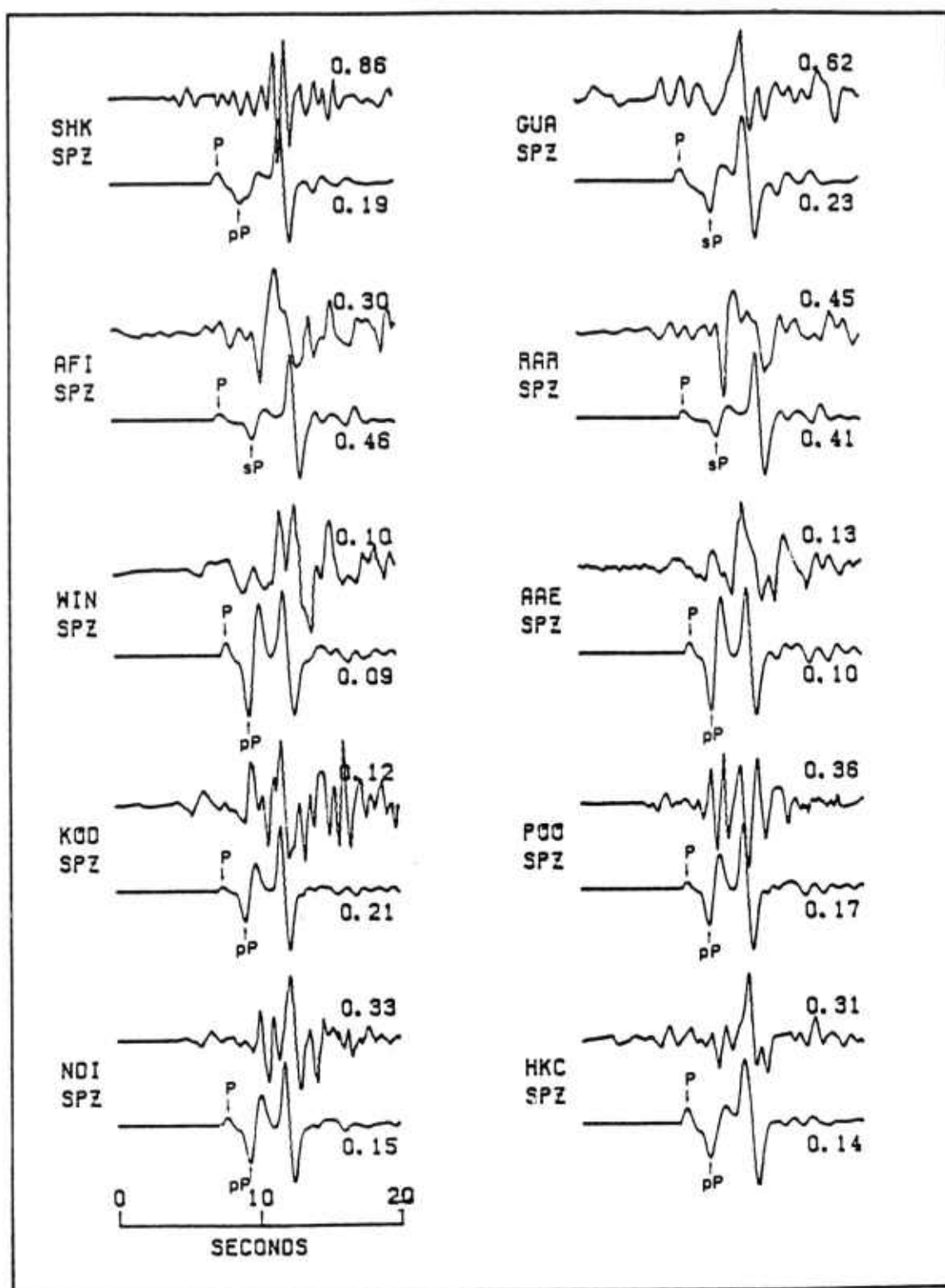
Figure 15.   Observed (above) and synthetic (below) short
period P waveforms for model 2. Arrivals of P,
pP and sP are indicated.

SECTION 6

Waveform Inversion for Five African Earthquakes

and Tectonic Implications for Continental

Deformation

by

Gregory S. Wagner

and

Charles A. Langston

July 24, 1986

Department of Geosciences

403 Deike Building

Pennsylvania State University

University Park, PA   16802

Summary

Source parameters for five moderate African intraplate events were obtained from body wave inversion for the moment tensor. Parameters determined for the events are as follows:

location	date	M_b	strike	dip	rake	depth
Ethiopia	4/05/69	5.8	327.1	69.2	-45.0	4
Congo	3/20/68	6.3	44.6	44.9	-81.5	10
Zambia	12/2/68	5.9	20.3	40.2	264.8	6
Zambia	5/15/68	5.7	49.1	39.8	263.2	28
S. Africa	9/29/69	5.6	123.5	89.4	-0.58	4

The Ethiopia and Congo events are both normal faults as would be expected for their rift zone locations. The 5/15/68 Zambia event is unusual since the inversion for this event yielded a high angle normal fault with a well constrained focal depth, from P-pP times, of 28km. The depth and focal mechanism of this event along with the mechanism for the 12/2/68 Zambia event suggest the possibility of southwest rift extension. Additionally, the May 15th event may be located well below the brittle/ductile transition zone which implies that strain rates in the area are higher than normal. Teleseismic vertical P waves from the South Africa event exhibit distortions that may be attributed to lateral inhomogeneities in the form of a coastward thinning crust at the source.

East African waveform inversion & tectonics

Introduction

The East African rift system is one of the most intriguing tectonic features in the world. It was one of the first tectonic features attributed to the extension of the earth's crust (McKenzie et al. 1970). Minster et al. (1974,1978) have not, however, been able to reconcile extension of the East African rift with kinematic plate models in their global plate modeling studies. The stress regimes associated with this rifting have been studied by many authors. McKenzie et al. (1970), Maasha & Molnar (1972), Fairhead & Girdler. (1971), and this paper, attempt to determine stress regimes and subsequent plate motions by studying the focal mechanisms of large magnitude (> 5.5) earthquakes of the Eastern Rift system. Previous authors used P wave first motion from long and short-period P records to determine source mechanisms. This study, conversely, uses body wave inversion for the moment tensor, and extracts source parameters from the moment tensor elements assuming a deviatoric point source. Inversion is advantageous in that it allows for more accurate and reliable mechanisms in addition to yielding more information about the source. The inversion matches the amplitude of each phase and allows for the determination of a source time function and focal depth. Substantial information about source crustal structure can also be obtained by matching source area crustal phases in the observed data.

The East African rift system, at a glance, has two

systems branching out from the graben of Lake Malawi (figure
1 - near 10° S lat, 33° E long). One branch goes to the
north-west, and the other to the north-east. The branch
continuing to the north-east splits again with one branch
continuing further to the north to connect with the Afar
depression which lies at a right angle to the juncture of the
Red Sea and the Gulf of Aden. Structurally, these rift
valleys are comprised of complex grabens frequently bounded
by multiple faults, and are often associated with varying
degrees of volcanism (Baker et al. 1972).

The five events studied here, combined with previous
studies, show that the African continent is under extensional
stresses from the Afar region to approximately 25°S. The
Ethiopia event demonstrates that Afar is still growing with
the Red Sea. The depth and mechanism of the Congo event
support the postulated tension field in the northern part of
the western branch of the rift system, and show that crustal
extension is occurring in this region. The two Zambia
events, the May 15, 1966 event in particular, show that the
western branch of the rift is extending southward.

In addition to tectonic implications derived from the
focal mechanisms, secondary features in the waveform data are
interpreted to yield additional information about near-source
crustal structure. In particular, distorted P waves from the
nearly pure strike slip South Africa event are attributed to
lateral heterogeneities in the crustal structure near the
source. Also, crustal thickness near the Ethiopia event can
be constrained by reverberations seen in the P wave data.

East African waveform inversion & tectonics

Data Analysis

Long-period WWSSN P and S wave data were used in this
study. Vertical P, NS and EW S wave seismograms were photo
copied from 70 mm film chips, digitized along the top and
bottom, and averaged to insure smooth wave forms. The
digitized data were linearly interpolated with a quarter
second sampling interval to yield the digital data. The NS
and EW data were further processed by rotating them into
their theoretical back azimuth to obtain the radial and
tangential components of displacement.

The Green's functions needed for the inversion were
computed using shallow dislocation source theory of Langston
& Helmberger (1975). For a detailed discussion on inversion
the reader is referred to papers by Wiggins (1972), Jackson
(1972), Langston (1981), and Barker & Langston (1981). Figure
2 compares P wave lower hemisphere focal spheres obtained by
inversion to those obtained by previous authors. Table 1
gives our moment tensor elements, source depths, source time
functions, and error estimates.

Inversion error was determined by looking at the
variance of the parameter changes [$\Delta\sigma_p$] and the resolution
matrix. The $\Delta\sigma_p$ (tables 1.1 & 1.2) are highly dependent on
the eigenvalues with small eigenvalues yielding high $\Delta\sigma_p$ and
a highly singular inverse opperator. Our $\Delta\sigma_p$ were computed
assuming 10% error in the data. Because of the importance of
the eigenvalues, we have included the condition number,
quotient of the highest and lowest eigenvalues, in table 1.3.

All our resolution matricies were identity matricies.

Figure 3 illustrates how the least square fit between the data and synthetics varied with source depth for each event; our final focal depths were those corresponding to the minimum least square error each event. Schematics of the source time function are included with the diagram for the Congo event to show how both the time function simplicity and the least square fit were used to determine the best focal depth for this event. These time functions also illustrate the trade off between source depth and source time function duration (each bar represents a one second boxcar), with the deeper sources having shorter time functions.

Ethiopia - April 5, 1969

McKenzie et al.(1970) were the first to determine a mechanism for this event. Their solution has fault planes that strike 333°, dip 90°, and strike 63°, dip 70°SE. They concluded that the event lies on a dextral transform fault that joins the East African rift valley and the Gulf of Tadjura because of observed ground displacement. Fairhead & Girdler (1971), conversely, choose the 63° striking plane because of reported ENE trending afterschocks; this choice is consistent with the rotation of the Danakil horst away from the Nubian Plate. These two interpretations illustrate the opposing views of the tectonic situation in the Afar region.

Our fault planes are slightly different then those

obtained by McKenzie et al. with strike 327°, dip 69°NE, and strike 77°, dip 49°SSE (figures 4a & b). The strikes of our planes are close to those of McKenzie et al., but the actual motion along these planes is different. We arrived at a focal depth of 4 km using a modified -- thinned by 9 km -- Gumper & Pomeroy (1970) crustal model.

Republic of Congo - March 20, 1966

This event has been the focus of both first motion and aftershock studies. Sykes (1967) used the first motion of P and PKP phases from long-period records, or short-period where no long-period data were available, to determine a mechanism. His fault planes strike 14°, dip 40° W, and strike 32°, dip 52° E. Wohlenberg (1966) reported a fault with a 40 km extent and 30-40 cm of vertical displacement with the western side moving up relative to the eastern side -- no horizontal displacement was observed. Loupenkine (1966) reported a 15-20 km rupture striking NNE with a throw of 2 meters -- the down throw being to the east. Based on these reports, Sykes selected the plane striking 14° as the primary node. His axis of maximum tension, subsequently, lies nearly perpendicular to the strike of the rift. No attempt was made to obtain a depth of focus.

First motion P data alone is insufficient to constrain the fault planes for this event -- this is also true for both Zambia events. Observational data (ie: ground displacement)

adds more credibility to a mechanism determined using first
motion data, but body wave inversion yields a more reliable
mechanism because of the constraints involved in the
procedure.   Inversion yielded a solution almost identical to
that of Sykes; the two planes we obtained strike 45°, dip
45°SE, and strike 213°, dip 46°NW (figures 5a & b).   A depth
of 10 km and a long time history (16 seconds) gave the lowest
least square error during the inversion.   The modified --
thinned by 9 km -- Gumper & Pomeroy crustal model was used
for this event also.

A glance at the long-period P waves from this event
suggests that the source may be much deeper than 10 km
because of the separation of two "phases" that could be
interpreted as P and pP (figure 5a).   The separation between
these "phases" is approximately 12 seconds which would put
the source at about 41 km.   This is well below the assumed
crust for this area and would cause interesting problems in
the tectonic interpretation.   Unfortunately, it is possible
to fit the P waves with a shorter time function and a source
depth of 35 km; Shudofsky (1985) obtained a 29 km focal depth
using body wave [P waves only] modeling.   This causes some
ambiguity which is resolved by the SH data.   The SH data have
no distinct sS arrivals as do the SH synthetics computed
using the 35 km P wave mechanism.   We therefore conclude that
the 16 second time function for our 10 km source includes the
main shock plus an aftershock -- Shudofsky (1985) notes
aftershocks just after the main shock -- and does represent
the correct mechanism for this event .   The ambiguity caused

East African waveform inversion & tectonics

by using only the P wave data illustrates some of the
problems that can arise with inversion; it also demonstrates
the trade off between source depth and time function
duration.

Zambia - May 15, 1968

Fairhead & Girdler (1971) obtained a fault plane
solution using first motion of long-period P and PKP phases;
they obtained a normal fault striking NNE. No surface effect
studies are available, but this solution is in good agreement
with north-east trending faults in the area. But because the
fault did not rupture the surface, and because the P wave
first motions put almost no constraints on the fault planes,
Fairhead & Girdler's mechanism is somewhat questionable. No
attempt was made to determine a depth of focus.   Their
mechanism, nonetheless, substantiates a WNW-ESE extensional
field for this region.

This event may well be the most significant of the
study. Inversion yielded a nearly pure dip slip fault with a
28 km depth of focus. Teleseismic P waves from this event
show that it occurred at depth; similarly, the short-period
records are a textbook example of how pP-P intervals can be
used to determine focal depths (figure 6). While this event
is shallow in seismological terms, its depth is 3-7 times
that of the other 4 events in this study. Inversion yielded
a high angle, nearly pure dip slip normal fault striking at

East African waveform inversion & tectonics

either 49° (dip 40°SE) or 238° (dip 51°NW), with a 4 second
source time function (figures 7a & b). The full 36 km Gumper
& Pomeroy crustal model was used in the inversion and
synthetic computations for this event.

Zambia - December 2, 1968

Fairhead & Girdler (1971) used first motions of P and
PKP phases to obtain a mechanism for this event also. Their
two planes strike 27°, dip 38°ESE, and strike 57°, dip 55°NW.
Their normal fault mechanism has a strike similar to the May
15, 1968 Zambia event which occurred approximately 350 km to
the south-east. There were no detectable aftershocks or
observable ground displacement, and no attempt was made to
obtain a depth of focus. As with the previous event, this
mechanism lacks credibility because of poor first motion
constraints and a lack of surface rupture.

Inversion yielded a nearly pure normal fault (figures 8a
& b) with planes striking 27°, (dip 40°ESE) or 207°, (dip
50°WNW). A focal depth of 6 km and a 4 second time function
yielded the lowest least square error. The strike of this
event is similar to that of the May 15, 1968 Zambia event;
both Zambia events, therefore, provide support for a NWN-ESE
extensional field for south central Africa. The full 36 km
thick Gumper & Pomeroy crustal model was used in inversion
and synthetic computations for this event also.

South Africa - September 29, 1966

P wave first motions alone provide enough information to constrain the fault planes of this event. Green & McGarr (1972) concluded that motion was almost pure strike slip with nodal planes at 42° and 131°. A significant difference exists between the fault plane inferred from their first motion study and that inferred from aftershocks which strike along approximately N61°W [119°] (Green & Bloch 1971). Nonetheless, aftershock data coincides much better with the nodal plane striking at 131° which dips 88° to the southwest. There was no evidence of faulting at the surface. Green & Bloch (1971) determined a maximum depth of focus of 10 km using S-P intervals and aftershock data.

Inversions yielded a nearly pure strike slip fault (dip 88°, or 89°) striking 124° or 217° (figures 9a & b). As with the May 15, 1968 Zambia event, direct and surface reflected phases (sP-P for this event) were used to determine a focal depth of 3-4 km (figure 10). Geologic maps show faulting in the area that strikes approximately 130°; we have, therefore, chosen the 124° striking plane as the actual fault plane. A thinned Gumper & Pomeroy crustal model was used in all the computations for this event [32 km thick crust]. However, some very peculiar problems arose during the inversion for this event.

Because an accurate solution can be obtained by simply using P first motions and a stereonet, it should follow that the P waves alone could be used in the inversion to obtain an

accurate solution. This was, however, not the case. Inversions run using solely P data resulted in mechanisms that did not agree with P first motion data. Inversions using only SH data, conversely, yielded solutions that were consistent with both P and SH first motions. The final solution was obtained using both P and SH waveforms and is consistent with all first motion data. This problem, nonetheless, was very puzzling and may be the result of complexities in the crustal structure near the source.

Langston (1977) notes that teleseismic P waves radiated from sources whose radiation pattern varies rapidly with azimuth (ie: strike slip faults) can be greatly distorted by dipping structure at the source -- this is particularly true for stations located near the nodal surfaces. We assumed this to be the cause of poor P wave inversion results and poor P wave fits. Synthetics were computed using Langston's dipping interface algorithm to explore the effects on the synthetic waveforms; results will be discussed in a later section.

Shudofsky (1985) used body wave modeling of P waves in a 45° sector [342°-27°] to determine a 30 km focal depth for this event, and notes similar problems in his waveform modeling. He concurs with the nearly pure strike-slip mechanisms obtained in other studies, but comments that he could not model the complex body waves using the simple source properties assumed for other African events. He attributes the complex wave forms to source directivity, multiple sources, or unusual source structure.

East African waveform inversion & tectonics

Picking first motions for this event was difficult. Some
of the long-period P records were low amplitude and had very
poor signal to noise ratios which made first motion picks
unreliable. Short-period records, when they were available,
were used to determine the arrival times for both the P and S
waveforms. Similarly, long-period records from stations KOD,
NDI, and SNG (figure 9), in particular, have "arrivals" that
may be interpreted as P and sP. Their separation suggest a 9
km source depth which is not substantiated by the long-period
SH data nor the short-period P or S data. A 9 km source is,
therefore, ruled out in favor of the shallower focus
determined from the short-period records and the least square
error from the inversion.

Discussion

The two major tectonic questions we will address are:
what is the state of stress at various locations, and how far
does the rift system extend through Africa. We have divided
our study area into 3 sections (figure 1): section #1 -
northern Afar (figure 11), sections #2a & #2b - central
Africa (figures 13a & 13b respectively), and section #3 -
South Africa (figure 14).

Afar Region

Two plate motion configurations have been postulated for

the Afar region. Earthquakes in this region are attributed to axial spreading (Girdler 1977) or northeasterly transform faults (McKenzie et al. 1970). An axial NW-SE alignment of active basalt shield volcanoes (Baker et al. 1972) implies extension in the NE and SW directions, and would single out the plane striking 327° (dip 69°NE) as the actual fault plane. This interpretation contradicts that of Fairhead & Girdler but agrees with McKenzie et al.'s interpretation.

In late 1967 and early 1968 Tazieff et al. (1968) mapped a 15,000 km} area (figure 12a of this somewhat controversial region. They concluded that the Northern Danakil Depression is a huge graben structure; an interpretation that contradicts formerly expressed opinions. Mohr's (1967b) WSW-ENE cross rift lineaments (figure 12b) were found to be non-existent. Conversely, a "tremendous quantity" of young, still actively moving NNW trending normal faults were observed. Knetsch (1968) led another party to the same region and concluded that Afar is widening or spreading in a WSW-ENE direction in the northern reaches, and in a SW-NE direction to the south. And Barberi et al. (1972) reported that the Afar depression exhibates only tensional faults.

From the above it appears that both previous fault mechanisms are misinterpretations of the situation in northern Afar. While McKenzie et al. choose a plane striking in the correct direction, their dip and rake appear to be incorrect; faulting in the area consist of normal faults, not strike-slip. And while Fairhead & Girdler sight ENE trending aftershocks to choose the actual plane, the young, actively

moving NNW trending normal faults are a better indicator of which node is the primary, and which the auxiliary. Our preferred mechanism for the April 5, 1969 Ethiopia event strikes 327° and dips 69°NE (rake -45°).

Several crustal models were tested for validity during the inversion for each event. Griffiths et al. (1971) proposed a 20 km two layer model similar to models for Iceland. Bonjer et al. (1971) also have a two layer model, with the crust extending to a depth of 40 km. Gumper and Pomeroy (1970) suggested a 3 layer, 36 km thick crust.

All three models and two additional models, modifications of the Gumper & Pomeroy model, were used in synthetic waveform computations (figure 12). A thinned, by 9 km, Gumper & Pomeroy model was required to match the [crustal] reverberation timing of the observed data to that of the synthetics, particularly for waveforms of the type observed at NDI and CHG. The 27 km thick [model a] crust used for this event is consistent with plate tectonic crustal thinning assumptions for extensional regimes.

The Afar region is comprised of mantle material ejected during the separation of Arabia and Africa; aeromagnetics show that this accretion occurred at a very slow rate (McKenzie et al. 1970). The Ethiopia event demonstrates that NNE-SSW extensional forces still exist in the region and subsequently, that the Afar region is still growing with the Red Sea. The low level of both seismic and volcanic activity in the area suggests that the process may have slowed, but there is no evidence to suggest that it has completely

stopped.

Central Africa

The second area we examined includes regions 2a and 2b
of figure 1. Area 2a (figure 13a) encloses the Congo event
of March 20, 1966; 2b (figure 13b) encloses both Zambia
events -- May 15, 1968 and December 2, 1968. The Congo event
is located within the western branch of the rift system,
while the Zambia events are located in an area that may
demonstrate southward continuation of the rift. The Congo
event, which occurred in the Ruwenzori massif between Lakes
Albert and Edward (figure 13a), will be discussed first.

Two independent micro earthquake studies (Rykounov et
al. 1972; Maasha 1975) have shown the Ruwenzori region to
be one of the most seismically active areas in the rift
system. This area of the rift is often used to show
similarities between the mid-oceanic spreading centers and
the Eastern rift system (Baker et al. 1972). Volcanism,
seismic velocities, attenuation, gravity anomalies, and
seismicity suggest or are consistent with the presence of
lateral discontinuities in the lithospheric mantle (Maasha &
Molnar 1972). Micro-earthquake data show a prevalence of E-W
tensional stresses (Maasha 1975). This information shows
that the March 20, 1966 Congo event occurred in a region that
is under E-W extensional stress.

Observational data can be used to determine which plane

is the primary node. While the two reports of observable
fault displacement (Loupenkine 1966; Wohlenberg 1966)
disagree as to the actual extent of faulting, both agree that
the western side of the fault moved up relative to the
eastern side. We, therefore, have chosen the node which
strikes 45° and dips 45°SE as the primary node. The nearly
pure dip slip nature of this fault combined with its 10 km
depth show that the crust in this area is subject to
extensional forces.

The 26 km thinned Gumper & Pomeroy crustal model was
used for this event. As with the Ethiopia event, it is not
unreasonable to have an abnormally thin crust in this area
because of suspected spreading and thinning. In any case,
crustal thickness has little effect on these waveforms.

The two Zambia events are located in a region (figure
13b) that is under scrutiny for some proof of southward rift
extension. Several authors (Reeves & Hutchins 1975; Scholz
et al. 1976; Chapman & Pollack 1977) have expressed their
views on the possibility of rift growth that was first
proposed by Fairhead & Girdler (1969) who postulated that the
western branch of the rift followed Lake Tanganyika and then
continued south through Lake Mweru. They suggested that rift
extension could continue through Zambia and then as far south
as 24°S, roughly along 26°E.

There is a growing body of evidence supporting the rift
extension theory. To the south of the Zambia events, in
Botswana, Reeves & Hutchins (1975) detected a linear feature
they named the Kalahari Seismicity Axis [KSA]. The location

East African waveform inversion & tectonics

of this feature was determined by epicenter data and supported by photogeological features. The KSA strikes NE-SW and divides the Bouguer anomaly map of the area into areas of distinctly different textures -- a Bouguer anomaly gradient follows much of the axis. The authors used this zone to demonstrate the existence of tectonic instability in the heart of the continental plate.

Scholz et al. (1976) note a zone of seismicity that runs south-west from Lake Tanganyika through Lake Mweru and then south through central Zambia to northern Botswana. Micro seismicity in this area is higher then that in Ethiopia, and comparable to that observed along the main rift valleys of East Africa. Active normal faulting on north-easterly striking faults provides evidence of a very recent onset of rifting attributed to southward propagation of the rift.

Chapman & Pollack (1977) suggest that heat-flow anomalies in Zambia are due to a thinned lithosphere in west and central Zambia. Additionally, incipient rifting may be the cause of a long wave length negative Bouguer gravity anomaly to the SWS of Lake Tanganyika; similar negative gravity anomalies that coincide with surface rift features in East Africa have been attributed to regions of thinning in the lithosphere.

Maasha & Molnar (1972) have shown that stress drops outside the rift in southern Africa suggest higher stress there than inside the rift to the north. They also point out that volcanism is older in Ethiopia than in Kenya, suggesting that the Eastern rift may have grown southward during its

East African waveform inversion & tectonics

formation.

The large number of earthquakes that occurred in the Lake Kariba area shortly after its infilling may not be strictly attributed to southward rift extension. Fairhead & Girdler (1969 & 1971), Gupta et al. (1972), and Gough & Gough (1970) show that events in the area of the lake are due to the load as opposed to regional stresses. A catalogue of earthquakes prepared in 1963 by Gorshokov shows that no earthquakes were reported in this region prior to the infilling of the lake (Gupta 1972). With the exception of four events, all epicenters lie in the rift valley which contains the lake (Gough & Gough 1970) with 12 events forming a remarkably tight cluster just below the dam where the water is the deepest (Fairhead & Girdler 1969). It is also significant to note that there is a remarkable correlation between the maximum lake filling due to seasonal rains, and the more recent earthquakes (Fairhead & Girdler 1969). The spatial and time distribution of these events show that they are largely, if not totally, due to the presence of the lake. These events, therefore, are not suitable to demonstrate rift extension but are consistent with the rift hypothesis.

Our steeply dipping NE-SW striking mechanisms provide further support for the southward rift extension theory by illustrating ENE-WNW extension. The May 15, 1968 event, in particular, gives substantial evidence for southward rift propagation. As previously mentioned, this event is a high angle normal fault that occurred at a depth of 28 km. The

high angle of faulting for this event shows that high
deviatoric tensional stresses continue to great depths and
abnormally high crustal temperatures are reflected in the
region's high heat flow. It is very likely that this event
occurred below the brittle/ductile transition zone which
would make high strain rates a necessity.

Meissner & Strehlau (1982), Strehlau & Meissner (1982),
and Strehlau (1985) show that very high strain rates are a
necessity for this event. Strehlau & Meissner (1982) suggest
that it is the temperature and not the petrological
properties that determines the cut-off depth of seismicity;
the orientation of the principle stresses and the subsequent
fault mechanism also play a minor role in determining the
depth of seismic and aseismic activity. Chapman & Pollack's
(1977) values for heat flow ($q = 7.1 \cdot 10^{-2}$ W/m} = 1.69 HFU),
thermal gradient ($dT/dz = 2.54 \cdot 10^{-2}$ K/m), and thermal
conductivity ($k = 2.81$ W/mK) would put the temperature at 28 km
above 600°C. This value is greater then the critical
seismic/aseismic transition temperature for normal faulting
obtained by Strehlau & Meissner -- 500°C q90°. This event,
subsiquently, is located well within Strehlau & Meissner's
"plastic domain" where stress release by bulk plastic flow
should prevent seismic activity. Based on these simple
models, very high strain rates are required for failure at 28
km.

These seismic and heat flow data suggest that tensile
stresses extending through the crust are separating the upper
lithosphere to allow the upwelling of hot mantle material.

The full 36 km Gumper & Pomeroy crustal model was used in the inversion and synthetic computations for both Zambia events. A thicker crust than that used for the Ethiopia or Congo events is consistent with plate tectonic assumptions for this area because well defined rifting or crustal thinning is not immediately evident. Additionally, the lack of well defined source crustal reverberation phases makes accurate crustal thickness determination for either event rather tenuous.

South Africa

No one, as of yet, has suggested that the rift extends the whole length of the continent. This would have to be the case if the South African event of September 29, 1969 is considered to be due to southward rift migration (figure 14). The geology of the Ceres area does not provide substantial evidence regarding stress orientation; most of southern Africa is a stable shield area and earthquakes the size of the September 29 event (6.3) are rare. In fact, no previous earthquake in South African recorded history has caused such extensive damage (Green & Bloch 1971).

An oddity of this event is that the fault plane from the main shock obtained by Green & McGarr (1972) does not coincide with the plane delineated by the carefully studied aftershocks (Green & Bloch 1971). Our corresponding plane, however, strikes approximately 124°, only 5° different than

East African waveform inversion & tectonics

the aftershock data. Green & McGarr (1972) report that there
are no inconsistent data and that both nodal planes are well
constrained.

Inversion yielded a nearly pure sinistral strike slip
fault, striking at about 124° -- there is no reported
evidence of faulting at the surface. The strike of this
fault coincides nicely with that of the Worcester fault zone
which apparently has not been active since the Cretaceous
(Green & McGarr 1972).

The P waves from this event, as previously mentioned,
could not be consistently modeled using simple plane layered
structure. The gross crustal structure in the area of the
source is dominated by a seaward thinning crust to the
SSW-SE, and/or the Karroo basin to the NE. Figure 15
illustrates how scattering caused by a dipping interface
distorts P waves recorded at stations on opposite sides of a
node; we used a 31 km, 3 layer crustal model with planar
layers and a seaward rising Moho (10°). While this figure
does not explain the wave form distortions recorded at the
stations to the NE, it does show how dramatically a simple
scatterer affects P waves radiated from a strike slip source.
The curved structure of the Karroo basin, located to the NE,
may be the cause of P wave distortions observed at stations
in that direction. Since there are few studies of crustal
heterogeneities in this area we cannot determine a causal
structure which produces the exact waveform changes observed.
However, this analysis suggests that lateral heterogeneities
in the source crust are a plausible explanation of the

effects observed, particularly considering the inconsistent P and SH mechanisms found in the inversions. It is also conceivable that multiple fault planes were involved in the rupture causing complex waveforms.

Summary & Conclusions

All of the mechanisms obtained in this study are somewhat different than mechanisms determined by previous workers using observational and P wave first motion data. Our normal fault mechanisms, for the Congo and both Zambia events, are more reliable then previous interpretations because of the inclusion of waveform constraints. The additional information provided by the inversion, focal depth in particular, allows for greater insight into the tectonic activity occuring in the area of each event.

Eastern Africa has been shown to be under extensional stress from the Afar region to approximately 25°S. The fault plane striking 327° and dipping 69°NE has been chosen as the primary node for the Ethiopia event based on observational data. This mechanism shows that the Afar area is under tensional stress, and spreading in a NNE-SSW direction. The Congo mechanism substantiates the accepted view that this area is undergoing crustal extension. Abundant and sundry geophysical evidence is making the southward rift extension theory nearly inescapable. The large, deep, high angle normal fault of May 15, 1968 (Zambia) shows that stress

East African waveform inversion & tectonics

accompanied by high strain rates extends, at the least,
throughout the entire crust. Distorted P waves from the
nearly pure strike slip September 29, 1969 South Africa event
demonstrate the existence of complex crustal structure in the
area of the event.

REFERENCES

Baker, B.H., Mohr, P.A., Williams, L.A.J., 1972. Geology of the Eastern Rift System; Geol. Soc. of Amer. Spec. Paper #136, 67 p.

Barker, J.S. & Langston, C.A., 1981. Inversion of teleseismic body waves for the moment tensor of the 1978 Thessaloniki, Greece, earthquake; Bull. Seismol. Soc. Am., 71, 1423-1444.

Barberi, F., Tazieff, H., & Varet, J., 1972, Volcanism in the Afar depression: its tectonic and magmatic significance. in: R. W. Girdler (editor), East African Rifts, Tectonophysics, 15(+), 19-29.

Bloch, S., Hales, A.L. & Landisman, M., 1969, Velocities in the crust and upper mantle of Southern Africa from multi-mode dispersion. Bull. Seismol. Soc. Am., 59(4), 1599-1629

Bonjer, K.P., Fuchs, K., & Wohlenberg, J., 1970. Crustal structure of the East African rift system from spectral response ratios of long-period body waves. Z. Geophys., 36, 287-297

Chapman, D.S. & Pollack, H.N., 1977. Heat flow and heat production in Zambia: evidence for lithospheric thinning in central Africa. Tectonophysics, 41,79-100

Fairhead, J.D. & Girdler, R.W., 1971. The seismicity of Africa. Geophys. J. R. Astr. Soc., 24,271-301

Fairhead, J.D. & Girdler, R.W., 1972. The seismicity of the East African rift system. in: R. W. Girdler (editor), East African Rifts, Tectonophysics, 15(+),115-122

Gilbert, F., 1970, Excitation of the normal modes of the earth by a point source, Geophys. J., 22,223-226.

Girdler, R.W., 1975. The great negative Bouger gravity anomaly over Africa. Trans. Am. Geophys. Union, 56, 516-519

Girdler, R.W., 1977. Comparison of the East African rift system and the Permain Oslo rift. in: Tectonics and geophysics of continental rifts, D. Reidel Publishing Co., Holland, pp 329-345

Gough, D.I. & Gough, W.I., 1970. Load-induced earthquakes at Lake Kariba-II. Geophys. J. R. Astr. Soc., 21,79-101

Green, A.G., 1978. An upper mantle P-wave velocity model for eastern and southern Africa. Birkhiuser Verlag, Basel, 116,1262-1273

Green, R.W.E., & Bloch, S., 1971. The Ceres, South Africa, earthquake of September 29, 1969 - I. report on some aftershocks. Bull. Seismol. Soc. Am., 61(4),851-859

Green, R.W.E. & McGarr, A., 1972. A comparison of the focal mechanism and aftershock distribution of the Ceres, South Africa earthquake of September 29, 1969. Bull. Seismol. Soc. Am., 60(3),869-871

Griffiths, D.H., King, R.F., Khan, M.A. & Blundell, D.J., 1971. Seismic refraction line in the Gregory rift. Nature Phys. Sci., 229,69-71

Gumper, F. & Pomeroy, P.W., 1970. Seismic wave velocities and earth structure on the African continent. Bull. Seismol. Soc. Am., 60,651-668

Gupta, H.K., Rastogi, B.K., Narain, H., 1972. Common features of the reservoir-associated seismic activities. Bull. Seismol. Soc. Am., 62(2),481-492

Hafner, W., 1961. Stress distributions and faulting, Bull. Geol. Soc. Am., 62,373-398

Jackson, D.D., 1972. Interpretation of inaccurate, insufficient, and inconsistent data. Geophys. J. R. Astr. Soc., 28,97-109

Jackson, D.D., 1979, The use of a priori data to resolve non-uniqueness in linear inversion, Geophys J.R. Astr. Soc., 57,137-157.

Knetsch, G., 1968, Danakil - reconnaissance 1968. in: Graben Problems, E. Schweizerbart'sche Verlagsbuchhandlung, Stuttgart, 1970. pp 267-279

Knopoff, L. & Schlue, J.W., 1972. Rayleigh wave phase velocities for the path Addis Ababa - Nairobi. in: R. W. Girdler (editor), East African Rifts, Tectonophysics, 15(+),157-163

Lahr, J. & Pomeroy, P.W., 1970. The foreshock-aftershock sequence of the March 20, 1966 earthquake in the Republic of Congo. Bull. Seismol. Soc. Am., 60(4),1245-1258

Langston, C.A. & Helmberger, D., 1975. A procedure for modeling shallow dislocation sources, Geophys J.R. Astr. Soc., 42,117-130.

Langston, C.A., 1977. The effect of planar dipping structure on source and receiver responses for constant ray parameter. Bull. Seismol. Soc. Am., 67(4),1029-1050

Langston, C.A., 1981. Source inversion of seismic wave forms: the Koyno, India, earthquake of September 13, 1967, Bull. Seismol. Soc. Am., 71,1-24.

Long, R.E., Backhouse, R.W., Maguire, P.K.H. & Sundarlingham, K., 1972. The structure of East Africa using surface wave dispersion and Durham seismic array data. in: R. W. Girdler (editor), East African Rifts, Tectonophysics, 15(+),165-178

Loupekine, I.S., 1966. Uganda,the Toro earthquake of 20 March 1966. Unesco, Paris, pp 1-38

Maasha, N. & Molnar, P., 1972. Earthquake fault parameters and tectonics in Africa. J. Geophys Res., 77(29), 5731-5743

Maasha, N., 1975. The seismicity of the Ruwenzori region of Uganda. J. Geophys Res., 80(11),1485-1496

McKenzie, D.P., Davis, D., & Molnar, P., 1970. Plate tectonics of the Red Sea and east Africa, Nature, 26, 243-248

Meissner, R. & Strehlau, J., 1982. Limits of stresses in continental crusts and their relation to the depth-frequency distribution of shallow earthquakes, Tectonics, 1(1),73-89

Minster, J.B., Jordan, T.H., Molnar, P., Haines, E., 1974. Numerical modeling of instantaneous plate tectonics, Geophys J.R. Astr. Soc., 36,541-576

Minster, B.J., Jordan, T.H., 1978. Present-day plate motions, J. Geophys. Res., 83(817),5331-5354

Mohr, P.A., 1967a. The Ethiopian rift system. Bull. Geophys. Observa. Addis Ababa, 11,1-65

Mohr, P.A., 1967b. Major volcanic-tectonic lineament in the Ethiopian rift system. Nature, Lond., 213,664-665

Mueller, St., 1968. Geophysical aspects of graben formation in continental rift systems. in: Graben Problems, E. Schweizerbart'sche Verlagsbuchhandlung, Stuttgart, 1970. pp 27-37

Ramberg, I.B. & Neumann, E.R. (eds), Tectonics and geophysics of continental Rifts. D. Reidel Publishing, 1977.

Reeves, C.V. & Hutchins, D.G., 1975. Crustal structure in central southern Africa. Nature, 254,408-409

Rykounov, L.N., Sedov, V.V., Savrina, L.A. & Bourmin,V., 1972. Study of microearthquakes in the rift zones of East Africa. in: R. W. Girdler (editor), East African Rifts, Tectonophysics, 15(+),123-130

Scholz, C.H., Koczynski, T.A. & Hutchins,D.G., 1976. Evidence of incipient rifting in southern Afrcia. Geophys J. R. astr. Soc., 44,134-144

Shudofsky, G.N., 1985. Source mechanisms and focal depths of East African earthquakes using Rayleigh-wave inversion and body-wave modelling. Geophys J. R. astr. Soc., 83,563-614

Strehlau, J. & Meissner, R., 1982. Earthquakes in continental crust: temperature dependence of maximum focal depth. submitted to J. Geophys. Res., Novermber 1982.

Strehlau, J., 1985. A discussion of the depth extent of rupture in large continental earthquakes. submitted to Proceedings of the 5th Maurice Ewing Symposium on Earthquake Source Mechanics

Stump, B.W. & Johnson, L.R., 1977. The determination of source properties by the linear inversion of seismograms. Bull. Seismol. Soc. Am., 67(6),1489-1502.

Sykes, L.R., Landisman, M., 1964. The seismicity of east Africa, the Gulf of Aden and the Arabian and Red Seas, Bull. Seismol. Soc. Am., 54(6),1927-1940.

Sykes, L.R., 1967. Mechanism of earthquakes and nature of faulting in the mid-oceanic ridges, J. Geophys. Res., 72(8),2131-2153.

Tazieff, H., 1968. Tectonics of northern Afar (or Danakil) rift. in, Graben Problems, E. Schweizerbart'sche Verlagsbuchhandlung, Stuttgart, 1970. pp 280-283

Wiggins, R.A., 1972. The general linear inverse problem: implications of surface waves and free oscillations on the earth structure. Rev. Geophys. and Space Phys., 10, 251-285.

Wohlenberg, J., 1966. Remarks on the Uganda earthquake of March 20, 1966. Chroniue de L'IRSAC (Institut pour la Recherche Scientifique en Afrique Centrale, Lwiro, Rep.

TABLE 1.1

moment tensor elements ($\times 10^{25}$ dyne cm)

event	M_{11}	M_{22}	M_{12}	M_{13}	M_{23}
Ethiopia	-0.742	0.272	-0.485	-0.076	-0.580
$\Delta\sigma_p$	.0716	.0666	.0538	.0072	.0345
Congo	-0.383	-0.606	0.493	0.074	0.074
$\Delta\sigma_p$	.0352	.0428	.0963	.0072	.0107
Zambia (Dec)	-0.150	-0.644	0.267	-0.099	0.103
$\Delta\sigma_p$	.0369	.0563	.0286	.0126	.0303
Zambia (May)	-0.632	-0.345	0.473	-0.196	0.050
$\Delta\sigma_p$	.0611	.0686	.0445	.0178	.0095
S. Africa	-0.956	0.956	0.293	0.002	0.014
$\Delta\sigma_p$	.0570	.0507	.0277	.0007	.0019

TABLE 1.2

time functions($\Delta\sigma_p$) - 1 second box cars

Time progresses from left to right, top to bottom.

Ethiopia	.08 (.014)	.23 (.026)	.39 (.048)
	.25 (.038)	.09 (.001)	-.05 (.001)
Congo	.11 (.017)	.09 (.018)	.08 (.007)
	.09 (.009)	.11 (.015)	.13 (.012)
	.15 (.008)	.14 (.012)	.14 (.008)
	.07 (.006)	.01 (.001)	.02 (.002)
	.03 (.003)	-.03 (.003)	-.09 (.005)
	-.07 (.006)		
Zambia (Dec)	.29 (.038)	.27 (.054)	.25 (.034)
	.17 (.031)	.11 (.026)	.01 (.002)
	-.09 (.003)		
Zambia (May)	.59 (.050)	.34 (.038)	.08 (.012)
	.02 (.009)	-.04 (.007)	
S. Africa	.51 (.033)	.24 (.058)	-.03 (.004)
	.08 (.005)	.19 (.024)	

TABLE 1.3

source depth and condition number

	depth(km)	condition number
Ethiopia	4	30
Congo	10	82
Zambia (Dec)	6	28
Zambia (May)	28	26
S. Africa	4	27
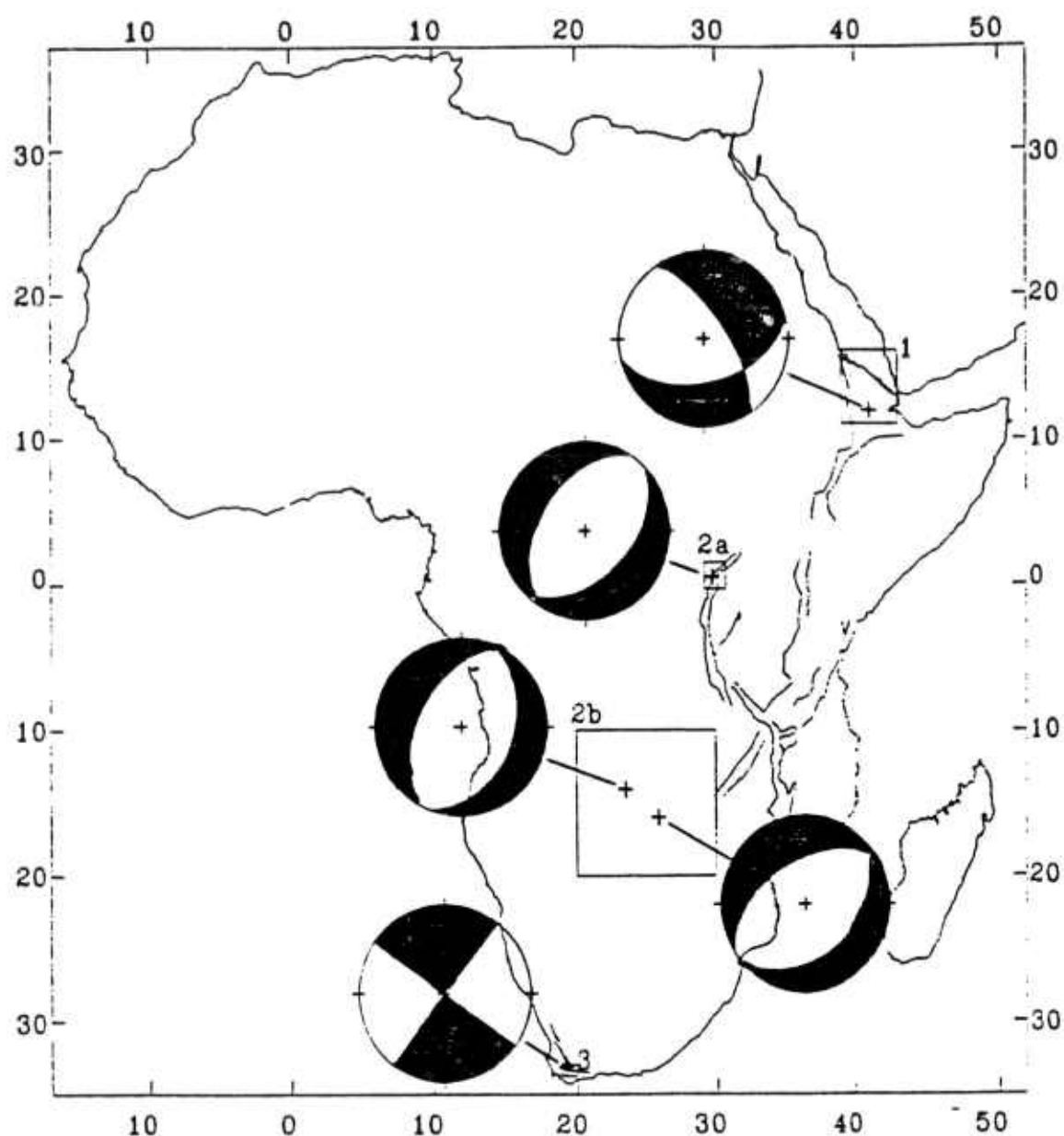
figure 1 - African rift system with lower hemisphere projections of
fault mechanisms determined in this study (black = compression).
Figure 8 shows the detail of block 1, figure 10 shows block 2a, figure
11 shows block 2b, and figure 12 shows detail of block 3.
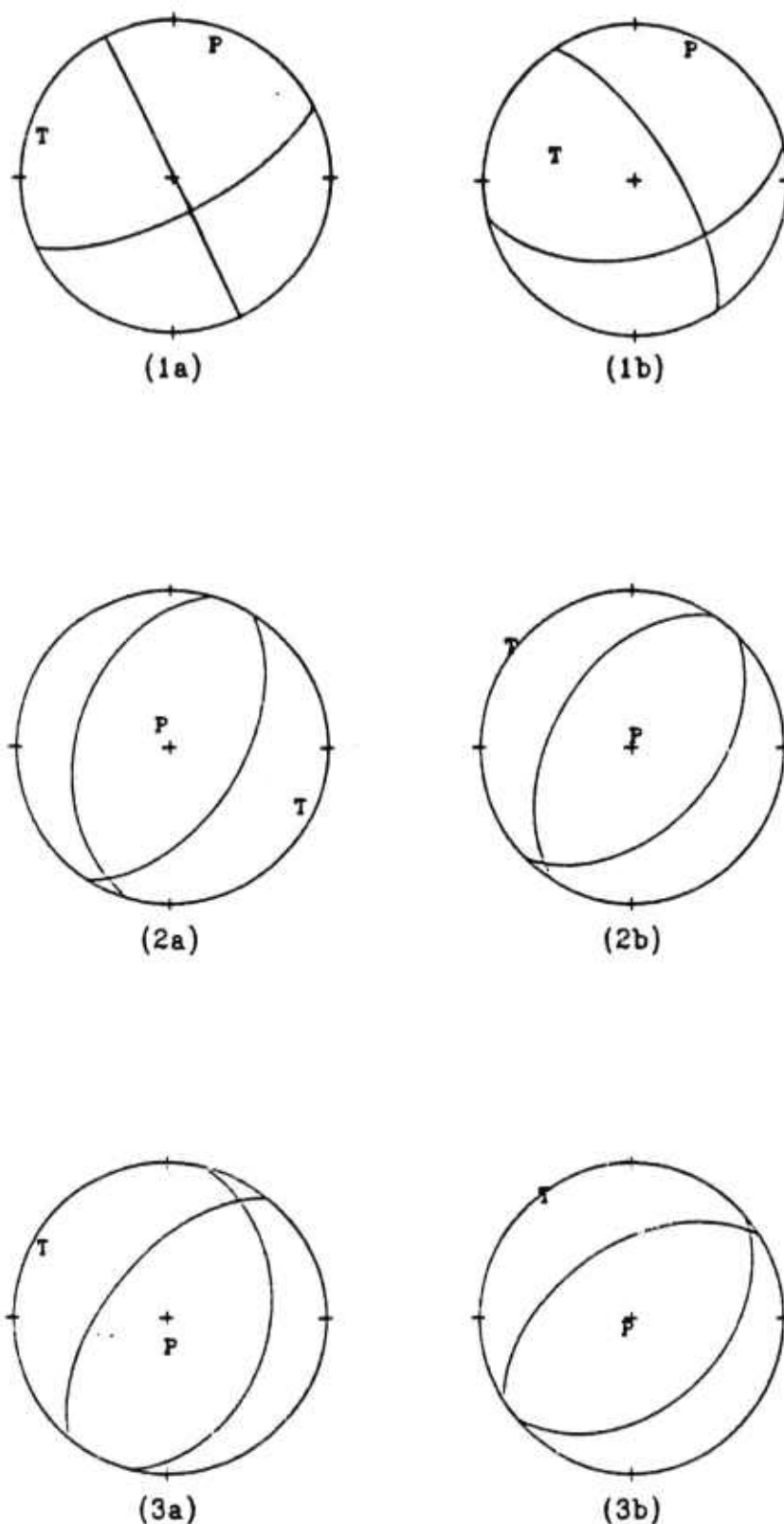
figure 2 - Lower hemisphere projections of mechanisms determined by previous authors and this study; P=pressure axis, T=tension axis.
1: Ethiopia event - (a) McKenzie et al. (1970), (b) this study. 2: Congo event - (a) Sykes (1967), (b) this study. 3: Zambia (December) - (a) Fairhead & Girdler (1971), (b) this study. 4: Zambia (May) - (a) Fairhead & Girdler (1971), (b) this study. 5: South Africa - (a) Maasha & Molnar (1972), (b) this study, (c) Fairhead & Girdler (1971), (d) Green & McGarr [shows range of fault planes] (1972).
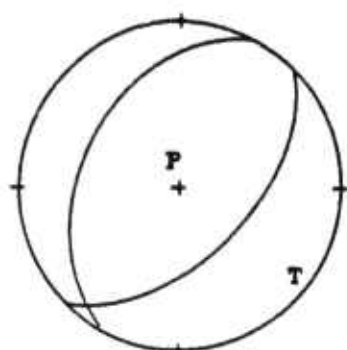
(4a)
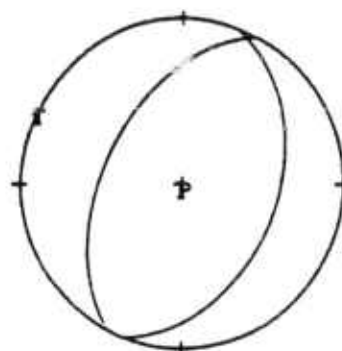
(4b)
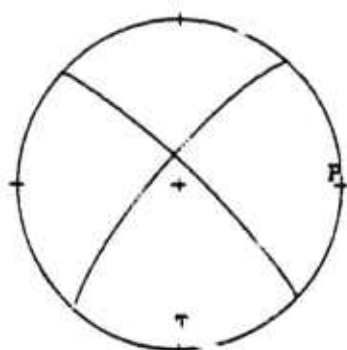
(5a)
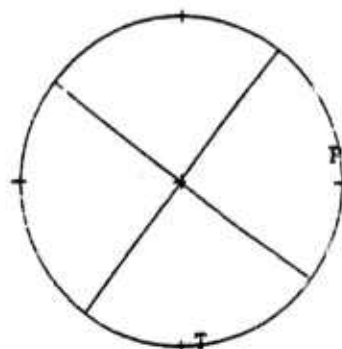
(5b)
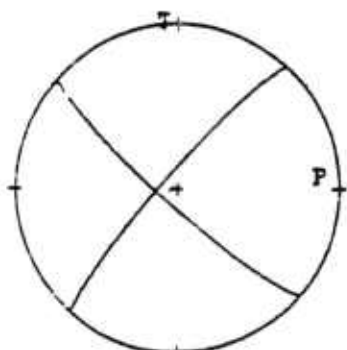
(5c)
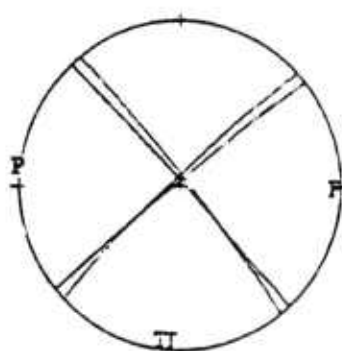
(5d)

figure 2 (cont.)
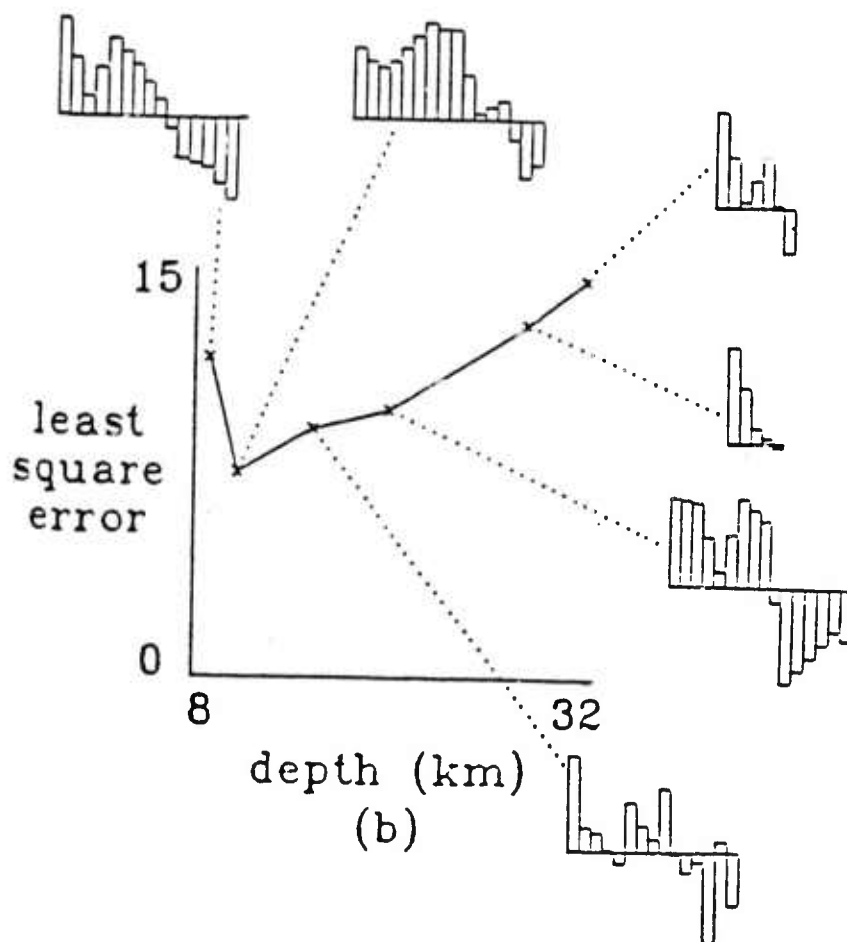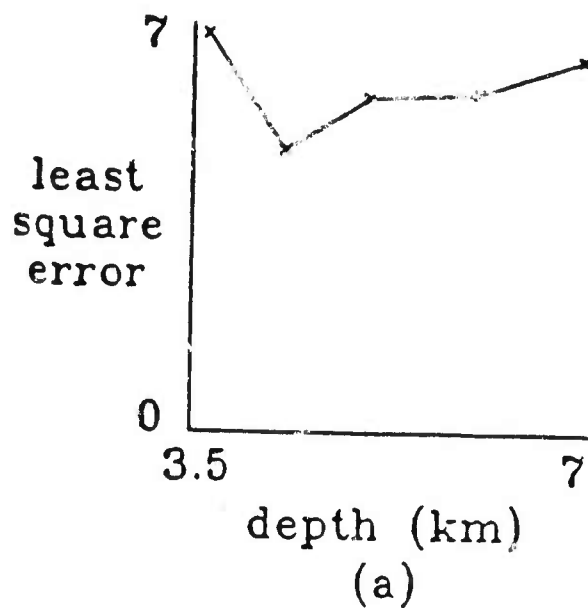
figure 3 - Least square error fit vs. focal depth for: (a) Ethiopia event, (b) Congo event, (c) Zambia event - 5/15/68, (d) Zambia event - 12/2/68, (e) South Africa. The diagram for the Congo event is plotted with its corresponding time functions - each bar represents one second.
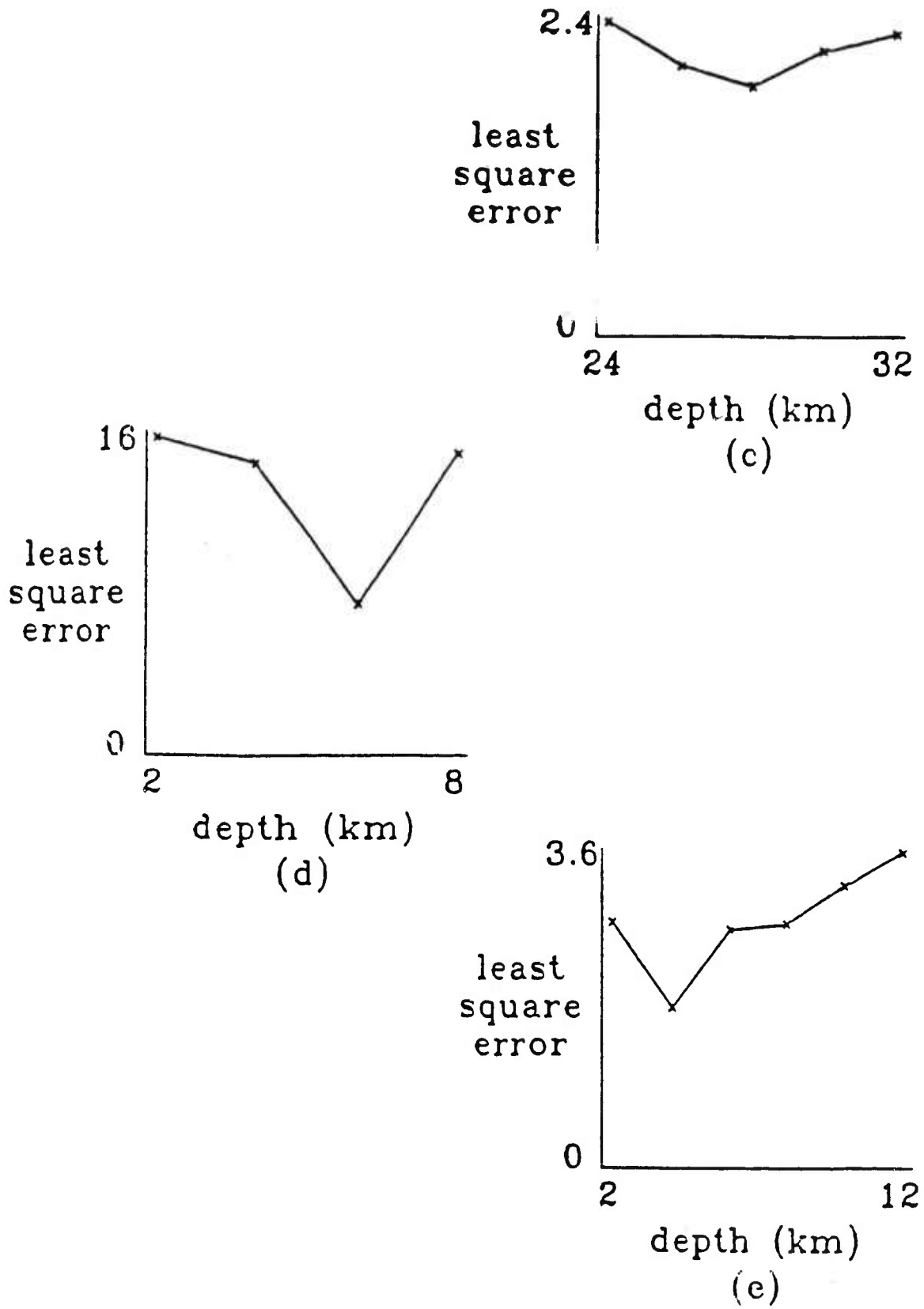
figure 3 (cont.)

Ethiopia (Sardo) (12.0 north - 41.35 east)

## April 5, 1969 - 2:18:30 - M=5.8

depth = 4 km

20 secs
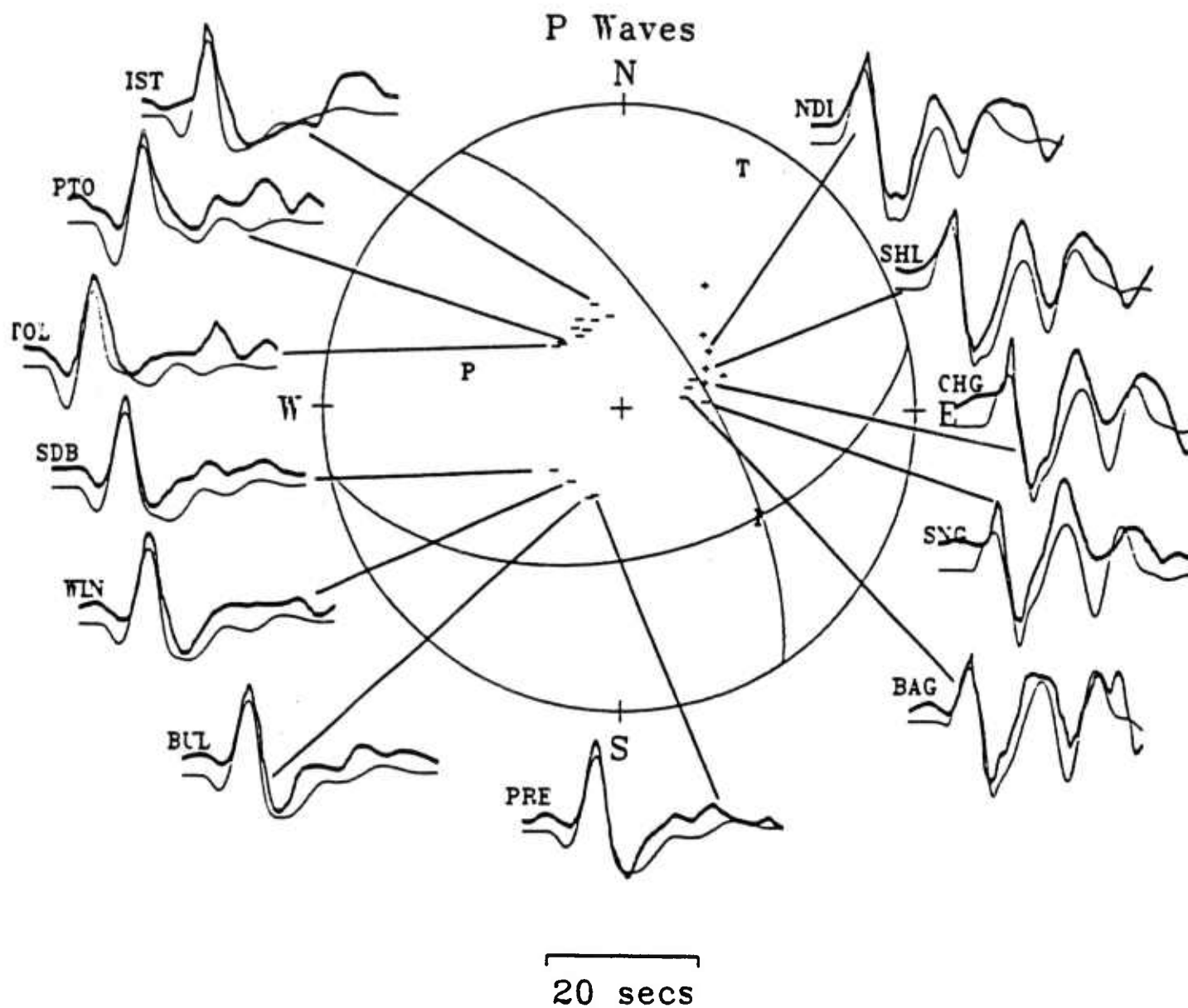
figure 4a

figure 4 - Lower hemisphere projections [(a) P waves, (b) SH waves] of
fault mechanism for the Ethiopia event of April 5, 1969; + signs represent
compression, and - dilatation. The pressure, tension and null axes are
represented by P, T and I respectively. The thicker, darker traces are
those of the observed data.

Ethiopia (Sardo) (12.0 north — 41.35 east)

April 5, 1969 — 2:18:30 — M=5.8

depth = 4 km

SH Waves

20 Secs
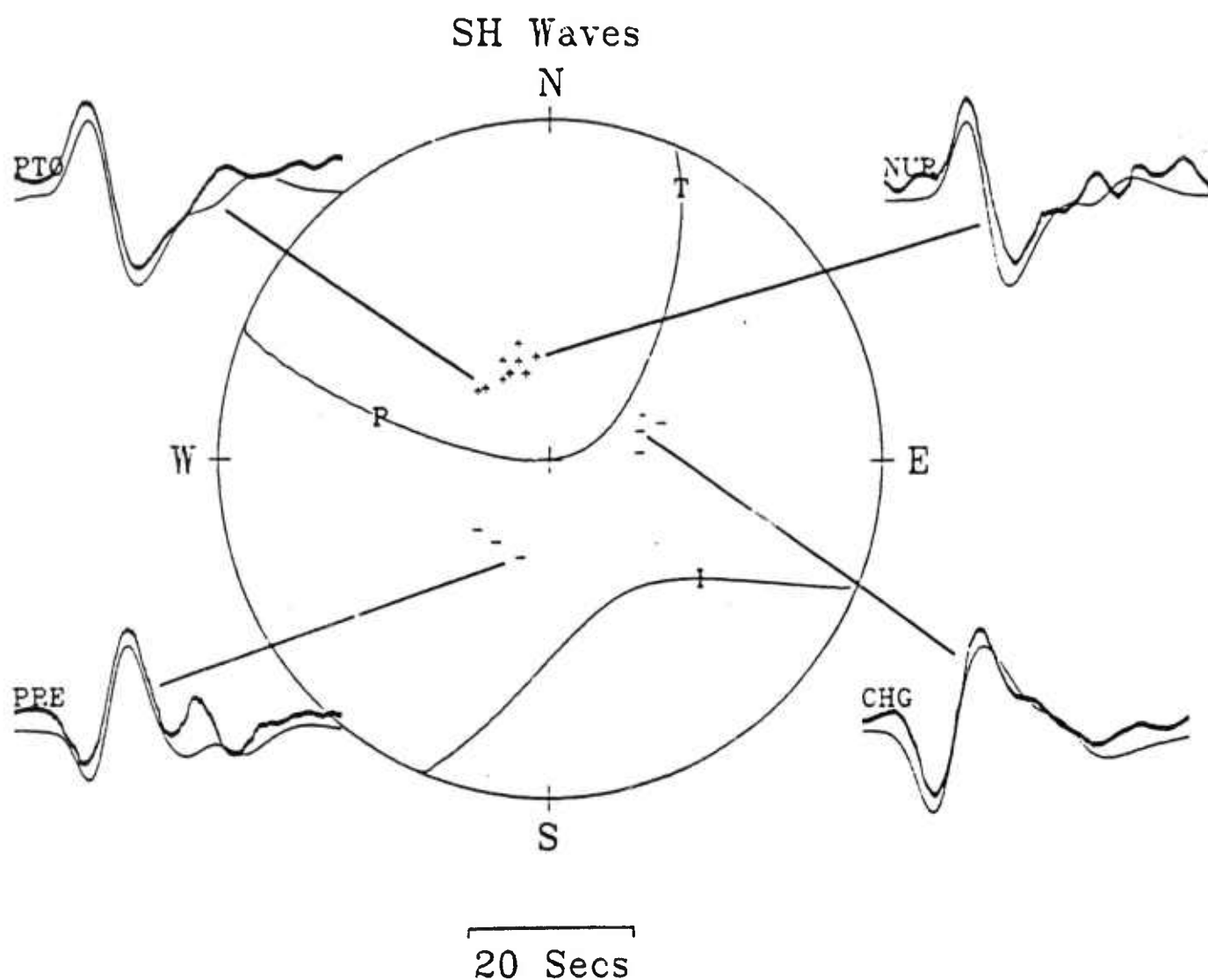
figure 4b

Congo (0.58 north − 30.02 east)
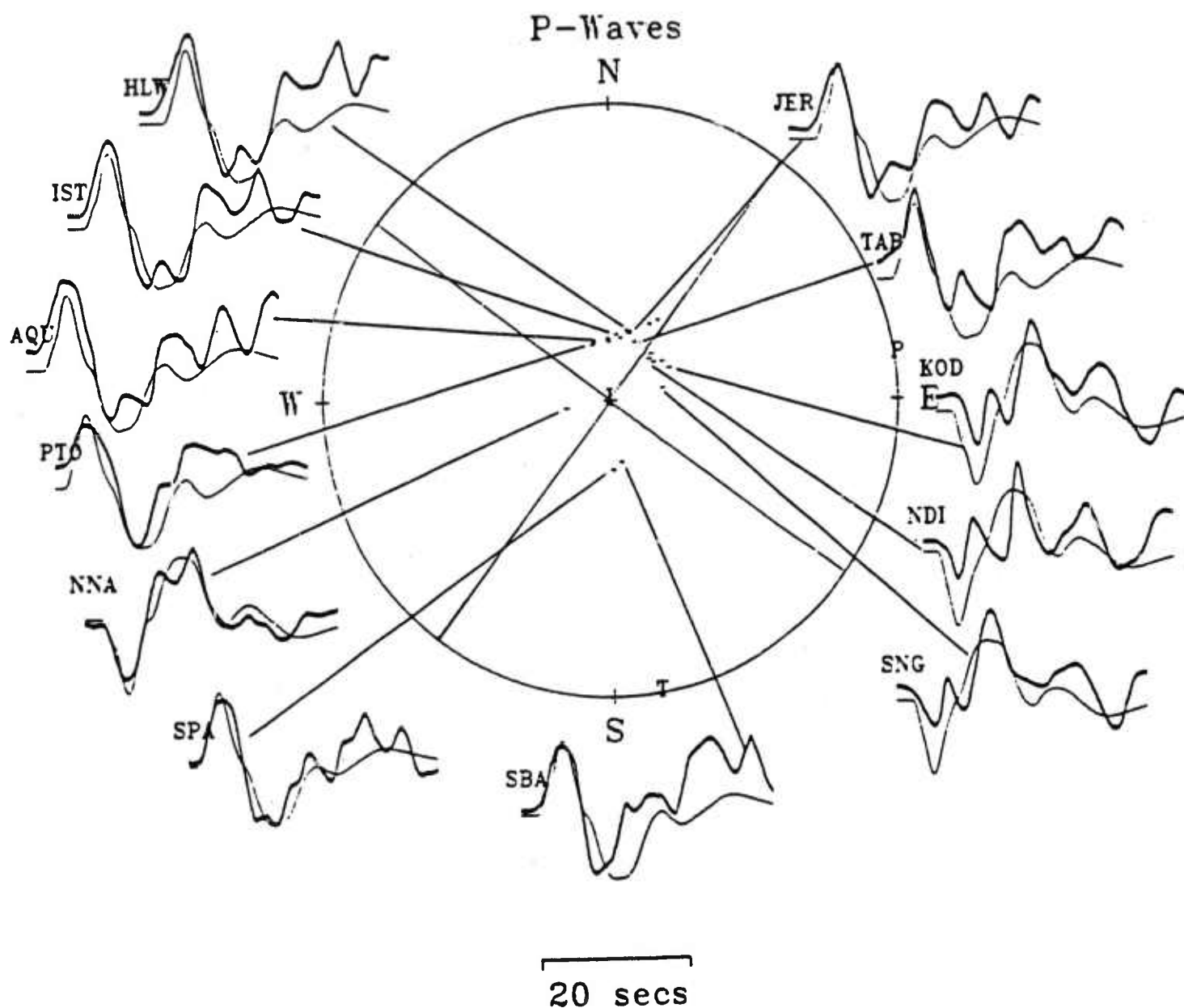
March 20, 1966 − 1:42:51 − M=6.3

depth = 10 km

20 secs
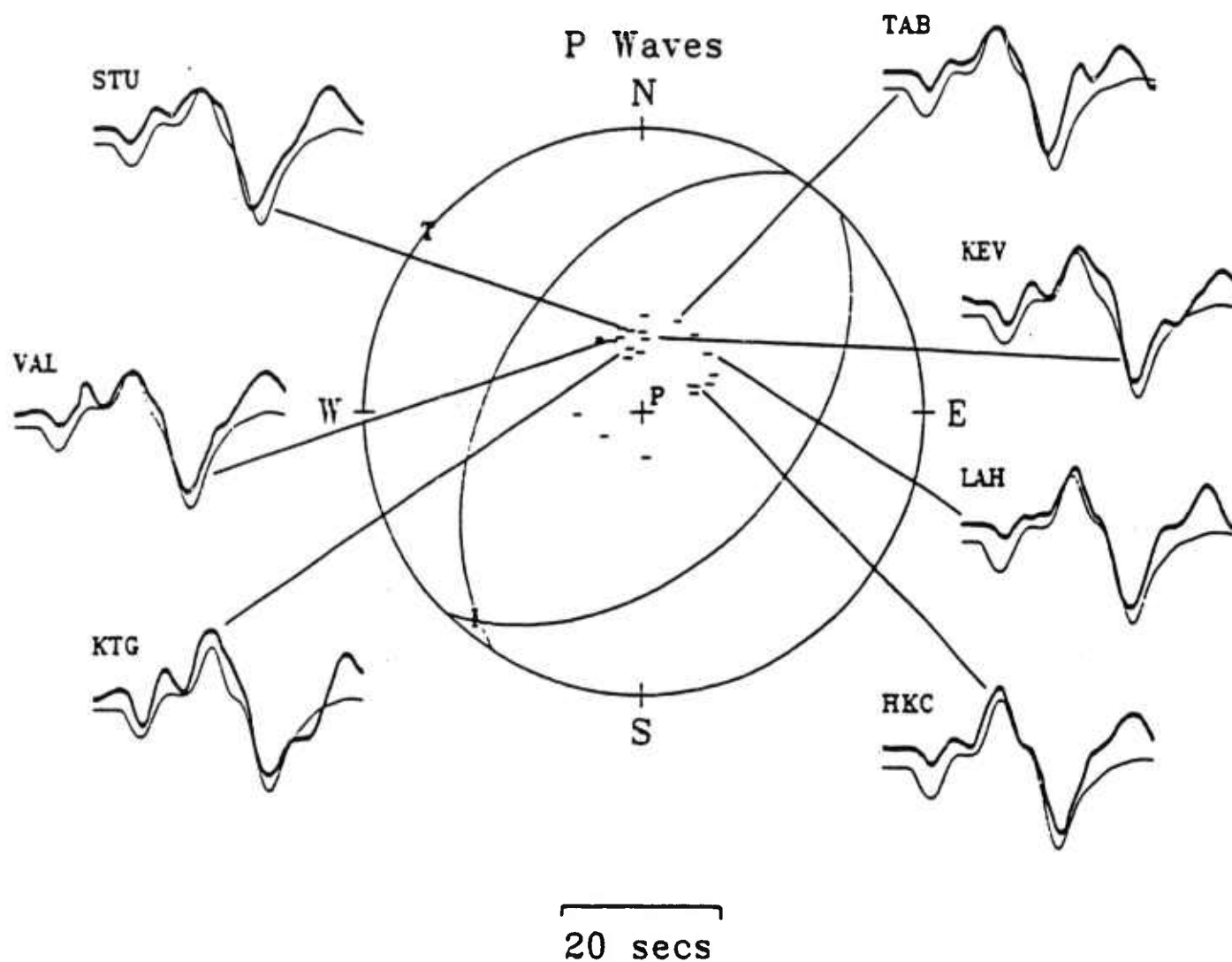
figure 5a

figure 5 − Lower hemisphere projections [(a) P waves, (b) SH waves] of fault mechanism for the Congo event of March 20, 1966; + signs represent compression, and − dilatation. The pressure, tension and null axes are represented by P, T and 1 respectively. The thicker, darker traces are those of the observed data.

Congo (0.58 north - 30.02 east)

March 20, 1966 - 1:42:51 - M=6.3

depth = 10 km

SH Waves

20 secs
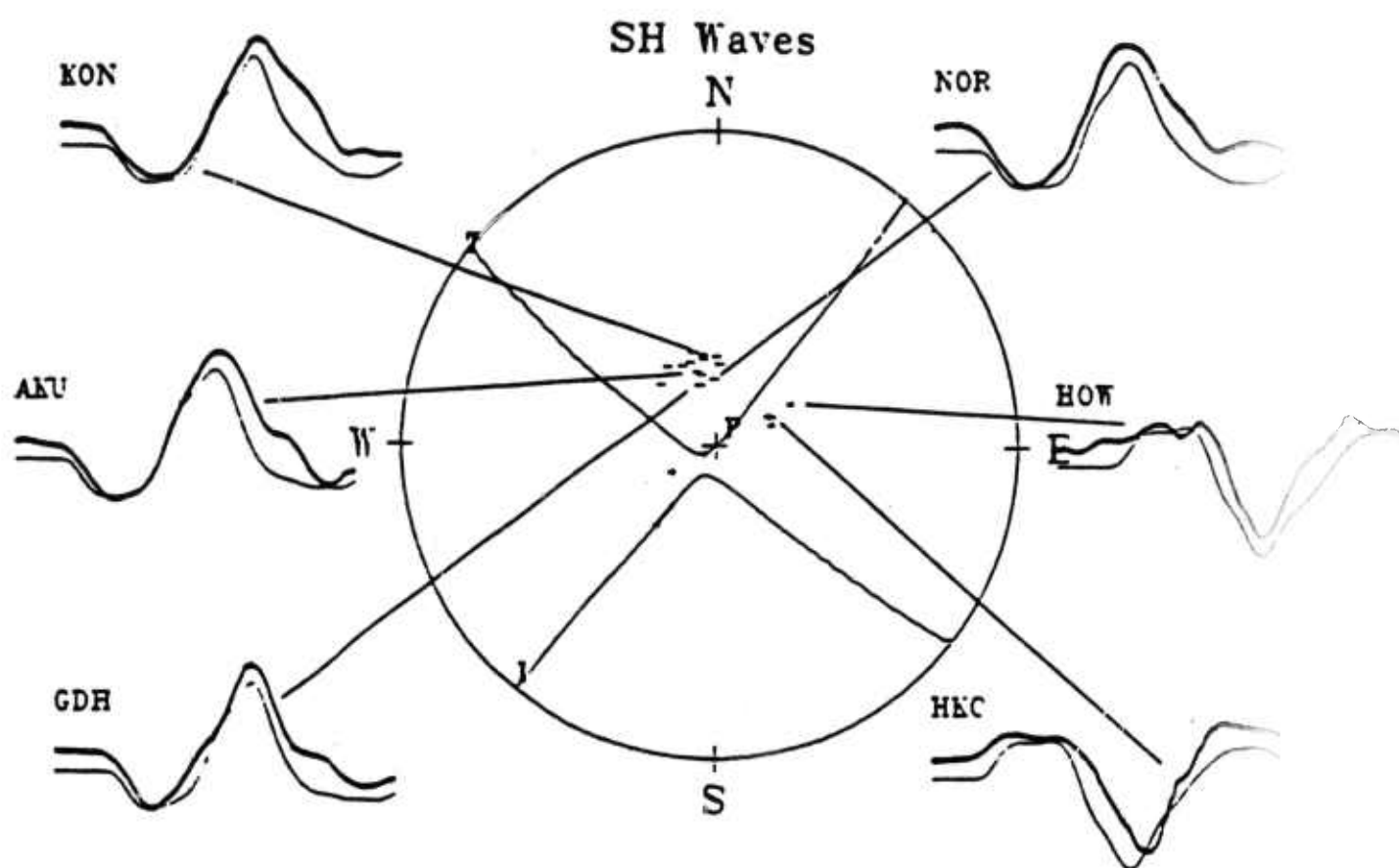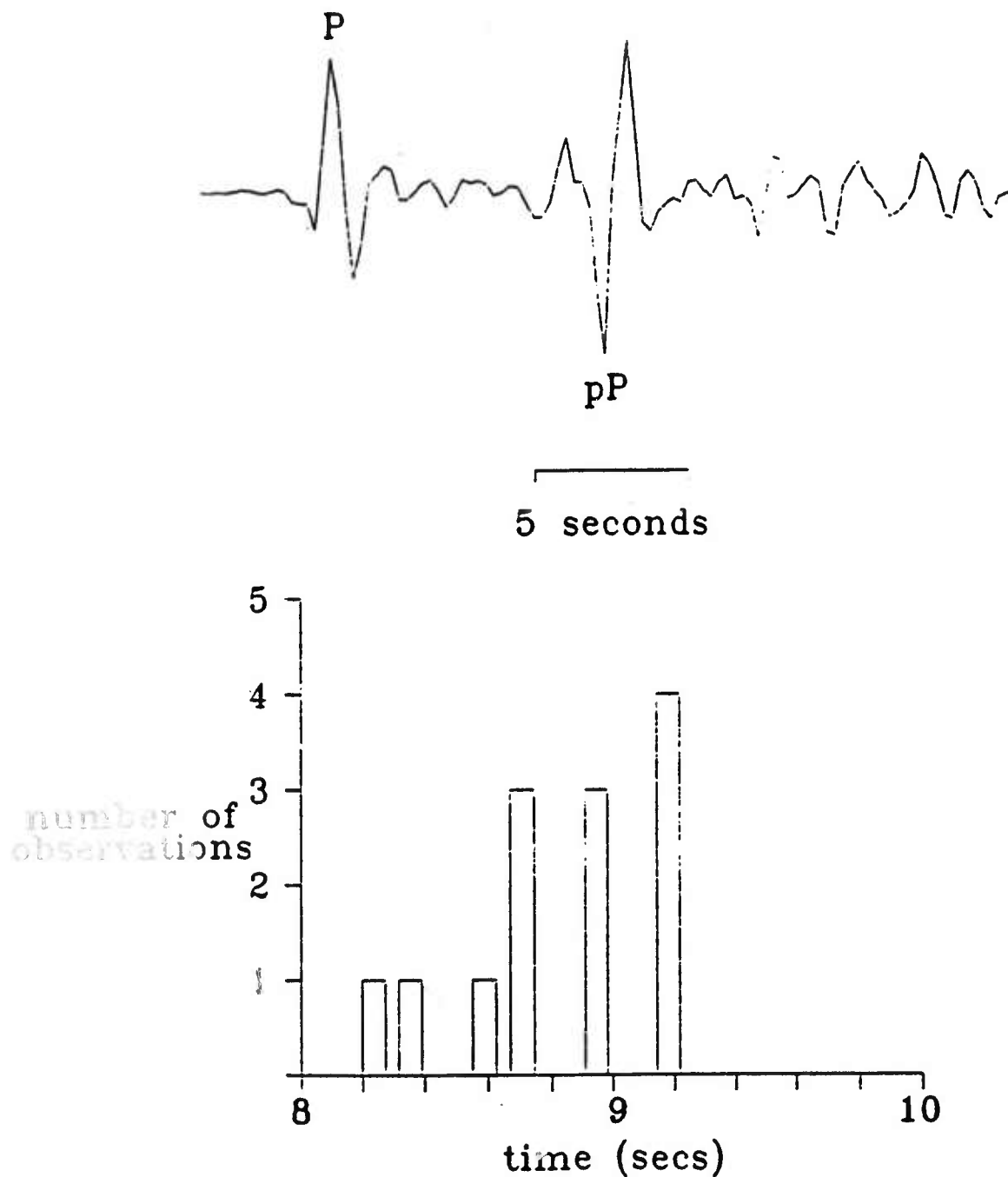
figure 5b

figure 6 - Histogram representing the number of short period records with a given pP-P time for the May 15, 1968 Zambia event. The short-period P wave recorded at POO (WWSSN station) shows pP-P separation.

Zambia (15.91 south — 26.16 east)

May 15, 1968 — 7:51:16.5 — M=5.7

depth = 28 km

20 secs
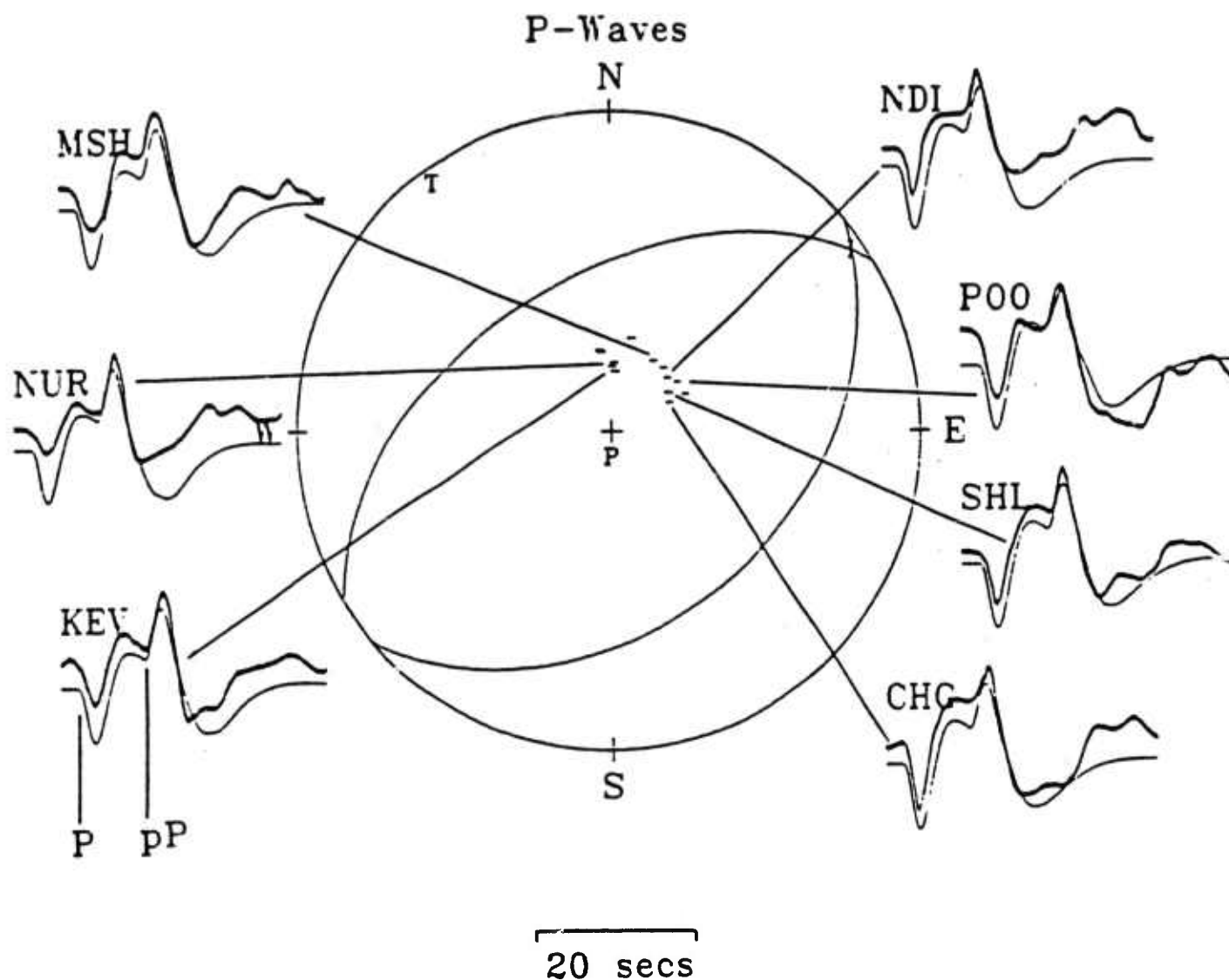
figure 7a

figure 7 - Lower hemisphere projections [(a) P waves, (b) SH waves] of fault mechanism for the Zambia event of May 15, 1968; + signs represent compression, and - dilatation. The pressure, tension and null axes are represented by P, T and I respectively. The thicker, darker traces are those of the observed data.

Zambia (15.91 south – 26.16 east)

May 15, 1968 – 7:51:16.5 – M=5.7

depth = 28 km
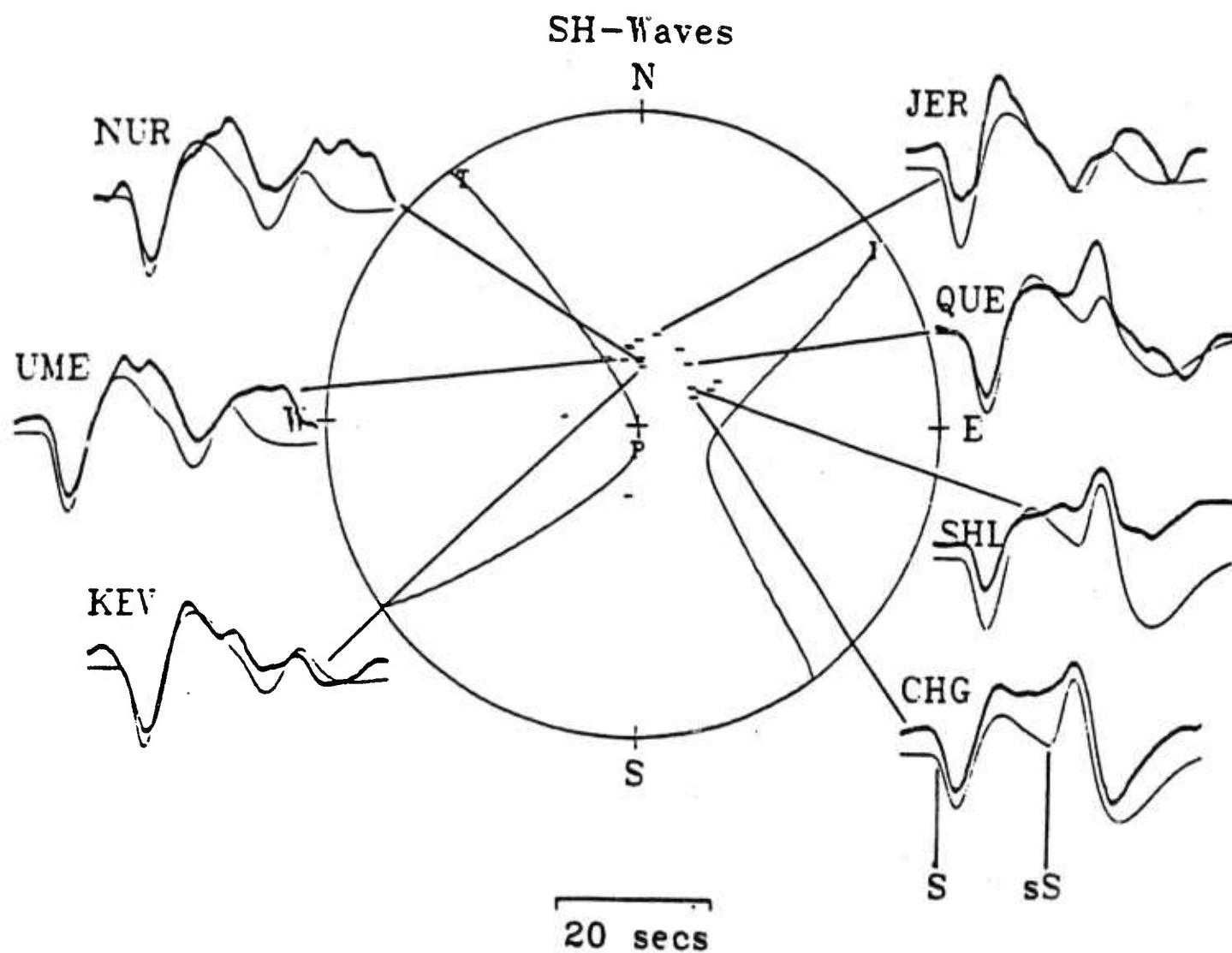
SH–Waves

figure 7b

Zambia (14.01 south – 23.82 east)

December 2, 1968 – 2:33:42.4 – M=5.9

depth = 6 km
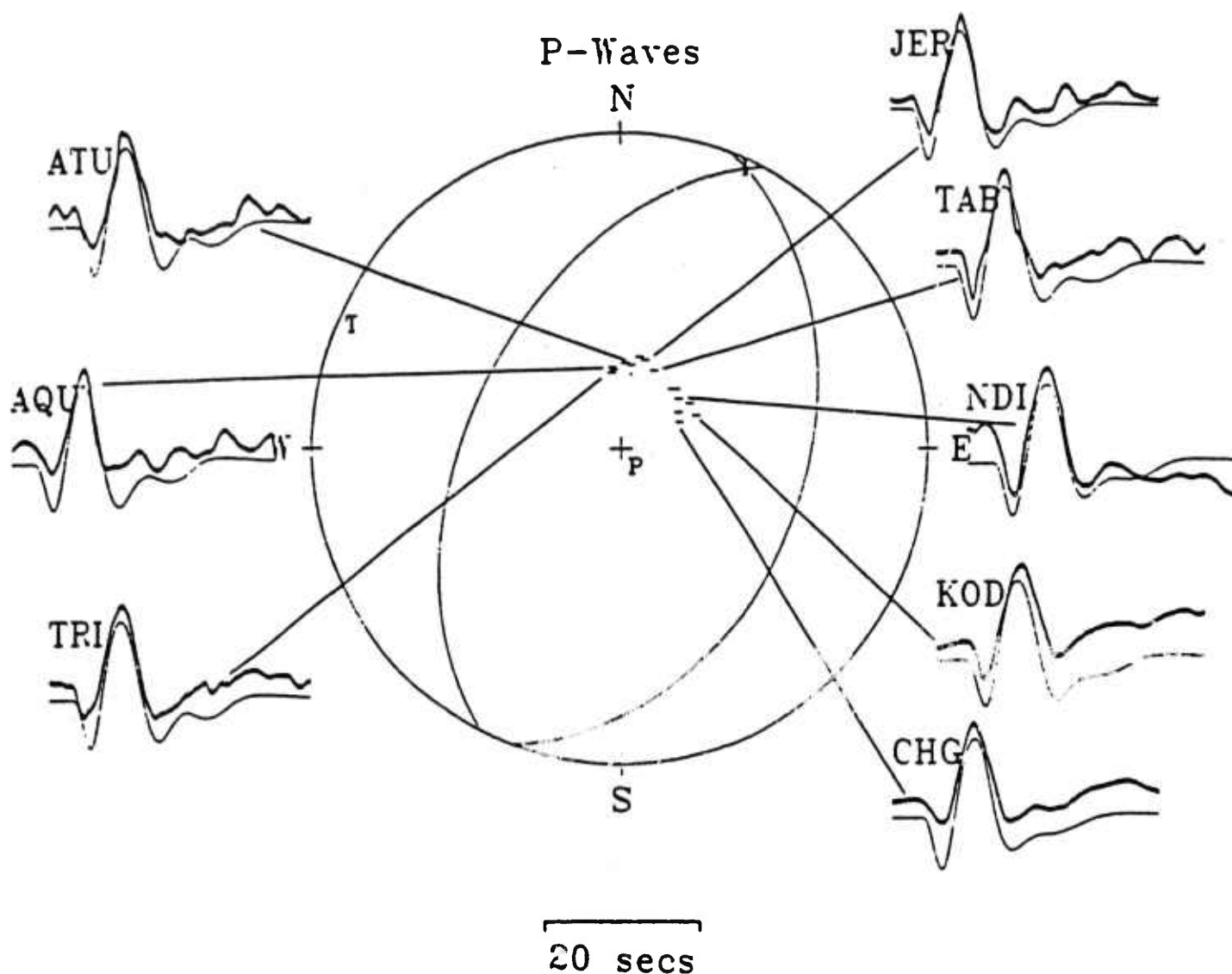
figure 8a

figure 8 - Lower hemisphere projections [(a) P waves, (b) SH waves] of fault mechanism for the Zambia event of December 2, 1968; + signs represent compression, and - dilatation. The pressure, tension and null axes are represented by P, T and I respectively. The thicker, darker traces are those of the observed data.

Zambia   (14.01 south   –   23.82 east)

December 2, 1968   –   2:33:42.4   –   M=5.9

depth = 6 km

figure 8b

South Africa (Ceres) (33.09 south – 19.52 east)

September 29, 1969 – 20:03:32 – M=5.6

depth = 3 km

figure 9a

figure 9 – Lower hemisphere projections [(a) P waves, (b) SH waves] of fault mechanism for the South Africa event of September 29, 1969; + signs represent compression, and – dilatation. The pressure, tension and null axes are represented by P, T and I respectively. The thicker, darker traces are those of the observed data.

South Africa (Ceres)   (33.09 south — 19.52 east)

September 29, 1969 — 20:03:32 — M=5.6

depth = 3 km

SH—Waves
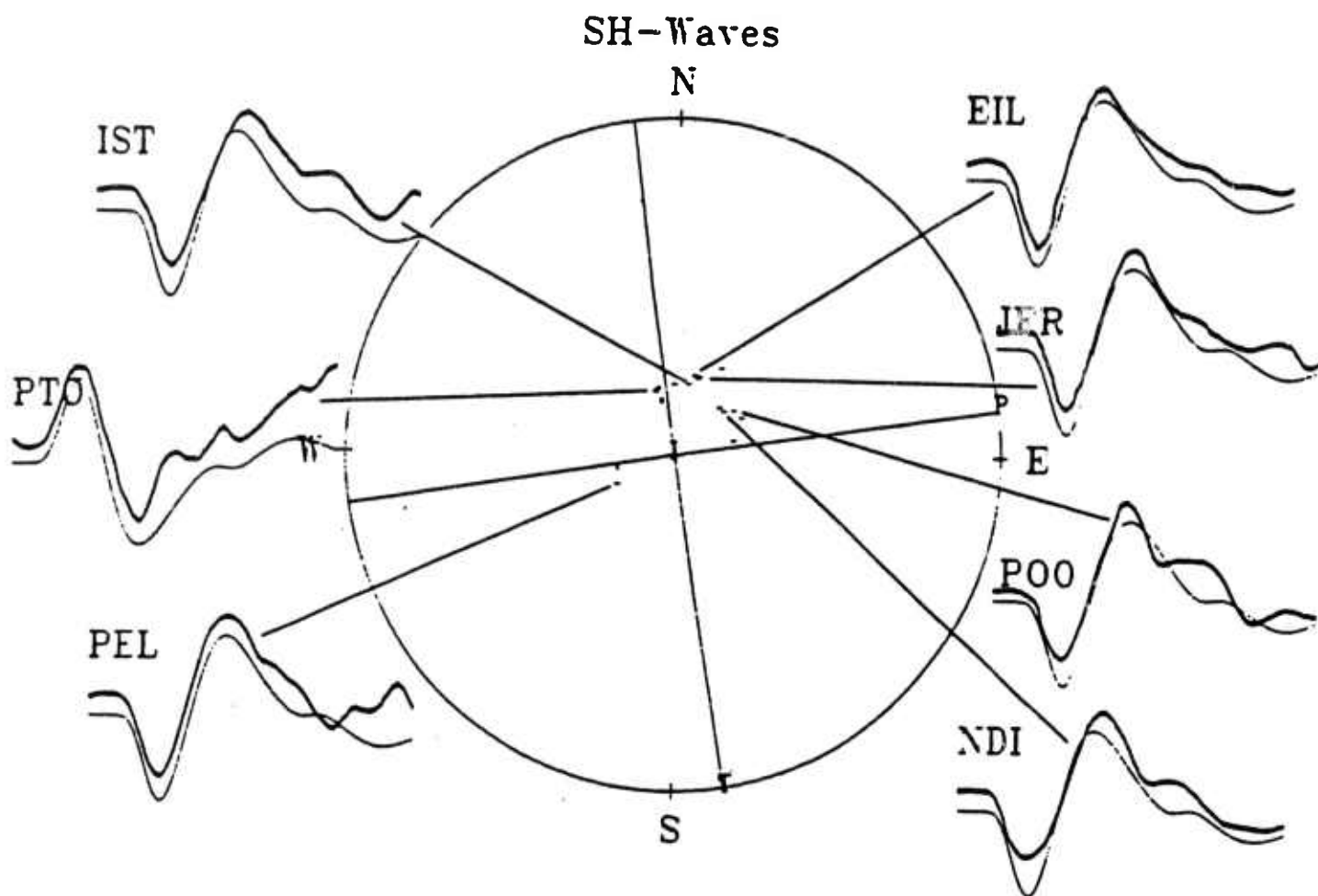
20 secs
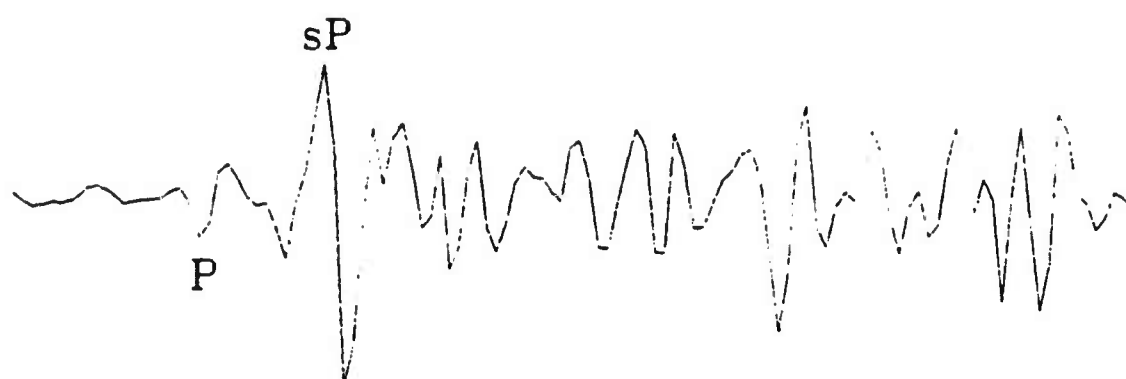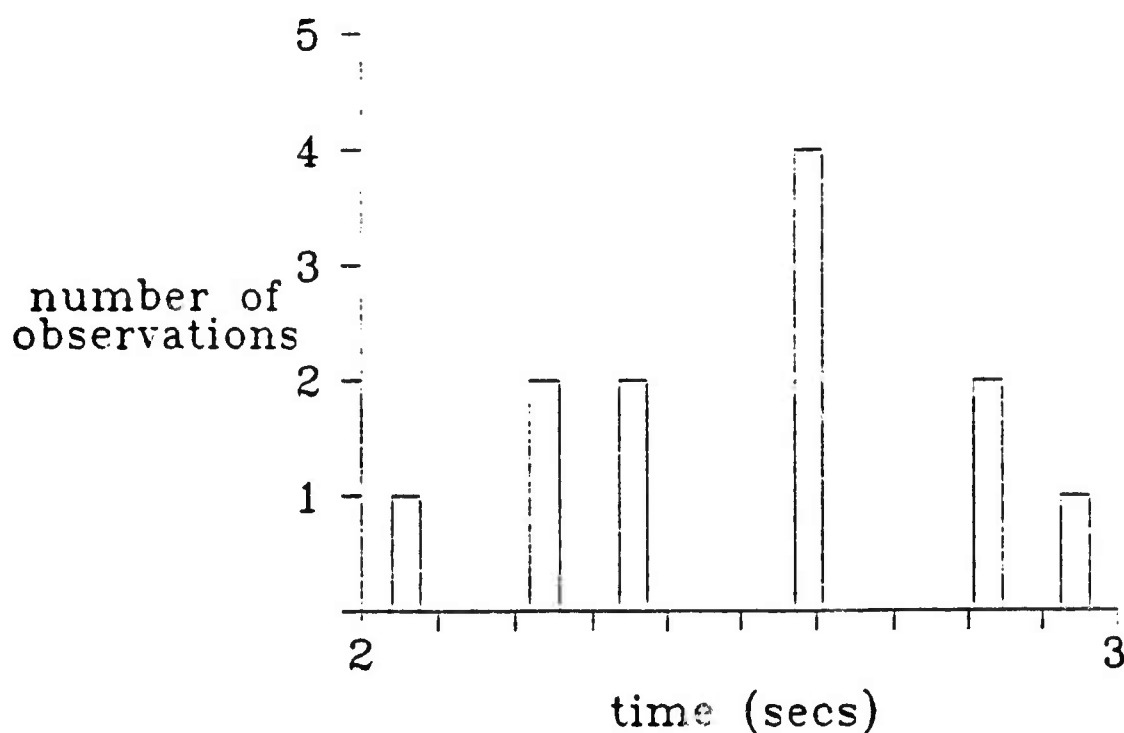
figure 9b

figure 10 - Histogram representing the number of short period records
with a given sP-P time for the September 29, 1969 South Africa event.
The short-period P wave recorded at ARE (WWSSN station) shows sP-P
separation. Measurement error is estimated to be q0.1 seconds.
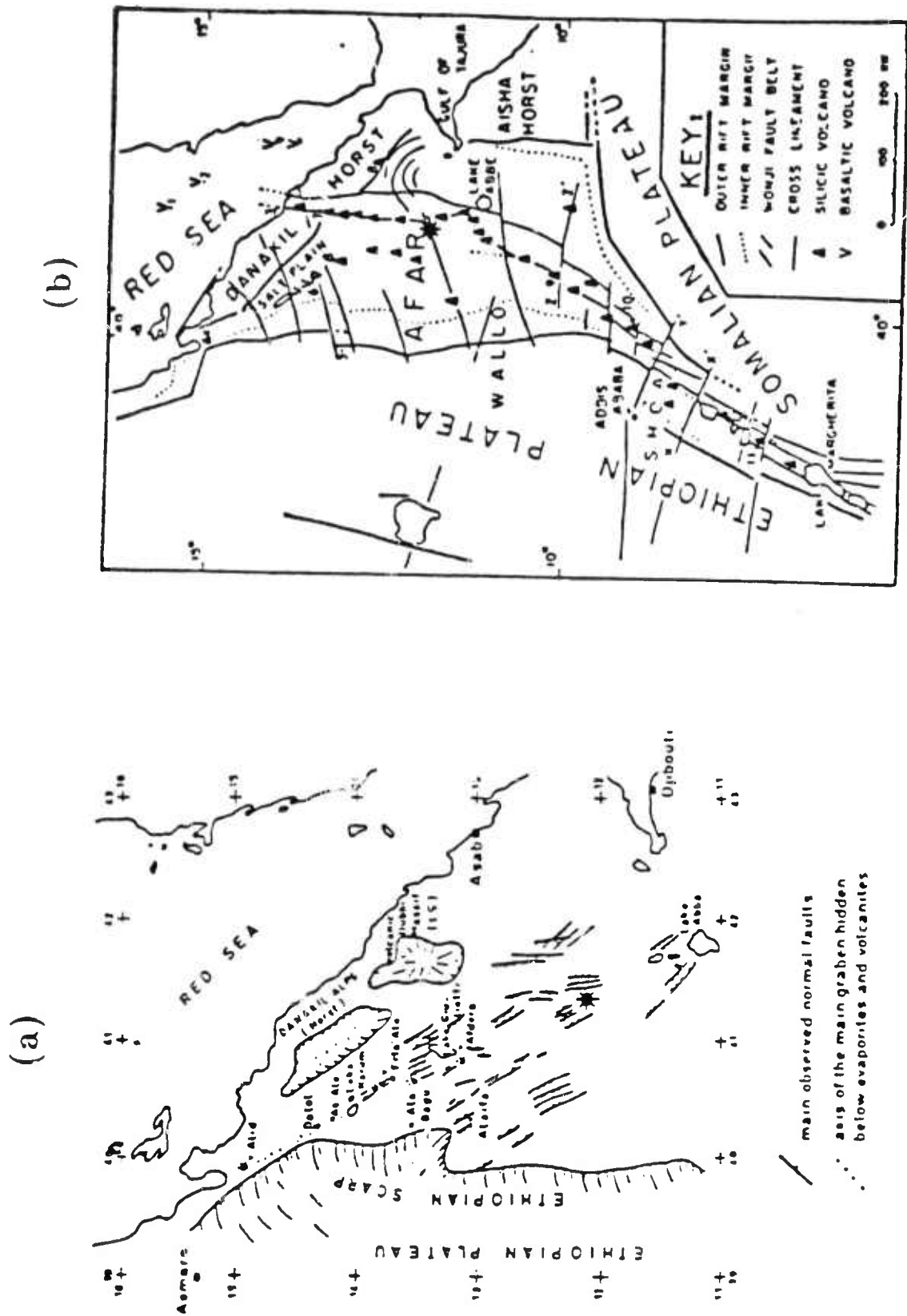
figure 11 - Interpretations of faulting in the Afar region by: (a) Tazieff (1968), and (b) Mohr (1967b - figure from St. Mueller, 1968). Epicenter of the April 5, 1969 Ethiopia event is denoted by the black star. This area is contained within block 1 of figure 1.
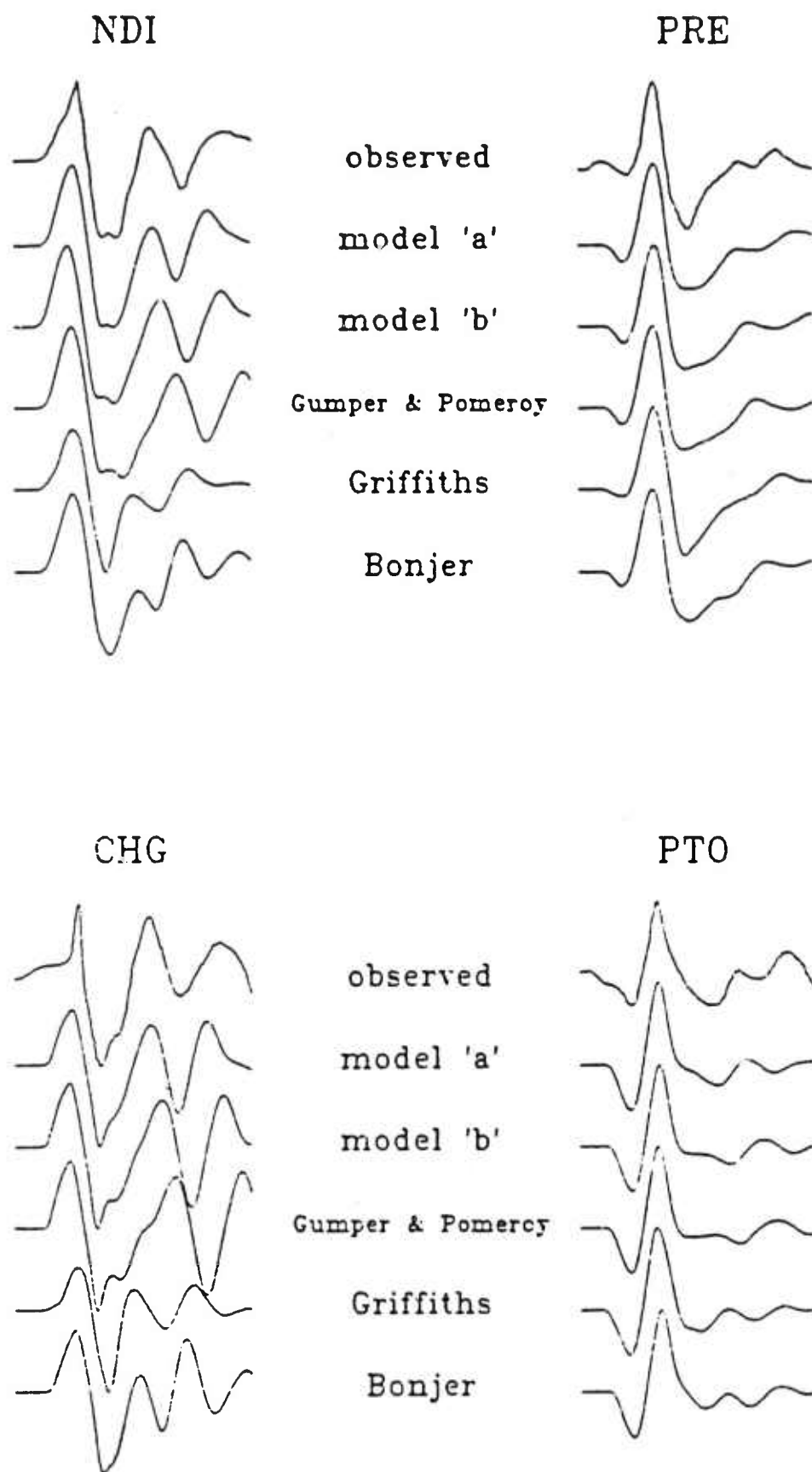
figure 12 - Observed data, and synthetics computed using the mechanism of
the April 5, 1969 Ethiopia event and several different crustal models.
Model (a) - 28 km thick, model (b) - 32 km thick, Gumper & Pomeroy (1970)
- 36 km thick, Griffiths et al. (1971) - 21 km thick, Bonjer et al. (1970)
- 40 km thick.
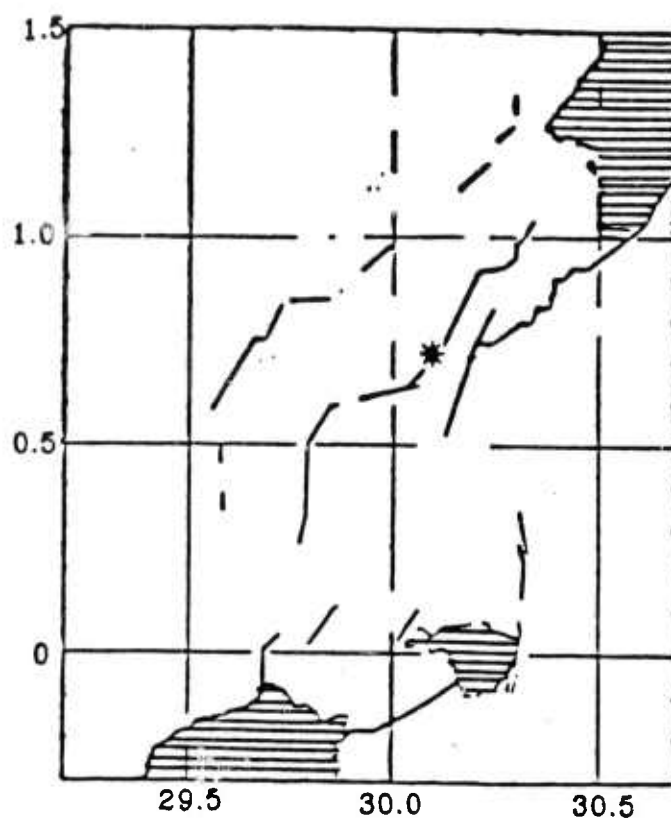
(a)
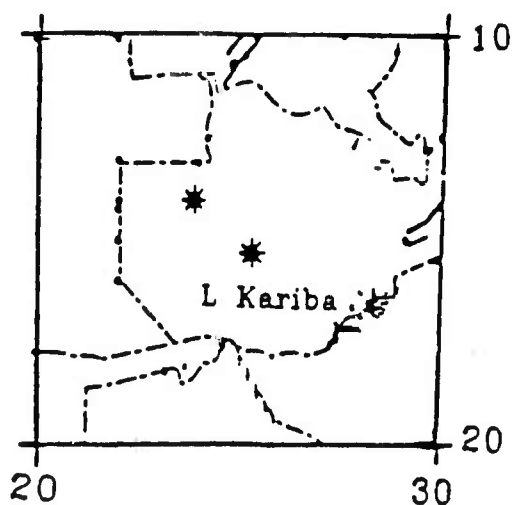
(b)

figure 13 - (a) - Epicenter location (black star) and faults in the area of the March 20, 1966 Congo event. Hatched area in the upper right is Lake Albert, and in the lower left is Lake Edward (Lahr & Pomeroy, 1970). This area is contained within block 2a of figure 1. (b) - Epicentral locations of the Zambia events, map from Chapman & Pollack (1977). Stars represent the location of the December 2nd (upper left), and May 15th (lower right) events. This area is contained within block 2b of figure 1.
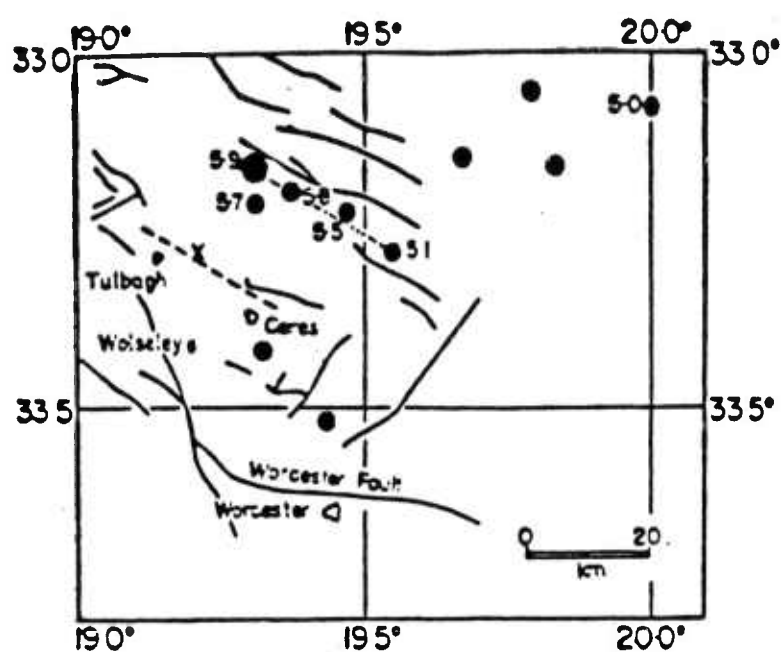
figure 14 - Faulting in the area of the September 29, 1969 South African event; the large (M=5.9) dot represents the main shock (Fairhead & Girdler, 1971). This area is contained within block 3 of figure 1.
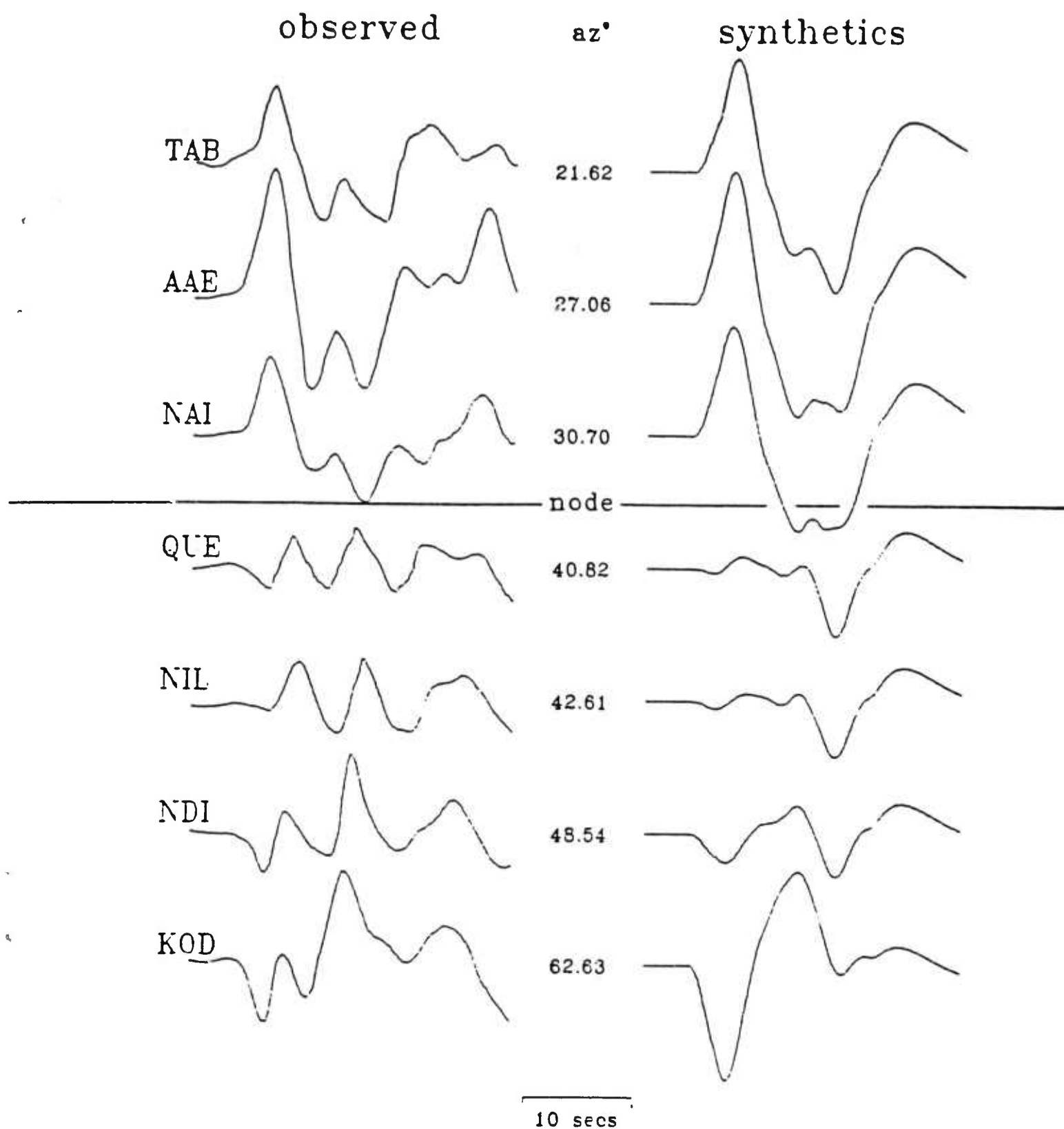
figure 15 – Observed P wave data from the September 29, 1969 South Africa event plotted adjacent to synthetics computed assuming a seaward thinning crust (dipping moho).

SECTION 7

The Pennsylvania State University

The Graduate School

Department of Geosciences

Upper Mantle P-Velocity Structure

between Eastern North America and Hispaniola

A Paper in

Geophysics

by

Nancy L. Niemann

Submitted in Partial Fulfillment
of the Requirements
for the Degree of

Master of Science

December 1986

Nancy L. Niemann

Nancy L. Niemann

We approve the thesis of Nancy L. Niemann.

Date of Signature:

August 7, 1986

Charles A. Langston
Professor of Geophysics,
Thesis Advisor

8 August 1986

Shelton S. Alexander
Professor of Geophysics,
Chairman of the Department
of Geosciences

8 August, 1986

Earl K. Graham, Jr.
Professor of Geophysics,
Chairman of the Geophysics
Graduate Program

8 August 1986

Roy J. Greenfield
Professor of Geophysics

ABSTRACT

Body-waveforms from the eastern Hispaniola earth-
quake of September 14, 1981, were compared to synthetic
seismograms to investigate the upper mantle P-velocity
structure of eastern North America. The event occurred
at an intermediate depth, 170 km, ensuring that phases
that arrived after direct P were sufficiently delayed
that they did not interfere with the triplicated direct
P phases. Triplicated phases are best observed in
intermediate-period data. In the model of this paper,
the lower discontinuity lies at 670 km, instead of at
650 km as in a published model for the region. The new
velocity model is identical to the published model above
640 km.

ACKNOWLEDGMENTS

INTRODUCTION

Seismic waveforms recorded at stations 15° to 30° from earthquake sources have produced as much knowledge about the methods used to study them as they have about the P and S velocities of the upper mantle. In the present study, an attempt to define a slight lateral variation in the depth of the 650-km discontinuity contributes to this knowledge.

The eastern Hispaniola earthquake of September 14, 1981, with body-wave magnitude 5.9 (International Seismological Centre, 1983), generated waveforms that are useful for studying wave propagation beneath the ocean off the southeast coast of the United States. The data used in this study are adequate to study the region defined by +'s in Figure 1. The earthquake source function is simpler than many that have been modeled in previous upper mantle waveform studies (cf. Burdick, 1981). The event's hypocenter was 172±1.9 km deep (International Seismological Centre, 1983). Phases arriving after direct P are sufficiently delayed that they do not interfere with the triplicated P phases. In principle, therefore, the simpler source function and greater depth should make observing the triplication branches easier.
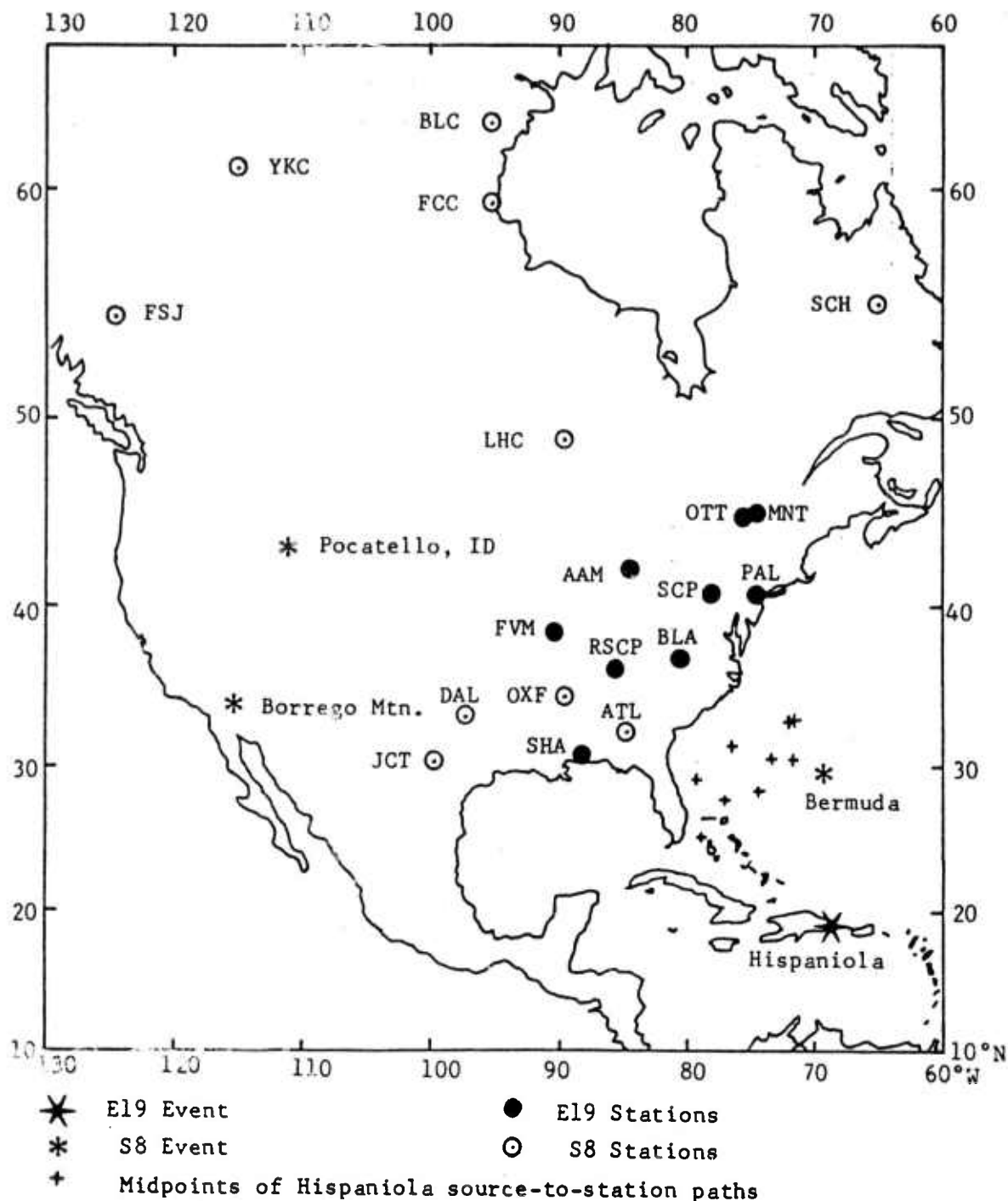
Figure 1. The locations of the eastern Hispaniola earthquake and WWSSN, RSTN, and Canadian network stations whose records were available for this study. Also shown are the events and stations used to derive mantle model S8. (Modified from Burdick, 1981.)

We attempt to interpret the P waveforms in the
first 5 to 10 seconds of the upper mantle records by
comparing them to synthetic seismograms calculated for
Burdick's (1981) S8 model for an adjacent and partially
overlapping region. Since S8 does not predict the
Hispaniola travel times and waveforms well, we attempt
to find a new model that does.

Johnson (1967) inverted $dT/d\triangle$ data to obtain a
P-velocity model for the western North American tectonic
region. Helmberger and Wiggins (1971) began their upper
mantle studies by inverting travel-time data to derive a
starting velocity model. They proceeded to manipulate
the model by trial and error until waveforms calculated
from it resembled observed waveforms.

If a published velocity model exists, then invert-
ing travel times to obtain a starting model is not nec-
essary. A number of authors have successfully manipu-
lated published starting models derived by waveform
analysis for regions that they were studying with more
recently available data (Helmberger, 1973, Wiggins and
Helmberger, 1973, Helmberger and Engen, 1974, Burdick
and Helmberger, 1978, Given and Helmberger, 1980,
Burdick, 1981, and Grand and Helmberger, 1984). The
availability of model S8 obviates inverting travel-time
data to obtain a starting velocity model here.

Burdick (1981) set out to demonstrate that varia-
tions in the upper mantle P-velocity structure beneath

North America are confined to the upper 250 km. He con-
structed two models, S8 for stable continental shield
and T9 for the tectonic region, that are identical below
250 km and different above. Given and Helmberger (1980,
p. 7183) found that, below 250 km, "there is no distin-
guishable difference between the model proposed for
northwestern Eurasia [their model] and models derived
for the U. S." Grand and Helmberger (1984) reached a
similar conclusion about S velocities. Their models SNA
for shield and TNA for tectonic areas of North America
differ only above 405 km. Cara's (1979) study of
higher-mode Rayleigh waves suggests that the main
variations in S velocity occur above 250 km.

Through trial-and-error inversion, we develop a
velocity model that satisfies the Hispaniola data, and
that is slightly different from S8 (Figure 2). The new
model, although otherwise identical to S8, has its deep-
est velocity jump at 670 km.

Applying the trial-and-error inversion technique
gives us considerable insight into the uniqueness of our
model and our ability to resolve depths at which changes
in the velocity profile occur. We interpret our results
by referring to the results of Given's (1984) formal
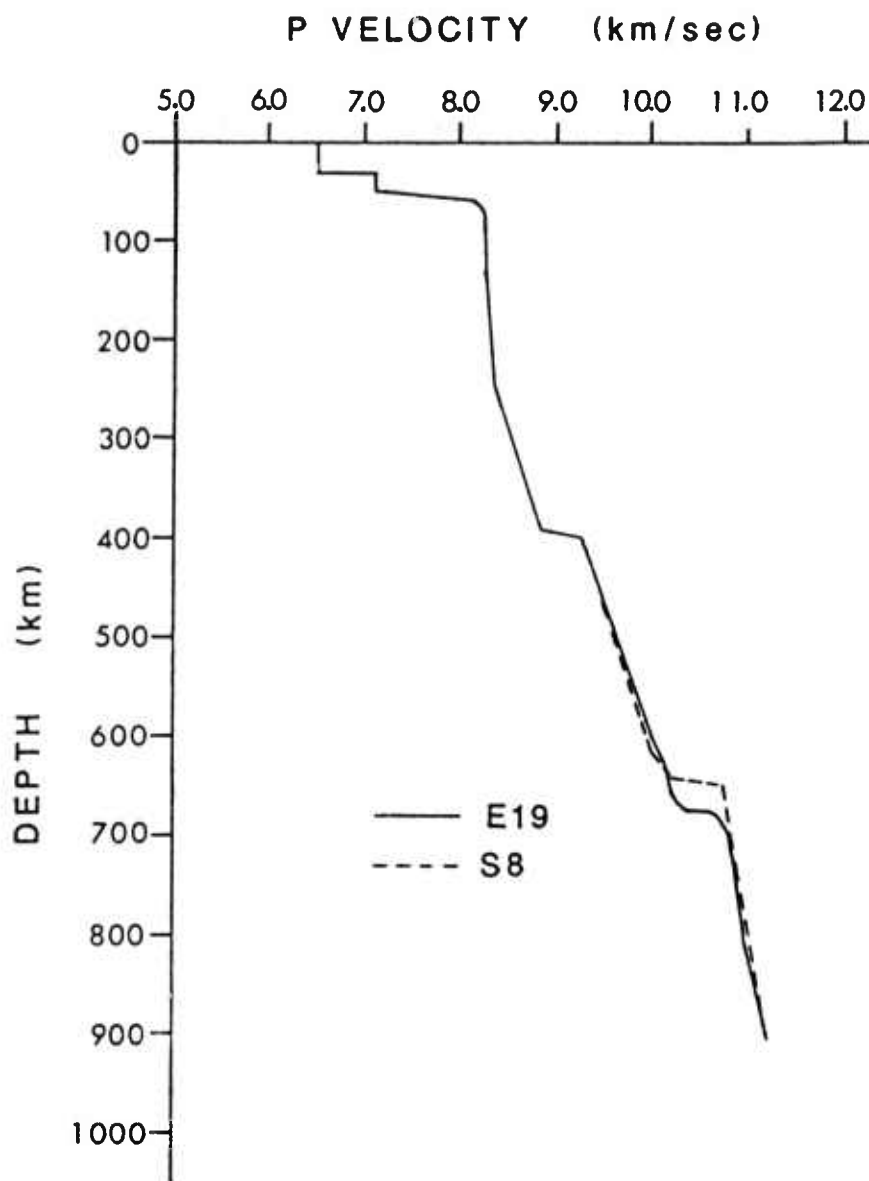inversion of waveforms for upper mantle structure.

Figure 2. P velocity models S8 (Burdick, 1981), dashed curve, and E19 (this study), solid curve. Note that the velocity models differ only below 640 km.

STUDY AREA

The Hispaniola earthquake of September 14, 1981, was recorded at stations in Bermuda and in eastern North America at ranges between 14° and 28° (Figure 1). The region of study is defined by the distribution of the bottoming points (+'s in Figure 1) of the source-to-station ray paths. The range in source-to-station azimuths of these stations is about 65°. Naturally the character of the wave propagation paths from the source to each station will change with azimuth and with distance.

Upper mantle velocity studies are traditionally conducted for geographic regions for which large numbers of upper mantle observations have accumulated. Clearly, the least ambiguous solution to the inversion problem will result if the observations are as evenly and closely distributed with distance as possible. We must balance the advantages of working with a large data set against the disadvantage of averaging too large a region, since the larger the area, the greater the chance of including regions of the upper mantle with slightly varying character.

Previous authors (Helmberger and Wiggins, 1971, Wiggins and Helmberger, 1973, and Burdick, 1981) have found that describing the upper mantle data of North America requires two velocity models: one for the tectonic area to the west and a second for the stable shield region. If the upper mantle beneath the stable continental shield region has little lateral variation, so that source-to-station wave propagation paths are similar, then one model should fit most of the data.

All of the North American stations at upper mantle distances from the Hispaniola event recorded waves that had traveled paths underneath first oceanic crust and then continental shelf and stable continental shield crust; each of the travel paths bottoms beneath oceanic crust. Model S8 was developed from source-to-station ray paths that, in almost every case, sampled the upper mantle beneath stable continental areas. North American records of the 1978 Bermuda earthquake are a subset of this data set. Like Hispaniola source-to-station paths, those from the Bermuda event are partly oceanic and bottom beneath oceanic crust. Since the region covered by the Hispaniola stations overlaps the Bermuda region from the south, upper mantle wave propagation should be similar in both cases. Since the S8 model averages European and North American upper mantle data, however, it may not fit the Hispaniola data very well.

DATA SET

Figures 3a and 3b show the reduced travel-time curves for P-wave rays from a source at a depth of 170 km for the S8 model and for our model E19 (Figure 2). The distance ranges over which arrivals are triplicated by the presence of a velocity discontinuity are obvious. For example, at any particular source-to-station distance between 21° and 24°, the P waveform will be complicated by the interference of two P arrivals from near the 650-km discontinuity. This information aids in selecting North American stations that are at distances from the Hispaniola epicenter such that their records would be affected by upper mantle discontinuities.

Long-period vertical-component records from nine North American WWSSN and Canadian Seismograph Network stations at ranges between 14° and 28° were available and of good quality. These photographic records were digitized at an irregular interval of one to three samples/second and then resampled at a constant interval of four samples/second.

Digital broad-band intermediate-period records were available from two North American stations. RSCP (of the Regional Seismic Test Network) has a sampling rate of four per second. The DWWSSN station SCP, which
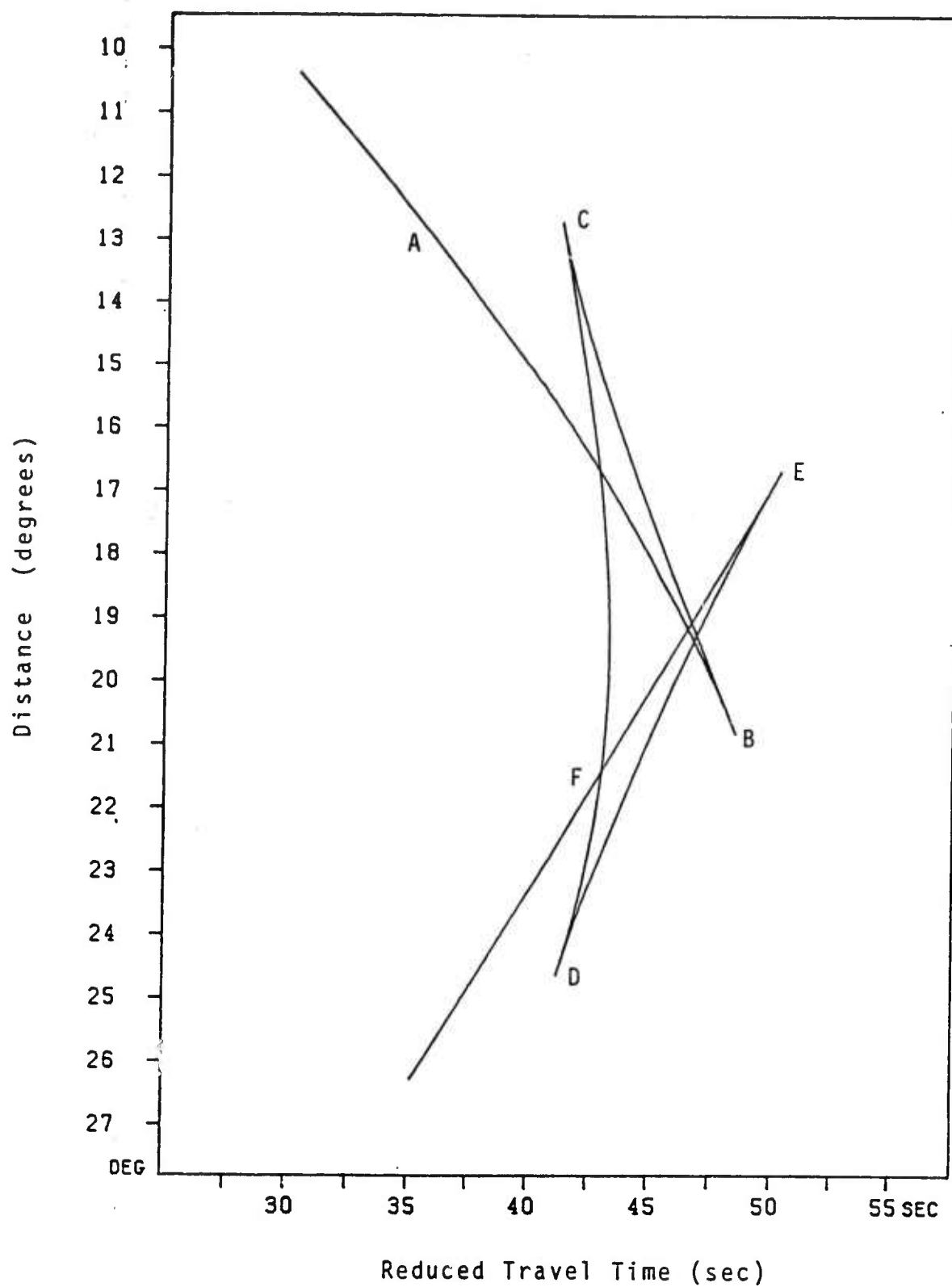
Figure 3a. Reduced travel-time curve for the S8 upper mantle velocity model. Travel times are reduced by 10.3 km/sec.

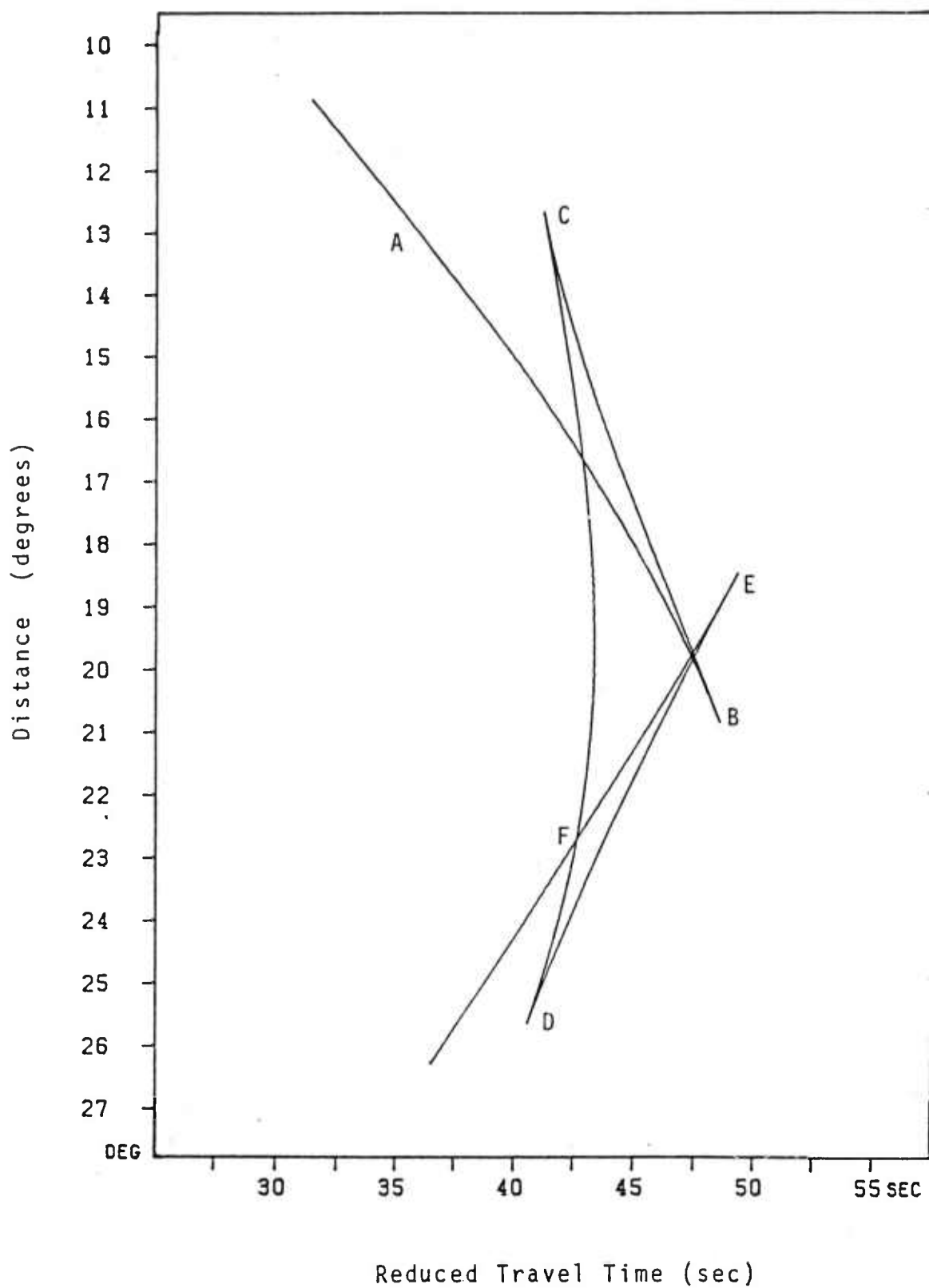Figure 3b.   Reduced travel-time curve for the E19 upper
mantle velocity model. Travel times are reduced by
10.3 km/sec.

samples signals at 10 samples/second, proved to be the single most useful data record available to this study. With proper adjustments to the S8 model, the synthetic seismogram that we calculated for SCP closely resembles the intermediate-period SCP data in waveform shape and smoothness.

SYNTHETIC SEISMOGRAM METHODS

It is reasonable to consider a far-field seismogram as a convolution of a number of operators. For example, the vertical displacement, R(t), is given by:

$$R(t) = E(t) * I(t) * A(t) * S(t) * M(t),$$

where E(t) is the earthquake source time function, I(t) is the instrument response, A(t) is the attenuation operator, S(t) represents the local source and receiver effects, M(t) is the mantle response operator, and * denotes convolution.

The mantle response operator M(t) consists of the set of Green's functions for waveforms propagating from the Hispaniola event through the mantle velocity models. Johnston and Langston (1984) determined the earthquake source parameters for the Hispaniola event by moment tensor inversion; M(t) includes the fault-plane orientation, seismic moment, and source depth of Model C of Johnston and Langston (1984). The WKBJ seismogram method of Chapman (1978) is used to calculate the mantle response. Advantages and disadvantages of calculating upper mantle seismograms with WKBJ theory are documented by Grand and Helmberger (1984) and Given (1984).

The displacement components, u_i, may be written

$$u_i = -Im \left\{ S(t) * \sum_{t=\theta} \frac{p^{\frac{1}{2}} R(p) K(p)}{\left| d\theta / dp \right|} \right\},$$

where $S(t)$ is the analytic time series,

$$S(t) = s(t) - i\mathcal{H}[s(t)],$$

$\mathcal{H}[s(t)]$ = the Hilbert transform of $s(t)$,

$$s(t) = \frac{M_0}{4\pi} s_f(t) * \frac{\partial}{\partial t} \left[-\frac{1}{\pi \sqrt{2r}} \frac{H(t)}{t^{\frac{1}{2}}} \right],$$

$$\theta(p) = pr + 2\int_0^Z \left(\frac{1}{v^2} - p^2 \right)^{\frac{1}{2}} dz,$$

$R(p)$ = product of reflection and transmission coefficients,

$K(p)$ = source radiation pattern, and

$s_f(t)$ = far-field time function.

We define the following variables and constants:

$v = v(z)$ = velocity as a function of depth,

p = ray parameter,

r = horizontal distance from source to receiver,

Z = ray bottoming depth, and

M_0 = seismic moment.

We represent the earthquake source time function, instrument, attenuation, and local source effects by a teleseismic wavelet, and calculate

$$U(t) = \text{Wavelet Operator} * M(t).$$

This method assumes, of course, that at teleseismic distances the earth's response to a propagating wave is a delta function which has been smoothed by attenuation. We also assume that the teleseismic waveforms are not affected by receiver complications. The observation that the Hispaniola teleseismic vertical-component waveforms (see Figure 4) are remarkably similar at different azimuths and distances validates these assumptions. Moreover, Given (1984) and Grand and Helmberger (1984) demonstrate that convolving a representative teleseismic wavelet with mantle impulse responses gives upper mantle synthetics that are comparable to waveforms calculated using theoretical operators.

Several long-period teleseisms for the Hispaniola event are shown in Figure 4. During the first 20 seconds of each record, two distinct pulses arrive. Direct P is consistently followed after about 7 seconds by an event with reversed polarity. Johnston and Langston (1984) interpreted the second event as an up-going ray from the source that reflects off the bottom of the low-velocity zone, then travels a path similar to that of P. To make this interpretation, they reconstructed the waveforms by convolving the earth response to the two rays (calculated using generalized ray theory) with the appropriate instrument, earthquake source time function, and attenuation operators. The
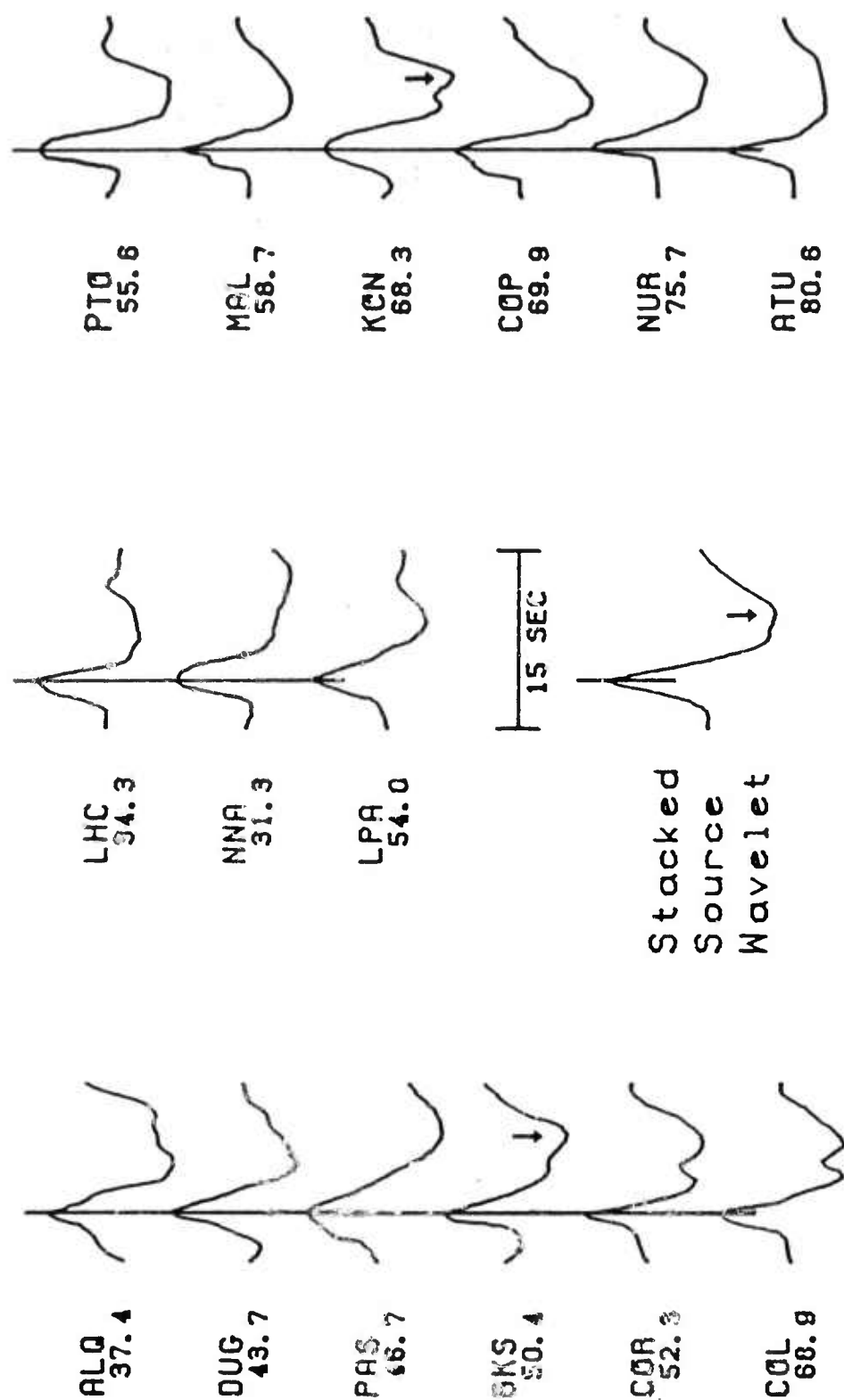
Figure 4. Long-period vertical teleseismic P wave records from the Hispaniola event, and the stacked source wavelet. The wavelets are aligned, summed, and averaged to form the source wavelet. The arrival marked by arrows is a reflection off the base of the low-velocity zone. Numbers are source-to-station distances in degrees.

interaction of P and the 7-second phase constitutes the local source effects operator, S(t).

The Wavelet Operator used to model long-period data is a stack of 15 long-period vertical-component tele-seisms (Figure 4). Steps taken to construct the wavelet were: 1) align the peaks of the first arrival of each teleseism, 2) normalize the amplitude of each teleseism to the amplitude of the first peak, 3) average the traces. Reversing the polarity of the LHC trace allowed its inclusion in the waveform stack. Slight variations in the teleseismic waveforms may represent interference of conversions near the source and/or receiver. Stacking the waveforms causes conversions with opposite polarities to cancel and reduces the contribution of other conversions.

Without intermediate-period teleseismic records to make a source wavelet, the interaction between P arrivals and the 7-second arrival cannot be modeled for intermediate-period waveforms. In the distance range where intermediate-period records are available (22° to 24°), however, all triplicated P phases arrive within 3 seconds of the onset of P (see Figures 3a and 3b). The synthetics calculated to model these data resulted from convolution of the mantle response with appropriate instrument operators and a source time function. F(t) in this case is a Brune time pulse (Brune, 1970) t t is

3 seconds long, as the source mechanism study of
Johnston and Langston (1984) determined.

RECEIVER FUNCTION

In this study, as in other upper mantle waveform
studies, a delta function represents the effect of
shallow structure beneath the receiver. The receiver
structure is generally not known. Assuming that it has
no effect on wave propagation in this case simplifies
the effort of calculating synthetic seismograms.

Of course, this assumption is valid only for
stations whose crustal structure does not create arri-
vals that are obvious in the P waveforms. It requires
stations at which converted phases and reverberations in
the crust are not strong enough to complicate the upper
mantle waveforms. Of the WWSSN stations that recorded
the Hispaniola event, Burdick and Langston (1977) sug-
gest that only MNT (Montreal, Canada) may be underlain
by crust with sharp velocity contrasts that cause impor-
tant crustal phases.

To determine whether a delta function closely
approximates the receiver function of each of the upper
mantle stations used here, the reasoning of Burdick and
Langston (1977) applies. The presence of SV energy,
indicating that crustal phases are interfering with the
vertical P waveform, is evident on the radial-component
record. If the P waveforms on the vertical- and radial-

component records are similar, then the receiver crust is "transparent" (Burdick and Helmberger, 1978, p. 1703) to propagating waves, and the single delta function is appropriate. If the horizontal components do not resemble the vertical, then the crustal structure contains sharp velocity contrasts whose effects on wave propagation cannot be ignored. In such a case, the complications in the vertical P waveform are not due simply to upper mantle structure.

RSCP's horizontal components were rotated into radial and transverse directions. MNT, OTT, and PAL are all within 11° of due north of the source; thus, they are nearly naturally rotated. Radial and vertical components in each case do not differ markedly. The transverse components are of very low amplitude, indicating that little SH energy is generated in the receiver crust.

For the purpose of this study, digitizing and rotating the horizontal components for the remaining stations were unnecessary. The NS and EW components for each station (except SCP) are similar enough to each other, and to the vertical component, that no station was discarded.

The NS-component intermediate-period record for SCP is not available. While the long-period data encourage us that SCP's crustal structure is acceptable, crustal phases should be less obvious on long-period records

than on short-period records (Burdick and Helmberger, 1978, and Given and Helmberger, 1980). For the first 3 to 5 seconds, the intermediate-period EW record for SCP is identical to the vertical, however, indicating insignificant crustal features. In support of this, Langston and Isaacs (1981) successfully modeled the crust and uppermost mantle beneath central Pennsylvania as a 41-km thick homogeneous layer over a halfspace.

TECHNIQUE AND RESULTS

Analysis of upper mantle P waveforms is at the heart of this study. We interpret an observed waveform by constructing a synthetic meant to predict features in the waveform and then by comparing the fit between the two. Determining the quality of the fit of predictions to observations is partly subjective in this study. This means that we must define the characteristics of a synthetic waveform that is a "good fit" to an observation. Of course the synthetics are only approximations to the observations and are limited by the assumptions that we have made. For example, we have attenuated the long-period synthetics too much and so have removed the high frequencies that are present in the observations. We pay attention then to matching the features of the waveforms that are evidence of triplicated direct P arrivals: the travel time of the first arrival, the relative timing of subsequent arrivals, the relative amplitudes of the pulses, the widths of the pulses, and the polarities of the pulses. Quantitatively, relative travel times that are within one second of those in the observations and relative amplitude measurements that are within 15% of those in the observations are acceptable.

For all stations, except SHA and RSCP, S8 predicts
synthetics that begin 1 to 4 seconds later than the
observed pulses. The S8 travel time for RSCP is 2
seconds early. At SHA and PAL the synthetic waveforms
start on time. Start times for SHA and BLA, at 21.38°
and 21.39° respectively, are separated by 2.5 seconds.
The event on the SHA photographic record begins right at
the left edge of the sheet of photographic paper where
it overlaps on the drum; as a consequence, an error in
digitizing the SHA record may have caused the discrepancy
between the SHA and BLA start times. Figures 5 and 6
show representative long-period synthetics calculated
for S8 and E19.

The waveform calculated with S8 to match BEC (Figure
7) recovers the fundamental shape of the observation.
The relative amplitudes of the troughs and peaks in the
entire record are correct, although at the zero-amplitude
crossing the first trough is 2 seconds narrow and the
first peak is 1 second wide. For both SHA and BLA
(Figure 8), the relative timing and widths of peaks are
reasonable, but the relative amplitudes need adjustment.
The PAL (Figure 8) prediction is very good. Excessive
delay of the first upswing distends the first trough in
the long-period SCP record; the first peak fits the data
nicely. In the intermediate-period SCP seismogram
(Figure 9) the pulses interfere with each other less
than they do in the long-period record; we can see the

Figure 5. Long-period synthetic seismograms calculated for S8. Absolute travel times are reduced by 10.3 km/sec and advanced by 20 sec. Amplitude of each trace is normalized to the maximum amplitude of the trace (shown).
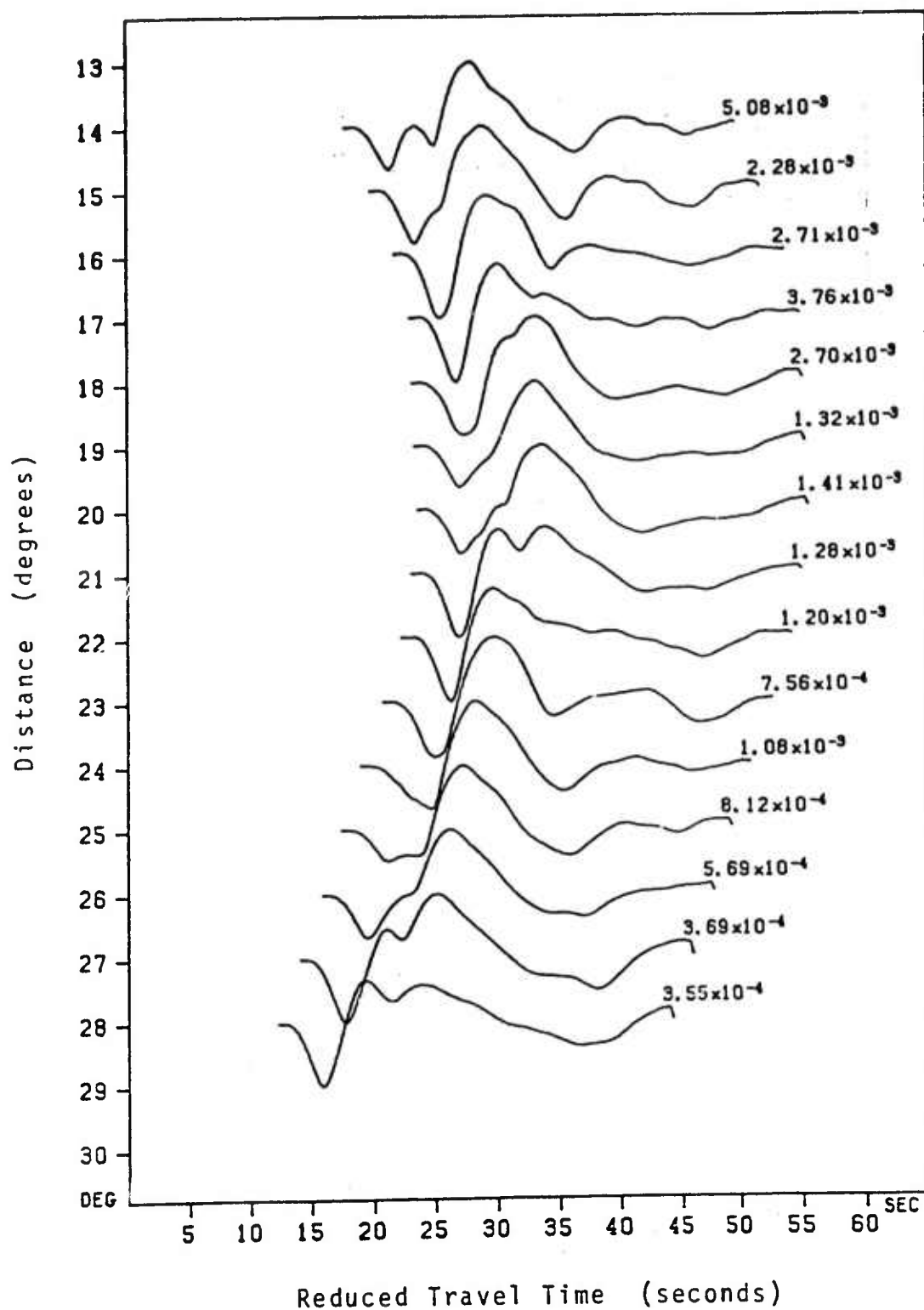
Figure 6. Long-period synthetic seismograms calculated for our model E19. Absolute travel times are reduced by 10.3 km/sec and advanced by 20 sec. Amplitude of each trace is normalized to the maximum amplitude of the trace (shown).
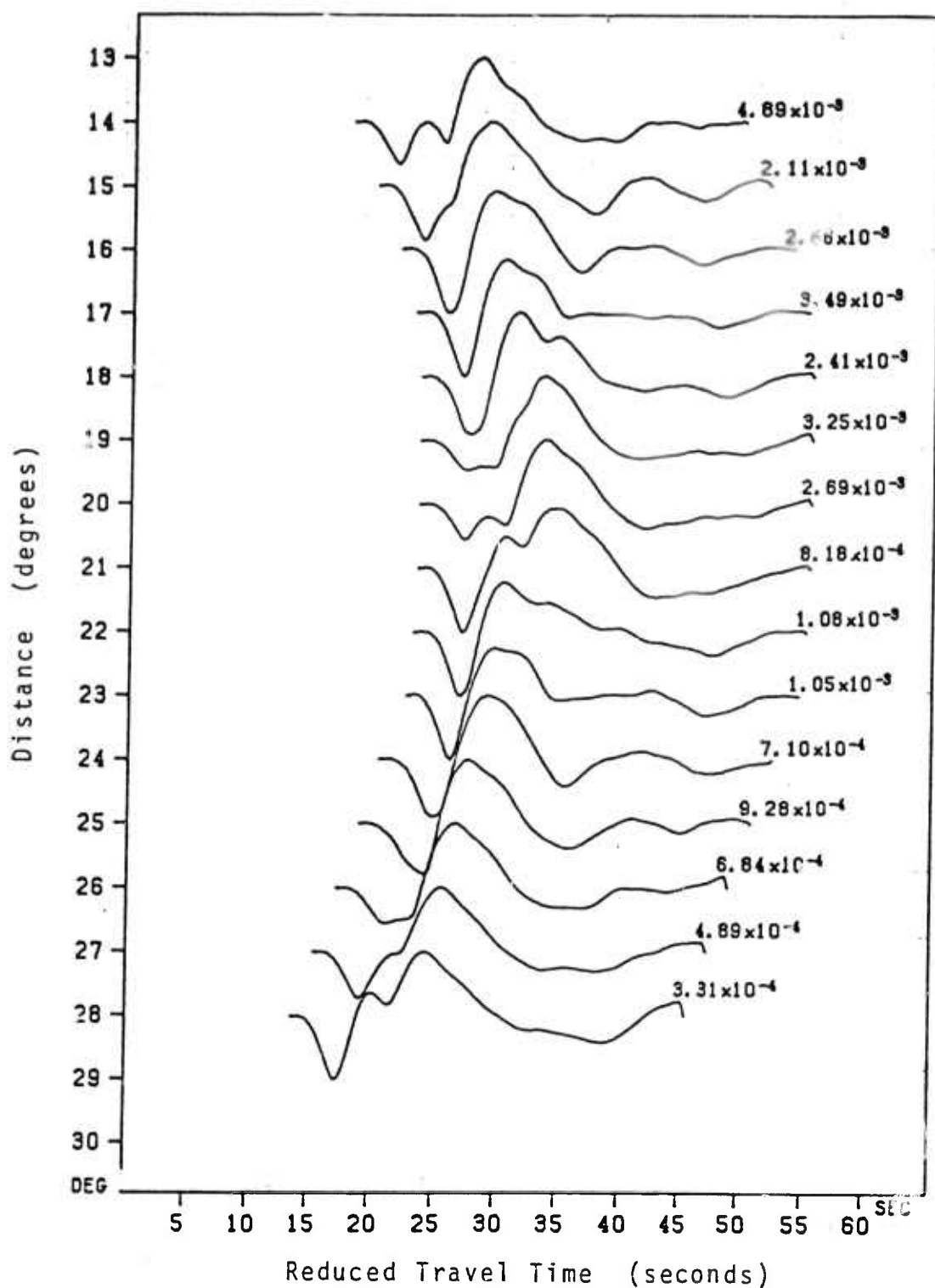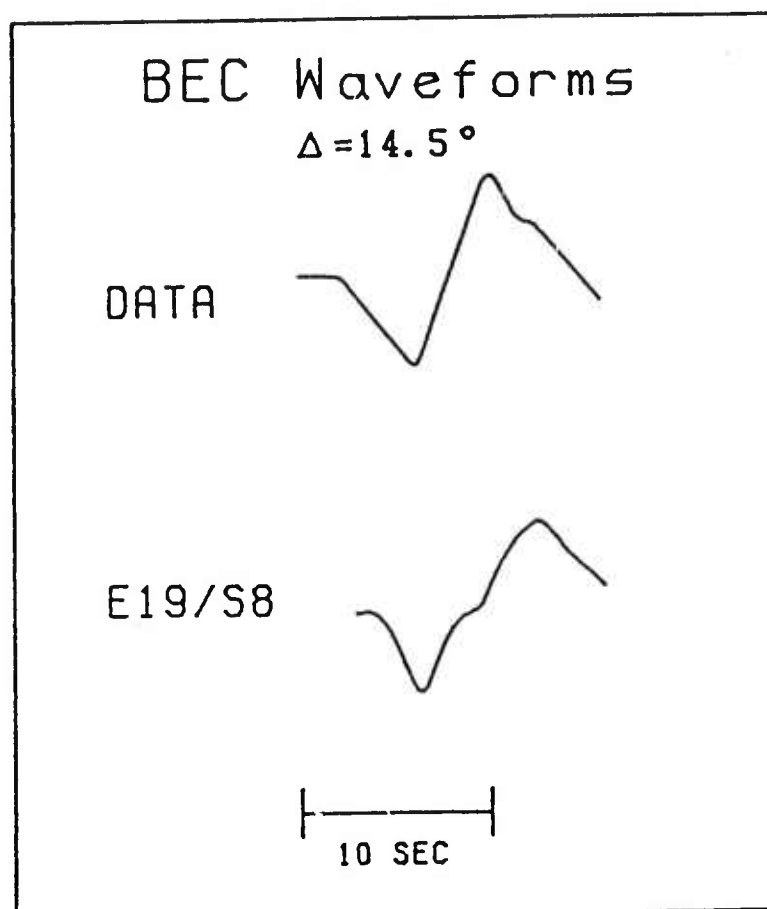
Figure 7.   Data and synthetics for BEC.
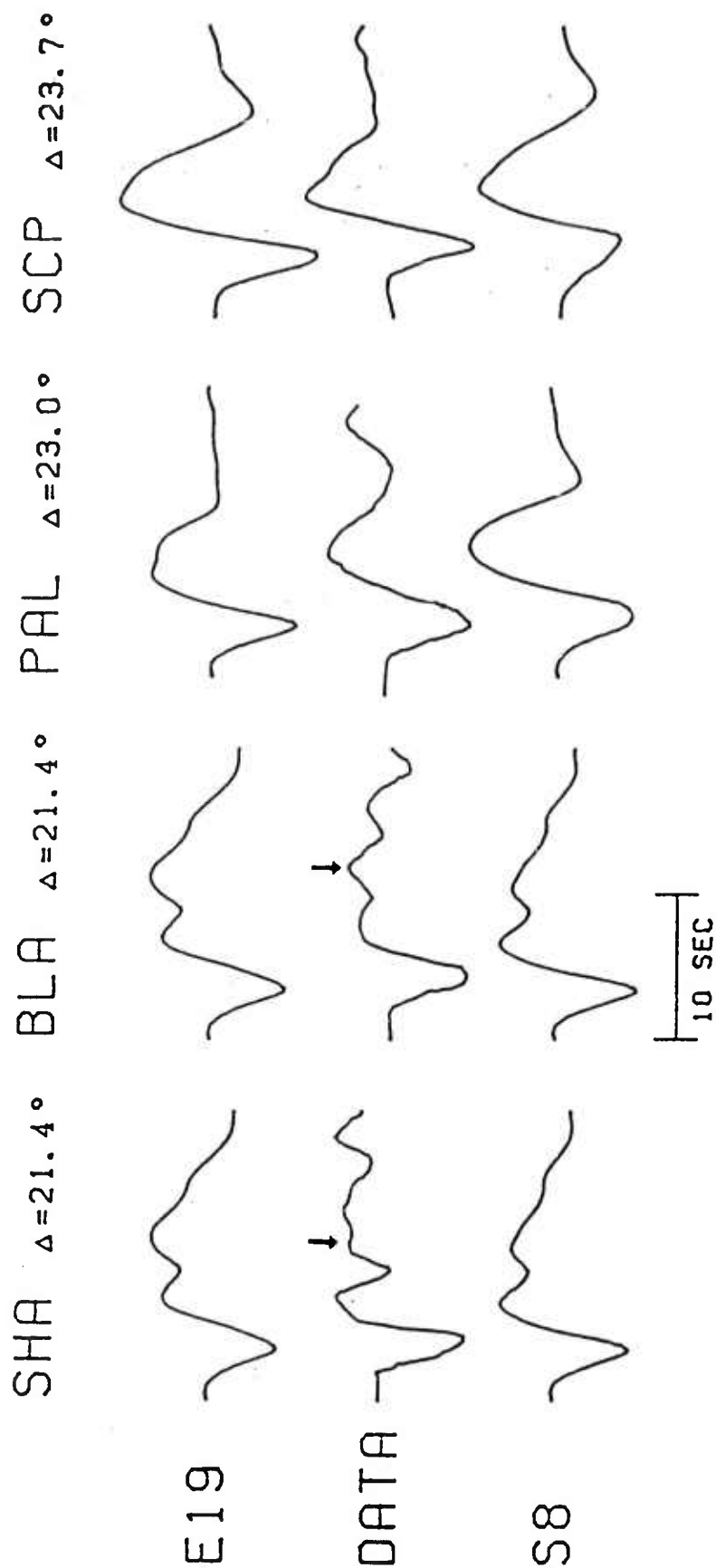
Figure 8. Long-period data and synthetics for stations from 21° to 24°. Arrows on the SHA and BLA observations mark arrivals from the vicinity of the 400-km discontinuity.

Figure 9. SCP intermediate-period data and synthetics. Pulses represent arrivals of rays that 1) turned just below the 670-km discontinuity, 2) turned just above it, and 3) traveled through it. The starred arrival in the data is not modeled by our assumptions.

shortcomings of S8 more clearly. The second trough is
delayed by 2.5 seconds. Furthermore, the amplitudes of
the first wavelet and the second downswing are too large.
S8 severely distorts waveforms between 27° and 27.6°
(see Figure 10). Indeed, the double peak mimics that of
the observations, but the double trough is missing. Our
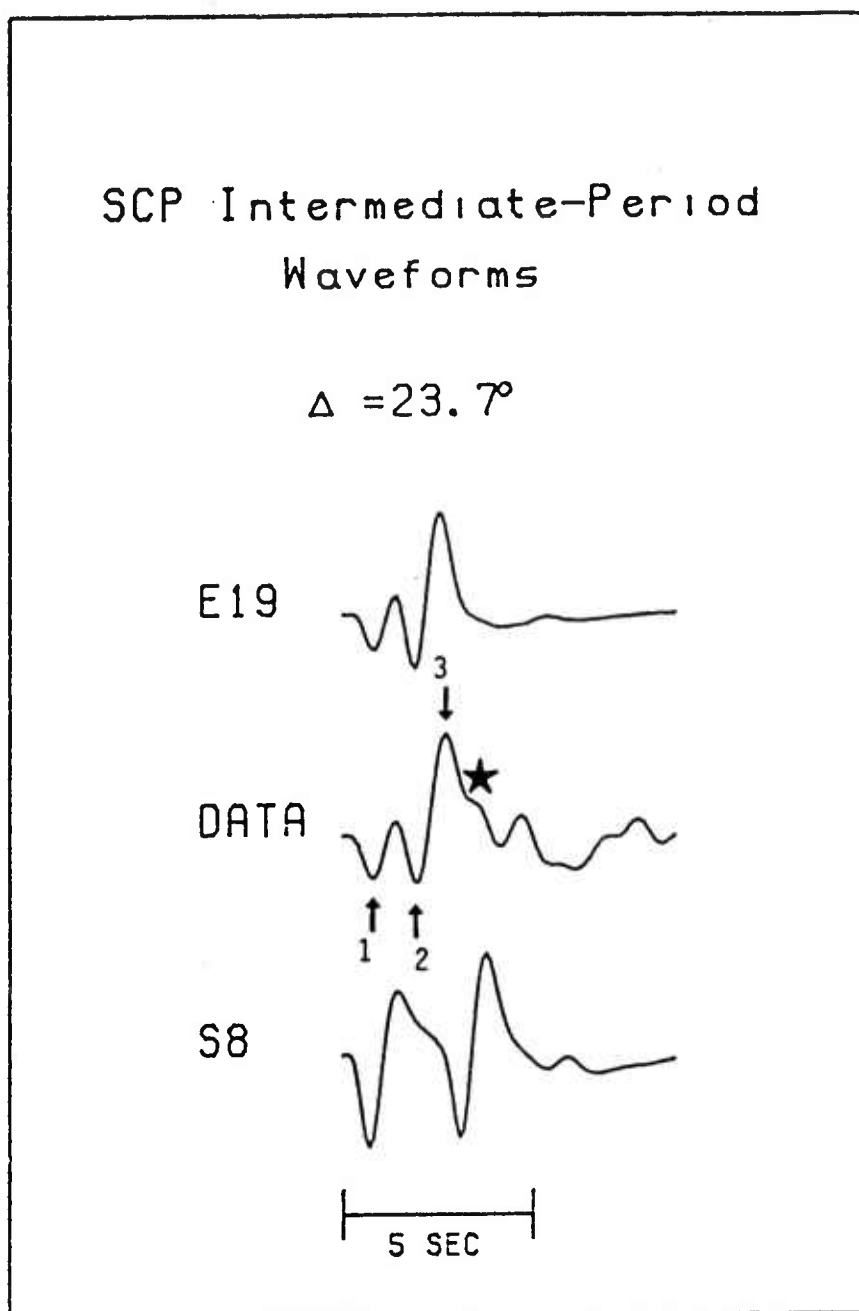investigation shows that the first peak is actually the
pulse that broadens the first trough in the observations;
S8 predicts an amplitude for the first peak that is much
too large. On close inspection of the records from 27.0°
to 27.5°, we observe the second pulse moving back in
time as distance increases, and changing from a trough
to a hump on the left side of the large upswing. We
eventually discover that the second peak in the data is
not a triplicated direct P phase at all.

Since S8 predicts BEC well enough, we have no
grounds for changing the upper 400 km of the starting
model. On the other hand, changing the model below 400
km can improve its performance in the 21°-to-28° range.

A quick look at the S8 waveforms in Figures 5 and
11 (intermediate-period synthetics from S8) suggests
that the observations resemble synthetics at distances
about 1.5° closer to the source. For example, SCP
(23.7°) looks like the waveform at 22.25°, and FVM
(27.2°) resembles that at 26.0°.

Waves that arrive at stations between 21° and 28°
have bottomed below the 400-km discontinuity. For this
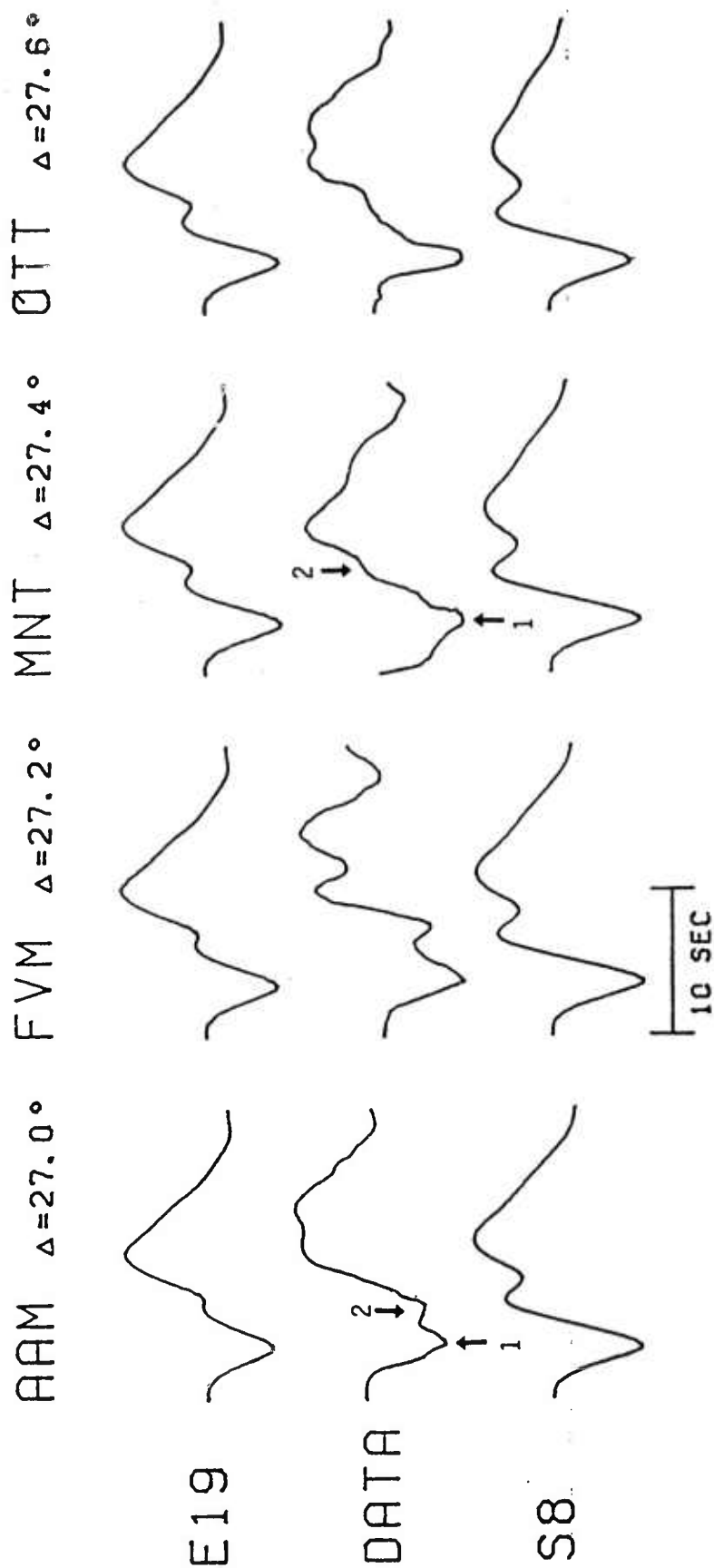
Figure 10. Long-period data and synthetics for stations from 27.0° to 27.6°. Our assumptions do not predict the second large peak at AAM, FVM, and OTT. Arrows mark pulses that are arrivals of rays from 1) just below the 670-km discontinuity, and 2) just above and within the discontinuity.
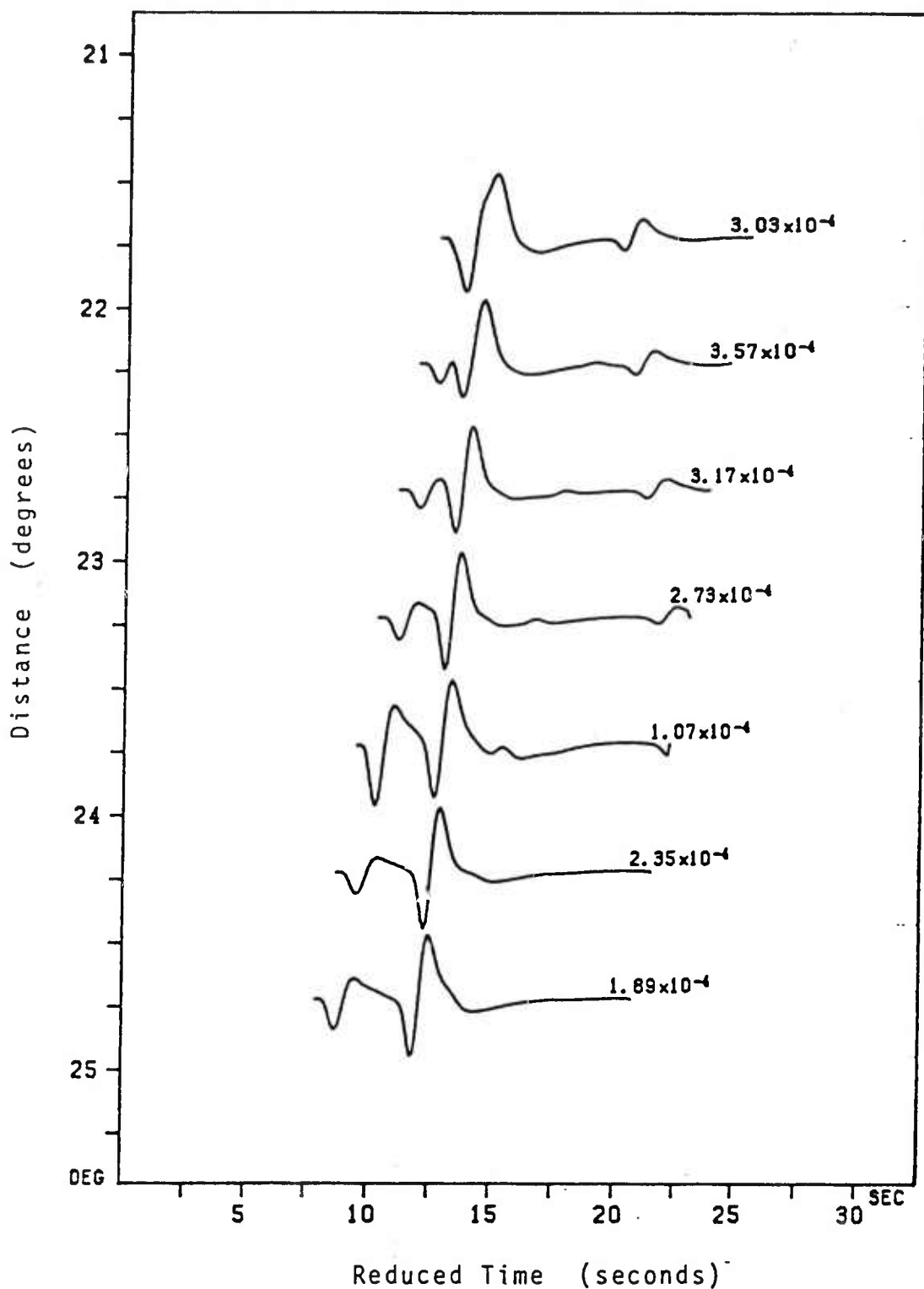
Figure 11. Intermediate-period synthetic seismograms calculated for S8. Absolute travel times are reduced by 10.3 km/sec and advanced by 30 seconds. Note that the SCP observation (figure 9) resembles the S8 synthetic at 22.25°

reason we attempt to modify the lower half of the velocity profile. We suggest that by shifting the 650-km triplication (DEF in Figure 3a) along the 10.3-km/sec branch, we will not only systematically delay travel times, but we will also change the relative timing of arrivals.

At a point to the right of F in Figure 3a, the shift will: 1) delay all arrivals, 2) change the relative timing of arrivals and, in particular, advance the CD branch with respect to the EF branch, and 3) compress the entire triplicated pulse.

To shift and reshape the 650-km triplication branches, we will adjust the starting velocity profile in the following ways:

1) lower the 650-km discontinuity to shift the triplication out in distance,

2) vary the gradient above and below the discontinuity and change the absolute size of the discontinuity to distort the triplication, and

3) sharpen or smooth the discontinuity to lengthen or shorten the duration of the triplication.

We manipulate the starting model according to these guidelines until we achieve a velocity profile whose synthetics satisfactorily match the data. The resulting model will represent only one combination of these activities, however. Since other combinations will shape

profiles that predict the observations as well, we conclude that our model is not unique.

Our strategy is to adjust the model so that it fits the SCP intermediate-period (IP) record (Figure 9). At this range, direct P arrivals are separated by about 1 to 2 seconds. A time separation of this order is resolval on the IP record. This record is so clean and noise-free that we can calculate synthetics that almost duplicate it. Once we have established this one data point on the travel-time curve, we proceed to fit the remaining observations as closely as possible. Representative waveforms for the new model are shown in Figure 6. S8 and the new velocity model E19 are listed in Table 1 and plotted in Figure 2.

The 400-km Discontinuity. Stations located between 12° and 20° from the source are in an excellent position to record triplicated P arrivals from the vicinity of the 400-km discontinuity. Of the stations whose records are available for this study, only BEC at 14.5° falls in this range. The S8 model predicts a waveform that fits the BEC observation acceptably well. The lack of observations from this distance range is troubling, however. Fortunately, observations of the AB branch (Figures 3a and 3b) beyond 21° help to confirm that the triplication caused by the upper discontinuity in the S8 velocity model satisfies the data.

Table 1. S8 and E19 P Velocity Models.

Depth	S8	E19
30.0 km	6.50 km/sec	6.500 km/sec
50.0	7.10	7.100
60.0	8.10	8.100
65.0	8.20	8.200
75.0	8.24	8.240
135.0	8.26	8.260
175.0	8.30	8.300
245.0	8.44	8.440
390.5	8.81	8.810
400.0	9.25	9.250
600.0		10.000
615.0	10.07	
625.0	10.11	10.175
645.0	10.25	
650.0	10.76	
660.0		10.225
667.5		10.275
672.5		10.350
675.0		10.400
675.1		10.650
680.0		10.700
690.0		10.775
705.0		10.850
805.0		11.060
905.0	11.26	11.260

From 21° to 24°, the spread between the AB and CD branches of the triplication increases from about 5 seconds to about 10 seconds. The position of the AB branch in this range represents the travel time of a diffracted arrival from just above the 400-km discontinuity. The WKBJ method predicts too large an amplitude for this pulse, which arrives beyond the B cusp of the travel-time curve. Despite this, the pulse's travel time is useful information. Before the pulse from the 400-km discontinuity arrives, of course, we see arrivals from the deeper discontinuity. At BLA and SHA the arrival from the region of the 400-km discontinuity causes the second peak in the waveform. By 23° at PAL and 23.7° at SCP (long-period record), the amplitude of the arrival has decreased abruptly and the AB branch has moved back in time. The disappearance of the AB branch is evidence that the first triplication should be no larger than it is.

The 670-km Discontinuity. Our model predicts observed absolute travel times to within 4 seconds at all stations. We overestimate the travel time at BEC by 2 seconds, at BLA by 2.5 seconds, at SCP, AAM, FVM, MNT, and OTT by 4 seconds, and underestimate at RSCP by 2 seconds. The SHA and PAL first arrivals are on time; perhaps the blame for inconsistency of the SHA time,

which should be closer to the BLA time, lies in error in digitizing the record, as we mentioned earlier.

Waveform fits to BLA and SHA are very good. The first cycle of the waveform is slightly broader than the source wavelet. The pulse from just above the 670-km discontinuity is followed after one second by the pulses that propagate through the discontinuity and along the underside of it (Cormier and Choy, 1981). The second peak is matched closely by a pulse that we predict arrives from the vicinity of the 400-km discontinuity. Our assumptions are not complete enough to explain the slight discrepancy in relative amplitudes between SHA and BLA. The discrepancy may be due to lateral variation in mantle structure. The azimuthal separation between these two stations with respect to the source is 25°.

Across the CD-EF intersection at SCP, the intermediate-period synthetic fits the observation almost exactly. The travel-time curve indicates a time spread between the EF branch and the back-branch of slightly less than 2 seconds; this is precisely the time spread between the first trough and the second peak in the data. The onset of the pulse from the CD branch, 0.8 seconds behind the EF branch, is distinct in the short-period digital record (Figure 12). This confirms the time separation between the first two arrivals. More importantly, the fact that no arrivals intervene between the two supports our interpretation that these pulses are indeed
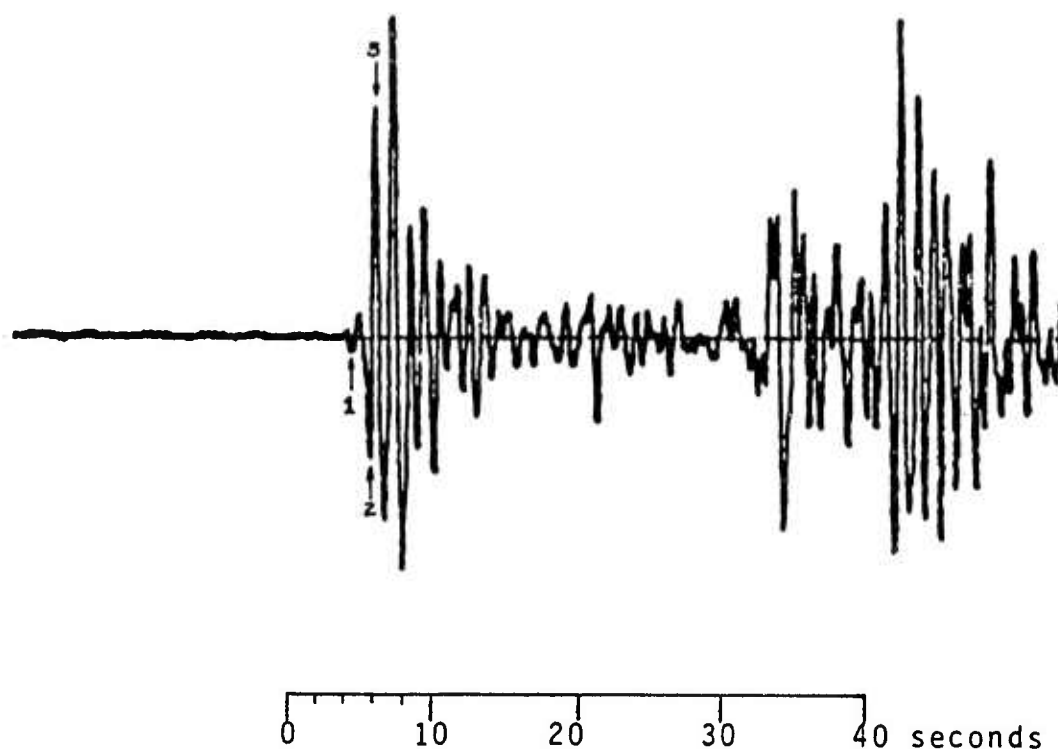
Figure 12. Short-period record of the Hispaniola event
recorded at SCP (DWWSSN). The first pulse (trough at 1)
arrives from below the 670-km discontinuity. The trough
at 2 represents a ray that turned above the discontinuity.
The peak at 3 corresponds to an arrival on the back branch
(DE in figure 3b), a ray that turned within the
discontinuity. Relative arrival times predicted by E19
are close to the timing of arrivals in this record.

triplicated direct P arrivals. We can see each of the three triplication branches despite slight interference among the pulses. The two pulses with negative polarity are arrivals from below the 670-km discontinuity and from just above it, in that order. Smoothing the corners of the discontinuity in the profile gave the pulses the correct relative amplitudes. The strong peak is the arrival of a ray that traveled through the discontinuity; this is the only record in which the 90-degree phase-shifted pulse from the back-branch is directly observable. The hump on the right side of the peak (* in Figure 9) is not modeled by our assumptions.

The quality of waveform fits at AAM, FVM, MNT, and OTT is very difficult to judge. MNT and OTT especially are very close to the P nodal plane; we expect the triplicated P arrivals to be of very low amplitude. Nevertheless, they are distinguishable from noise, and vital in confirming the position of the CD branch. The first trough in the synthetics corresponds to the first trough in each of the observations. The relative timing of peaks and troughs that our model predicts agrees well with the data. The relative amplitudes of the first trough and second peak are almost exact in each case. The amplitude of the first peak, however, is slightly high, especially at AAM and FVM. The first trough represents the head wave that travels underneath the 670-km discontinuity. The second pulse, the superposition of

the arrivals from just above and within the 670-km discontinuity, follows the first after about 3.5 seconds at AAM and 4.0 seconds at OTT. Its advent is marked by the second trough in the AAM and FVM waveforms, and by the top of the shoulder on the left side of the first peak at MNT and OTT. These data constrain the separation of the EF and CD branches. The WKBJ seismogram overestimates the amplitude of the second pulse; these stations are 1.5° to 2.0° beyond the D cusp of the travel-time curve.

We have had great success modeling data received at points on the travel-time curve that are away from the CD-EF crossover. Manipulating the model so that it locates the crossover accurately, however, would have required an immense effort. RSCP and PAL are available to help to pin down the crossover point. Our synthetics do not fit these two observations satisfactorily. Although we predict the travel time to PAL well, our travel time to RSCP is 2.0 seconds early. The RSCP waveform (Figure 13) exhibits a second arrival about 1 second after the first. Our experience allows us to interpret the broadening of PAL's trough and peak to indicate the same. Based on waveform shapes alone, we conclude that the CD-EF crossover should move closer to the source.

E19 overestimates absolute travel times by 2 to 4 seconds at all stations but two. A delay of 2 seconds in the origin time of the earthquake (12:44:30.1 $\pm$ 0.18,
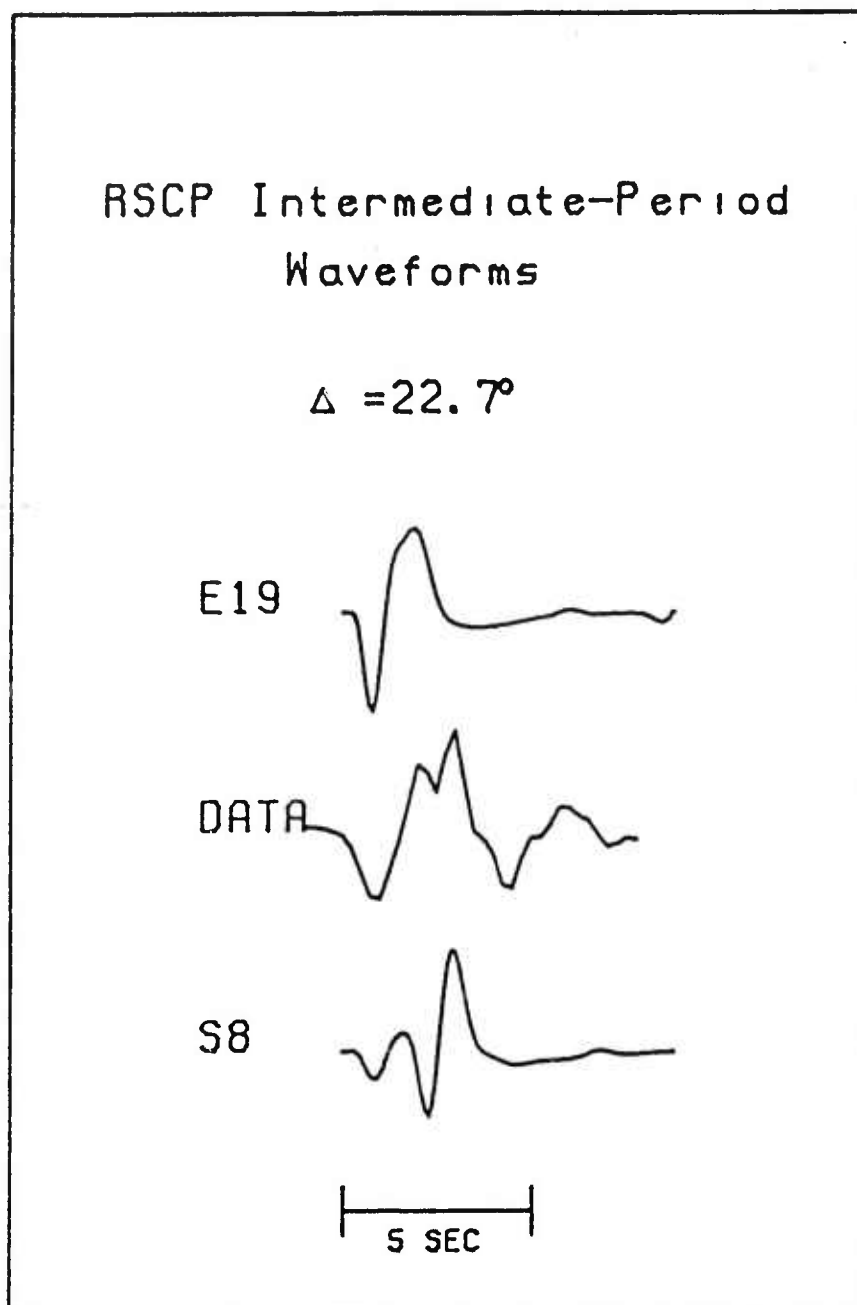
Figure 13. RSCP intermediate-period data and synthetics. Neither model predicts the data well. The synthetics appear to be extremely sensitive to the position of the intersection of the CD and EF branches of the travel-time curve. We had no success in modeling this observation.

International Seismological Centre, 1983) would bring predicted times closer to the data. This shift in travel times would be accomplished without changing the triplications. On the other hand, thinning the crust in the model is a more likely solution. The crust in E19 is 60 km thick, which could be characteristic of some stable continental shield regions on other continents, but is too thick for the crust beneath SCP and likely for the other stations as well. Substituting a 40-km thick crustal model with velocities of 6.0 km/sec for the upper 20 km and 6.8 km/sec for the lower 20 km would shorten the travel time through the crust by 1.1 seconds.

DISCUSSION

Burdick's (1981) model S8 has been modified to satisfy a new set of upper mantle data from eastern North America. The new model, E19, is identical to S8 above about 640 km. Features that distinguish E19 from S8 are:

1) the deepest velocity jump occurs at 670 km instead of at S8's 650 km;

2) the velocity jump is not discontinuous as in S8; the velocity jump occurs over a depth range of about 30 km.

The increased amount of structure resolvable near the 670-km discontinuity, feature 2 above, is a direct benefit of the use of the intermediate-period SCP record. This record was sufficiently noise-free that we were able to reproduce its first 3 to 4 seconds exceptionally well. Greater availability of such high quality broad-band digital data would no doubt enhance similar studies.

The claim of Burdick and other authors that mantle velocity is laterally homogeneous below about 250 km raises questions about the validity of the new model. Does disagreement about the position of the lower discontinuity imply inhomogeneity? Is a difference in

position of 20 km at a depth of 650 km resolvable? Could another model satisfy the Hispaniola data?

Given (1984) has recently discussed the two unmentionable unknowns of trial-and-error inversions for upper mantle structure: resolution and uniqueness. Using the computer to perform a formal inversion of SH waveforms and travel times for velocity structure, he could quantify the effects of making repeated small perturbations in a starting velocity model. With his insight, we attempt to answer the above questions.

The S velocity profile that Given (1984) derived for the tectonic western U. S. has increases in velocity at about 400 km and 650 km which are much more gradual than those in any models that have been published since Helmberger and Wiggins (1971) began trial-and-error inversions of waveforms in short-period observations. His upper velocity change consists of an 8.5% increase spread between 360 km and 420 km. Likewise, his lower "discontinuity" is an even more gradual change, a 14% increase between 600 km and 750 km. A model with sharp velocity changes is admittedly simple. Of the models that Given's method created to satisfy the data, however, his final model (with smoothed "discontinuities") is the simplest. Given's data set did not allow resolution of sharp discontinuities. We reason, then, that trial-and-error inversion of data sets of equal or lesser quality

to Given's cannot distinguish differences in 20 km in the position of a change in gradient.

The fact remains that the new model fits the Hispaniola data better than S8 does. The new model is not unique, however. Given (1984, p. 55) described the uniqueness problem in trial-and-error inversions in this way: "The difficulty of finding a velocity model that satisfied the data is implicitly used as an argument that the model was unique." We noted that particular combinations of gradient steepness, discontinuity depth, and velocity jump would satisfy the data. The new model is one combination. Other combinations would fit the data as well. Adding more observations would permit others, until we accumulate enough data so that we may begin to better constrain the model. Even though the average distance spacing of Burdick's observations is 0.5° to 1.0°, S8 is not unique either.

REFERENCES

Brune, J. N. (1970). Tectonic stress and the spectra of seismic waves from earthquakes, J. Geophys. Res. 75, 4997-5009.

Burdick, L. J. (1981). A comparison of the upper mantle structure beneath North America and Europe, J. Geophys. Res. 86, 5926-5936.

Burdick, L. J., and D. V. Helmberger (1978). The upper mantle P velocity structure of the western United States, J. Geophys. Res. 83, 1699-1712.

Burdick, L. J., and C. A. Langston (1977). Modeling crustal structure through the use of converted phases in teleseismic body-wave forms, Bull. Seism. Soc. Am. 67, 677-691.

Cara, M. (1979). Lateral variations of S velocity in the upper mantle from higher Rayleigh modes, Geophys. J. 54, 649-670.

Chapman, C. H. (1978). A new method for computing synthetic seismograms, Geophys. J. 54, 481-518.

Cormier, V. F., and G. L. Choy (1981). Theoretical body wave interactions with upper mantle structure, J. Geophys. Res. 86, 1673-1678.

Given, J. W. (1984). Inversion of body-wave seismograms for upper mantle structure, Ph. D. Thesis, California Institute of Technology, Pasadena, California.

Given, J. W., and D. V. Helmberger (1980). Upper mantle structure of northwestern Eurasia, J. Geophys. Res. 85, 7183-7194.

Grand, S. P., and D. V. Helmberger (1984). Upper mantle shear structure of North America, Geophys. J. 76, 399-438.

Helmberger, D. V. (1973). Numerical seismograms of long-period body waves from seventeen to forty degrees, Bull. Seism. Soc. Am. 63, 633-646.

Helmberger, D. V., and L. J. Burdick (1979). Synthetic seismograms, Ann. Rev. Earth Planet. Sci. 7, 417-442.

Helmberger, D. V., and G. R. Engen (1974). Upper mantle shear structure, J. Geophys. Res. 79, 4017-4028.

Helmberger, D. V., and R. A. Wiggins (1971). Upper mantle structure of midwestern United States, J. Geophys. Res. 76, 3229-3245.

International Seismological Centre (1983). Regional Catalogue of Earthquakes 18 (July-December 1981).

Johnson, L. R. (1967). Array measurements of P velocities in the upper mantle, J. Geophys. Res. 72, 6309-6325.

Johnston, D. E., and C. A. Langston (1984). The effect of assumed source structure on inversion for earthquake source parameters: the eastern Hispaniola earthquake of 14 September 1981, Bull. Seism. Soc. Am. 74, 2115-2134.

Langston, C. A., and C. M. Isaacs (1981). A crustal thickness constraint for central Pennsylvania, Earthquake Notes 52, 13-22.

Wiggins, R. A., and D. V. Helmberger (1973). Upper mantle structure of the western United States, J. Geophys. Res. 78, 1870-1880.

Dr. Monem Abdel-Gawad
Rockwell International Science Center
1049 Camino Dos Rios
Thousand Oaks, CA 91360

Professor Keiiti Aki
Center for Earth Sciences
University of Southern California
University Park
Los Angeles, CA 90089-0741

Professor Shelton S. Alexander
Geosciences Department
403 Deike Building
The Pennsylvania State University
University Park, PA 16802

Professor Charles B. Archambeau
Cooperative Institute for Research in
    Environmental Sciences
University of Colorado
Boulder, CO 80309

Dr. Thomas C. Bache Jr.
Science Applications Int'l Corp.
10210 Campus Point Drive
San Diego, CA 92121

Dr. James Bulau
Rockwell International Science Center
1049 Camino Dos Rios
P.O. Box 1085
Thousand Oaks, CA 91360

Dr. Douglas R. Baumgardt
Signal Analysis and Systems Division
ENSCO, Inc.
5400 Port Royal Road
Springfield, VA 22151-2388

Dr. S. Bratt
Science Applications Int'l Corp.
10210 Campus Point Drive
San Diego, CA 92121

Professor John Ebel
Department of Geology & Geophysics
Boston College
Chestnut Hill, MA 02167

Woodward-Clyde Consultants
Attn: Dr. Lawrence J. Burdick
        Dr. Jeff Barker
P.O. Box 93245
Pasadena, CA 91109-3245   (2 copies)

Dr. Roy Burger
1221 Serry Rd.
Schenectady, NY 12309

Professor Robert W. Clayton
Seismological Laboratory
Division of Geological and Planetary
        Sciences
California Institute of Technology
Pasadena, CA 91125

Dr. Vernon F. Cormier
Earth Resources Laboratory
Department of Earth, Atmospheric and
        Planetary Sciences
Massachusetts Institute of Technology
42 Carleton Street
Cambridge, MA 02142

Professor Anton M. Dainty
Earth Resources Laboratory
Department of Earth, Atmospheric and
        Planetary Sciences
Massachusetts Institute of Technology
42 Carleton Street
Cambridge, MA 02142

Dr. Zoltan A. Der
Teledyne Geotech
314 Montgomery Street
Alexandria, VA 22314

Prof. Adam Dziewonski
Hoffman Laboratory
Harvard University
20 Oxford St.
Cambridge, MA 02138

Professor John Ferguson
Center for Lithospheric Studies
The University of Texas at Dallas
P.O. Box 830688
Richardson, TX 75083-0688

Dr. Jeffrey W. Given
Sierra Geophysics
11255 Kirkland Way
Kirkland, WA 98033

Prof. Roy Greenfield
Geosciences Department
403 Deike Building
The Pennsylvania State University
University Park, PA 16802

Professor David G. Harkrider
Seismological Laboratory
Division of Geological and Planetary
    Sciences
California Institute of Technology
Pasadena, CA 91125

Professor Donald V. Helmberger
Seismological Laboratory
Division of Geological and Planetary
    Sciences
California Institute of Technology
Pasadena, CA 91125

Professor Eugene Herrin
Institute for the Study of Earth & Man
Geophysical Laboratory
Southern Methodist University
Dallas, TX 75275

Professor Robert B. Herrmann
Department of Earth and Atmospheric
    Sciences
Saint Louis University
Saint Louis, MO 63156

Professor Lane R. Johnson
Seismographic Station
University of California
Berkeley, CA 94720

Professor Thomas H. Jordan
Department of Earth, Atmospheric and
    Planetary Sciences
Massachusetts Institute of Technology
Cambridge, MA 02139

Dr. Alan Kafka
Department of Geology & Geophysics
Boston College
Chestnut Hill, MA 02167

Professor Charles A. Langston
Geosciences Department
403 Deike Building
The Pennsylvania State University
University Park, PA 16802

Professor Thorne Lay
Department of Geological Sciences
1006 C.C. Little Building
University of Michigan
Ann Arbor, MI 48109-1063

Dr. George R. Mellman
Sierra Geophysics
11255 Kirkland Way
Kirkland, WA 98033

Professor Brian J. Mitchell
Department of Earth and Atmospheric
    Sciences
Saint Louis University
Saint Louis, MO 63156

Professor Thomas V. McEvilly
Seismographic Station
University of California
Berkeley, CA 94720

Dr. Keith L. McLaughlin
Teledyne Geotech
314 Montgomery Street
Alexandria, VA 22314

Professor Otto W. Nuttli
Department of Earth and Atmospheric
    Sciences
Saint Louis University
Saint Louis, MO 63156

Professor Paul G. Richards
Lamont-Doherty Geological Observatory
 of Columbia University
Palisades, NY 10964

Dr. Norton Rimer
S-Cubed
A Division of Maxwell Laboratory
P.O. 1620
La Jolla, CA 92038-1620

Professor Larry J. Ruff
Department of Geological Sciences
1006 C.C. Little Building
University of Michigan
Ann Arbor, MI 48109-1063

Professor Charles G. Sammis
Center for Earth Sciences
University of Southern California
University Park
Los Angeles, CA 90089-0741

Dr. David G. Simpson
Lamont-Doherty Geological Observatory
  of Columbia University
Palisades, NY 10964

Dr. Jeffrey L. Stevens
S-CUBED,
A Division of Maxwell Laboratory
P.O. Box 1620
La Jolla, CA 92038-1620

Professor Brian Stump
Institute for the Study of Earth
    and Man
Geophysical Laboratory
Southern Methodist University
Dallas, TX 75275

Professor Ta-liang Teng
Center for Earth Sciences
University of Southern California
University Park
Los Angeles, CA 90089-0741

Dr. R. B. Tittmann
Rockwell International Science Center
1049 Camino Dos Rios
P.O. Box 1085
Thousand Oaks, CA 91360

Professor M. Nafi Toksoz
Earth Resources Laboratory
Department of Earth, Atmospheric and
    Planetary Sciences
Massachusetts Institute of Technology
42 Carleton Street
Cambridge, MA 02142

Professor Terry C. Wallace
Department of Geosciences
Building #11
University of Arizona
Tucson, AZ 85721

Prof. John H. Woodhouse
Hoffman Laboratory
Harvard University
20 Oxford St.
Cambridge, MA 02138

Dr. G. Blake
US Dept of Energy/DP 331
Forrestal Building
1000 Independence Ave.
Washington, D.C. 20585

Dr. Michel Bouchon
Universite Scientifique et
    Medicale de Grenoble
Laboratoire de Geophysique
Interne et Tectonophysique
I.R.I.G.M.-B.P. 68
38402 St. Martin D'Heres
Cedex FRANCE

Dr. Hilmar Bungum
NTNF/NORSAR
P.O. Box 51
Norwegian Council of Science,
Industry and Research, NORSAR
N-2007 Kjeller, NORWAY

Dr. Alan Douglas
Ministry of Defense
Blacknest, Brimpton, Reading RG7-4RS
UNITED KINGDOM

Professor Peter Harjes
Institute for Geophysik
Rhur University
Bochum
P.O. Box 102148
4630 Bochum 1
FEDERAL REPUBLIC OF GERMANY

Dr. James Hannon
Lawrence Livermore National Laboratory
P.O. Box 808
Livermore, CA 94550

Dr. E. Husebye
NTNF/NORSAR
P.O. Box 51
N-2007 Kjeller, NORWAY

Dr. Arthur Lerner-Lam
Lamont-Doherty Geological Observatory
        of Columbia University
Palisades, NY 10964

Mr. Peter Marshall
Procurement Executive
Ministry of Defense
Blacknest, Brimpton, Reading RG7-4F"
UNITED KINGDOM

Dr. B. Massinon
Societe Radiomana
27, Rue Claude Bernard
75005, Paris, FRANCE

Dr. Pierre Mechler
Societe Radiomana
27, Rue Claude Bernard
75005, Paris, FRANCE

Mr. Jack Murphy
S-CUBED
Reston Geophysics Office
11800 Sunrise Valley Drive
Suite 1212
Reston, VA 22091

Dr. Svein Mykkeltveit
NTNF/NORSAR
P.O. Box 51
N-2007 Kjeller, NORWAY

Dr. Carl Newton
Los Alamos National Laboratory
P.O. Box 1663
Mail Stop C 335, Group ESS3
Los Alamos, NM 87545

Dr. Peter Basham
Earth Physics Branch
Department of Energy and Mines
1 Observatory Crescent
Ottawa, Ontario
CANADA   K1A 0Y3

Professor J. A. Orcutt
Geological Sciences Division
Univ. of California at San Diego
La Jolla, CA 92093

Dr. Frank F. Pilotte
Director of Geophysics
Headquarters Air Force Technical
   Applications Center
Patrick AFB, Florida 32925-6001

Professor Keith Priestley
University of Nevada
Mackay School of Mines
Reno, Nevada 89557

Mr. Jack Raclin
USGS - Geology, Rm 3C136
Mail Stop 928 National Center
Reston, VA 22092

Dr. Frode Ringdal
NTNF/NORSAR
P.O. Box 51
N-2007 Kjeller, NORWAY

Dr. George H. Rothe
Chief, Research Division
Geophysics Directorate
Headquarters Air Force Technical
   Applications Center
Patrick AFB, Florida 32925-6001

Dr. Alan S. Ryall, Jr.
Center for Seismic Studies
1300 North 17th Street
Suite 1450
Arlington, VA 22209-2308

Dr. Jeffrey L. Stevens
S-CUBED,
A Division of Maxwell Laboratory
P.O. Box 1620
La Jolla, CA 92038-1620

Dr. Lawrence Turnbull
OSWR/NED
Central Intelligence Agency
CIA, Room 5G48
Washington, DC 20505

Professor Steven Grand
Department of Geology
245 Natural History Bldg
1301 West Green Street
Urbana, IL 61801

DARPA/PM
1400 Wilson Boulevard
Arlington, VA 22209

Defense Technical Information Center
Cameron Station
Alexandria, VA 22314   (12 copies)

Defense Intelligence Agency
Directorate for Scientific and
  Technical Intelligence
Washington, D.C. 20301

Defense Nuclear Agency
Shock Physics Directorate/SS
Washington, D.C. 20305

Defense Nuclear Agency/SPSS
ATTN: Dr. Michael Shore
6801 Telegraph Road
Alexandria, VA 22310

AFOSR/NPG
ATTN: Director
Bldg 410, Room C222
Bolling AFB, Washington, D.C. 20332

AFTAC/CA (STINFO)
Patrick AFB, FL 32925-6001

AFWL/NTESC
Kirtland AFB, NM 87171

U.S. Arms Control & Disarmament Agency
ATTN: Mrs. M. Hoinkes
Div. of Multilateral Affairs, Rm 5499
Washington, D.C. 20451

U.S. Geological Survey
ATTN: Dr. T. Hanks
National Earthquake Research Center
345 Middlefield Road
Menlo Park, CA 94025

SRI International
333 Ravensworth Avenue
Menlo Park, CA 94025

Center for Seismic Studies
ATTN: Dr. C. Romney
1300 North 17th Street
Suite 1450
Arlington, VA 22209   (3 copies)

Dr. Robert Blandford
DARPA/GSD
1400 Wilson Boulevard
Arlington, VA 22209-2308

Ms. Ann Kerr
DARPA/GSD
1400 Wilson Boulevard
Arlington, VA 22209-2308

Dr. Ralph Alewine III
DARPA/GSD
1400 Wilson Boulevard
Arlington, VA 22209-2308

Mr. Edward Giller
Pacific Sierra Research Corp.
1401 Wilson Boulevard
Arlington, VA 22209

Science Horizons, Inc.
Attn: Dr. Bernard Minster
       Dr. Theodore Cherry
710 Encinitas Blvd., Suite 101
Encinitas, CA 92024   (2 copies)

Dr. Jack Evernden
USGS - Earthquake Studies
345 Middlefield Road
Menlo Park, CA 94025

Dr. Lawrence Braile
Department of Geosciences
Purdue University
West Lafayette, IN 47907

Dr. G.A. Bollinger
Department of Geological Sciences
Virginia Polytechnical Institute
21044 Derring Hall
Blacksburg, VA 24061

Dr. L. Sykes
Lamont Doherty Geological Observatory
Columbia University
Palisades, NY 10964

Dr. S.W. Smith
Geophysics Program
University of Washington
Seattle, WA 98195

Dr. L. Timothy Long
School of Geophysical Sciences
Georgia Institute of Technology
Atlanta, GA 30332

Dr. N. Biswas
Geophysical Institute
University of Alaska
Fairbanks, AK 99701

Dr. Freeman Gilbert
Institute of Geophysics &
Planetary Physics
Univ. of California at San Diego
P.O. Box 109
La Jolla, CA 92037

Dr. Pradeep Talwani
Department of Geological Sciences
University of South Carolina
Columbia, SC 29208

University of Hawaii
Institute of Geophysics
Attn: Dr. Daniel Walker
Honolulu, HI 96822

Dr. Donald Forsyth
Department of Geological Sciences
Brown University
Providence, RI 02912

Dr. Jack Oliver
Department of Geology
Cornell University
Ithaca, NY 14850

Dr. Muawia Barazangi
Geological Sciences
Cornell University
Ithaca, NY 14853

Rondout Associates
Attn: Dr. George Sutton
Dr. Jerry Carter
Dr. Paul Pomeroy
P.O. Box 224
Stone Ridge, NY 12484 (3 copies)

Dr. M. Sorrells
Geotech/Teledyne
P.O. Box 28277
Dallas, TX 75228

Dr. Bob Smith
Department of Geophysics
University of Utah
1400 East 2nd South
Salt Lake City, UT 84112

Dr. Anthony Gangi
Texas A&M University
Department of Geophysics
College Station, TX 77843

Dr. Gregory B. Young
ENSCO, Inc.
5400 Port Royal Road
Springfield, CA 22151

Dr. Ben Menaheim
Weizman Institute of Science
Rehovot, ISRAEL 951729

Weidlinger Associates
Attn: Dr. Gregory Wojcik
620 Hansen Way, Suite 100
Palo Alto, CA 94304

Dr. Leon Knopoff
University of California
Institute of Geophysics & Planetary
Physics
Los Angeles, CA 90024

Dr. Kenneth H. Olsen
Los Alamos Scientific Laboratory
Post Office Box 1663
Los Alamos, NM 87545

Prof. Jon F. Claerbout
Prof. Amos Nur
Dept. of Geophysics
Stanford University
Stanford, CA 94305   (2 copies)

Dr. Robert Burridge
Schlumberger-Doll Research Ctr.
Old Quarry Road
Ridgefield, CT 06877

Dr. Eduard Berg
Institute of Geophysics
University of Hawaii
Honolulu, HI 96822

Dr. Robert Phinney
Dr. F.A. Dahlen
Dept. of Geological & Geophysical Sci.
Princeton University
Princeton, NJ 08540   (2 copies)

Dr. Kin-Yip Chun
Geophysics Division
Physics Department
University of Toronto
Ontario, CANADA M5S 1A7

New England Research, Inc.
Attn: Dr. Randolph Martin III
P.O. Box 857
Norwich, VT 05055

Sandia National Laboratory
Attn: Dr. H.B. Durham
Albuquerque, NM 87185

Dr. Gary McCartor
Mission Research Corp.
735 State Street
P. O. Drawer 719
Santa Barbara, CA 93102

Dr. W. H. K. Lee
USGS
Office of Earthquakes, Volcanoes,
    & Engineering
Branch of Seismology
345 Middlefield Rd
Menlo Park, CA 94025

AFGL/XO
Hanscom AFB, MA 01731-5000

AFGL/LW
Hanscom AFB, MA 01731-5000

AFGL/SULL
Research Library
Hanscom AFB, MA 01731-5000_ (2 copies)

Secretary of the Air Force (SAFRD)
Washington, DC 20330

Office of the Secretary Defense
DDR & E
Washington, DC 20330

HQ DNA
Attn: Technical Library
Washington, DC 20305

Director, Technical Information
DARPA
1400 Wilson Blvd.
Arlington, VA 22209

Los Alamos Scientific Laboratory
Attn: Report Library
Post Office Box 1663
Los Alamos, NM 87544

Dr. Thomas Weaver
Los Alamos Scientific Laboratory
Los Alamos, NM 87544

Dr. Al Florence
SRI International
333 Ravenswood Avenue
Menlo Park, CA 94025-3493